

Radial Force Control of Bearingless Multi-Sector Permanent Magnet Machines

Giorgio Valente

Submitted to the University of Nottingham for the degree of Doctor of Philosophy, May 2018.

Abstract

The radial force control has been widely investigated for a variety of machine topologies aiming at the reduction of the mechanical stress on bearings as well as the overall vibration. Furthermore, it can be also applied to bearingless drives where the force control can be exploited to suspend the rotor element. Traditional radial force control techniques rely on two independent sets of windings dedicated to torque and suspension force, respectively. However, different winding structures can be employed to reduce the overall system complexity. Multiphase machines, in particular, offer the possibility to embed the radial force and torque generation in a single winding set and possess an enhanced fault tolerant capability.

This thesis presents an alternative radial force and torque control technique for a multiphase sectored permanent magnet synchronous machine. The mathematical model of the machine and the theoretical investigation of the force production principle are provided. A force control methodology based on the minimization of the copper losses is described and adopted to calculate the d-q axis current references. The predicted performances of the test machine are benchmarked against finite elements analysis.

An experimental rig has been manufactured in order to validate the radial force and torque control. The experimental validation focuses on the suppression of selected vibration frequencies at different speeds.

The radial force control has been also exploited to levitate the rotor in order to obtain a two degrees of freedom bearingless drive. The fault tolerant capabilities have been investigated and experimentally tested considering the open-circuit of one three-phase winding. The tuning of the $x - y$ axis position controller has been investigated and a state space approach has been followed to synthesize different position controllers.

The manuscript is organised as follow:

- Chapter 1: introduction. The content and objectives of the PhD project are presented and the definitions of active magnetic bearings and bearingless machines are given.

- Chapter 2: literature review and state of the art of the radial force control and of the bearingless and multiphase machine technology.

- Chapter 3: electromagnetic model of the machine considered. The latter is characterized in terms of voltage equations. The mathematical model of the force and torque generation is then presented for healthy and open-circuit fault operating conditions and a reference current computation strategy is proposed.

- Chapter 4: position controller design. A transfer function-based approach is followed at first to calculate the controller gains. The controller synthesis is then obtained in the state space domain taking into account its robustness. A more complex controller is presented consisting of parallel-connected resonant controllers in order to suppress position oscillations caused by period force disturbances.

- Chapter 5: finite elements and numerical simulation results of the force and torque production and of the bearingless operations in both healthy and open-circuit fault operating conditions.

- Chapter 6: experimental validation of the torque and radial force technique presented. The experimental rig is described in all its parts. The force control is exploited to suppress selected vibration detected on the motor housing at different speeds. In this test the rotor is equipped with mechanical ball bearings. The position control is then validated performing a two degrees of freedom levitation in both healthy and faulty operating conditions.

- Chapter 7: summary of achievements, conclusions and tasks for future works.

Acknowledgements

I would like to thank my supervisors for the patient and continuous guidance and encouragement they have provided during my PhD studies and for sharing their scientific knowledge and experience.

I must thank the numerous colleagues, PhD students and researchers, with whom I shared moments of frustration and excitement throughout this long process sometimes felt as extremely lonely. I am also grateful to them for never refusing technical advices when needed.

Last but not least, a very special thank goes to my parents for the unconditional support and encouragement throughout my studies.

List of Terms

BM - Bearingless Motor

AMB - Active Magnetic Bearing

DC - Direct Current

AC - Alternated Current

PM - Permanent Magnet

$BPMSM$ - Bearingless Permanent Magnet Synchronous Motor

UMP - Unbalanced Magnetic Pull

DOF - Degree of Freedom

$DAVC$ - Direct Active Vibration Control

EMF - Electro-Motive Force

$MSPM$ - Multi-Sector Permanent Magnet

VSD - Vector Space Decomposition

FEA - Finite Elements Analysis

PID - Proportional-Integral-Derivative

LQR - Linear Quadratic Regulator

LMI - Linear Matrix Inequality

MRC - Multi-Resonant Controller

FFT - Fast Fourier Transformation

THD - Total Harmonic Distortion

PIM - Pseudo Inverse Matrix

FTD - Force Torque Decoupled

$HFTD$ - Harmonic Force Torque Decoupled

ISF - Incremental Scale Factor

$FPGA$ - Field Programmable Gate Array

Nomenclature

s - Sector number label.

p - Pole pairs number.

ϑ_e - Electrical rotor angular position [rad].

ϑ_m - Mechanical rotor angular position [rad].

ω_e - Electrical rotating speed [rad/s].

${}^s\gamma$ - Angular position of the magnetic axis of sector s with respect the $x-$ axis [rad].

γ_0 - Angular position of the magnetic axis of sector 1 with respect the $x-$ axis [rad].

n_s - Number of sectors.

B_{res} - PM remanence flux density [T].

R_g - Mid-airgap radius [m].

μ_r - PM relative permeability.

I_{rated} - Rated peak current [A].

v_{rated} - Rated speed [rpm].

N_c - Number of turns.

${}^s\Lambda_{PM}$ - PM flux of one sector [Wb].

k_T - Torque constant [Nm/A].

k_V - Line to line voltage constant [V/krpm].

l - Active machine length [m].

g_0 - Airgap length [m].

h_m - Magnet thickness [m].

t - Time [s].

$\bar{v}$ - vector of the nine-phase voltages.

$\bar{i}$ - vector of the nine-phase currents.

$\bar{\lambda}$ - vector of the nine-phase fluxes.

$\bar{\lambda}_{PM}$ - vector of the nine-phase fluxes produced by the PM.

$\bar{\lambda}_i$ - vector of the nine-phase fluxes produced by the currents.

${}^1v_u$ - Voltage of phase u_1 [V].

${}^1v_v$ - Voltage of phase v_1 [V].

${}^1v_w$ - Voltage of phase w_1 [V].

${}^2v_u$ - Voltage of phase u_2 [V].

${}^2v_v$ - Voltage of phase v_2 [V].

${}^2v_w$ - Voltage of phase w_2 [V].

${}^3v_u$ - Voltage of phase u_3 [V].

${}^3v_v$ - Voltage of phase v_3 [V].

${}^3v_w$ - Voltage of phase w_3 [V].

${}^1i_u$ - Current of phase u_1 [A].

${}^1i_v$ - Current of phase v_1 [A].

${}^1i_w$ - Current of phase w_1 [A].

${}^2i_u$ - Current of phase u_2 [A].

${}^2i_v$ - Current of phase v_2 [A].

${}^2i_w$ - Current of phase w_2 [A].

${}^3i_u$ - Current of phase u_3 [A].

${}^3i_v$ - Current of phase v_3 [A].

${}^3i_w$ - Current of phase w_3 [A].

${}^1\lambda_u$ - Flux linkage to phase u_1 [Wb].

${}^1\lambda_v$ - Flux linkage to phase v_1 [Wb].

${}^1\lambda_w$ - Flux linkage to phase w_1 [Wb].

${}^2\lambda_u$ - Flux linkage to phase u_2 [Wb].

${}^2\lambda_v$ - Flux linkage to phase v_2 [Wb].

${}^2\lambda_w$ - Flux linkage to phase w_2 [Wb].

${}^3\lambda_u$ - Flux linkage to phase u_3 [Wb].

${}^3\lambda_v$ - Flux linkage to phase v_3 [Wb].

${}^3\lambda_w$ - Flux linkage to phase w_3 [Wb].

${}^1e_u$ - Bak-EMF of phase u_1 [V].

${}^1e_v$ - Bak-EMF of phase v_1 [V].

${}^1e_w$ - Bak-EMF of phase w_1 [V].

${}^2e_u$ - Bak-EMF of phase u_2 [V].

${}^2e_v$ - Bak-EMF of phase v_2 [V].

${}^2e_w$ - Bak-EMF of phase w_2 [V].

${}^3e_u$ - Bak-EMF of phase u_3 [V].

${}^3e_v$ - Bak-EMF of phase v_3 [V].

${}^3e_w$ - Bak-EMF of phase w_3 [V].

$\mathbf{R}$ - Resistance matrix of the machine.

R_{ph} - Phase resistance [Ohm].

$\mathbf{L}_{ph}$ - Phase inductance matrix of the machine.

$\mathbf{T}_{P,9}$ - Nine-phase Park direct transformation.

$\mathbf{T}_{P,9}^{-1}$ - Nine-phase Park inverse transformation.

$\mathbf{T}_P$ - Three-phase Park direct transformation.

$\mathbf{T}_P^{-1}$ - Three-phase Park inverse transformation.

$\bar{v}_{dq}$ - vector of the $d-q$ axis voltages of the machine.

$\bar{i}_{dq}$ - vector of the $d-q$ axis currents of the machine.

$\bar{e}_{dq}$ - vector of the $d-q$ axis back-EMFs of the machine.

$\mathbf{L}_{dq,t}$ - $d-q$ axis inductance matrix of the machine.

$\mathbf{L}$ - Self-inductance matrix of one sector.

$\mathbf{M}$ - Mutual inductance matrix between two sectors.

L_{uu} - Self-inductance of phase u [H].

L_{vv} - Self-inductance of phase v [H].

L_{ww} - Self-inductance of phase w [H].

M_{uv} - Mutual inductance between phases u and v [H].

M_{uw} - Mutual inductance between phases u and w [H].

M_{vw} - Mutual inductance between phases v and w [H].

M_c - Mutual inductance between phases of different sectors [H].

$\mathbf{L}_{dq}$ - $d-q$ self-inductance matrix of one sector.

$\mathbf{M}_{dq}$ - $d-q$ mutual inductance matrix between two sectors.

α_s - Stator angular position [rad].

B_r - Total radial airgap flux density [T].

B_ϑ - Totoal tangential airgap flux density [T].

$B_{r,PM}$ - Radial airgap flux density produced by the PM [T].

$B_{\vartheta,PM}$ - Tangential airgap flux density produced by the PM [T].

$B_{r,w2}$ - Second harmonic of the radial airgap flux density produced by the winding [T].

$B_{\vartheta,w2}$ - Second harmonic of the tangential airgap flux density produced by the winding [T].

$B_{r,w4}$ - Forth harmonic of the radial airgap flux density produced by the winding [T].

$B_{\vartheta,w4}$ - Forth harmonic of the tangential airgap flux density produced by the winding [T].

σ - Radial Maxwell stress tensor [Pa].

τ - Tangential Maxwell stress tensor [Pa].

T_E - Electromagnetic torque [Nm].

$F_{E,x}$ - $x-$ axis electromagnetic force [N].

$F_{E,y}$ - $y-$ axis electromagnetic force [N].

$F_{E,z}$ - $z-$ axis electromagnetic force [N].

${}^s\mathbf{K}_E$ - Matrix of the force and torque coefficients of one sector.

${}^s\mathbf{K}_{E,F}$ - Matrix of the force coefficients of one sector.

${}^s\bar{K}_{E,T}$ - Matrix of the torque coefficients of one sector.

${}^s\bar{i}_{\alpha\beta}$ - vector of the $\alpha-\beta$ axis currents of one sector.

${}^s\bar{i}_{dq}$ - vector of the $d-q$ axis currents of one sector.

δ - Amplitude of the rotor radial displacement [m].

Φ_d - Angle of the rotor radial displacement [rad].

k_m - Magnetic stiffness [N/m].

P_{cu} - Copper losses of the machine [W].

$\mathbf{K}_{E,f1}$ - Matrix of the force and torque coefficients of the machine for open-circuit fault in sector 1.

$\mathbf{K}_{E,f2}$ - Matrix of the force and torque coefficients of the machine for open-circuit fault in sector 2.

$\mathbf{K}_{E,f3}$ - Matrix of the force and torque coefficients of the machine for open-circuit fault in sector 3.

m - Machine mass [kg].

J_d - Machine diametral moment of inertia [kgm^2].

J_p - Machine polar moment of inertia [kgm^2].

$G(s)$ - Mechanical plant transfer function.

k_p - Controller proportional gain.

k_i - Controller integral gain.

k_d - Controller derivative gain.

ω_c - First order low-pass filter cut-off frequency.

$T_{dq}(s)$ - Transfer function from disturb to output position.

x_p - State vector of the mechanical plant.

y_p - Output of the mechanical plant.

u_p - Input of the mechanical plant.

A_p - State matrix of the mechanical plant.

B_p - Input matrix of the mechanical plant.

C_p - Output matrix of the mechanical plant.

e - Integrator state.

x_B - State vector of the plant extended with the integrator.

u_B - Input of the plant extended with the integrator.

A_B - State matrix of the plant extended with the integrator.

B_B - Input matrix of the plant extended with the integrator.

K_B - Feedback gain vector of the basic controller.

J_{LQR} - Cost function of the LQR.

Q_B - State weight matrix for the basic controller.

R_B - Input weight matrix for the basic controller.

x_f - Filter state.

A_{pf} - State matrix of the plant extended with the filter.

B_{pf} - Input matrix of the plant extended with the filter.

x_{pf} - State vector of the plant extended with the filter.

u_{pf} - Input of the plant extended with the filter.

A - State matrix of the plant extended with the integrator and filter.

B_2 - Input matrix of the plant extended with the integrator and filter.

C - Output matrix of the plant extended with the integrator and filter.

x - State vector of the plant extended with the integrator and filter.

u - Input of the plant extended with the integrator and filter.

K_e - Feedback gain vector of the improved controller.

Q - State weight matrix for the improved controller.

R - Input weight matrix for the improved controller.

$S(s)$ - Sensitivity function.

M_s - Maximum of the sensitivity function.

$L(s)$ - Open loop transfer function of the controller and mechanical plant.

J_2 - H_2 norm.

J_∞ - H_∞ norm.

$x_{r,n}$ - State vector of the n^{th} order resonant.

$y_{r,n}$ - Output of the n^{th} order resonant.

$u_{r,n}$ - Input of the n^{th} order resonant.

$A_{r,n}$ - State matrix of the n^{th} order resonant.

$B_{r,n}$ - Input matrix of the n^{th} order resonant.

$C_{r,n}$ - Output matrix of the n^{th} order resonant.

x_r - State vector of the n^{th} order resonant.

y_r - Output of the MRC.

u_r - Input of the MRC.

A_r - State matrix of the MRC.

B_r - Input matrix of the MRC.

C_r - Output matrix of the MRC.

$\hat{Q}$ - State weight matrix for the improved controller and MRC.

Contents

1 Introduction **2**

1.1 Objectives of the PhD project 2

1.2 Definition of Bearingless Machines 3

1.3 Chapter Summary 5

2 Literature Review **6**

2.1 Introduction 6

2.2 Radial Force Control and its Applications 7

2.3 Overview of Bearingless Machines 10

2.3.1 Theoretical Description 10

2.3.1.1 Force production principle 10

2.3.1.2 Mathematical model 11

2.3.2 Classification of BM by the number of actively controlled DOF 13

2.3.2.1 1-DOF ($z-$axis) 13

2.3.2.2 2-DOF ($x-y$ axis) 14

2.3.2.3 3-DOF ($x-y-z$ axis) 15

2.3.2.4 4-DOF ($x-y$ axis and ϑ_x, ϑ_y tilting movement) . . . 15

2.3.2.5 5-DOF ($x-y-z$ axis and ϑ_x, ϑ_y tilting movement) 16

2.3.3 Bearingless motor topologies 16

2.3.3.1 DC brushless motors 16

2.3.3.2 Reluctance motors 17

2.3.3.3 Permanent magnet motors 17

2.3.3.4 Induction motors 18

2.4 Radial force and torque generation strategies 19

2.4.1 Separate torque and suspension windings 20

2.4.2 Single three-phase winding structure with parallel path 24

2.4.3 Five-phase winding with multiple orthogonal d-q planes for force and torque generation 26

2.4.4 Six-phase winding structure with fault-tolerant capability . . . 28

2.4.5 Triple three-phase winding structure with decoupled torque and radial force control 30

2.4.6 Triple three-phase winding structure with Vector Space Decomposition (VSD) method employed for the force and torque control 32

2.5 Multi-Phase Motors 34

2.5.1 Applications 34

2.5.2 Modelling 35

2.5.2.1 Modelling in Park's coordinates 35

2.5.2.2 Vector-Space Decomposition 37

2.5.3 Fault tolerant capabilities 39

2.6 Levitating Systems for Vibration Suppression 40

2.7 Chapter Summary 42

3 Electromagnetic Model of the Multi-Sector PM Synchronous Machine 43

3.1 Introduction 43

3.2 $d-q$ Axis Voltage Equation Model in State Space 45

3.2.1 The machine structure 45

3.2.2 State space representation of the $d-q$ axis voltage equation . 47

3.2.3 Matrix representation of the $d-q$ axis inductances 51

3.2.4 Calculation of the $d-q$ axis inductance values 54

3.3 Mathematical Model of the Torque and Force Generation 59

3.3.1 Torque and force generation principle 59

3.3.2 Matrix formulation neglecting the rotor radial displacement . 63

3.3.3 Matrix coefficients calculation 66

3.3.3.1 Torque coefficients 66

3.3.3.2 Force coefficients 68

3.3.4 Matrix formulation considering the rotor radial displacement . 74

3.4 Reference Current Calculation Technique 78

3.4.1 Problem formulation 78

3.4.2 Problem solution 79

3.4.3 Open-circuit fault of one sector 83

3.5 Chapter Summary 87

4 Radial Position Control Design **88**

4.1 Introduction 88

4.2 Transfer Function-Based Design Method 89

4.2.1 The rotor dynamic system 89

4.2.2 Standard Controller Designed with a Transfer Function-Based Method 92

4.2.3 Numerical values of the controller gains 95

4.3 State Space Design 99

4.3.1 State Space Rotor-Dynamic Model of the Mechanical Plant . . 99

4.3.2 Standard position controller 101

4.3.2.1 Basic controller 102

4.3.2.2 Improved controller 103

4.4 Robustness Analysis 106

4.4.1 Generalities of the robustness analysis 106

4.4.2 H_2 optimal control 108

4.4.3 H_∞ method 109

4.5 Integration of MRC in the standard position control 112

4.6 Gain Calculation 115

4.6.1 Gain calculation in the whole frequency range 115

4.6.2 Numerical values of the controllers gains 117

4.7 Conclusions 121

5 Simulation Results **123**

5.1 Introduction 123

5.2 FE Simulation Results 124

5.2.1 Healthy operating condition and centred rotor 125

5.2.2 Open-circuit operating condition 130

5.2.3 Eccentric rotor 137

5.2.3.1 Static eccentricity 138

5.2.3.2 Dynamic eccentricity 139

5.2.4 Comparison with different force and torque generation techniques 140

5.2.5 Joule losses calculation 145

5.3 Numerical Simulation Results 148

5.3.1 Structure of the Simulation Model 148

5.3.2 2-DOF levitation the standard controller designed with the transfer function-based method 151

5.3.2.1 Healthy operating condition 152

5.3.2.2 Open-circuit fault 156

5.3.3 2-DOF levitation using standard and MR controllers designed in state space 160

5.4 Conclusions 162

6 Experimental Results **164**

6.1 Introduction 164

6.2 Experimental Rig Design 165

6.2.1 Mechanical Structure 165

6.2.2 Power converters and control platform 169

6.2.3 Vibration Transducer System 171

6.2.4 Proximity Transducer System 172

6.3 Electrical Parameters Identification 175

6.3.1 Back-EMF 176

6.3.2 Machine inductances 178

6.4 Vibration Suppression Results 181

6.4.1 No load vibration spectrum 181

6.4.2 Vibration suppression 183

6.4.3 Post-processing analysis 185

6.5 Bearingless Operation 191

6.5.1 Preliminary tests 191

6.5.2 Levitation results for the standard controller designed with pole placement method 197

6.5.2.1 Healthy operation 197

6.5.2.2 Open-circuit fault 202

6.5.3 Levitation results for the standard and the MR controller designed in state space 206

6.6 Conclusions 210

7 Conclusions **212**

7.1 Summary of Achievements and Conclusion 212

7.2 Future Work 214

A Invertion Matrix Verification **217**

B Flux Density Prediction **220**

B.1 No rotor displacement 221

B.2 Rotor displacement 227

C $d-q$ Axis Reference Current Calculation **230**

C.1 Healthy operating condition 230

C.2 Open-circuit operating condition 232

D Published Papers **236**

List of Figures

1.1 Machines configurations to reach the full rotor levitation: a) 2 AMBs b) 1 AMB and 1 BM 4

2.1 Schematic representation of the balancer [1] 8

2.2 Rigid rotor free to move with six-DOF in the three-dimensional space. 13

2.3 PM bearingless motor rotor topologies: a) Surface mounted. b) Inset. c) Interior. [2] 17

2.4 Force generation principles: a) $x-$axis force generation. b) $y-$axis force generation. The 4-pole motor winding and the 2-pole suspension force winding are represented in the $\alpha - \beta$ reference frame in the picture. 21

2.5 Block diagram of the control algorithm 23

2.6 Parallel path winding structure. a) Schematic of the motor and suspension inverter connections. b) Force generation principle for phase u. [3] 24

2.7 Cross section of a six-phase PMSM [4] 28

2.8 Cross section of the sectored BPMSM [5] 30

3.1 Cross section of the 18 slot - 6 poles 3 sectors PMSM with three single layer distributed three-phase windings. 45

3.2 FE and analytical results for the phase inductances: a) waveforms of the inductances; b) FFT of the inductance waveforms obtained with FEA. 57

3.3 $d-q$ axis inductances: a) elements of $\mathbf{L}_{dq}(\vartheta_e)$; b)elements of $\mathbf{M}_{dq}(\vartheta_e)$ 58

3.4 3^{rd}, 2^{nd} and 4^{th} spatial harmonic distributions of the PM and winding flux densities for a generic rotor position ϑ_e: a) radial components; b) tangential components. 61

3.5 FE and analytical torque coefficient against rotor angular position. . 66

3.6 Analytical and FE torque trend as a function of the i_q current. 67

3.7 FE and analytical force coefficient against the rotor angular position: a) $x-$axis coefficients; b) $y-$axis coefficients. 68

3.8 Amplitude of harmonic decomposition of the force coefficients obtained with FEA. 71

3.9 Magnitude of the force coefficients as a function of the current: a) ${}^1K_{x\alpha}$ vs i_α; b) ${}^1K_{x\beta}$ vs i_β; c) ${}^1K_{y\alpha}$ vs i_α; d) ${}^1K_{y\beta}$ vs i_β. The picture shows the analytical and both linear and non-linear FE trends. 72

3.10 Flux density at no-load operating condition and at I_{rated} and 25 A $\alpha-$axis current supplied to sector 1. 73

3.11 Cross-section of the eccentric rotor with stator and rotor reference frames. 74

3.12 Open-circuit $x-y$ force components $F_{x,ecc}$ and $F_{y,ecc}$ as a function of the rotor eccentricity: a) varying δ at $\phi_d = 0$; b) varying ϕ_d at $\delta = \delta_{max}$. 76

3.13 Torque production for centred and eccentric rotor ($\delta = \delta_{max}$). 77

3.14 Variation of the force coefficients amplitudes against the rotor displacement δ. 77

3.15 Coefficients of the pseudo inverse matrix. $\mathbf{K}_E^+(r,c)$ stands for the coefficient in the r^{th} row and c^{th} column. 82

3.16 Comparison in terms of harmonic content between the coefficients of matrix $\mathbf{K}_E^+$ (healthy machine), matrix $\mathbf{K}_{E,f1}^+$ (fault in sector 1), matrix $\mathbf{K}_{E,f2}^+$ (fault in sector 2) and matrix $\mathbf{K}_{E,f3}^+$ (fault in sector 3). 86

4.1 Schematic representation of the rotor fixed to the self-alignment bearing and geometrical reference frame representation: a) $x-$ axis rotor view; b) $y-$ axis rotor view. 89

4.2 Structure of the radial position controller. 92

4.3 Poles map of the overall system (controller together with mechanical plant) for coincident and Butterworth pole configuration. 97

4.4 Step response of the overall system (controller together with mechanical plant) for coincident and Butterworth pole configuration. 97

4.5 Bode diagram of the closed loop transfer function $T_{dq}(s)$ for coincident and Butterworth pole configuration. 98

4.6 Representation of the mechanical plant. 100

4.7 Block scheme of the basic position controller. 102

4.8 Block scheme of the standard position controller including the low-pass filter. 103

4.9 Block scheme of the standard position controller where the mechanical plant has been extended with the low-pass filter. 105

4.10 Basic closed loop control system. 106

4.11 Basic closed loop control system. 108

4.12 Schematic representation of the position control scheme with the low-pass filter and the disturbance signal. 110

4.13 Block scheme of the MR position controller. 114

4.14 Poles map of the MRC controller: a) tuning with a single speed value; b) tuning with different speed values to cover the whole speed range. 115

4.15 Sensitivity functions: a) standard controller; b) MRC in the whole speed range. 117

4.16 Poles map of the standard controller tuned with the LQR method for different values of q_i and with the LMI method with $q_i = 3e23$. 119

4.17 Bode diagram of the closed loop transfer function from disturb to output for standard controller and MR controller with $\omega_m = 50$ Hz. . . . 121

5.1 Force generation in healthy operating condition. Different force reference magnitudes $|F_E|$ and directions $\angle F_E$ are used. Zero and rated torque operating conditions are considered. 125

5.2 20 N force generation at zero and at rated torque. 126

5.3 Harmonic content of F_x and F_y with and without torque production: a) FFT of F_x; b) FFT of F_y 127

5.4 Torque generation in healthy operating condition for zero and 20 N force production. 128

5.5 Phase current required to generate $|F_E| = 200$ N in the $\angle F_E = 0$ direction and $T_E = 0$: a) phase current of sector 1; b) phase current of sector 2; c) phase current of sector 3. 129

5.6 Phase current required to generate $|F_E| = 20$ N in the $\angle F_E = 0$ direction at $T_E = 0$ and $T_E = T_{rated}$: a) phase current of sector 1; b) phase current of sector 2; c) phase current of sector 3. 130

5.7 Force and torque generation with open-circuit fault in sector 1: a) $x-y$ axis force production for $T_{ref} = 0$; b) $x - y$ axis force production for $T_{ref} = 2.7[Nm]$; c) torque production setting $T_{ref} = 2.7[Nm]$. 132

5.8 Force and torque generation with open-circuit fault in sector 2: a) $x-y$ axis force production for $T_{ref} = 0$; b) $x - y$ axis force production for $T_{ref} = 2.7[Nm]$; c) torque production setting $T_{ref} = 2.7[Nm]$. 133

5.9 Force and torque generation with open-circuit fault in sector 3: a) $x-y$ axis force production for $T_{ref} = 0$; b) $x - y$ axis force production for $T_{ref} = 2.7[Nm]$; c) torque production setting $T_{ref} = 2.7[Nm]$. 134

5.10 Phase current required to generate $|F_E| = 100$ N in the $\angle F_E = 0$ direction at $T_E = 0$ for healthy condition and open-circuit in sector 1: a) phase current of sector 1; b) phase current of sector 2; c) phase current of sector 3. 135

5.11 Harmonic content of the phase current i_{u2} in healthy condition and with fault in sector 1. 136

5.12 Difference between static and dynamic rotor eccentricity. 137

5.13 Force generation for static eccentricity with and without the force control: a) $\delta = 0.15$ mm, $\Phi_d = 0$ deg; b) $\delta = 0.15$ mm, $\Phi_d = 270$ deg; c) $\delta = 0.15$ mm, $\Phi_d = 150$ deg. 138

5.14 Force and torque generation for dynamic eccentricity with and without the force control: a) force generation; b) torque generation. 140

5.15 Amplitude gain k_h and direction angle error Φ_h: a) $k_h(\vartheta_e)$; b) $\Phi_h(\vartheta_e)$. 141

5.16 Comparison of the force generation with the PIM, FTD and HFTD methods: a) $|F_E| = 100$ N, $\angle(F) = 0$ deg ; b) $|F_E| = 100$ N, $\angle(F) = 60$ deg. 142

5.17 Comparison of the force and torque generation with the PIM, FTD and HFTD methods for $|F_E| = 20$ N, $\angle(F) = 0$ deg, $T_{ref} = 5$ Nm: a) force generation; b) torque generation. 143

5.18 Comparison of the magnitude THD and phase error between the PIM, FTD and HFTD methods for $|F_E| = 100$ N, $\angle(F) = 0$ deg. 144

5.19 Joule losses at rated torque operating condition with and without the 20 N force generation for the PIM method. 146

5.20 Joule losses at no-load with 100 N force generation for healthy and open-circuit fault operating conditions for the PIM method. 147

5.21 Joule losses at no-load with 100 N force generation for PIM, FTD and HFTD methods. 147

5.22 Overall control scheme of the bearingless MSPMSM. 148

5.23 Comparison of the current waveforms obtained with the analytical and FE models: a) stand still operation and DC voltage supply of the three sectors: $v_u = 1$ V, $v_v = -0.5$ V, $v_w = -0.5$ V; b) stand still operation and sinusoidal voltage supply of the three sectors: $v_u = \cos(2\pi 50t)$ V, $v_v = -\frac{1}{2}\cos(2\pi 50t - \frac{2\pi}{3})$ V, $v_w = -\frac{1}{2}\cos(2\pi 50t - \frac{4\pi}{3})$ V; c) 1000 [rpm] operating speed and sinusoidal voltage supply of the three sectors: $v_u = \cos(2\pi 50t)$ V, $v_v = -\frac{1}{2}\cos(2\pi 50t - \frac{2\pi}{3})$ V, $v_w = -\frac{1}{2}\cos(2\pi 50t - \frac{4\pi}{3})$ V. 150

5.24 Result of the numerical simulation for bearingless operation in healthy condition: a) $x - y$ axis rotor position; b) $x - y$ axis generated forces and $y-$axis force disturb. 153

5.25 Result of the numerical simulation for bearingless operation in healthy condition: a)rotor speed; b) generated torque. 154

5.26 Result of the numerical simulation for bearingless operation in healthy condition: :a) $d - q$ axis currents sect. 1; b) $d - q$ axis currents sect. 2; c) $d - q$ axis currents sect. 3. 155

5.27 Result of the numerical simulation for bearingless operation in open-circuit fault condition: a) $x - y$ axis rotor position; b) $x - y$ axis generated forces and $y-$axis force disturb. 157

5.28 Result of the numerical simulation for bearingless operation in open-circuit fault condition: a)rotor speed; b) generated torque. 158

5.29 Result of the numerical simulation for bearingless operation in open-circuit fault condition: :a) $d-q$ axis currents sect. 1; b) $d-q$ axis currents sect. 2; c) $d-q$ axis currents sect. 3. 159

5.30 Simulative comparison between standard and MR controllers during a speed transient: a) rotating speed; b) force disturbance; c) $x-y$ axis position with standard controller; d) $x-y$ axis position with MRC. . 161

6.1 Axial section of the mechanical parts of the rig. 165

6.2 Top view of the rig mechanical assembly. 166

6.3 Assembled mechanical rig: a) MSPM machine coupled with the DC load; b) detail of the coupling realized by means a universal joint. . . 168

6.4 a) Three three-phase inverters; b) uCube control board. 170

6.5 Vibration analyser module. 171

6.6 Detail of the MSPM motor with the $x-y$ axis acceleration transducers mounted on one of the angular plates. 172

6.7 Elements composing the proximity transducer system. 173

6.8 Circuit schematic of one of the two channels (the other is identical) of the interface board. 175

6.9 Experimental line to line back-EMF waveforms of the three sectors of the MSPM motor at ω_{rated}. 176

6.10 Comparison between the experimental, FE and analytical back-EMF trends against the rotation speed. The back-EMF between phase u and v of each motor sector has been included in the graph. 177

6.11 Comparison of the harmonic spectrum between measured, FE and analytical back-EMFs between phase u_1 and v_1. 178

6.12 $d-q$ axis inductances as a function of the current. 179

6.13 Comparison between the measured current i_d and the output of the simulated system $i_{d,sim}$. 181

6.14 No-load vibrations waterfall plot. 182

6.15 80 Hz vibration harmonic amplitudes for different speeds with and without vibration suppression. 183

6.16 Suppression of the 80 Hz vibration at 800 rpm, 1200 rpm, 1600 rpm and 2400 rpm. 184

6.17 Suppression of the 425 Hz vibration at 1500 rpm. 185

6.18 Suppression of the 440 Hz vibration at 2200 rpm. 185

6.19 Measured $d-q$ axis currents absorbed by the three sectors for the 80 Hz vibration compensation at 800 rpm: a) $d-$ axis current; b) $q-$ axis current 186

6.20 Measured $d-q$ axis currents absorbed by the three sectors for the 80 Hz vibration compensation at 1200 rpm: a) $d-$ axis current; b) $q-$ axis current 186

6.21 Measured $d-q$ axis currents absorbed by the three sectors for the 80 Hz vibration compensation at 1600 rpm: a) $d-$ axis current; b) $q-$ axis current 187

6.22 Measured $d-q$ axis currents absorbed by the three sectors for the 80 Hz vibration compensation at 2400 rpm: a) $d-$ axis current; b) $q-$ axis current 187

6.23 FFT amplitudes of the measured, reference and analytical $d-q$ axis currents absorbed by sector 1 for the 80 Hz vibration compensations. 190

6.24 Proximity sensors mounted on the probe supports. 192

6.25 View of the MSPM machine stator and of the multi-phase sectored winding. 193

6.26 Open loop force control: a) rotating force reference; b) measured rotor position. 194

6.27 Rotor trajectory before and after the offset correction. 195

6.28 Closed loop radial rotor position control with a rotating position reference: a) rotor trajectory before and after the correction; b) force trajectory before and after the correction. 196

6.29 Start up of the 2-DOF levitation setting $\omega_0 = 2\pi 170$ rad/s: a) $x-y$ axis position; b) $x-y$ axis force output of the position controller . . 198

6.30 Start up of the 2-DOF levitation setting $\omega_0 = 2\pi 20$ rad/sz: a) $x-y$ axis position; b) $x-y$ axis force output of the position controller . . 199

6.31 Bearingless operation test for a speed transient from 0 to 3000 rpm: a) $x-y$ position; b) rotor angular speed. 200

6.32 Rotor trajectory obtained at no load and load ($T_E = T_{rated}$) operating conditions at different rotating speeds: a) 1000 rpm; b) 2000 rpm; c) 3000 rpm. 201

6.33 Measured $d - q$ axis current of the three sector during bearingless operation at 3000 rpm for no load and load ($T_E = T_{rated}$) operating conditions: a) sector 1; b) sector 2; c) sector 3. 202

6.34 Simulation results for open-circuit fault in sector 1 at 2000 rpm operating speed and $T_E = 3$ Nm: a) $x - y$ axis position b) phase currents of sector 1; c) phase currents of sector 2; d) phase currents of sector 3. 204

6.35 Simulation results for open-circuit fault in sector 1 at 3000 rpm operating speed and $T_E = 2$ Nm: a) $x - y$ axis position b) phase currents of sector 1; c) phase currents of sector 2; d) phase currents of sector 3. 205

6.36 Simulation results for open-circuit fault in sector 1 at 3000 rpm operating speed and $T_E = 3$ Nm: a) $x - y$ axis position b) phase currents of sector 3. 206

6.37 Rotor trajectory obtained with the standard and with the MR position controllers: a) 30 Hz rotating speed; b) 40 Hz rotating speed; c) 50 Hz rotating speed; 207

6.38 Harmonic spectrum carried out with the fast Fourier transform of the $x-$axis position measurement. The compensation of the multi-frequency position oscillation can be appreciated. 208

6.39 Transient bearingless operation results using the standard and the MR controllers: a) rotating speed; b) $x - y$ axis position obtained with the standard controller; c) $x - y$ axis position obtained with the MR controller. 209

A.1 Trend of $det\big(\mathbf{A}(\vartheta_e)\big)$ against ϑ_e. 219

B.1 Open-circuit airgap flux density for $\vartheta_e = 0$ [deg]: a) radial component; b) tangential component. 223

B.2 Armature-reaction flux density at the airgap produced by ${}^1i_\alpha = const. = 1[A]$ and ${}^1i_\beta = 0[A]$: a) radial component; b) tangential component. . 226

B.3 Armature-reaction flux density at the airgap produced by ${}^1i_\alpha = 0[A]$ and ${}^1i_\beta = const. = 1[A]$: a) radial component; b) tangential component. 227

List of Tables

3.1 Machine parameters 47

3.2 Phase inductance values 52

3.3 $d-q$ inductance values 54

3.4 Phase Coils Angular Positions 55

3.5 Force Coefficients 70

4.1 Controller Gains for Coincident Poles Config. 96

4.2 Controller Gains for Butterworth Poles Config. 96

4.3 Standard Controller Gains 120

4.4 MR Controller Gains 120

5.1 THD of the force generation 136

5.2 Qualitative comparison 145

6.1 Resistor values 175

6.2 Vibration Suppression Parameters 184

B.1 Machine geometrical parameters 221

C.1 Parameters of force coefficients 231

C.2 Parameters of force coefficients for fault in sect. 1 234

C.3 Parameters of torque coefficients for fault in sect. 1 235

Chapter 1

Introduction

This Chapter is an introduction to this manuscript. In particular, the objectives of the PhD project are provided. Finally, the concepts of active magnetic bearing and bearingless machine are presented.

1.1 Objectives of the PhD project

The main objective of the PhD project is to develop a radial force and torque control technique for the multiphase machine considered. Therefore, a large portion of the PhD period has been spent analysing the considered machine to derive and validate through FE simulations the mathematical formulation of the radial force and torque production. An alternative radial force and torque generation technique has been proposed and applied to the multiphase PMSM. The latter presents three non-overlapped and independently supplied three-phase windings. Each three-phase winding occupies an equal portion of the stator circumference (120 deg), named sector. Exploiting the aforementioned winding configuration, radial force can be produced controlling the current in each three-phase winding in order to unbalance the magnetic field in

the airgap. The latter can be strengthened or weakened in correspondence of each sector producing electromagnetic forces. Each sector produces an independent force that can be controlled in order to get the desired resultant force.
In parallel with the theoretical investigations an experimental rig has been designed and manufactured and the mathematical model of the radial force and torque production has been adopted for two purposes: 1) suppression of selected vibrations in the motor equipped with mechanical bearings; 2) magnetic levitation of the rotor controlling two degrees of freedom ($x - y$ axis). The former relies on the open-loop force control to inject a rotating force in order to damp selected vibrations. The latter, instead, relies on a rotor suspension controller in order to keep the rotor in the stator centre. Therefore, a rotor suspension controller has been developed during the PhD period and validated through numerical simulations. Both stability and robustness issues have been taken into account in the controller design. Furthermore, a multi-resonant controller has been synthesized in order to eliminate multi-frequency position oscillations caused by period force disturbances. The bearingless operation performance could then be improved employing the multi-resonant controller.
Finally, in the last months of the PhD period, the fault tolerant capabilities of the considered BM have been studied and tested considering the open-circuit fault of three-phase winding as case study.

1.2 Definition of Bearingless Machines

In the last few decades performances of electric drives have dramatically increased paving the way for more and more sophisticated applications. In this context of high precision micro and power electronics and sensing systems, the active control of radial force has started being implemented for several purposes. Active magnetic bearings (AMB) and bearingless motors (BM) are one of those and relatively recently have become a topic of great interest.
A magnetic bearing is a machine that utilizes a magnetic levitation force to suspend

a rotor without any mechanical contact. The excellent characteristics of the magnetic bearings are: no friction, no wear, no lubrication, high speed and long operating life. Therefore, magnetic bearings have been applied to special machines such as high-speed and super high-speed drives [6, 7], centrifugal pumps [8], artificial hearts [9], and high-speed flywheel storage systems [10].

Since magnetic bearings can only produce levitation force, a motor element has to be installed in order to generate torque. The result of the assembly is a rather big and complex system (Figure 1.1 a)).

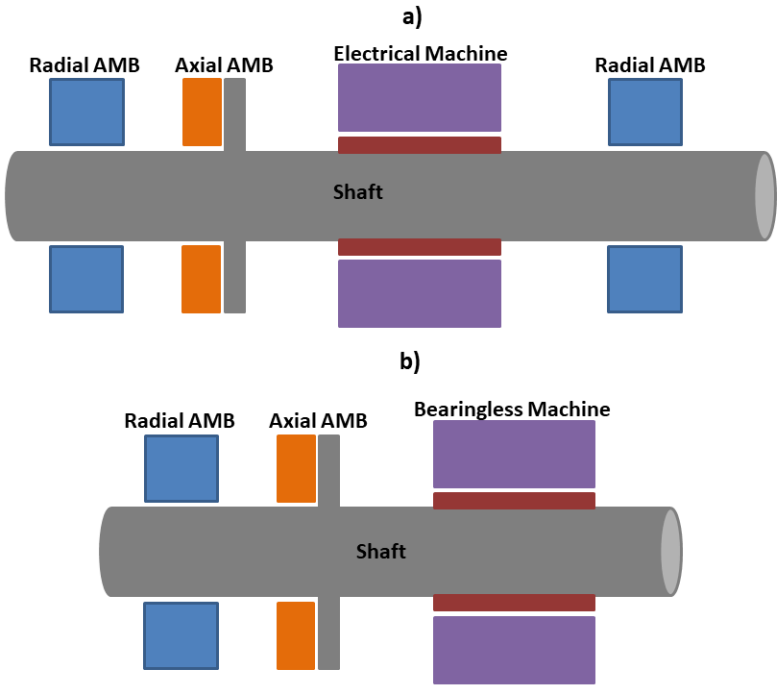


Figure 1.1: Machines configurations to reach the full rotor levitation: a) 2 AMBs b) 1 AMB and 1 BM

In order to overcome these problems, torque and suspension windings are wound together in a single stator to produce radial suspension force and torque simultaneously (Figure 1.1 b)). Compared with the magnetic bearing, the bearingless motor, sometimes also referred as self-bearing motor, presents a simpler structure, more compactness and a reduced cost. Furthermore, because no lubricant is needed and no wear caused by friction is occurring, bearingless motors can be used under ex-

treme conditions such as vacuum and fluid pumps in chemical, pharmaceutical and semiconductor industries where an ultra-high cleanness environment has to be guaranteed [2, 11, 12].

A primitive bearingless motor prototype was proposed by Hermann in the middle of 1970s [13]. Then, only in the early 1990s the BM technology started attracting growing interest [14–17]. As a matter of facts many bearingless motor structures have been developed, such as bearingless brushless DC motors, reluctance motors, induction motors, permanent magnet synchronous motors [18–22]. Among all these bearingless motor typologies, BPMSMs are of particular interest because of their advantage of simple structure, reliability, high efficiency and high torque density [23]. Originally, the radial suspension force and torque generation relied on two separated windings, hence an additional winding for force production needs to be installed leading to a bigger outer diameter than that of the conventional motor. Different winding arrangements have been introduced in order to embed radial suspension force and torque generation in a single winding set. Multiphase winding structures are one of the most promising thanks to their high power density, simple structure and fault tolerant capability.

1.3 Chapter Summary

In this Chapter the objectives of the PhD project are presented together with a brief description of the multiphase machine considered and of the force production principles. Then, the bearingless machine technology is introduced and some applications are described.

Chapter 2

Literature Review

2.1 Introduction

This Chapter is the result of the bibliographic research that has been done to study the principles and the state of the art in the field of radial force control in electrical machines.

At first, the motivations that led to investigate radial forces are introduced and a general description of different approaches that can be employed to reduce stress on the bearing elements and vibrations are presented. Among them, the active control of radial forces is of great interest since it allows the suspension of the rotor, opening the possibility for the production of new electromagnetic devices such as AMBs and BMs. Several examples of industrial applications where these devices have found space are described.

The bearingless technology is then analysed more in details in a dedicated section. After presenting a brief description of the radial suspension force principle and mathematical models, bearingless motors are classified according to different criteria such as number of actively controlled degrees of freedom, different motor topologies and

different radial suspension force techniques adopted to achieve the rotor levitation. A multiphase winding structure is chosen for this PhD project, hence an overview of multiphase machines is given in a dedicated section.
Finally, different position control algorithms employed to enhance the levitation performances are presented in the last section. As a matter of fact, different disturbances can occur causing periodic multi-frequency oscillations in the rotor position justifying the investigation of more complex position controllers to reject them.

2.2 Radial Force Control and its Applications

Application requirements for electrical machines vary from case to case, however there is a general trend towards increasing their lifetime and their reliability as well as reducing their maintenance and noise. Indeed, acoustic noise and mechanical vibrations are an increasingly important design criterion when comes to the optimization of the machine structure [24–26]. The impact of mechanical bearings on the reliability and maintenance of electrical machines is typically severe [27, 28]. The active control of radial forces could lead to significant improvement in terms of noise reduction and vibration dampening [29–33]. This would also enable the compensation of external forces acting on the rotating structure such as unbalance magnetic pull (UMP), inertial forces and forces of other nature. The UMP, in particular, has been widely investigated and its minimization is often considered from a design point of view. This undesired disturbance is caused by an uneven airgap flux density distribution that rises electromagnetic forces between the rotor and the stator. It can be caused by the effect of the rotor eccentricity, or by the machine geometric features (such as rotor and stator structures in certain machine topologies) [30, 31], as well as by the combination of poles and slots number [26, 34].
Sometimes the design does not succeed in the elimination of the UMP. Furthermore, mass unbalance is often present after the manufacturing process consisting of the principal rotor axis of inertia not coincident with its geometric axis [1], again, causing

mechanical vibrations. The trend to move towards higher density machines clearly implies increasing the operational speed that in turn increases the centrifugal unbalance forces. Therefore, vibration control and active balancing techniques have become fundamental. They have been adopted to achieve longer bearing life time and to avoid unscheduled shut-downs.

Passive devices can be introduced into the rotating machinery to damp the vibration as presented in [35]. However, it has been shown in [36] that active vibration control techniques have many advantages over the passive ones. In fact, despite their more complicated implementation, the formers are more flexible since they can be employed when several vibration modes are excited and in general they can be adjusted during the motor operation according to the vibration characteristics.

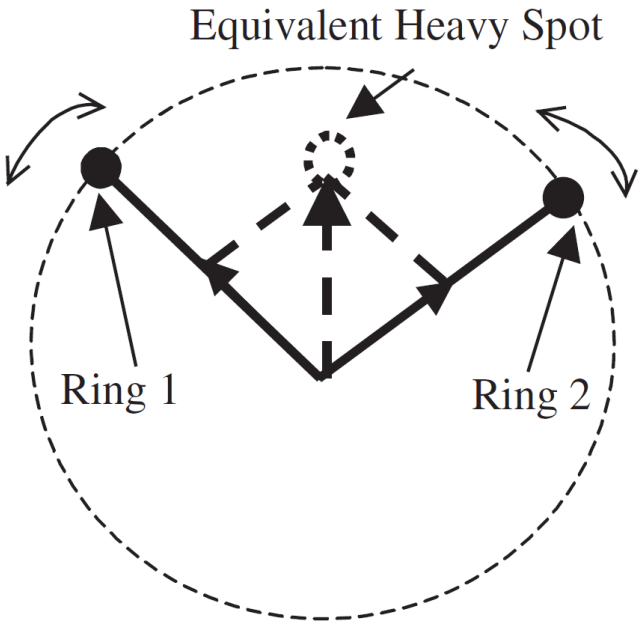


Figure 2.1: Schematic representation of the balancer [1]

There are mainly two methods for active balancing and vibration control for rotating machinery: the active balancing technique and the direct active vibration control (DAVC). The former performs a mass redistribution by means of an actuator mounted

on the rotor that can change the mass centre of the machinery. At first, the rotating system vibration is measured and the mass unbalance is estimated. Then, the redistribution actuator is activated and its mass centre changed to offset the system unbalance. An example of an active real-time balancing technique can be found in the diagram of the balancer in Figure 2.1. It consists of two heavy rings whose rotation can be controlled in order to create a resultant equivalent ring with magnitude and position changing according to the mass unbalance to be compensated [37]. Active balancing techniques, in general, can provide huge compensation forces but they are rather slow if compared with their counterpart DAVC. Indeed, the DAVC can generate a fast-changing radial force that can be employed to suppress the total vibration on the machine, including the synchronous vibration and the vibration modes. On the other hand, the limitation of these techniques is given by the maximum force that the force actuators are capable to produce; these, for high rotational speed, can be not sufficient to compensate the unbalance-induced force. Therefore, when very big forces are required active balancing techniques are often preferred.

As far as active vibration control techniques are concerned, many kinds of actuators can be employed, including electromagnetic, piezoelectric and so on. Among them, the active magnetic bearings is an establish technology that is finding an increasing number of industrial applications. More recently bearingless machines (BM) are attracting growing attention because of their more compact structure. The AMB solution consists in a rather bulky and complex structure since several electric machines are required to stably suspend and rotate the rotor while the BM technology allows to embed the characteristic of AMBs into the motor structure.

The reasons that pushed the development of the bearingless technology are mainly the high failure rate of mechanical bearings, high rotation speed applications, oil-free requirement for high purity environments and chemical resistance. To be more specific, the most targeted applications for BMs are centrifugal pumps [8, 18, 38, 39] and artificial hearts [9, 40], mixers for chemical and pharmaceutical applications [41–43] and fans [44, 45]. Furthermore, a full levitating system is particularly convenient when high and ultra-high rotation speeds have to be achieved [6, 7, 46] since it al-

lows the full rotor-dynamic control on the rotating component and provides damping effects while crossing critical frequencies. It is the case of compressors [47], spindles [48], flywheels [6, 49, 50] and generators, where high rotational speed operation means minimizing weight, dimensions, cost, while maximizing the efficiency of the whole system [11].

2.3 Overview of Bearingless Machines

This section presents an in-depth overview of the bearingless machine technology including their mathematical models, a classification considering the number of actively controlled DOF and different motor topologies.

2.3.1 Theoretical Description

The mathematical model is extremely important to obtain accurate mathematical expressions of the electromagnetic torque T_E and radial suspension forces $F_{E,x}$ and $F_{E,y}$, therefore to realize stable suspension operation to the BM.

2.3.1.1 Force production principle

Two magnetic fields of identical spatial harmonic orders are necessary to produce a net torque in an electrical machine. The main harmonic order is usually the one related to the number of pole pairs (p), hence, for torque generation, the armature of the machine has to produce a magnetic field of order p. On the other hand, a controllable suspension force can be produced commanding a magnetic field of order $p \pm 1$ [51].

According to the electromagnetic theory, two types of magnetic forces can be produced in an electrical machine supplied with a three-phase current: Lorentz and Maxwell forces [2]. The former is associated with the force generated by the interaction of current-carrying conductors and the magnetic field. Hence, if the winding, allocated in the stator, is placed in a magnetic field a force is generated on it and, according to the Newton's third law, opposite force appears in the rotor. Maxwell force, instead, exists in a magnetic circuit at the boundary surfaces of materials having different permeabilities, such as the airgap and the iron core. This kind of force arises when the magnetic field distribution at the airgap is uneven. In fact, if the rotor is positioned in the stator centre and the magnetic field distribution is symmetrical, the Maxwell force is zero. However, when the rotor eccentricity occurs this symmetry will be broken and a Maxwell force, whose direction is given by the eccentricity's direction, is produced. This force tends to attract the rotor to the stator and it increases with the rotor eccentricity making the system inherently unstable. Therefore, a controllable magnetic force is necessary to stably levitate the rotor. It can be produced exploiting the stator winding in order to command a magnetic flux that unbalances the airgap field.

2.3.1.2 Mathematical model

The virtual displacement method is the most common approach to obtain the mathematical expression of the $x-y$ axis force components and torque as a function of the motor currents. Once the inductance matrices of the windings are derived according to the equivalent magnetic circuit principle, the expression of the electromagnetic energy W_m can be written for the considered machine [52,53]. Finally, the expression of the electromagnetic torque and radial suspension forces is obtained by the following equation:

$$\begin{bmatrix} F_{E,x} \\ F_{E,y} \\ T_E \end{bmatrix} = \begin{bmatrix} \frac{dW_m}{dx} \\ \frac{dW_m}{dy} \\ \frac{dW_m}{d\vartheta_e} \end{bmatrix} \tag{2.1}$$

where x and y are the $x-$ and $y-$direction displacement, respectively while ϑ_e is the rotor electric moving angle.

It is also possible to derive the mathematical model exploiting Lorentz and Maxwell force equations [50, 54–57]. Neglecting the tangential Maxwell force component, the radial and tangential stress tensors are given by the Maxwell and Lorentz equations respectively, as follows [55]

$$\sigma(\alpha_s) = \begin{bmatrix} \frac{B_r^2(\alpha_s)}{2\mu_0} \\ A(\alpha_s)B_n(\alpha_s) \end{bmatrix} \tag{2.2}$$

where B_r is the radial airgap flux density, A is the current distribution, μ_0 is the vacuum magnetic permeability and α_s is the angular position on the stator surface. It is now possible to write the expressions of the resultant radial suspension force and of the torque as

$$\begin{aligned} F &= R_g l \int_0^{2\pi} \begin{bmatrix} \cos(\alpha_s) & -\sin(\alpha_s) \\ \sin(\alpha_s) & \cos(\alpha_s) \end{bmatrix} \cdot \begin{bmatrix} \frac{B_n^2(\alpha_s)}{2\mu_0} \\ A(\alpha_s)B_r(\alpha_s) \end{bmatrix} d\alpha_s \\ T_E &= R_g^2 l \int_0^{2\pi} A(\alpha_s)B_n(\alpha_s)d\alpha_s \end{aligned} \tag{2.3}$$

where l is the active machine length and R_g is the mid-airgap radius.

The aforementioned methods do not take into account the eccentricity, that inevitably affects any rotor after the manufacture assembly, and the coupling between force and torque production. These will considerably complicate the mathematical model [58, 59] and consequently the expression of the torque and of the suspension forces,

but it is often neglected in at first instance.

2.3.2 Classification of BM by the number of actively controlled DOF

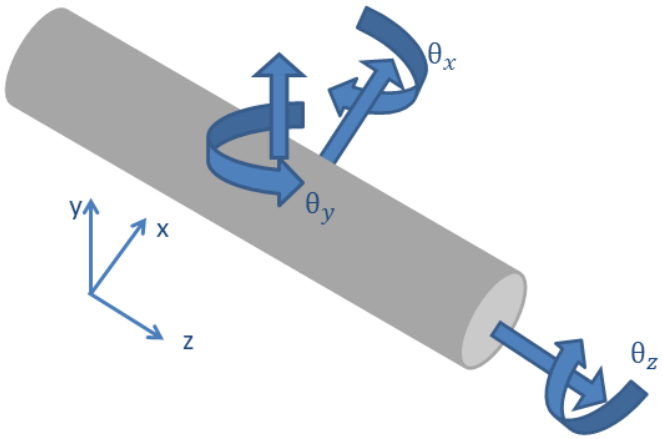


Figure 2.2: Rigid rotor free to move with six-DOF in the three-dimensional space.

It is of fundamental importance to define for a BM the number of DOF for active positioning control. A rigid body in the three-dimensional space has six DOF (see Figure 2.2), therefore, given that the motoring torque is separately controlled, five DOF (displacement along x-, y- and z-direction, and the tilting movement ϑ_x and ϑ_y) have to be controlled in order to stably suspend the rotor. On the other hand, it is possible to suspend the rotor without actively controlling all the five DOF using passive systems.

2.3.2.1 1-DOF ($z-$axis)

The most extreme solution is the 1-DOF bearingless motor proposed in [60] where only the $z-$axis displacement is actively controlled while the radial $x-y$ axis displacement

and the tilting are passively stabilized. The advantages of a single-drive BM consists in the reduce size, power consumption, cost and simpler control systems compared to higher DOF BM since only one converter is required. However, the full rotor-dynamic behaviour of the motor cannot be controlled reducing the operational speed that the drive can achieve. This is the main drawback of the 1-DOF BM and it is clearly stated in [60] that the rotation speed has to be limited at 1400 r/min to avoid excessive vibrations due to the tilting movements. Despite this drawback, this BM solution is particularly interesting because the torque and suspension force generation rely only on one three-phase winding. The $z-$axis force and torque equations can be summarized as:

$$\begin{cases} F_{E,z} = f_d(i_q^2) + K_i i_d + K_z(i_q^2) z \\ T_E = \frac{I_p i_q M'}{g_0} \end{cases} \tag{2.4}$$

where K_i and K_z are the suspension force constant and axial stiffness, respectively, i_d and i_q are the $d-q$ axis current of the machine, f_d is the disturbance function of the square of i_q current, I_p is the PM equivalent current, M' is the derivative of the mutual inductance and g_0 is the physical airgap. It can be noticed that the torque is only function of the i_q current, while the axial force is related to both $d-q$ axis currents. However, only the i_d current is controlled to suspend the rotor and $f_d(i_q^2)$ is treated as a disturbance that the position regulator has to compensate.

2.3.2.2 2-DOF ($x-y$ axis)

The 2-DOF BM is usually used as a principle prototype in the laboratory in order to investigate different radial force control technique. They typically have a self-aligned bearing mounted on one side of the shaft, while the other side is suspended controlling the $x-y$ axis position. The levitation is only partial, hence this configuration cannot find any practical implementation. However, it is one of the most common in the BM

literature since it allows a quick experimental verification of the radial force control techniques applied to the rotor suspension without the need of the full levitation that would require a more complex set-up.
A full levitating 2-DOF controlled bearingless motor has been proposed, instead, in [61]. It consists of an inner-disk-rotor-type bearingless motor, also called slice motor [12, 62, 63], where the radial motion (x, y) of the rotor is actively regulated and the remaining DOF, except the rotational motion, are passively stabilized. To successfully suspend the rotor, two displacement sensors, two sets of three-phase windings, and two three-phase inverters are required for the considered configuration. These kinds of disk-rotor BMs have found several applications in the pharmaceutical industries as mixers and centrifugal pumps [8,42,43]. Indeed, they present high purity features since they do not mount mechanical bearings hence they are lubricant-free.

2.3.2.3 3-DOF ($x - y - z$ axis)

A three-DOF bearingless drive can be found in a AMB [64, 65] where the axial and the radial directions are controlled by DC and three-phase power converters, respectively. The axial and radial bias magnetic fluxes are provided with only one radially magnetized PM ring.

2.3.2.4 4-DOF ($x - y$ axis and ϑ_x, ϑ_y tilting movement)

A 4-DOF BM can be realised connecting two 2-DOF BM units with a rigid coupling. Only the four radial DOFs can be controlled and the axial movement is constrained by a spherical roller bearing [2].

2.3.2.5 5-DOF ($x-y-z$ axis and ϑ_x, ϑ_y tilting movement)

This kinds of BM present a very complex mechanical structure, long axial length and limited critical rotor speed resulting in problems of big volume, high power and high cost. Indeed, a 5-DOF BM typically consists of two 2-DOF BM and an axial magnetic bearing unit [66, 67]. To overcome the above mentioned disadvantages a 5-DOF formed by a 3-DOF axial-radial magnetic bearing and a 2-DOF BM is presented in [68]. The structure is therefore simplified and the axial length of the rotor is reduced promoting an increase of the critical speed of the motor.

2.3.3 Bearingless motor topologies

The levitation principle can be implemented in different motor topologies depending on the application requirements. Below a comprehensive overview of different bearingless motor types is presented underlining the motivation for their choice.

2.3.3.1 DC brushless motors

Brushless DC motors are widely used in applications where the reduction of system complexity and costs are the main targets. They are now employed in particular in small capacity pumps in the semiconductor, chemical, or medical industry [18, 69]. Typically, permanent-magnet-excited rotor disk are used so that only the radial position needs to be actively controlled while the axial and tilting movement is passively stabilized. In [69] five concentrated coils are mounted on the DC BM so that both motoring torque and radial suspension force can be generated with one single set of winding further simplifying the mechanical design. The radial force and torque control are coupled and highly non-linear when concentrated coils are adopted, hence [69] proposes a non-linear control technique for a DC BM.

A toraidally-wound DC BM is presented in [70]. Thanks to the slotless structure no cogging torque is generated and the iron losses are negligible. Furthermore, its simple control and compactness make it suitable for artificial heart pumps or micro-size flywheel energy storage systems [71].

2.3.3.2 Reluctance motors

Switched and synchronous reluctance BMs [14, 19, 20, 58, 67, 72–74] are particularly suitable for special environments thanks to their advantages such as robustness, fail safe, operations under high temperature or intense temperature variation. Furthermore, not relying on PMs, their cost is remarkably lower than PM synchronous motors. However, they have limitation regarding vibration and noise.
The radial force is generated by the suspension winding current and motor winding current, hence force and torque generation are coupled and highly non-linear. Therefore, these motors need a complex design and control method to achieve good performance.

2.3.3.3 Permanent magnet motors

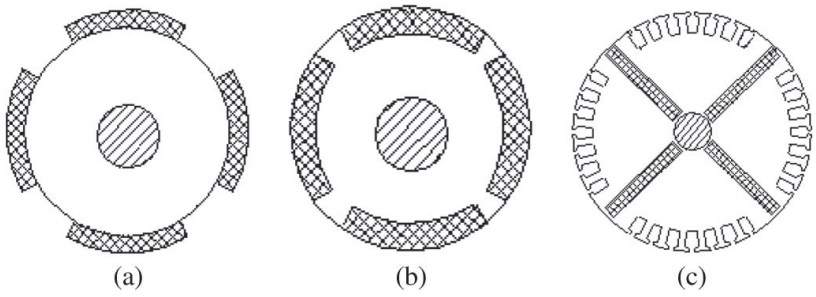


Figure 2.3: PM bearingless motor rotor topologies: a) Surface mounted. b) Inset. c) Interior. [2]

PM bearingless motors have attracted considerable interest in applications where high efficiency and power density are a requirement. Depending on the position of the PMs in the rotor, these machines can be further classified as surface-mounted [52], inset [53] and interior topologies [75] (Figure 2.3).

Among them, surface-mounted bearigless PMSM is probably the most investigated category. Being the effective airgap the sum of PMs thickness and the physical airgap they present low winding inductances and reduced radial suspension force [52]. Therefore, thin PMs are preferred leading to demagnetization problems in BPMSM since not only the flux of the motor winding, but also the one of the additional suspension force one exist. [76] proposes a method to design the rotor taking into account the aforementioned problem leading to the PM thickness being a function of the maximum demagnetization current.

In order to overcome the issue of large effective airgap, buried-type inset BPMSM are proposed to enhance the radial force production. Other advantages with respect to the surface-mounted types consist in higher operation speeds (the PMs are protected against large centrifugal forces by the rotor iron core) and reluctance torque generation.

The interior BPMSM topology has the PMs buried inside the rotor. It has the advantage of potentially having a higher airgap flux density than the PM flux density and to have a considerable reluctant torque. In [75] authors show that the buried-type bearingless PMSM presents the benefit of higher rotating speed, torque and suspension force and easy control capability compared to the previous two kinds of BPMSM.

2.3.3.4 Induction motors

Bearingless induction motors [21, 77, 78] present the advantage of having the highest radial suspension force production among the considered motor topologies thanks to the very reduced airgap length. On the other hand, the control of the radial force

and torque is coupled resulting in a more complex control system. [79] proposes a hybrid rotor with the advantages of both PM and induction rotors. It consists of two additional rotor cores added to the PM one. Larger radial forces and torque can be produced and a vector control strategy can be easily implemented to realize decoupled position and rotation control.

2.4 Radial force and torque generation strategies

It is interesting to consider the different strategies that have been chosen by researchers around the world to generate a controllable radial force and torque. These consist of different winding structures combined with different force and torque generation methods while the mathematical models are always carried out exploiting either the virtual displacement method or the Maxwell and Lorentz equations.
The radial force and torque generation strategies considered are the following:

- Separate torque and suspension windings.
- Single three-phase winding structure with parallel path.
- Five-phase winding with multiple orthogonal $d-q$ planes for force and torque generation.
- Six-phase winding structure with fault-tolerant capability.
- Triple three-phase winding structure with decoupled torque and radial force control.
- Triple three-phase winding structure with Vector Space Decomposition (VSD) method employed for the force and torque control.

2.4.1 Separate torque and suspension windings

Most of the solutions proposed by researchers make use of two separate windings, one for torque and another one for suspension force production. In order to generate the torque and the radial suspension force simultaneously, the torque and the suspension winding are wound together in the same stator slots of the BM. Normally, the power required by the torque winding is much greater than the one required by suspension force winding, hence the former typically occupies $60\% - 90\%$ of the total stator slot area.

The controllable radial suspension force can be generated when the following conditions are met [51]:

$$\begin{aligned} P_f &= P_t \pm 1 \\ \omega_t &= \omega_f \end{aligned} \tag{2.5}$$

where P_t and ω_t are the pole-pair number and current pulsation of the torque winding respectively, while P_f and ω_f are the corresponding quantities of the suspension force windings.

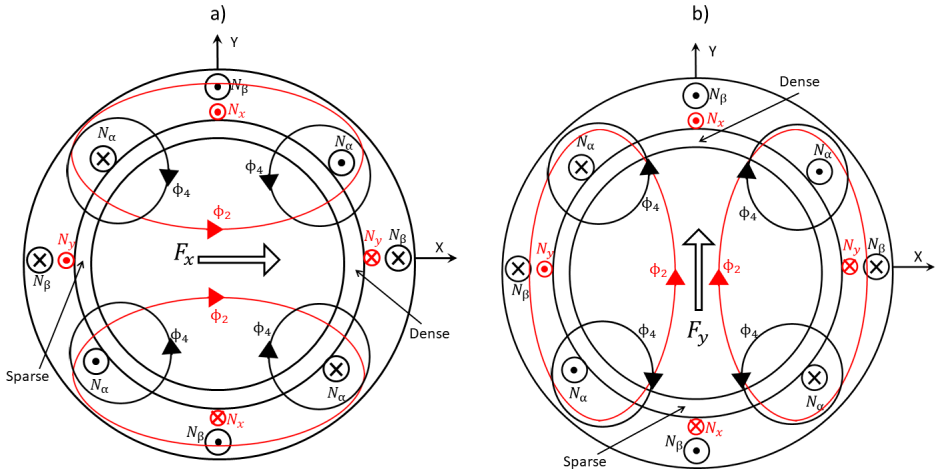


Figure 2.4: Force generation principles: a) $x-$axis force generation. b) $y-$axis force generation. The 4-pole motor winding and the 2-pole suspension force winding are represented in the $\alpha - \beta$ reference frame in the picture.

The principles of radial force production are depicted in Figure 2.4. The motor presents a 4-pole winding for torque production and a 2-pole winding for suspension force production. The 4-pole flux Φ_4 can be produced either by the PMs, in a PM machine, or by the 4-pole winding in synchronous reluctance or induction machines [51]. Therefore, if the current of the radial force winding N_x is positive, a 2-pole magnetic flux Φ_2 is generated with the result of unbalancing the flux density in the airgap as depicted in Figure 2.4 a). The radial force is then generated in the positive $x-$direction. If the current in N_x is negative, radial force can be produced in the negative $x-$direction. Controlling the current in the N_y windings, radial forces can be produced in the $y-$direction as shown in Figure 2.4 b). Therefore, radial magnetic force can be produced in any direction and magnitude only regulating the amplitude and direction of N_x and N_y winding currents.

The virtual displacement method has been used in [52] in order to obtain the mathematical expression of the radial suspension forces. Therefore, the relationship between flux linkages and currents has to be known to obtain the magnetic energy W_m . This relationship, for the considered motor, can be written as follow:

$$\begin{bmatrix} \Phi_\alpha \\ \Phi_\beta \\ \Phi_x \\ \Phi_y \end{bmatrix} = \begin{bmatrix} L_2 & 0 & -M'x & M'y \\ 0 & L_2 & M'y & M'x \\ -M'x & M'y & L_4 & 0 \\ M'y & M'x & 0 & L_4 \end{bmatrix} \cdot \begin{bmatrix} i_\alpha \\ i_\beta \\ i_x \\ i_y \end{bmatrix} \tag{2.6}$$

where Φ_α, Φ_β, Φ_x and Φ_y, i_α, i_β, i_x and i_y are the flux linkages and current of N_α, N_β, N_x, N_y winding, respectively. L_2 and L_4 are the self-inductances of the torque and radial force windings respectively, in the 2-phase coordinates, x, y are the rotor spatial displacement and M' is the derivatives of the mutual inductance between motor and radial force windings with respect to x and y. Finally, i_α and i_β, i_x and i_y are the $\alpha - \beta$ currents of the motor windings and suspension force windings, respectively. The magnetic energy W_m can be written as:

$$W_m = \frac{1}{2} \begin{bmatrix} i_\alpha & i_\beta & i_x & i_y \end{bmatrix} \cdot \begin{bmatrix} L_2 & 0 & -M'x & M'y \\ 0 & L_2 & M'y & M'x \\ -M'x & M'y & L_4 & 0 \\ M'y & M'x & 0 & L_4 \end{bmatrix} \cdot \begin{bmatrix} i_\alpha \\ i_\beta \\ i_x \\ i_y \end{bmatrix} \tag{2.7}$$

The radial force components $F_{E,x}$ and $F_{E,y}$ can be calculated as in (2.1) and their expression as a function of the suspension force winding currents is given by:

$$\begin{bmatrix} F_{E,x} \\ F_{E,y} \end{bmatrix} = M' I_p \begin{bmatrix} -\cos(\vartheta_e) & \sin(\vartheta_e) \\ \sin(\vartheta_e) & \cos(\vartheta_e) \end{bmatrix} \cdot \begin{bmatrix} i_x \\ i_y \end{bmatrix} \tag{2.8}$$

where ϑ_e is the electrical rotor angular position and I_p is the equivalent current of the permanent magnets. Equation (2.8) can be rearranged in order to obtain the suspension force winding currents as a function of the radial force components:

$$\begin{bmatrix} i_x \\ i_y \end{bmatrix} = \frac{1}{M' I_p} \begin{bmatrix} -\cos(\vartheta_e) & \sin(\vartheta_e) \\ \sin(\vartheta_e) & \cos(\vartheta_e) \end{bmatrix} \cdot \begin{bmatrix} F_{E,x} \\ F_{E,y} \end{bmatrix} \tag{2.9}$$

The relationship in equation (2.9) can be used in the control circuit of Figure 2.5 where the $x-y$ axis positions and the speed ω are independently controlled.

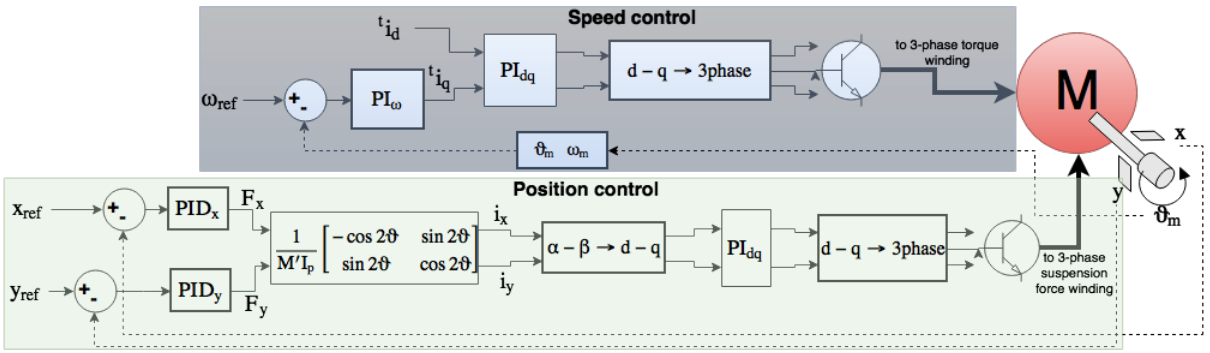


Figure 2.5: Block diagram of the control algorithm

2.4.2 Single three-phase winding structure with parallel path

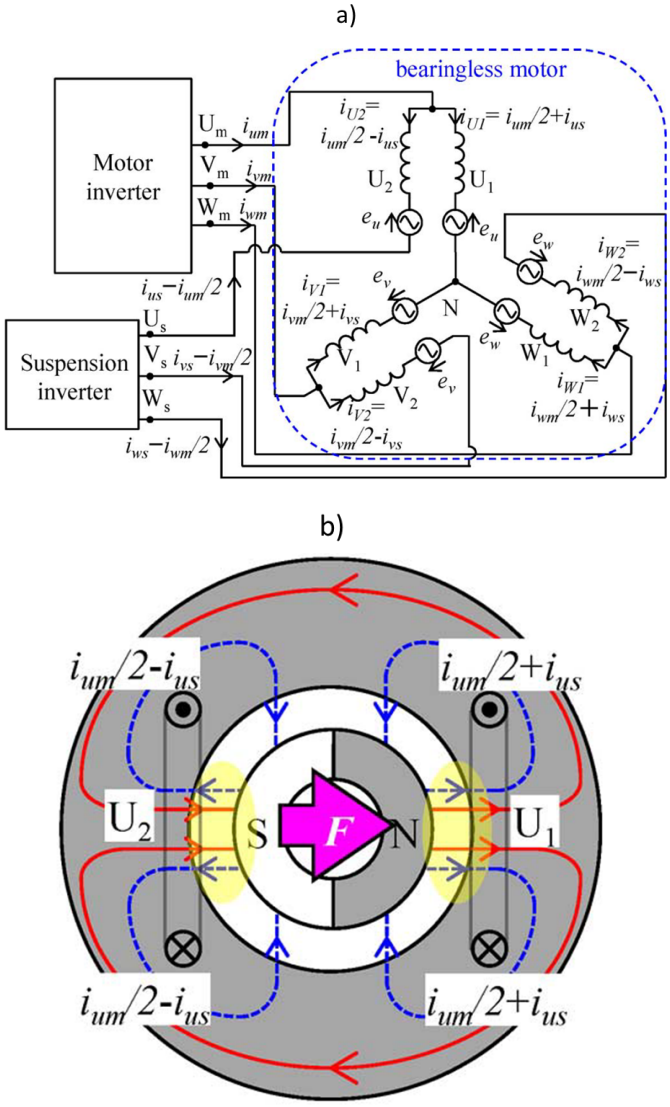


Figure 2.6: Parallel path winding structure. a) Schematic of the motor and suspension inverter connections. b) Force generation principle for phase u. [3]

The elimination of the additional suspension force winding is desirable to reduce the overall size of the machine and to enhance its efficiency. Two winding topologies can be employed to produce radial force with a single three-phase winding: the parallel

winding configuration [3, 80] and the bridge winding configuration [81–83]. The force production principle is very similar for the two winding structures and in this paragraph the parallel winding configuration shown in Figure 2.6 a) will be presented in detail. Considering for instance phase U, it is possible to observe that it is composed of two parallel coils, namely U1 and U2. The motor inverter is connected to the mid-point of the phase (in between the coils U1 and U2) while the radial suspension force inverter is connected to one of the phase terminals. The other phase terminal is connected to the neutral point of the star connected three-phase winding.
The radial force production principle for this kind of winding configuration can be appreciated in Figure 2.6 b). Being the current in coils U1 and U2

$$\begin{aligned} i_{U1} &= i_{um}/2 - i_{us} \\ i_{U2} &= i_{um}/2 + i_{us} \end{aligned} \tag{2.10}$$

respectively, and the 2-poles PM flux symmetrical, the airgap flux density around U1 is higher than the one around U2, hence a net radial force is generated in the $x-$axis direction. Changing the sign of the suspension current i_{us} the force is produced in the opposite direction. Radial forces can be generated in the same way in phases V and W, hence the total radial force results in the vector sum of each phase contribution and can be controlled in magnitude and direction controlling the suspension currents i_{us}, i_{vs} and i_{ws}. The amplitude of the radial suspension force and torque are proportional to the suspension and motor current magnitude, respectively [3].
A similar approach was proposed already in 1993 and published in [16] where the authors used an induction machine with four poles and split one of the phases so that each pole of that phase could be supplied independently and used to control the radial rotor position.

2.4.3 Five-phase winding with multiple orthogonal d-q planes for force and torque generation

Multiphase motors are employed to generate simultaneously torque and suspension force with a single winding set simplifying the mechanical structure and reducing the overall size of the BM. The multiphase winding possesses the characteristic of multiple orthogonal $d-q$ planes that can be exploited for various uses [84–86]. In following paragraph, extracted by [84], a five-phase winding fed by a single five-phase inverter is presented. Two orthogonal $d-q$ planes are generated with the function of equivalent torque winding (for torque production) and suspension force winding (for suspension force production).

As it has been previously stated, it is necessary to obtain two magnetic fields with a difference in pole-pair numbers equal to one to control the torque and the suspension force. Therefore both odd and even fields are simultaneously needed. Since the phase winding function for the conventional winding is symmetric even-order space harmonic do not exist, hence, half-coiled windings can be adopted to meet the requirement.

The winding function of such a machine is asymmetric and it is given, for phase a by:

$$N_a(\alpha_s) = \sum_{v=1,2,3,\ldots} \frac{4}{v\pi}\frac{N}{2}\sin(\frac{y_1}{2\tau}v\pi)\cos(v\alpha_s)) \tag{2.11}$$

where α_s is the spatial stator angle, v is the space harmonic order, y_1 is the coil pitch, τ is the pole pitch, and N is the number of turns per slot. The current in phase a is given by:

$$i_a(\omega t) = \sum_{u=1,2,3,\ldots} \frac{4}{u\pi} I\sin(u\omega t) \tag{2.12}$$

where ω is the angular speed, u is the time harmonic order and I is the magnitude of the phase current.

The total magneto-motive force (MMF) is given by the sum of each phase contribution. In [84], it is demonstrated that combining the vth spatial harmonic with the uth time harmonic gives the following expression of the total MMF:

$$MMF_{vu} = \frac{m}{uv}\left(\frac{4}{\pi}\right)^2 \frac{NI}{4}[K_{vu-}\sin(A_1) + K_{vu+}\sin(A_2)] \tag{2.13}$$

where $A_1 = u\omega t + v\alpha_s$, $A_2 = u\omega t - v\alpha_s$, K_{vu-} represents a backward rotating field and K_{vu+} a forward rotating field. Their expressions are given in [84]. The motor considered features two permanent magnets (pole pair number $p = 1$), hence the torque and the suspension force are produced by the one- and the two-pole pair forward rotating magnetic fields, respectively. Therefore the magnitude of the first and second space harmonics of the winding functions N_1 and N_2 can be considered as the resultant number of series turns per phase of the equivalent torque and suspension winding, respectively.

From this point, the procedure to obtain the radial suspension force components is the same as the one where two electrically isolated three-phase windings were adopted. The inductance matrix of the equivalent suspension winding is necessary in order to calculate the magnetic energy. Then, the radial forces $F_{E,x}$ and $F_{E,y}$ are derived from the partial derivatives of the magnetic energy with respect to displacements x and y, respectively. Their expressions are reported in (2.14).

$$\begin{bmatrix} F_{E,x} \\ F_{E,y} \end{bmatrix} = M' I_p \begin{bmatrix} \cos(\vartheta_e) & \sin(\vartheta_e) \\ -\sin(\vartheta_e) & \cos(\vartheta_e) \end{bmatrix} \cdot \begin{bmatrix} i_{\alpha 2} \\ i_{\beta 2} \end{bmatrix} \tag{2.14}$$

where M' is the derivative of the mutual inductance between torque and suspension windings, I_p is the PM equivalent current, and $i_{\alpha 2}$ and $i_{\beta 2}$ are the suspension current in the stationary coordinates. It can be noticed that the expression in (2.14) is very similar to the one obtained in (2.8).

2.4.4 Six-phase winding structure with fault-tolerant capability

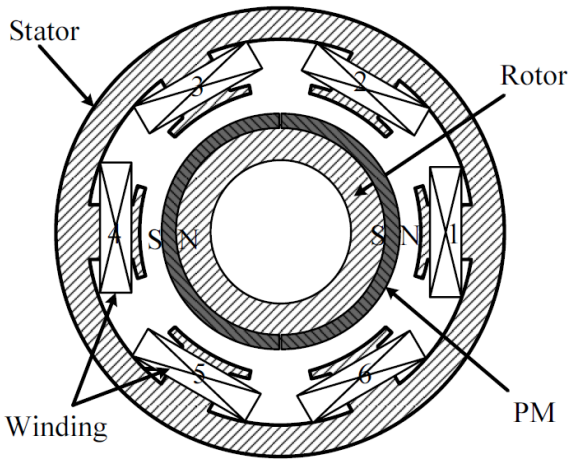


Figure 2.7: Cross section of a six-phase PMSM [4]

An interesting solution for BPMSM has been investigated in [4] where a six-phase bearingless PMSM is used for the experimental verifications. The motor, shown in Figure 2.7, presents two poles and six teeth distributed equally in the stator with a concentrated winding. Each phase in controlled independently, hence, six single-phase converters are necessary

The levitation force and torque models can be derived according to the principle of equivalent magnetic circuit and virtual energy. The model of a general multi-phase PM bearingless motor can be expressed as:

$$Q = M(\vartheta_m) i_s \tag{2.15}$$

where ϑ_m is the mechanical rotor angle, $Q = [F_{E,x}, F_{E,y}, T_E]^T$ is the vector consisting of the torque T_E and the suspension force components $F_{E,x}$ and $F_{E,y}$, $i_s = [i_1, ..., i_k, ..., i_N]^T$ is the stator current vector of each phase $k = 1, 2, ..., N$, $(N = 6)$. The expression of the $\mathbb{R} \in 3 \times 6$ matrix $M(\vartheta_m)$ is reported in [4]

Based on the equation above, the levitation forces and the torque can be obtained knowing the instantaneous value of the phase currents. However, the number of phase current variables is greater than the system equations number, hence additional contrains should be included to optimize the power output. For instance, the minimization of the power losses can be adopted via solving:

$$min\{i_s^{*T} R i_s^*\} \tag{2.16}$$

where $R = diag\{r_1, r_2, ..., r_N\}$ represents the resistance of the stator winding. In order to solve the optimization problem, the a Lagrangian function is constructed in [4] and the desired current vector is deduced as

$$i_s^* = Z(\vartheta_m) Q^* \tag{2.17}$$

where $Z(\vartheta_m)$ $\mathbb{R}^{\in N \times 3}$ is a matrix obtained solving the Lagrangian function.
In [4] two kinds of open-circuit faults are considered: one phase open-circuit and two phases open-circuits. When a fault occurs in one of the phases, the relative column of matrix $M(\vartheta_m)$ is set to zero. It is demonstrated that the bearingless machine considered can still operate with one and with two adjacent and opposite open-circuited phases. However the fault tolerant controllability is infeasible when two inverted or three adjacent phases are open-circuited.

2.4.5 Triple three-phase winding structure with decoupled torque and radial force control

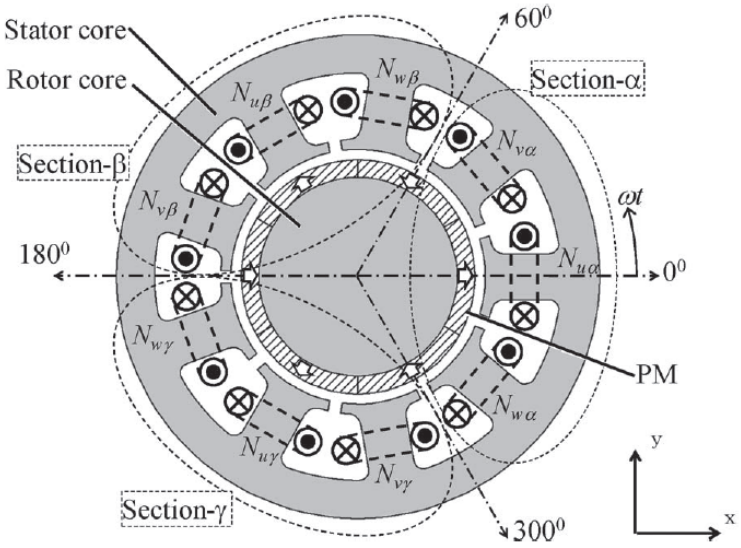


Figure 2.8: Cross section of the sectored BPMSM [5]

A decoupled model has been considered in [5, 87] to design a radial force control strategy levering on the $d-q$ axis modelling of the machine. The latter consists of a surface PM synchronous motor with three sectored three-phase windings as depicted in Figure 2.8.

The torque demand and the force vector are generated by controlling the three $q-$axis and $d-$axis components of the current in the synchronous reference frame, respectively. Levering on the magnetically isotropic structure of the MSPM machine, the torque is controlled only by means of the $q-$axis current components of each sector. The total $q-$axis current demand is obtained considering the torque expression (11).

$$T_E = \sum_{n=1}^{3} {}^n k_T \, {}^n i_q = 3 k_T i_q \Rightarrow {}^n i_q = \frac{T_E}{3 k_T} \tag{2.18}$$

where k_T is the torque constant of the motor.

The transformation of the forces developed by each sector to the rectangular forces component on the overall rotor structure is introduced aiming to a reduction of the order of the problem. Under the assumption of electromagnetic forces related with only the $d-$axis currents components, (2.18), (2.19) define the complete model of the MSPM machine

$$\begin{bmatrix} {}^1i_d \\ {}^2i_d \\ {}^3i_d \end{bmatrix} = \frac{2}{3}\frac{1}{k_F} \begin{bmatrix} \cos(\gamma_1) & \sin(\gamma_1) \\ \cos(\gamma_2) & \sin(\gamma_2) \\ \cos(\gamma_3) & \sin(\gamma_3) \end{bmatrix} \cdot \begin{bmatrix} F_{E,x} \\ F_{E,y} \end{bmatrix} \tag{2.19}$$

where k_F is the force coefficient.

The implementation of the above described force control method results in a considerable magnitude and phase ripple in the radial force generated [5], hence a harmonic compensator is introduced. The oscillation in the commanded force component occurs due to the geometric and magnetic structure of the machine, generally referred to as UMP. The compensation of the aforementioned harmonic component is required in order to reduce the time dependent stress on the bearing element. In [5] an harmonic compensator is presented as the solution of the highlighted phase error. The ratio of the dynamic force magnitude developed (rotor in motion at constant mechanical speed:$\omega_m = const.$) with respect the static force (rotor in stall: $\omega_m = 0$) defines the amplitude gain k_h while the difference between the dynamic and static direction angles represents the direction angle error Φ_h. The expressions are reported in (2.20).

$$\begin{aligned} k_h(\vartheta_e) &= \tfrac{|F(\vartheta_e)|}{|F(0)|} \\ \Phi_h(\vartheta_e) &= \Phi(\vartheta_e) - \Phi_0 \end{aligned} \tag{2.20}$$

The force reference components input of the control system expressed by (2.19), are corrected by means of a harmonic compensation (2.21).

$$\begin{bmatrix} F_{x,c} \\ F_{y,c} \end{bmatrix} = \frac{1}{k_h(\vartheta_e)} \begin{bmatrix} \cos\left(\Phi_h(\vartheta_e)\right) & \sin\left(\Phi_h(\vartheta_e)\right) \\ -\sin\left(\Phi_h(\vartheta_e)\right) & \cos\left(\Phi_h(\vartheta_e)\right) \end{bmatrix} \cdot \begin{bmatrix} F_{E,x} \\ F_{E,y} \end{bmatrix} \tag{2.21}$$

The parameters $k_h(\vartheta_e)$ and $\Phi_h(\vartheta_e)$ have to be calculated using FEA. The control strategy therefore presents the harmonic compensator in the form of a lookup table as the coefficients require to be updated according to the rotor position and torque load condition [87] in order to guarantee stable operation of the bearingless machine.

2.4.6 Triple three-phase winding structure with Vector Space Decomposition (VSD) method employed for the force and torque control

The machine presented in Figure 2.8 is considered in this paragraph. The VSD method proposed in [88, 89] considers the nine-phase sectored machine as an unique device that can be controlled to generate appropriate field harmonics in the airgap. The vector formulation of the torque and radial force as a function of the field harmonics is described by the following relation:

$$\begin{bmatrix} \bar{F}_{p-1} \\ \bar{F}_{p+1} \\ T_E \end{bmatrix} = k_c \begin{bmatrix} \bar{H}_{M,p}\bar{H}^*_{C,p+1}e^{-jp\theta_m} \\ \bar{H}_{M,p}\bar{H}^*_{C,p-1}e^{jp\theta_m} \\ 2\delta\ \Re\{jp\bar{H}_{M,p}\bar{H}^*_{C,p}e^{jp\theta_m}\} \end{bmatrix} \tag{2.22}$$

$$\bar{F} = \bar{F}_{p-1} + \bar{F}_{p+1} \tag{2.23}$$

where $\bar{F}$ is the resulting force vector ($F_x + jF_y$ or $Fe^{j\theta_f}$), $\bar{F}_{p-1}$ and $\bar{F}_{p+1}$ are the contributions to the force of the $(p-1)^{th}$ and $(p+1)^{th}$ field harmonics. k_c is equal to $\frac{\pi}{2}\mu_0 RL$, $\bar{H}_{M,p}$ represents the p^{th} harmonic of permanent magnet field (of the Fourier series of the field spatial distribution) in the rotor reference frame, $\bar{H}_{C,p-1}$, $\bar{H}_{C,p}$ and $\bar{H}_{C,p+1}$ represents the $(p-1)^{th}$, p^{th} and $(p+1)^{th}$ harmonics of the armature field; L is the stator active length; R is the middle radius of the airgap; δ is the airgap thickness

including the magnets.

The relation between the field harmonics produced by the currents and the space vectors of the currents, introduced in [88] in order to allow the independent control of the field harmonics, is as follows:

$$\bar{H}_{C,\rho} = \frac{24 N_c sin\frac{\rho\Delta\varphi}{2}}{\rho\pi\delta}\bar{i}_\rho \tag{2.24}$$

where N_c is the number of turns per phase, $\Delta\varphi$ is the coil pitch and $\bar{i}_\rho$ is the ρ-th current space vector defined by the following Clarke transformation, adapted to the analysed machine:

$$\bar{i}_\rho = \frac{2}{9}\underbrace{\sum_{k=18,1,2,6,7,8,12,13,14}}_{slots} i_k e^{j\rho\varphi_k} \tag{2.25}$$

where k is the number of the slot where each phase appears following the slots clockwise, i_k is the current in the k^{th} slot and φ_k is equal to $\frac{2\pi}{18}(k-1)$.

The expression of the resultant force vector can be written as follows, observing (2.24) and (2.25), and considering the pole pairs number of the machine ($p = 3$):

$$\bar{F} = (F_2 + F_4)e^{j\theta_f} = K_{F2}\bar{i}_2^* e^{j3\theta_m} + K_{F4}\bar{i}_4 e^{-j3\theta_m}. \tag{2.26}$$

The evaluation of the force constants K_{F2} and K_{F4} is presented in [88, 89]. Finally, the current space vector needed to generate the torque and radial force are defined by

$$\begin{bmatrix} \bar{i}_{2,ref} \\ \bar{i}_{4,ref} \\ \bar{i}_{3,ref} \end{bmatrix} = \begin{bmatrix} (F2_{ref}/K_{F2})e^{j3\theta_m - \theta_f} \\ (F4_{ref}/K_{F4})e^{j3\theta_m + \theta_f} \\ j(T_{ref}/K_T)e^{j3\theta_m} \end{bmatrix} \tag{2.27}$$

where K_T is the torque constant, $F2$ and $F4$ are the contributions of the 2^{nd} and 4^{th} magnetic field harmonics to the total force production, as in (2.26). It is worth to note that in the three vectorial equations in (2.27), the fist two are responsible for the force generation and the third one describes completely the torque production. Because the 2^{nd} and 4^{th} current space vectors can be controlled independently by the 3^{rd} one, the control of the force by the VSD method is completely independent from

the torque one [88, 89]. Furthermore, each current space vector can be controlled in a reference frame synchronous with the reference vector as:

$$\begin{bmatrix} \bar{i}_{2,syn,ref} \\ \bar{i}_{4,syn,ref} \\ \bar{i}_{3,syn,ref} \end{bmatrix} = \begin{bmatrix} (F2_{pu})F_{ref}/K_{F2} \\ (1-F2_{pu})F_{ref}/K_{F4} \\ jT_{ref}/K_T \end{bmatrix} \tag{2.28}$$

where $F2_{pu}$ is the force, in per unit, produced by the 2^{nd} order harmonic of the armature field. In other words, this new quantity is the ratio between the contribution of 2^{nd} magnetic field harmonic to the force and the force magnitude.

2.5 Multi-Phase Motors

The previous section showed different examples of multiphase motors employed to control simultaneously motoring torque and radial suspension force. As anticipated in the introduction a multiphase PMSM has been considered in this PhD project, therefore this section provides a state of the art of the multiphase technology.

2.5.1 Applications

Multiphase motor drives have been already adopted almost 50 years ago when, in 1969, a five-phase voltage source inverter-fed induction motor drive was proposed [90]. For the following 20 years multiphase motors have attracted a rather limited attention, till the 1990s, when researchers from all over the world started looking with great interest to their potentiality [91]. In particular, their field of application are electric ship propulsion [92–94], electric vehicle and locomotive traction [93, 95–97] and aircraft [98–100]. All the aforementioned applications require large power converters. Therefore, the possibility of splitting the power into several converters is

of great interest since the cost and the stress of the electronic components will drop. Furthermore, a multiphase winding presents a greater number of degrees of freedom than a three-phase machine that can be exploited for different scopes:

- Independent control of MMF spatial harmonic components that can be exploited, for instance, to produce suspension force in a BM [84–86] or to increase the torque density of the drive synchronizing the third harmonic with the fundamental [101].
- Multimotor drives consisting in a set of multiphase machines with the stator windings connected in series with an opportune permutation of the phases [102, 103].
- Fault tolerant capabilities of the motor drive can be successfully improved with a multiphase winding structure.

2.5.2 Modelling

Multiphase machines can be modelled following two different approaches: Vector-Space Decomposition [104] and Park's theory [105–107].

2.5.2.1 Modelling in Park's coordinates

An extension of the two-axis Park's theory is particularly utilized for the so called phase-split multiphase machines consisting in N three-phase windings displaced $60/N$ electrical degrees apart. The triplets of the electrical quantities of each three-phase set are represented through N rotating space vectors and homopolar components that are then projected onto an orthogonal $d-q$ axis plane [106].
Assuming linear magnetic behaviour of the materials, the voltage equation of a phase-

split synchronous machine with N three-phase windings can be written as in (2.29) [106].

$$\begin{bmatrix} \mathbf{v}_1 \\ \vdots \\ \mathbf{v}_N \\ \hat{\mathbf{v}}_r \end{bmatrix} = \begin{bmatrix} \mathbf{R} & \dots & \mathbf{0}_3 & \mathbf{0}_3 \\ \vdots & \ddots & \vdots & \vdots \\ \mathbf{0}_3 & \dots & \mathbf{R} & \mathbf{0}_3 \\ \mathbf{0}_3 & \dots & \mathbf{0}_3 & \mathbf{R}_r \end{bmatrix} \begin{bmatrix} \mathbf{i}_1 \\ \vdots \\ \mathbf{i}_N \\ \hat{\mathbf{v}}_r \end{bmatrix} + \begin{bmatrix} \mathbf{L}_{1,1} & \dots & \mathbf{L}_{1,N} & \mathbf{L}_{1,r} \\ \vdots & \ddots & \vdots & \vdots \\ \mathbf{L}_{N,1} & \dots & \mathbf{L}_{N,N} & \mathbf{L}_{N,r} \\ \mathbf{L}_{r,1} & \dots & \mathbf{L}_{r,N} & \hat{\mathbf{L}}_{r,r} \end{bmatrix} \frac{d}{dt} \begin{bmatrix} \mathbf{i}_1 \\ \vdots \\ \mathbf{i}_N \\ \hat{\mathbf{v}}_r \end{bmatrix} \tag{2.29}$$

where $\mathbf{v}_j = \begin{bmatrix} v_{a,j} & v_{b,j} & v_{c,j} \end{bmatrix}^T$, $\mathbf{i}_j = \begin{bmatrix} i_{a,j} & i_{b,j} & i_{c,j} \end{bmatrix}^T$ are stator variables while $\hat{\mathbf{v}}_r = \begin{bmatrix} 0 & 0 & v_f \end{bmatrix}^T$, $\hat{\mathbf{v}}_r = \begin{bmatrix} i_{kd} & i_{kq} & i_f \end{bmatrix}^T$ are rotor variables. Subscripts kd, kq, and f stand for $d-q$ axis rotor damper circuit and rotor field circuit (or equivalent PM current), respectively $\mathbf{R}$ and $\mathbf{R}_r$ are the stator and rotor resistance matrix, $\mathbf{L}_{i,j}$ the stator inductance matrix and $\mathbf{L}_{r,r}$, $\mathbf{L}_{j,r} = \mathbf{L}_{r,i}$ the rotor inductance matrices ($i, j = 1, ..., N$). [106] details the structure of the aforementioned matrices while [107] gives their numerical values for a chosen prototype synchronous machine. The quantities under $\hat{}$ are expressed in the $d-q-0$ reference frame.

The extended Park's transformation is given by

$$\mathbf{T} = \begin{bmatrix} \mathbf{T}_1 & \dots & \mathbf{0}_3 & \mathbf{0}_3 \\ \vdots & \ddots & \vdots & \vdots \\ \mathbf{0}_3 & \cdots & \mathbf{T}_N & \mathbf{0}_3 \\ \mathbf{0}_3 & \cdots & \mathbf{0}_3 & \mathbf{I}_N \end{bmatrix} \tag{2.30}$$

where

$$\mathbf{T}_{j+1} = \sqrt{\frac{2}{3}} \begin{bmatrix} \cos(\vartheta_e - j\alpha) & \sin(\vartheta_e - j\alpha) & 0 \\ -\sin(\vartheta_e - j\alpha) & \cos(\vartheta_e - j\alpha) & 0 \\ 0 & 0 & 1 \end{bmatrix} \begin{bmatrix} 1 & -1/2 & -1/2 \\ 0 & \sqrt{3}/2 & -\sqrt{3}/2 \\ 1/\sqrt{2} & 1/\sqrt{2} & 1/\sqrt{2} \end{bmatrix} \tag{2.31}$$

and $j = 0, 1, ..., N-1$. The machine quantities in (2.29) can be now transformed into the $d-q-0$ reference frame whose model can be found in (2.32).

$$\begin{bmatrix} \hat{\mathbf{v}}_1 \\ \vdots \\ \hat{\mathbf{v}}_N \\ \hat{\mathbf{v}}_r \end{bmatrix} = \begin{bmatrix} \mathbf{R} & \dots & \mathbf{0}_3 & \mathbf{0}_3 \\ \vdots & \ddots & \vdots & \vdots \\ \mathbf{0}_3 & \dots & \mathbf{R} & \mathbf{0}_3 \\ \mathbf{0}_3 & \dots & \mathbf{0}_3 & \mathbf{R}_r \end{bmatrix} \begin{bmatrix} \hat{\mathbf{i}}_1 \\ \vdots \\ \hat{\mathbf{i}}_N \\ \hat{\mathbf{i}}_r \end{bmatrix} + \omega_e \begin{bmatrix} \mathbf{J} & \dots & \mathbf{0}_3 & \mathbf{0}_3 \\ \vdots & \ddots & \vdots & \vdots \\ \mathbf{0}_3 & \dots & \mathbf{J} & \mathbf{0}_3 \\ \mathbf{0}_3 & \dots & \mathbf{0}_3 & \mathbf{0}_3 \end{bmatrix} \frac{d}{dt} \begin{bmatrix} \hat{\mathbf{i}}_1 \\ \vdots \\ \hat{\mathbf{i}}_N \\ \hat{\mathbf{i}}_r \end{bmatrix} + \\ + \begin{bmatrix} \hat{\mathbf{L}}_{1,1} & \dots & \hat{\mathbf{L}}_{1,N} & \hat{\mathbf{L}}_{1,r} \\ \vdots & \ddots & \vdots & \vdots \\ \hat{\mathbf{L}}_{N,1} & \dots & \hat{\mathbf{L}}_{N,N} & \hat{\mathbf{L}}_{N,r} \\ \hat{\mathbf{L}}_{r,1} & \dots & \hat{\mathbf{L}}_{r,N} & \hat{\mathbf{L}}_{r,r} \end{bmatrix} \frac{d}{dt} \begin{bmatrix} \hat{\mathbf{i}}_1 \\ \vdots \\ \hat{\mathbf{i}}_N \\ \hat{\mathbf{i}}_r \end{bmatrix} \quad (2.32)$$

where $\hat{v} = \begin{bmatrix} \hat{v}_1 \\ \vdots \\ \hat{v}_N \\ \hat{v}_r \end{bmatrix} = \mathbf{T} \begin{bmatrix} v_1 \\ \vdots \\ v_N \\ \hat{v}_r \end{bmatrix}$, $\hat{i} = \begin{bmatrix} \hat{i}_1 \\ \vdots \\ \hat{i}_N \\ \hat{i}_r \end{bmatrix} = \mathbf{T} \begin{bmatrix} i_1 \\ \vdots \\ i_N \\ \hat{i}_r \end{bmatrix}$, $\mathbf{J} = \mathbf{T}_j \frac{d\mathbf{T}_j^T}{d\vartheta_e}$, $\hat{\mathbf{L}}_{j,r} = \hat{\mathbf{L}}_{r,j}^T = \mathbf{T}_j \mathbf{L}_{j,r}$
and $\hat{\mathbf{L}}_{i,j} = \hat{\mathbf{L}}_{j,i}^T = \mathbf{T}_i \mathbf{L}_{i,j} \mathbf{T}_j^T$.

2.5.2.2 Vector-Space Decomposition

When a symmetrical multiphase winding is chosen (phase progression of $360/N$) the VSD transformation can rely on consolidated and well known methods, based on Fortescue transform [108]. The number of phases N can be either even or odd and they are assumed to be connected in star with a single neutral point. The transformation maps the machine original $N-$dimensional voltage and current vectors into new two-dimensional and orthogonal subspaces [104]. The matrix that provides the transformation is the generalized Clarke's transformation written in (2.33) [91].

$$\mathbf{C} = \sqrt{\frac{2}{N}} \begin{bmatrix} 1 & \cos\alpha & \cos 2\alpha & \cos 3\alpha & \dots & \cos 3\alpha & \cos 2\alpha & \cos\alpha \\ 0 & \sin\alpha & \sin 2\alpha & \sin 3\alpha & \dots & -\sin 3\alpha & -\sin 2\alpha & -\sin\alpha \\ 1 & \cos 2\alpha & \cos 4\alpha & \cos 6\alpha & \dots & \cos 6\alpha & \cos 4\alpha & \cos 2\alpha \\ 0 & \sin 2\alpha & \sin 4\alpha & \sin 6\alpha & \dots & -\sin 6\alpha & -\sin 4\alpha & -\sin 2\alpha \\ 1 & \cos 3\alpha & \cos 6\alpha & \cos 9\alpha & \dots & \cos 9\alpha & \cos 6\alpha & \cos 3\alpha \\ 0 & \sin 3\alpha & \sin 6\alpha & \sin 9\alpha & \dots & -\sin 9\alpha & -\sin 6\alpha & -\sin 3\alpha \\ \vdots & \vdots & \vdots & \vdots & \vdots & \vdots & \vdots & \vdots \\ 1 & \cos(\frac{N-2}{2})\alpha & \cos 2(\frac{N-2}{2})\alpha & \cos 3(\frac{N-2}{2})\alpha & \dots & \cos 3(\frac{N-2}{2})\alpha & \cos 2(\frac{N-2}{2})\alpha & \cos(\frac{N-2}{2})\alpha \\ 0 & \sin(\frac{N-2}{2})\alpha & \sin 2(\frac{N-2}{2})\alpha & \sin 3(\frac{N-2}{2})\alpha & \dots & -\sin 3(\frac{N-2}{2})\alpha & -\sin 2(\frac{N-2}{2})\alpha & -\sin(\frac{N-2}{2})\alpha \\ \frac{1}{\sqrt{2}} & \frac{1}{\sqrt{2}} & \frac{1}{\sqrt{2}} & \frac{1}{\sqrt{2}} & \dots & \frac{1}{\sqrt{2}} & \frac{1}{\sqrt{2}} & \frac{1}{\sqrt{2}} \\ \frac{1}{\sqrt{2}} & -\frac{1}{\sqrt{2}} & \frac{1}{\sqrt{2}} & -\frac{1}{\sqrt{2}} & \dots & -\frac{1}{\sqrt{2}} & \frac{1}{\sqrt{2}} & -\frac{1}{\sqrt{2}} \end{bmatrix} \tag{2.33}$$

where $\alpha = 2\pi/N$. The first two rows of matrix $\mathbf{C}$ define the fundamental $\alpha - \beta$ components for the flux and torque production while the last two rows represent the two zero-sequence components. The last row is omitted when N is an odd number. The rows in between are $(N-4)/2$ (or $(N-3)/2$ if N is odd) orthogonal subspaces that do not contribute to the torque production if the flux around the airgap is assumed having a sinusoidal distribution.

On the other hand, when the phase progression is $180/N$ the above transformation has to be modified. It is the case of the so called phase-split machine, among which the dual three-phase is certainly the best know example The latter consists of two three-phase windings shifted of $180/N = 30$[deg] and it has been modelled using the VSD approach in [104]. In [109, 110] a generalized VSD method is proposed in order to write the model of a general phase-split machine.

2.5.3 Fault tolerant capabilities

In order to provide a rotating magnetic field in a three-phase motor when one phase of the motor or the inverter is faulty, a zero-sequence current is needed, hence the neutral point has to be connected to the middle point of a divided DC link. As a matter of facts, when one supply phase is opened the currents of the remaining two phases are identical in magnitude and opposite in phase displacement if the machine is star-connected and with isolated neutral point. Hence, they cannot be independently controlled. One of the greatest advantage of multiphase machines is their fault tolerant capabilities without the need of the neutral point connection. This remarkable feature is possible thanks to the phase redundancy that allows a N phase machine to continue operating for any number of faulty phases up to $N-3$ [91]. In particular, it is possible to exploit the additional degrees of freedom that can be used to enhance torque in healthy condition to design a suitable fault control strategy.
Several examples of fault tolerant multiphase machines can be found in the literature. [111] presents a fault tolerant control technique of a six-phase PM motor for drivetrain applications. [112], instead, analyses the fault tolerant capabilities of a five-phase PM motor for ship propulsion.
A complete analysis of the healthy and fault capabilities of a dual three-phase PM fractional-slot machine has been carried out in [113, 114] where three different winding configurations were arranged: 1) the two windings are completely separated and each one occupies 180 [deg] in the stator circumference; 2) the phases of the winding are alternated along the stator circumference; 3) the single coils are alternated according to same phase order and different windings. It results that configuration 1) presents higher average torque and lower torque ripple than the other two configurations when one of the three-phase windings is open circuited. Furthermore, 1) features the highest average torque and smallest short circuit current in the case of both single-phase and three-phase short circuits. On the other hand, the UMP generated during an open circuit of one the three-phase winding is huge compared to the other configurations (configuration 3) has the smallest UMP) and configuration

3) allows the implementation of VSD control resulting in the best performances for healthy condition. The conclusion drawn in [113] is that configuration 3) is the most suitable for the dual three-phase machine considered with the drawback of having the highest mutual coupling between the windings, involving lower torque during short circuit faults and the presence of undesired mutual back-EMF in the winding.
As it has been shown, the multiphase winding approach can be also applied to bearingless motors enhancing their reliability. Different control approaches can be found in the literature to guarantee a stable rotor suspension in the case of open-circuit fault [4, 84, 89, 115]. On the other hand, the short-circuit fault is studied for a single-winding bearingless switched reluctance motor in [19] and for a six-phase bearingless PM motor in [116].

2.6 Levitating Systems for Vibration Suppression

In the literature review presented so far the active control of radial force was purely applied to the rotor suspension. However, as it has been stated in 2.2, radial forces can be controlled to actively suppress vibrations in rotating machinery. In the next Chapters, experimental results will show that the radial position control presents a periodic fluctuation caused by vibration forces acting on the rotor element. Therefore, a proper position controller alghorithm will be introduced to suppress the rotor oscillation and to improve the levitation performance.
In this section, different vibration suppression solutions proposed in the literature are presented. The forces acting on the machine rotor can be both electromagnetic and mechanical. They typically present specific frequencies which are related to the design of the machine and the operating condition (number of poles, stator and rotor slotting, rotor bars, stator slots, rotational speed, load, saturation, eccentricity and eventual faults, etc.) [117]. The main mechanical source is the rotor mass unbalance that produces forces synchronous with the rotation frequency and its multiples and sub-multiples [117].

Several position controller configurations have been proposed to suppress the periodic disturbances using AMB. In [118] a notch filter is implemented to eliminate the synchronous disturb. In [119] a disturbance observer is implemented in state space and applied to reject the time-varying disturbances. A multi-frequency force disturbance elimination is proposed in [120] consisting of several resonant controllers connected in parallel. In [121], a robust controller is designed based on the H_2 and H_∞ optimal controller theory. In order to calculate the weighting vectors for the controller synthesis an identification of the system is carried out.
As far as the bearingless machines are concerned, [117, 122] present a position controller involving a stabilizing controller and a harmonic compensator for a two-pole bearingless induction motor. The former has the only task to keep the rotor stably suspended within the mechanical bounds and it is designed as a state feedback control with a state estimator since the state vector cannot be measured. The stabilizing controller does not present good periodic disturbance rejection, hence a harmonic compensator is necessary. Being f_r and f_s the rotation and the two-pole supply frequencies respectively, the three vibration frequencies considered in [117, 122] are:

- f_r: caused by the rotor mass unbalance.
- $2f_s - f_r$: caused by the slotting and eccentricity in a two-pole motor [123, 124].
- f_s: caused by the interaction between homopolar flux [125] and two-pole supply flux.

A vibration suppression technique for a flexible shaft of a bearingless induction motor has been proposed by [126]. The radial force control is employed to damp the vibrations while going through the first bending critical speed. A simplified position controller is proposed including proportional, integral and, so called, practical derivative blocks. A forth order high-cut filter is implemented in the practical derivative block. It is shown that the proposed position controller significantly suppress the

rotor vibration while crossing the critical speed at around 7000 [r/min] preventing the touchdown of the shaft on the backup bearings.

2.7 Chapter Summary

The various applications of the radial force control in electrical machines have been exposed in this Chapter with a particular focus on the bearingless technology. After a brief introduction that presents several engineering fields where the radial force control has been employed, BMs have been analysed more in detail and classified under different aspects.

An overview of the different radial force control techniques that has been proposed to reach the goal of the rotor suspension were also presented. The multiphase winding arrangement has shown several advantages over the two-winding or the parallel path structures and was chosen in this PhD project in order to develop a novel suspension force method.

A dedicated section for multiphase machines was also included in order to present more in details the advantages of adopting a poly-phase winding structure and the different models that can be chosen to study them.

Finally, in the last section the topic of vibration suppression applied to levitating systems is more carefully analysed. Different solution to suppress the rotor oscillation due to the periodic disturbances are presented for both AMB and bearingless motors.

Chapter 3

Electromagnetic Model of the Multi-Sector PM Synchronous Machine

3.1 Introduction

This Chapter deals with the analytical model of the analysed multi-three-phase machine. To start with, the phase voltage formulation is presented and employed to obtain the expression of the state space electrical model representation in the rotor synchronous reference frame. Then, the matrix formulation and numerical values of the $d-q$ axis inductances are presented.

In the following section, an alternative radial force and torque control technique is applied to the MSPM machine. The distribution of the three-phase windings (sectors) enables to achieve an independent control of the $x-y$ force components and torque over each sector. The modelling and characterization of the machine is performed in combination with the force/torque generation technique. The mathematical model

introduced takes into account the cross-coupling between the torque and the forces developed by the machine as well as the rotor radial displacement.

The winding configuration chosen is similar to the one proposed in [5, 88, 89], but the radial force and torque generation methods used are very different. In [5] the suspension force and torque are assumed decoupled and they are produced by $d-$ and $q-$axis current, respectively. This assumption leads to a remarkable suspension force ripple that would compromise the levitation performance of the machine. Therefore, an harmonic compensator has been introduced in order to calculate the current references that reduce the force ripple. A lookup table is employed in the harmonic compensator increasing the commissioning time of the control technique. In [88, 89] the VSD technique has been used to generate appropriate magnetic field space harmonics in the airgap in order to produce the radial force and torque.

None of the aforementioned works take into account the optimization of the reference current signals. [4] dealt with the problem of the reference current calculation with the constrain of minimizing the copper losses. The machine considered was a six-phase slice PM bearingless motor with concentrated windings. Each phase was connected to a converter, hence six single-phase inverters were required to control the BM resulting in a rather complicated system.

In the last section, the reference currents are calculated setting as objective the minimization of the Joule losses. The open-circuit fault of a whole three-phase machine sector is also considered in this section.

The multi-three-phase current components are fed into the machine by adopting a set of conventional three-phase inverters in combination with a single control platform. The resultant drive includes more three-phase inverters then a conventional one, however the power rating of each inverter can be decreased to 1/3 that of a conventional machine. Furthermore, thanks to the inverters number, the fault tolerant capability of the resultant system can be enhanced.

3.2 $d-q$ Axis Voltage Equation Model in State Space

3.2.1 The machine structure

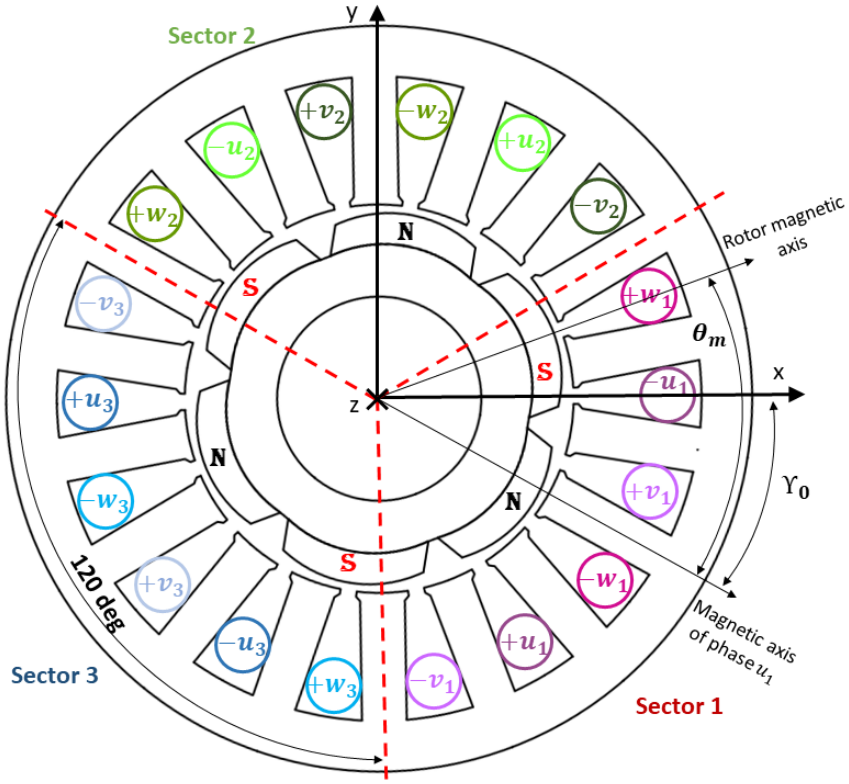


Figure 3.1: Cross section of the 18 slot - 6 poles 3 sectors PMSM with three single layer distributed three-phase windings.

A conventional 18 slot - 6 poles surface mounted PMSM that was available within the facilities of the Power Electronic Machine and Control (PEMC) group of the University of Nottingham has been adopted as test machine. Surface mounted PMSM are well known for their high efficiency and power density and they are widely investigated for what concerns bearingless applications because of their relatively simple

control system [2].

The main characteristics of the considered machine are listed in Table 3.1. The original three-phase winding has been modified and a multi-three-phase one created. Figure 3.1 presents the cross-section of the considered machine highlighting the sectored multi-three-phase winding arrangement. The signs + and − in front of the phase labels indicate current flowing out and into the plane of the paper, respectively. Each of the three-phase sectors has a full-pitched distributed winding with a floating star point. The left superscript s in this manuscript will be adopted in order to define quantities related to the single s^{th} sector. The machine under investigation has a number of sectors $n_s = p$, where p is the pole pairs number. The angular position of the generic sector s with respect the $x-$axis is given by ${}^s\gamma = (s-1)\,(2\pi/n_s) + \gamma_0$ where γ_0 defines the angular position of the magnetic axis of the sector 1 with respect to the $x-$axis. Finally, the electrical angular position of the rotor magnetic axis with respect the winding magnetic axis is defined as $\vartheta_e = p\,\vartheta_m$.

As it will be demonstrated, the independent current control of each sector allows for both torque and radial force control.

Table 3.1: Machine parameters

Parameter	**Value**
Pole number ($2p$)	6
PM material	NdFeB
PM remanence flux density B_{res}	1.24 T
PM relative permeability μ_r	1.031
Power rating	1.5 kW
Peak value of the current (I_{rated})	13 A
Rated Speed (v_{rated})	3000 rpm
Turn/coil (N_c)	22
PM flux of one sector ($^s\Lambda_{PM}$)	0.0284 Wb
Torque constant (k_T)	0.128 Nm/A
Line to line voltage constant (k_V)	15.5 V/krpm
Outer Stator diameter	95 mm
Inner Stator diameter	49.5 mm
Axial length (l)	90 mm
Airgap length (g_0)	1 mm
Magnets thickness (h_m)	4 mm

3.2.2 State space representation of the $d-q$ axis voltage equation

The electrical model presented in this section was carried out with the assumption of linear magnetic behaviour of the materials and centred rotor.
The nine-phase voltage equations of the analysed machine can be written in matrix form as in (3.1).

$$\bar{v} = \mathbf{R}\bar{i} + \frac{\partial \bar{\lambda}}{\partial t} \tag{3.1}$$

where

$$\begin{aligned}
&\bar{v} = \begin{bmatrix} {}^1v_u & {}^1v_v & {}^1v_w & {}^2v_u & {}^2v_v & {}^2v_w & {}^3v_u & {}^3v_v & {}^3v_w \end{bmatrix}^T \\
&\bar{i} = \begin{bmatrix} {}^1i_u & {}^1i_v & {}^1i_w & {}^2i_u & {}^2i_v & {}^2i_w & {}^3i_u & {}^3i_v & {}^3i_w \end{bmatrix}^T \\
&\bar{\lambda} = \bar{\lambda}_i + \bar{\lambda}_{PM} = \begin{bmatrix} {}^1\lambda_u & {}^1\lambda_v & {}^1\lambda_w & {}^2\lambda_u & {}^2\lambda_v & {}^2\lambda_w & {}^3\lambda_u & {}^3\lambda_v & {}^3\lambda_w \end{bmatrix}^T \\
&\mathbf{R} = R_{ph}\mathbf{I}
\end{aligned} \tag{3.2}$$

$\mathbf{I}$ is the identity matrix while $\bar{v}$, $\bar{i}$ and $\bar{\lambda}$ are the vectors of the nine-phase voltages, phase currents and flux linkages of the multi-three-phase machine, respectively. $\bar{\lambda}$ is expressed with its two contributions: phase currents ($\bar{\lambda}_i$) and permanent magnets ($\bar{\lambda}_{PM}$). R_{ph} is the phase resistance. Assuming the phase inductance matrix $\mathbf{L}_{ph}$ position independent, as justified in the next paragraph, (3.1) can be written as

$$\bar{v} = \mathbf{R}\bar{i} + \mathbf{L}_{ph}\frac{\partial \bar{i}}{\partial t} + \bar{e} \tag{3.3}$$

where

$$\bar{e} = \frac{\partial \bar{\lambda}_{PM}}{\partial t} = \begin{bmatrix} {}^1e_u & {}^1e_v & {}^1e_w & {}^2e_u & {}^2e_v & {}^2e_w & {}^3e_u & {}^3e_v & {}^3e_w \end{bmatrix}^T \tag{3.4}$$

$\bar{e}$ is the vector of the nine back-EMFs of the machine.

The direct nine-phase Park transformation matrix is defined as

$$\mathbf{T}_{P,9}(\vartheta_e) = \begin{bmatrix} \mathbf{T}_P(\vartheta_e) & \mathbf{0} & \mathbf{0} \\ \mathbf{0} & \mathbf{T}_P(\vartheta_e) & \mathbf{0} \\ \mathbf{0} & \mathbf{0} & \mathbf{T}_P(\vartheta_e) \end{bmatrix} \tag{3.5}$$

while the inverse transformation is

$$\mathbf{T}^{-1}_{P,9}(\vartheta_e) = \begin{bmatrix} \mathbf{T}^{-1}_P(\vartheta_e) & \mathbf{0} & \mathbf{0} \\ \mathbf{0} & \mathbf{T}^{-1}_P(\vartheta_e) & \mathbf{0} \\ \mathbf{0} & \mathbf{0} & \mathbf{T}^{-1}_P(\vartheta_e) \end{bmatrix} \tag{3.6}$$

Considering the amplitude-invariant transformation, $\mathbf{T}_P(\vartheta_e)$ and $\mathbf{T}_P^{-1}(\vartheta_e)$ are given by

$$\mathbf{T}_P(\vartheta_e) = \frac{2}{3}\begin{bmatrix} \cos(\vartheta_e) & \cos(\vartheta_e - 2\pi/3) & \cos(\vartheta_e - 4\pi/3) \\ -\sin(\vartheta_e) & -\sin(\vartheta_e - 2\pi/3) & -\sin(\vartheta_e - 4\pi/3) \\ 1/2 & 1/2 & 1/2 \end{bmatrix} \tag{3.7}$$

and

$$\mathbf{T}_P^{-1}(\vartheta_e) = \begin{bmatrix} \cos(\vartheta_e) & -\sin(\vartheta_e) & 1 \\ \cos(\vartheta_e - 2\pi/3) & -\sin(\vartheta_e - 2\pi/3) & 1 \\ \cos(\vartheta_e - 4\pi/3) & -\sin(\vartheta_e - 4\pi/3) & 1 \end{bmatrix} \tag{3.8}$$

The homopolar component will be omitted in the following equations since each three-phase winding presents an isolated neutral point, hence the zero-sequence current cannot circulate. Therefore, the last row in $\mathbf{T}_P(\vartheta_e)$ and the last column in $\mathbf{T}_P^{-1}(\vartheta_e)$ are neglected. As depicted in Figure 3.1 $\vartheta_e = 0$ when the axis of phase u of each sector is aligned with the correspondent PM. With this assumption the voltage equations in the $d-q$ axis synchronous reference frame can be written as in (3.9).

$$\bar{v}_{dq} = \mathbf{R}\bar{i}_{dq} + \mathbf{L}_{dq,t}(\vartheta_e)\frac{\partial \bar{i}_{dq}}{\partial t} + \frac{\partial \mathbf{L}_{dq,t}(\vartheta_e)}{\partial t}\bar{i}_{dq} + \omega_e \mathbf{J}_t \mathbf{L}_{dq,t}(\vartheta_e)\bar{i}_{dq} + \bar{e}_{dq} \tag{3.9}$$

where

$$\mathbf{J}_t = \mathbf{T}_{P,9}(\vartheta_e)\frac{\partial \mathbf{T}_{P,9}^{-1}(\vartheta_e)}{\partial t} = \begin{bmatrix} \mathbf{J} & \mathbf{0}_2 & \mathbf{0}_2 \\ \mathbf{0}_2 & \mathbf{J} & \mathbf{0}_2 \\ \mathbf{0}_2 & \mathbf{0}_2 & \mathbf{J} \end{bmatrix}; \mathbf{J} = \begin{bmatrix} 0 & -1 \\ 1 & 0 \end{bmatrix} \tag{3.10}$$

and

$$\begin{aligned}
\bar{v}_{dq} &= \begin{bmatrix} {}^1v_d & {}^1v_q & {}^1v_d & {}^2v_q & {}^3v_d & {}^3v_q \end{bmatrix}^T \\
\bar{i}_{dq} &= \begin{bmatrix} {}^1i_d & {}^1i_q & {}^2i_d & {}^2i_q & {}^3i_d & {}^3i_q \end{bmatrix}^T \\
\bar{\lambda}_{dq,PM} &= \begin{bmatrix} {}^1\Lambda_{PM} & 0 & {}^2\Lambda_{PM} & 0 & {}^3\Lambda_{PM} & 0 \end{bmatrix}^T \\
\bar{e}_{dq} &= \omega_e \mathbf{J}_t \bar{\lambda}_{dq,PM} = \omega_e \begin{bmatrix} 0 & {}^1\Lambda_{PM} & 0 & {}^2\Lambda_{PM} & 0 & {}^3\Lambda_{PM} \end{bmatrix}^T
\end{aligned} \tag{3.11}$$

The position dependent $d-q$ axis inductance matrix $\mathbf{L}_{dq,t}$ will be calculated in the next paragraph.

The state equation form in the $d-q$ reference frame is written in (3.12) having defined the symbolic representation of the time derivative of the generic variable x as $\frac{\partial x}{\partial t} = \dot{x}$.

$$\dot{\bar{i}}_{dq} = \mathbf{A}(\vartheta_e)\bar{i}_{dq} + \mathbf{B}(\vartheta_e)\bar{v}_{dq} + \mathbf{D}(\vartheta_e) \tag{3.12}$$

where state matrix $\mathbf{A}(\vartheta_e)$, the input matrix $\mathbf{B}(\vartheta_e)$ and the disturbance matrix $\mathbf{D}(\vartheta_e)$ are defined as:

$$\begin{aligned}
\mathbf{A}(\vartheta_e) &= -\mathbf{L}_{dq,t}^{-1}(\vartheta_e)\big(\mathbf{R} + \omega_e \mathbf{J}_t \mathbf{L}_{dq,t}(\vartheta_e) + \tfrac{\partial}{\partial t}(\mathbf{L}_{dq,t}(\vartheta_e))\big) \\
\mathbf{B}(\vartheta_e) &= \mathbf{L}_{dq,t}^{-1}(\vartheta_e) \\
\mathbf{D}(\vartheta_e) &= -\mathbf{L}_{dq,t}^{-1}(\vartheta_e)\bar{e}_{dq}
\end{aligned} \tag{3.13}$$

3.2.3 Matrix representation of the $d-q$ axis inductances

The phase matrix inductance $\mathbf{L}_{ph}(\vartheta_e) \in \mathbb{R}^{3n_s \times 3n_s}$ of the three three-phase machine can be found in (3.14).

$$\mathbf{L}_{ph}(\vartheta_e) = \begin{bmatrix} \mathbf{L}(\vartheta_e) & \mathbf{M} & \mathbf{M} \\ \mathbf{M} & \mathbf{L}(\vartheta_e) & \mathbf{M} \\ \mathbf{M} & \mathbf{M} & \mathbf{L}(\vartheta_e) \end{bmatrix} \tag{3.14}$$

with the self-inductance matrix

$$\mathbf{L}(\vartheta_e) = \begin{bmatrix} L_{uu}(\vartheta_e) & M_{vu}(\vartheta_e) & M_{wu}(\vartheta_e) \\ M_{uv}(\vartheta_e) & L_{vv}(\vartheta_e) & M_{wv}(\vartheta_e) \\ M_{uw}(\vartheta_e) & M_{vw}(\vartheta_e) & L_{ww}(\vartheta_e) \end{bmatrix} \tag{3.15}$$

and the mutual inductance matrix

$$\mathbf{M} = \begin{bmatrix} -M_c & M_c & M_c \\ M_c & -M_c & -M_c \\ M_c & -M_c & -M_c \end{bmatrix} \tag{3.16}$$

The coefficients of $\mathbf{L}(\vartheta_e) \in \mathbb{R}^{3\times3}$ are the self and mutual inductances of a single three-phase sector, while $\mathbf{M} \in \mathbb{R}^{3\times3}$ includes the mutual inductances between phases belonging to different sectors. The aforementioned parameters are listed as follow:

$$
\begin{aligned}
&L_{uu}(\vartheta_e) = L_1 + L_2\cos\left(2\vartheta_e\right)\\
&L_{vv}(\vartheta_e) = L_1 + L_2\cos\left(2(\vartheta_e - 2\pi/3)\right)\\
&L_{ww}(\vartheta_e) = L_1 + L_2\cos\left(2(\vartheta_e - 4\pi/3)\right)\\
&M_{uv}(\vartheta_e) = M_{vu}(\vartheta_e) = M_1 + M_2\cos\left(2(\vartheta_e - \pi/3)\right)\\
&M_{uw}(\vartheta_e) = M_{wu}(\vartheta_e) = M_1 + M_2\cos\left(2(\vartheta_e + \pi/3)\right)\\
&M_{vw}(\vartheta_e) = M_{wv}(\vartheta_e) = M_{1d} + M_{2d}\cos\left(2\vartheta_e\right)\\
&M_c = constant
\end{aligned}
\tag{3.17}
$$

The parameters in (3.17) are obtained with FEA as presented in the next section and they have been reported in Table 3.2.

Table 3.2: Phase inductance values

	L_1	L_2	M_1	M_2	M_{1d}	M_{2d}	M_c
Value [mH]	0.447	0.126e-2	-0.123	0.304e-2	0.0404	0.303e-2	0.0407

It is straightforward to notice that the sinusoidal terms in (3.17) are small due to the isotropic structure of the rotor and they will be neglected in this work. Therefore, matrix $\mathbf{L}$ can be re-written in (3.18).

$$
\mathbf{L} = \begin{bmatrix} L_1 & M_1 & M_1 \\ M_1 & L_1 & M_{1d} \\ M_1 & M_{1d} & L_1 \end{bmatrix} \tag{3.18}
$$

The phase inductance $\mathbf{L}$ differs from the one of a conventional three-phase motor because $M_{1d} \neq M_1$. This phenomena can be easily explained observing one of the three-phase windings of the machine. Indeed, phase u overlaps phases v and w embracing the same number of stator teeth (2 in the case considered). On the other hand, only one stator tooth is embraced by the overlapping of phases v and w resulting in a smaller flux linkage between the two phases.

The $d-q$ axis inductance matrix $\mathbf{L}_{dq,t}$ can be obtained in (3.19) exploiting the Park transformation matrix for a triple three-phase system written in (3.5).

$$\mathbf{L}_{dq,t}(\vartheta_e) = \mathbf{T}_{P,9}(\vartheta_e)\mathbf{L}_{ph}\mathbf{T}_{P,9}^{-1}(\vartheta_e) = \begin{bmatrix} \mathbf{L}_{dq}(\vartheta_e) & \mathbf{M}_{dq}(\vartheta_e) & \mathbf{M}_{dq}(\vartheta_e) \\ \mathbf{M}_{dq}(\vartheta_e) & \mathbf{L}_{dq}(\vartheta_e) & \mathbf{M}_{dq}(\vartheta_e) \\ \mathbf{M}_{dq}(\vartheta_e) & \mathbf{M}_{dq}(\vartheta_e) & \mathbf{L}_{dq}(\vartheta_e) \end{bmatrix} \tag{3.19}$$

where

$$\mathbf{L}_{dq}(\vartheta_e) = \begin{bmatrix} L_d(\vartheta_e) & L_{qd}(\vartheta_e) \\ L_{dq}(\vartheta_e) & L_q(\vartheta_e) \end{bmatrix} \tag{3.20}$$

and

$$\mathbf{M}_{dq}(\vartheta_e) = \begin{bmatrix} M_d(\vartheta_e) & M_{qd}(\vartheta_e) \\ M_{dq}(\vartheta_e) & M_q(\vartheta_e) \end{bmatrix} \tag{3.21}$$

The parameters in $L_{dq}(\vartheta_e)$ and $M_{dq}(\vartheta_e)$ are listed as follow:

$$\begin{aligned} L_d(\vartheta_e) &= L_{d1} + L_{d2}\cos\left(2\vartheta_e\right) \\ L_q(\vartheta_e) &= L_{q1} - L_{q2}\cos\left(2\vartheta_e\right) \\ L_{dq}(\vartheta_e) &= L_{qd}(\vartheta_e) = -L_{dq2}\sin\left(2\vartheta_e\right) \\ M_d(\vartheta_e) &= M_d + M_d\cos\left(2\vartheta_e\right) \\ M_q(\vartheta_e) &= M_q - M_q\cos\left(2\vartheta_e\right) \\ M_{dq}(\vartheta_e) &= M_{qd}(\vartheta_e) = M_{dq}\sin\left(2\vartheta_e\right) \end{aligned} \tag{3.22}$$

Since the rotor presents an isotropic structure the $d-$ and $q-$axis inductances can be considered identical. Therefore, fewer paramenters are needed to identify the inductances in (3.22) since $L_{d1} = L_{q1}$, $L_{d2} = L_{q2}$ and $M_d = M_q = M_{dq}$. The amplitude of the terms in (3.22) can be found in Table 3.3.

Table 3.3: $d-q$ inductance values

	L_{d1}	L_{d2}	L_{dq2}	M_d
Value [mH]	0.52	0.107	0.109	-0.0548

It can be noticed that although $\mathbf{L}_{ph}$ is position independent, in $\mathbf{L}_{dq,t}$ the sinusoidal terms are not negligible (around 20% of the constant terms). This is due to the non-symmetrical structure of the phase matrix inductance $\mathbf{L}$ previously discussed.
In the next paragraph the analytical calculation of the above introduced inductance values is presented. The analytical values are then validated through comparison with FE results.

3.2.4 Calculation of the $d-q$ axis inductance values

The machine presents surface PMs mounted on the rotor, hence it can be considered isotropic for what concerns the calculation of the inductance values. The self-inductance matrix $\mathbf{L}$ and the mutual inductance matrix $\mathbf{M}$ have to be identified to characterize the whole inducance matrix $\mathbf{L}_{ph}$ of the machine.
The generic inductance parameter can be evaluated as follow.

$$L_{ph1,ph2} = \frac{\lambda_{ph1,ph2}}{i_{ph2}} \tag{3.23}$$

where $\lambda_{ph1,ph2}$ is the flux linkage with phase $ph1$ generated by the current flowing in phase $ph2$ and i_{ph2} is the current flowing in phase $ph2$.
Assuming linear magnetic behaviour of the materials, the flux density in the airgap can be calculate in Appendix B for each machine phase. Then, the flux linkage $\lambda_{ph1,ph2}$ can be easily calculated in (3.24) neglecting the contribution of the tangential flux density and assuming the radial flux density independent from the axial position.

$$\lambda_{ph1,ph2} = 2\pi l N_c \int_{\xi_{ph1}}^{\zeta_{ph1}} B_{r,ph2}(\alpha_s) d\alpha_s \tag{3.24}$$

where α_s is the stator angular coordinate, $B_{r,ph2}$ is the radial component of the flux density produced by the current flowing in phase $ph2$ and ξ_{ph1} and ζ_{ph1} are the phase coil $ph1$ initial and final angular positions on the stator circumference, respectively. The above mentioned angular positions are referred to the axis of phase u_1 of sector 1. The values of ξ_{ph1} and ζ_{ph1} can be found in Table 3.4.

Table 3.4: Phase Coils Angular Positions

	ξ_{ph1} [rad]	ζ_{ph1} [rad]
$u1$	-$\pi/6$	$\pi/6$
$v1$	-$5\pi/18$	$\pi/18$
$w1$	-$\pi/18$	$5\pi/18$
$u2$	$\pi/2$	$5\pi/6$
$v2$	$7\pi/18$	$13\pi/18$
$w2$	$11\pi/18$	$17\pi/18$
$u3$	$7\pi/6$	$9\pi/6$
$v3$	$19\pi/18$	$25\pi/18$
$w3$	$23\pi/18$	$29\pi/18$

For instance

$$
\begin{aligned}
L_{u1,u1} = L_1 = \tfrac{\lambda_{u1,u1}}{i_{u1}} &= \tfrac{2\pi l N_c}{i_{u1}} \int_{-\pi/6}^{\pi/6} B_{r,u1}(\alpha_s)d\alpha_s \\
L_{v1,v1} = L_1 = \tfrac{\lambda_{v1,v1}}{i_{v1}} &= \tfrac{2\pi l N_c}{i_{v1}} \int_{-5\pi/18}^{\pi/18} B_{r,v1}(\alpha_s)d\alpha_s \\
L_{w1,w1} = L_1 = \tfrac{\lambda_{w1,w1}}{i_{w1}} &= \tfrac{2\pi l N_c}{i_{w1}} \int_{-\pi/18}^{5\pi/18} B_{r,w1}(\alpha_s)d\alpha_s \\
M_{u1,v1} = M_1 = \tfrac{\lambda_{u1,v1}}{i_{v1}} &= \tfrac{2\pi l N_c}{i_{v1}} \int_{-\pi/6}^{\pi/6} B_{r,v1}(\alpha_s)d\alpha_s \\
M_{u1,w1} = M_1 = \tfrac{\lambda_{u1,w1}}{i_{w1}} &= \tfrac{2\pi l N_c}{i_{w1}} \int_{-\pi/6}^{\pi/6} B_{r,w1}(\alpha_s)d\alpha_s \\
&\vdots \\
M_{v1,w1} = M_{1d} = \tfrac{\lambda_{v1,w1}}{i_{w1}} &= \tfrac{2\pi l N_c}{i_{w1}} \int_{-\pi/18}^{5\pi/18} B_{r,w1}(\alpha_s)d\alpha_s \\
&\vdots \\
M_{u2,u1} = -M_c = \tfrac{\lambda_{u1,u2}}{i_{u2}} &= \tfrac{2\pi l N_c}{i_{u2}} \int_{\pi/2}^{5\pi/6} B_{r,u1}(\alpha_s)d\alpha_s \\
&\vdots
\end{aligned}
\tag{3.25}
$$

The analytical values of the phase inductances of matrix $\mathbf{L}_{ph}$ are compared in Figure 3.2 a) with the ones obtained through FEA, using MagNet 7.7.1.

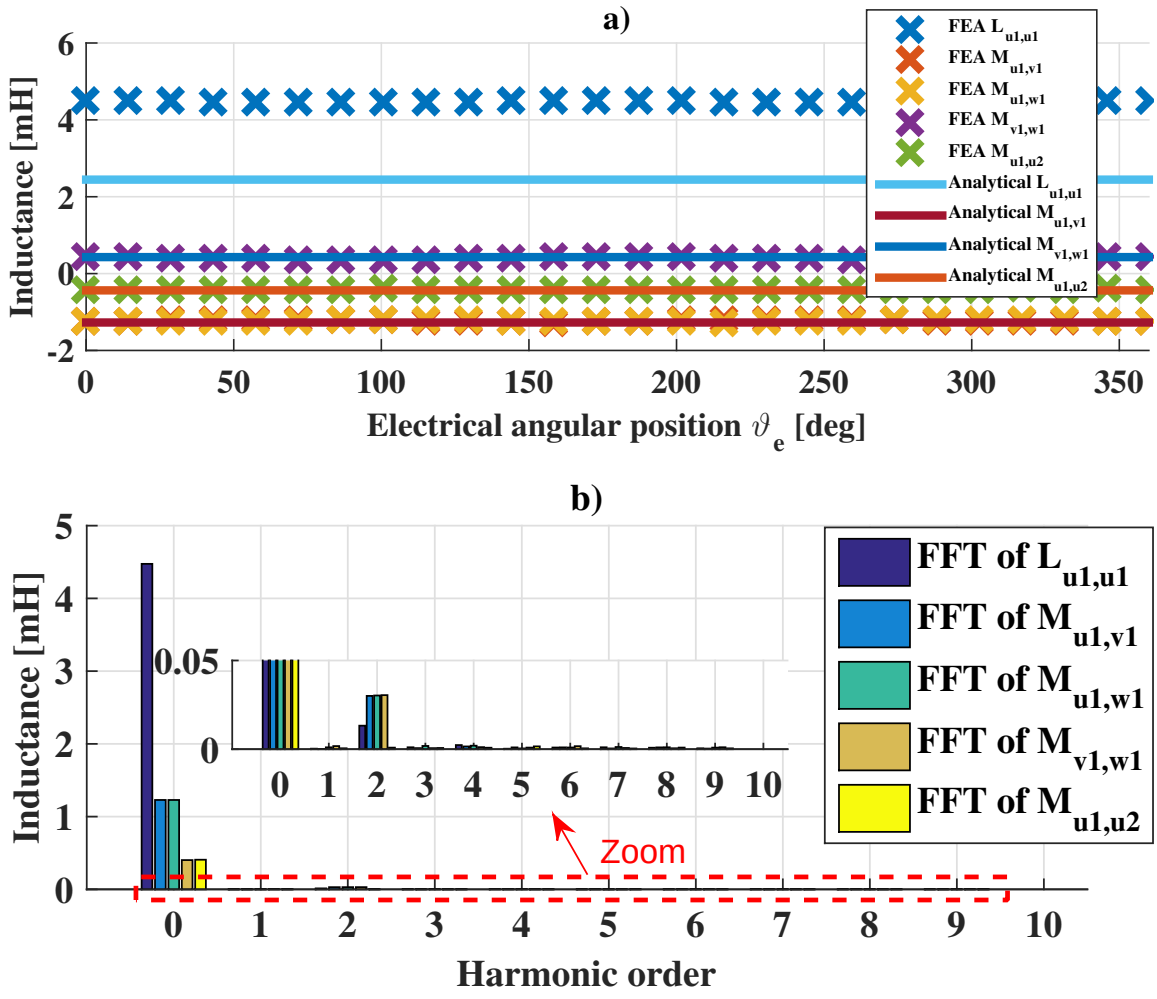


Figure 3.2: FE and analytical results for the phase inductances: a) waveforms of the inductances; b) FFT of the inductance waveforms obtained with FEA.

Multi-static linear FE simulations are performed to obtain the FE results. In each simulation the considered phase is supplied with a constant current value of 1 A and the rotor is rotated of one electrical period. The flux linkage values are recorded and subtracting to the ones produced by the PMs. Then, the inductances can be calculated with equation (3.23). It can be noticed that analytical and FE results are in good agreement. Only the analytical and FE values of the self-inductance $L_{u1,u1}$ are

very different. This is probably due to the presence of the leakage flux, and therefore of the leakage inductance L_0, in the FE result. The very small sinusoidal terms in the FE results (see Figure 3.2 b)) justifies the assumption of considering matrix $\mathbf{L}_{ph}$ position independent.

The $d-q$ axis inductance matrix $\mathbf{L}_{dq,t}(\vartheta_e)$ can be finally obtained applying equation (3.19) where the previously obtained FE values have been used in $\mathbf{L}_{ph}$. The waveforms of the elements of matrix $\mathbf{L}_{dq,t}(\vartheta_e)$ are shown in Figure 3.3.

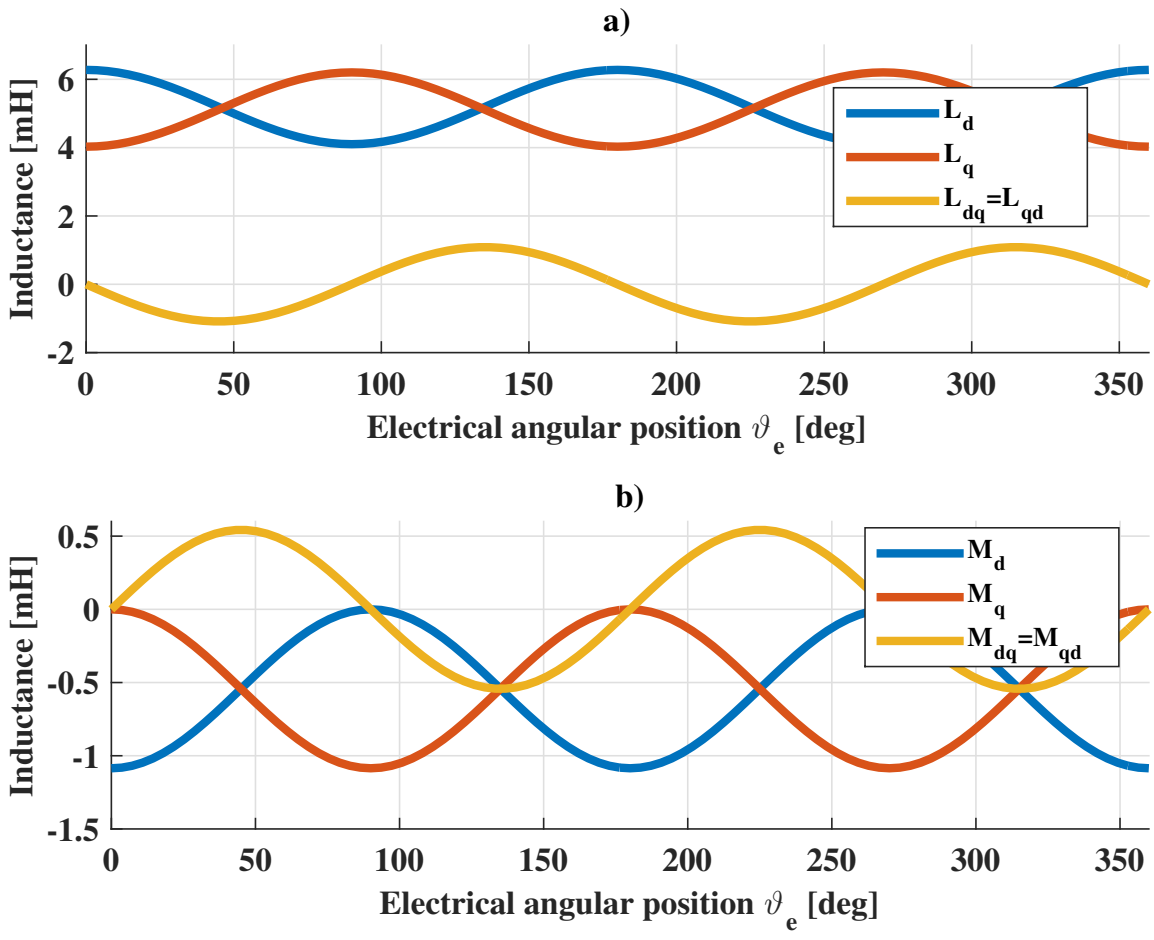


Figure 3.3: $d-q$ axis inductances: a) elements of $\mathbf{L}_{dq}(\vartheta_e)$; b)elements of $\mathbf{M}_{dq}(\vartheta_e)$

It can be noticed that, although all the phase inductances are assumed constant, the elements of $\mathbf{L}_{dq,t}(\vartheta_e)$ present a remarkable oscillation at $2\vartheta_e$ due to the non-symmetrical structure of the self-inductance matrix $\mathbf{L}$. Inductances $L_{dq}(\vartheta_e) = L_{qd}(\vartheta_e)$ and $M_{dq}(\vartheta_e) = M_{qd}(\vartheta_e)$ present zero mean value while the inductances on the main diagonal ($L_d(\vartheta_e)$, $L_q(\vartheta_e)$) have the biggest one. This is in good agreement with the analytical expressions reported in (3.22).

3.3 Mathematical Model of the Torque and Force Generation

3.3.1 Torque and force generation principle

Qualitatively, it is possible to state that the torque of the considered motor is generated in the same way of a standard three-phase PMSM with the only difference that each sector winding contributes to $1/n_s$ of the total torque. Furthermore, the independent current control of each sector allows to unbalance the flux density distribution of the airgap producing a net radial force. For instance, if $\gamma_0 = 0$, strengthening the flux density in the airgap underneath sector 1 and weakening the ones in correspondence of sector 2 and 3 produces a resultant force along the positive $x-$ axis direction.
More in the details, it is interesting to examine the torque and force generation principles analysing the interactions between different magnetic field spatial harmonics in the airgap. [127] presents a detailed analysis of the torque and force generation in PM synchronous motors highlighting the different contributions of the $d-$axis and $q-$axis current. In order to produce a net torque in a PM machine, the harmonic orders of the armature and PM fields have to be identical. The main PM harmonic order n_{PM} is usually the one related to the number of pole pairs (p). On the other hand, controllable radial force can be produced commanding a magnetic field of order

$n_w = n_{PM} \pm 1$ [51]. Hence, being $p = 3$ in the analysed machine, the interaction of the 3^{rd} PM field harmonic with the 2^{nd} and 4^{th} armature magnetic field harmonics produces the radial force. The explanation of this phenomena can be carried out considering the fundamental spatial harmonic of the PMs, $n_{PM} = 3$, and neglecting the higher harmonics. The radial and tangential components of the airgap flux density distribution that contribute to the force production are

$$B_r(\alpha_s, \vartheta_e) = B_{r,PM}(\alpha_s, \vartheta_e) + B_{r,w2}(\alpha_s, \vartheta_e) + B_{r,w4}(\alpha_s, \vartheta_e) = \hat{B}_{r,PM}\cos(3\alpha_s - \vartheta_e + \phi_{r,PM}) + \hat{B}_{r,w2}\cos(2\alpha_s - \vartheta_e + \phi_{r,w2}) + \hat{B}_{r,w4}\cos(4\alpha_s - \vartheta_e + \phi_{r,w4}) \quad (3.26)$$

$$B_\vartheta(\alpha_s, \vartheta_e) = B_{\vartheta,PM}(\alpha_s, \vartheta_e) + B_{\vartheta,w2}(\alpha_s, \vartheta_e) + B_{\vartheta,w4}(\alpha_s, \vartheta_e) = \hat{B}_{\vartheta,PM}\cos(3\alpha_s - \vartheta_e + \phi_{\vartheta,PM}) + \hat{B}_{\vartheta,w2}\cos(2\alpha_s - \vartheta_e + \phi_{\vartheta,w2}) + \hat{B}_{\vartheta,w4}\cos(4\alpha_s - \vartheta_e + \phi_{\vartheta,w4}) \quad (3.27)$$

where ϑ_e is the rotor angular position and α_s is the stator angular coordinate. $\hat{B}_{r,PM}$, $\hat{B}_{\vartheta,PM}$ and $\phi_{r,PM}$, $\phi_{\vartheta,PM}$ are the magnitudes and phase shift of the radial and tangential PM flux density distribution respectively while $\hat{B}_{r,w2}$, $\hat{B}_{r,w4}$, $\phi_{r,w2}$, $\phi_{r,w4}$ and $\hat{B}_{\vartheta,w2}$, $\hat{B}_{\vartheta,w4}$, $\phi_{\vartheta,w2}$, $\phi_{\vartheta,w4}$ are the radial and tangential 2^{nd} and 4^{th} harmonics magnitudes and phase shifts of the armature flux density distribution, respectively. All the phase shifts are referred to the magnetic axis of phase u_1. The above described quantities can be found in Figure 3.4. Indeed, Figure 3.4 a) and b) show the radial and tangential components of the PM and winding flux densities respectively highlighting their phase shifts. Only the spatial harmonics considered in (3.26), (3.27) are represented. Furthermore, it is important to add that the aim of the Figure is helping the reader to visualize a generic spatial harmonic distribution of the flux densities for a given rotor position angle ϑ_e, hence their magnitudes are indicative values and should not be considered as the actual ones. The calculation of the flux density in the airgap for the analysed machine is presented in Appendix B.

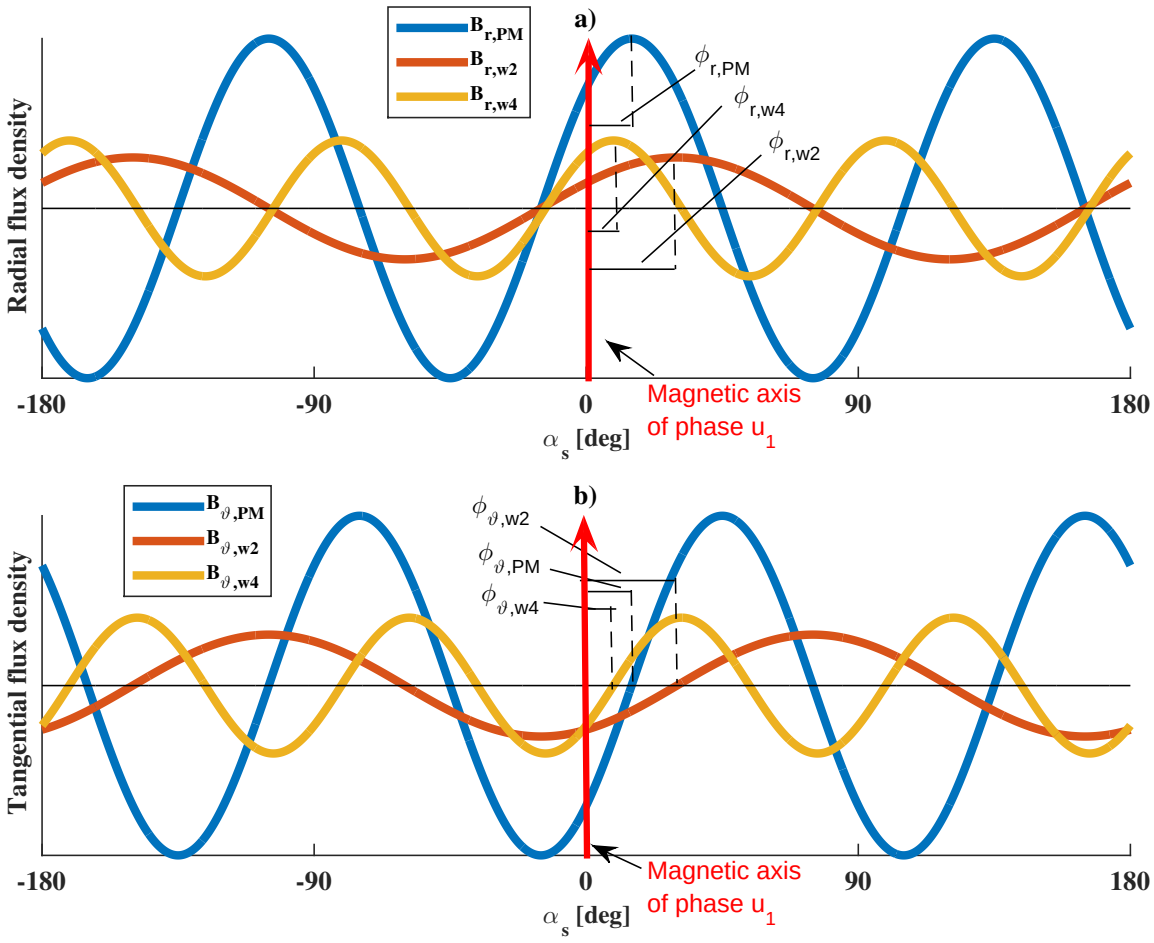


Figure 3.4: 3^{rd}, 2^{nd} and 4^{th} spatial harmonic distributions of the PM and winding flux densities for a generic rotor position ϑ_e: a) radial components; b) tangential components.

$\phi_{r,PM}$ and $\phi_{\vartheta,PM}$ are equal to 0 in the considered example. Furthermore, it is assumed that $\phi_{r,w2} = \phi_{r,w4} = \phi_{\vartheta,w2} = \phi_{\vartheta,w4} = \phi$. It is also assumed that $\gamma_0 = 0$.
The $x - y$ force components can be obtained through the integration along the mid-airgap circumference of the radial and tangential Maxwell stress tensor equations

$$\sigma(\alpha_s, \vartheta_e) = \frac{B_r(\alpha_s,\vartheta_e)^2 - B_\vartheta(\alpha_s,\vartheta_e)^2}{2\mu_0}$$
$$\tau(\alpha_s, \vartheta_e) = \frac{B_r(\alpha_s,\vartheta_e) B_\vartheta(\alpha_s,\vartheta_e)}{\mu_0} \tag{3.28}$$

as follow [128]:

$$\begin{aligned} F_{x,r}(\vartheta_e) &= R_g l \int_0^{2\pi} \sigma(\alpha_s, \vartheta_e)\cos(\alpha_s) d\alpha_s \\ F_{y,r}(\vartheta_e) &= R_g l \int_0^{2\pi} \sigma(\alpha_s, \vartheta_e)\sin(\alpha_s) d\alpha_s \\ F_{x,\vartheta}(\vartheta_e) &= -R_g l \int_0^{2\pi} \tau(\alpha_s, \vartheta_e)\sin(\alpha_s) d\alpha_s \\ F_{y,\vartheta}(\vartheta_e) &= R_g l \int_0^{2\pi} \tau(\alpha_s, \vartheta_e)\cos(\alpha_s) d\alpha_s \end{aligned} \tag{3.29}$$

where R_g is the mid-airgap radius and l is the active length. Equations (3.26),(3.27), (3.28) and (3.29) can be combined obtaining the $x-y$ force components as a function of the flux density:

$$\begin{aligned} F_{x,r} &= \tfrac{R_g l\pi}{2\mu_0}\left[\hat{B}_{r,PM}(\hat{B}_{r,w2}+\hat{B}_{r,w4}) - \hat{B}_{t,PM}(\hat{B}_{\vartheta,w2}+\hat{B}_{\vartheta,w4})\right]\cos(\phi) \\ F_{y,r} &= \tfrac{R_g l\pi}{2\mu_0}\left[\hat{B}_{r,PM}(\hat{B}_{r,w2}-\hat{B}_{r,w4}) - \hat{B}_{t,PM}(\hat{B}_{\vartheta,w2}-\hat{B}_{\vartheta,w4})\right]\sin(\phi) \\ F_{x,\vartheta} &= \tfrac{R_g l\pi}{2\mu_0}\left[\hat{B}_{r,PM}(\hat{B}_{\vartheta,w2}-\hat{B}_{\vartheta,w4}) - \hat{B}_{t,PM}(\hat{B}_{r,w2}-\hat{B}_{r,w4})\right]\cos(\phi) \\ F_{y,\vartheta} &= \tfrac{R_g l\pi}{2\mu_0}\left[\hat{B}_{r,PM}(\hat{B}_{\vartheta,w2}+\hat{B}_{\vartheta,w4}) - \hat{B}_{t,PM}(\hat{B}_{r,w2}+\hat{B}_{r,w4})\right]\sin(\phi) \end{aligned} \tag{3.30}$$

hence

$$\begin{aligned} F_{E,x} &= F_{x,r} + F_{x,\vartheta} \\ F_{E,y} &= F_{y,r} + F_{y,\vartheta} \end{aligned} \tag{3.31}$$

It can be noticed in (3.30) that ϑ_e is eliminated from the expression of the $x-y$ force

components, hence the generated force vector is independent from the rotor angular position. Furthermore, it can be appreciated how varying the amplitudes $\hat{B}_{r,w2}$, $\hat{B}_{r,w4}$, $\hat{B}_{\vartheta,w2}$ and $\hat{B}_{\vartheta,w4}$ it is possible to control the force components magnitudes while ϕ gives the direction of the resultant force vector.

3.3.2 Matrix formulation neglecting the rotor radial displacement

The mathematical model of the torque-force characteristic of the considered machine is derived in a generic form that can be extended to every MSPM machine. Under the assumptions of linear magnetic behaviour of the materials, magnetic decoupling between sectors and taking advantage of the geometrical and electromagnetic symmetries featured, only one machine sector is considered and the superposition principle is applied.

The total torque $\vec{T_E}$ results as the vector sum of the torque developed by the single sector:

$$\vec{T_E} = T_E\,\hat{\mathbf{z}} = \Big(\sum_s {}^sT_E\Big)\hat{\mathbf{z}} \tag{3.32}$$

where the coordinate axis $\hat{\mathbf{z}}$ is defined as in Figure 3.1. Similarly, the total vector of force $\vec{F_E}$ acting on the rotor results as the vector sum of the forces developed by each sector which mathematically results as $\vec{F_E} = \sum_s {}^s\vec{F}_E$. According to the Cartesian reference frame defined in Figure 3.1, the total force vector can be expressed as the algebraic sum of the projection of ${}^s\vec{F}_E$ along each coordinate axis as expressed in (3.33).

$$\vec{F_E} = F_{E,x}\,\hat{\mathbf{x}} + F_{E,y}\,\hat{\mathbf{y}} = \Big(\sum_s {}^sF_{E,x}\Big)\hat{\mathbf{x}} + \Big(\sum_s {}^sF_{E,y}\Big)\hat{\mathbf{y}} \tag{3.33}$$

The simplified model proposed in this paragraph does not account for rotor eccentricity as the rotor is assumed to be rigid, centred and fixed by infinitely stiff mechanical

ball-bearings. Further considerations to include the effect of the rotor displacement in the $x-y$ plane will be exposed later in this Chapter. The equivalent description of the electromagnetic quantities in the reference frame is adopted to simplify the mathematics. The torque and the forces developed by s^{th} sector of the machine are therefore considered as a function of its current components ${}^{s}i_{\alpha}$ and ${}^{s}i_{\beta}$, the electrical angular rotor position position ϑ_e and the geometrical angular position ${}^{s}\gamma$ of the windings magnetic axis with respect the reference $x-$axis. Introducing the generalized electromagnetic wrench vector ${}^{s}\bar{W}_E \in \mathbb{R}^{n_m \times 1}$ [129] of each sector defined by piling the force components ${}^{s}F_{E,x}$, ${}^{s}F_{E,y}$ and the electromagnetic torque ${}^{s}T_E$, its pseudo-linear decomposition form leads to the matrix formulation (3.34) which expresses the mechanical output state function for the s^{th} sector of the machine.

$$ {}^{s}\bar{W}_E(\vartheta_e, {}^{s}\gamma, {}^{s\bar{}}i_{\alpha\beta}) = \begin{bmatrix} {}^{s}F_{E,x} \\ {}^{s}F_{E,y} \\ {}^{s}T_E \end{bmatrix} = {}^{s}\mathbf{K}_E(\vartheta_e, {}^{s}\gamma)\ {}^{s\bar{}}i_{\alpha\beta} \tag{3.34} $$

where ${}^{s}\mathbf{K}_E(\vartheta_e, {}^{s}\gamma)$ is the matrix that characterizes the electro-magneto-mechanical output through mapping the current to $x-y$ force and torque coefficients. ${}^{s\bar{}}i_{\alpha\beta}$ is the vector of the α-β axis currents of sector s defined as

$$ {}^{s\bar{}}i_{\alpha\beta} = \mathbf{T}_C\, {}^{s\bar{}}i = \mathbf{T}_C \begin{bmatrix} {}^{s}i_u & {}^{s}i_v & {}^{s}i_w \end{bmatrix}^T \tag{3.35} $$

where $\mathbf{T}_C$ is the direct three-phase Clarke transformation written in (3.36) neglecting the zero-sequence component.

$$ \mathbf{T}_C = \frac{2}{3} \begin{bmatrix} 1 & -1/2 & -1/2 \\ 0 & \sqrt{3}/2 & -\sqrt{3}/2 \end{bmatrix} \tag{3.36} $$

Considering the number of mechanical outputs $n_m = 3$, the matrix ${}^{s}\mathbf{K}_E \in \mathbb{R}^{3\times 2}$ can be expressed as (3.37).

$$ {}^{s}\mathbf{K}_E(\vartheta_e, {}^{s}\gamma) = \begin{bmatrix} {}^{s}\mathbf{K}_{E,F}(\vartheta_e, {}^{s}\gamma) \\ {}^{s}\bar{K}_{E,T}(\vartheta_e) \end{bmatrix} \tag{3.37} $$

where

$$
{}^{s}\mathbf{K}_{E,F}(\vartheta_e, {}^{s}\gamma) = \begin{bmatrix} {}^{s}k_{x,\alpha}(\vartheta_e, {}^{s}\gamma) & {}^{s}k_{x,\beta}(\vartheta_e, {}^{s}\gamma) \\ {}^{s}k_{y,\alpha}(\vartheta_e, {}^{s}\gamma) & {}^{s}k_{y,\beta}(\vartheta_e, {}^{s}\gamma) \end{bmatrix}
$$

$$
{}^{s}\bar{K}_{E,T}(\vartheta_e) = \begin{bmatrix} {}^{s}k_{T,\alpha}(\vartheta_e) & {}^{s}k_{T,\beta}(\vartheta_e) \end{bmatrix} \tag{3.38}
$$

${}^{s}\mathbf{K}_{E,F}(\vartheta_e, {}^{s}\gamma)$ and ${}^{s}\bar{K}_{E,T}(\vartheta_e)$ consist in a set of coefficient ${}^{s}k_{*,\times}$ where $*, \times$ defines the wrench ($x - y$ forces and torque) and the current components, respectively. It can be noticed that the torque coefficients defined in the second equation of (3.38) are not affected by the parameter ${}^{s}\gamma$ since each sector is considered identical and magnetically independent to the others. On the other hand, the sub-matrix of the electromagnetic forces ${}^{s}\mathbf{K}_{E,F}(\vartheta_e, {}^{s}\gamma) \in \mathbb{R}^{2\times 2}$ can be expressed with respect the sub-matrix ${}^{1}\mathbf{K}_{E,F}(\vartheta_e, {}^{1}\gamma)$ of the reference sector (arbitrary defined, labelled as $s = 1$). The compact expression of the force-torque characteristic of the s^{th} sector of the device is reported in (3.39), suggesting that only one sector has to be characterized with respect the parameter ϑ_e to account for the main aspects of the machine.

$$
{}^{s}\mathbf{K}_{E}(\vartheta_e, {}^{s}\gamma) = \mathbf{R}_T({}^{s}\gamma)\, {}^{1}\mathbf{K}_{E}(\vartheta_e, {}^{1}\gamma) \tag{3.39}
$$

The effect of the geometric position of each sector can be accounted introducing the rotation matrix $\mathbf{R}_T({}^{s}\gamma)$ expressed in (3.40).

$$
\mathbf{R}_T({}^{s}\gamma) = \begin{bmatrix} \cos({}^{s}\gamma) & -\sin({}^{s}\gamma) & 0 \\ \sin({}^{s}\gamma) & \cos({}^{s}\gamma) & 0 \\ 0 & 0 & 1 \end{bmatrix} \tag{3.40}
$$

The coefficients of ${}^{s}\bar{K}_{E,T}(\vartheta_e)$ and ${}^{1}\mathbf{K}_{E,F}(\vartheta_e, {}^{1}\gamma)$ are calculated in next paragraph.

3.3.3 Matrix coefficients calculation

3.3.3.1 Torque coefficients

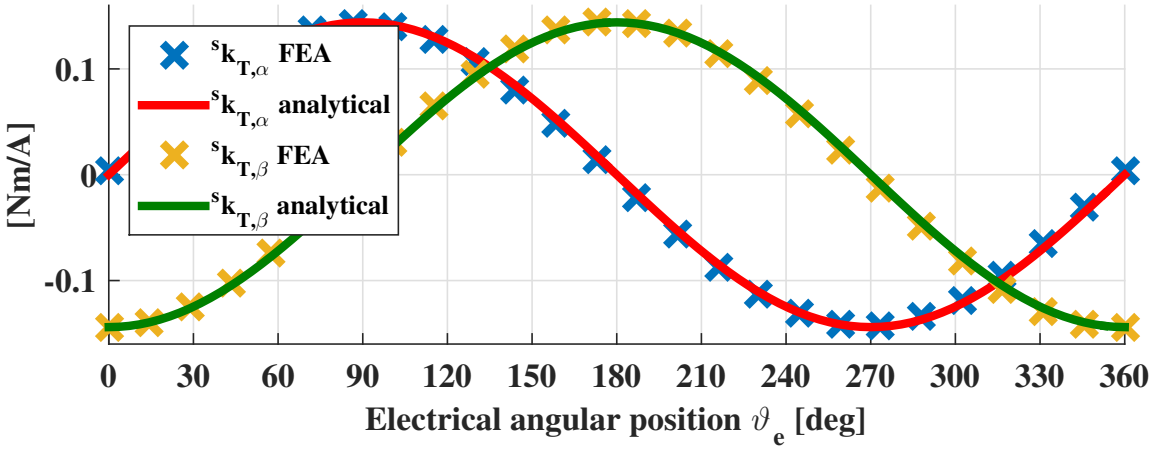


Figure 3.5: FE and analytical torque coefficient against rotor angular position.

The elements of the electromagnetic torque constant vector ${}^{s}\bar{K}_{E,T}(\vartheta_e) \in \mathbb{R}^{1\times 2}$ are defined in (3.41).

$$\begin{cases} {}^{s}k_{T,\alpha}(\vartheta_e) = {}^{s}k_T \sin(\vartheta_e) \\ {}^{s}k_{T,\beta}(\vartheta_e) = -\,{}^{s}k_T \cos(\vartheta_e) \end{cases} \tag{3.41}$$

where ${}^{s}k_T = k_T \,\forall s$ is the torque constant resulting identical for each sector of the machine. The well-known torque equation under sinusoidal approximation for surface PM synchronous machines is reported in (3.42) [130] referred to the generic s^{th} sector.

$${}^{s}T_E({}^{s}\bar{i}_{\alpha\beta}, \vartheta_e) = \frac{3}{2} p \, {}^{s}\Lambda_{PM} \big(\sin(\vartheta_e) {}^{s}i_\alpha - \cos(\vartheta_e) {}^{s}i_\beta \big) \tag{3.42}$$

where ${}^{s}\Lambda_{PM}$ is the fundamental peak of the no-load flux linkage with the winding structure.

Under the assumption of identical sectors, the combination of (3.41) and (3.42) leads to the expression of the torque constant that characterizes the elements of ${}^{s}\bar{K}_{E,T}(\vartheta_e)$ resulting in $k_T = 3/2\, p \, {}^{s}\Lambda_{PM}$. Figure 3.5 shows the waveform of the torque coefficients

obtained analytically with equation (3.41) and with FEA showing good agreements in the result. The FE result is obtained with two linear time stepping simulations feeding only the three-phase winding of sector 1 with constant ${}^{1}\bar{i}_{\alpha\beta} = [1\ 0]^T\ A$ and ${}^{1}\bar{i}_{\alpha\beta} = [0\ 1]^T\ A$ respectively for the α and β coefficients. During the two simulations the rotor electrical angular position ϑ_e varies from 0 to 2π.

The equivalent formulation of (3.41) in the reference frame synchronous with the rotor is obtained adopting the Park transformation. Considering only $q-$ axis current supply for the sector s, the developed torque can be expressed as

$$ {}^{s}T_E = k_T\ {}^{s}i_q \tag{3.43}$$

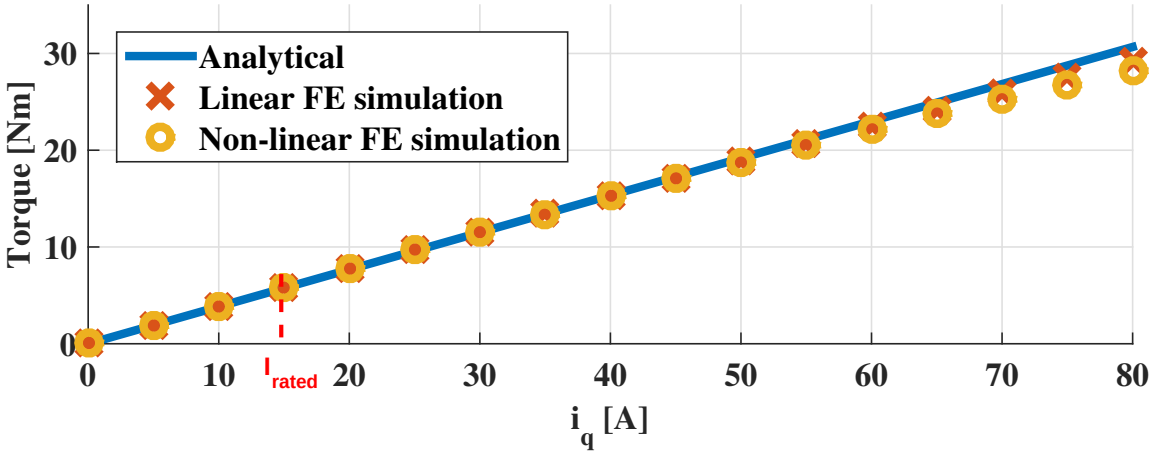


Figure 3.6: Analytical and FE torque trend as a function of the i_q current.

The trend of the total torque $T_E = \sum_s {}^{s}T_E$ as a function of the $q-$axis current of each sector is shown in Figure 3.6, where the linear and non-linear FE simulation results are compared with the analytical one. The rated current of each sector s is highlighted in the picture with a red dashed line. Its value is equal to 13 A. It can be noticed that the effect of the machine core saturation on the torque generation occurs for current values much higher than the rated current. Therefore, it is possible to conclude that the torque production is a linear function of the i_q current if the latter is within its rated value.

3.3.3.2 Force coefficients

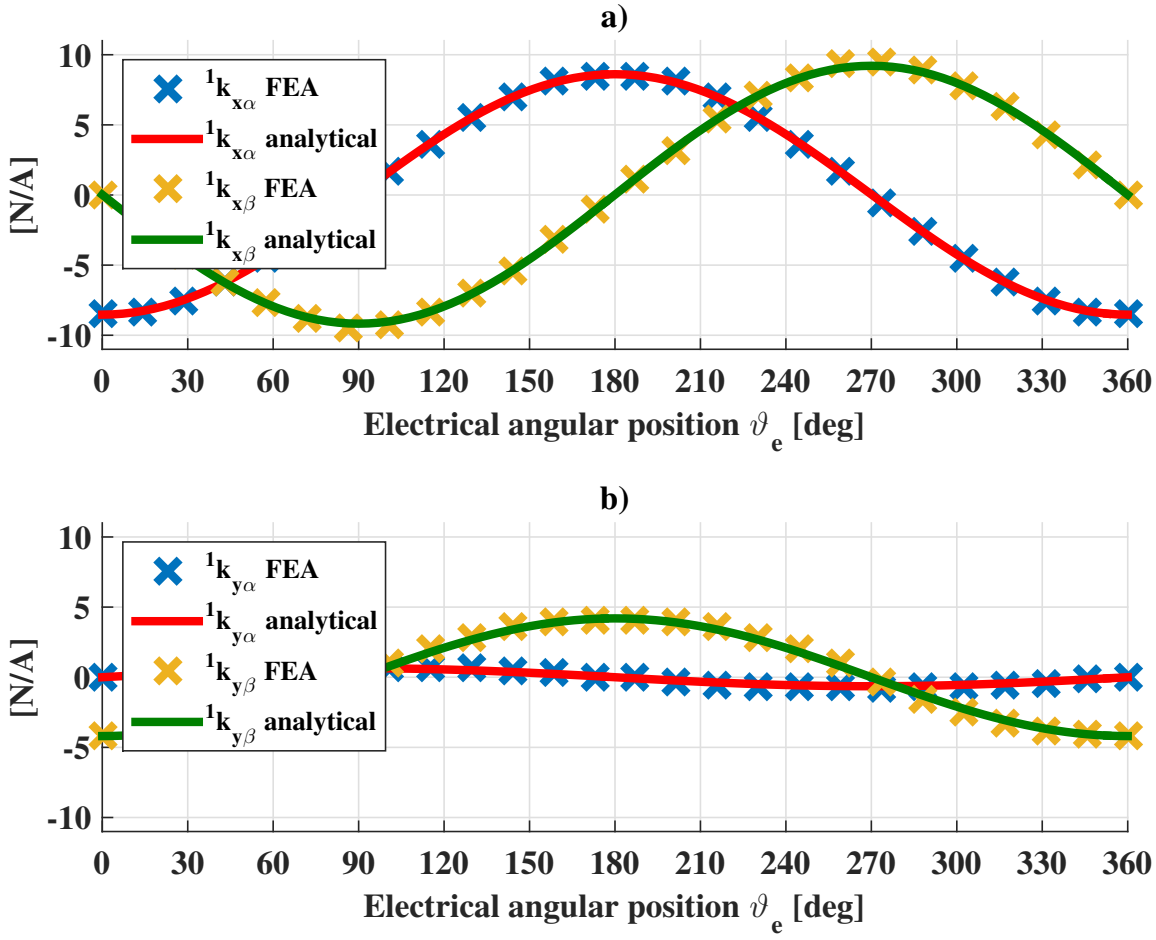


Figure 3.7: FE and analytical force coefficient against the rotor angular position: a) $x-$axis coefficients; b) $y-$axis coefficients.

Considering $^1\gamma = 0$, the coefficients of the matrix $^1\mathbf{K}_{E,F}(\vartheta_e, 0)$ characterises the force capabilities of the machine. Each element of the matrix is computed by means FEA and compared with analytical prediction in Figure 3.7 showing good agreement. The same FE simulations described in the previous paragraph were employed.

The analytical evaluation of the coefficients of $^1\mathbf{K}_{E,F}(\vartheta_e, 0)$ is performed through the

integration of the Maxwell stress tensor equations (3.28) along the airgap circumference as expressed in 3.44.

$$
\begin{aligned}
{}^1k_{x,\times} &= R_g l\Big(\int_0^{2\pi} \sigma_\times \cos(\alpha_s) d\alpha_s - \int_0^{2\pi} \tau_\times \sin(\alpha_s) d\alpha_s\Big) \\
{}^1k_{y,\times} &= R_g l\Big(\int_0^{2\pi} \sigma_\times \sin(\alpha_s) d\alpha_s + \int_0^{2\pi} \tau_\times \cos(\alpha_s) d\alpha_s\Big)
\end{aligned}
\tag{3.44}
$$

In (3.44), subscription $\times$ stands for either $\alpha-$ or $\beta-$ axis current. As a matter of fact, four coefficients are required to define the matrix ${}^1\mathbf{K}_{E,F}$: ${}^1k_{x,\alpha}$, ${}^1k_{y,\alpha}$, ${}^1k_{x,\beta}$ and ${}^1k_{y,\beta}$. Each of them can be obtained adopting a proper current pattern for the armature-flux density prediction. For instance, ${}^1k_{x,\alpha}$ and ${}^1k_{y,\alpha}$ are obtained with ${}^1\bar{i}_{\alpha\beta} = \begin{bmatrix} 1 & 0 \end{bmatrix}^T$ A while ${}^1k_{x,\beta}$ and ${}^1k_{y,\beta}$ with ${}^1\bar{i}_{\alpha\beta} = \begin{bmatrix} 0 & 1 \end{bmatrix}^T$ A.
A close form expression of the force coefficients can be found in (3.45).

$$
\begin{aligned}
{}^1k_{x,\alpha}(\vartheta_e) &= K_{x,\alpha} \cos(\vartheta_e + \varphi_{x,\alpha}) \\
{}^1k_{y,\alpha}(\vartheta_e) &= K_{y,\alpha} \cos(\vartheta_e + \varphi_{y,\alpha}) \\
{}^1k_{x,\beta}(\vartheta_e) &= K_{x,\beta} \cos(\vartheta_e + \varphi_{x,\beta}) \\
{}^1k_{y,\beta}(\vartheta_e) &= K_{y,\beta} \cos(\vartheta_e + \varphi_{y,\beta})
\end{aligned}
\tag{3.45}
$$

where

$$
\begin{aligned}
K_{x,\alpha} &= \tfrac{\pi l R_g}{2\mu_0}\big(\tilde{B}_{r,PM} R_{x,\alpha} + \tilde{B}_{\vartheta,PM} T_{x,\alpha}\big) \\
K_{y,\alpha} &= \tfrac{\pi l R_g}{2\mu_0}\big(\tilde{B}_{r,PM} R_{y,\alpha} + \tilde{B}_{\vartheta,PM} T_{y,\alpha}\big) \\
K_{x,\beta} &= \tfrac{\pi l R_g}{2\mu_0}\big(\tilde{B}_{r,PM} R_{x,\beta} + \tilde{B}_{\vartheta,PM} T_{x,\beta}\big) \\
K_{y,\beta} &= \tfrac{\pi l R_g}{2\mu_0}\big(\tilde{B}_{r,PM} R_{y,\beta} + \tilde{B}_{\vartheta,PM} T_{y,\beta}\big)
\end{aligned}
\tag{3.46}
$$

and

$$\begin{aligned}
R_{x,\alpha} &= \tilde{B}_{\vartheta,\alpha 2} - \tilde{B}_{\vartheta,\alpha 4} - \tilde{B}_{r,\alpha 2} - \tilde{B}_{r,\alpha 4} \\
T_{x,\alpha} &= \tilde{B}_{r,\alpha 2} - \tilde{B}_{r,\alpha 4} - \tilde{B}_{\vartheta,\alpha 2} - \tilde{B}_{\vartheta,\alpha 4} \\
R_{y,\alpha} &= \tilde{B}_{\vartheta,\alpha 2} + \tilde{B}_{\vartheta,\alpha 4} - \tilde{B}_{r,\alpha 2} + \tilde{B}_{r,\alpha 4} \\
T_{y,\alpha} &= \tilde{B}_{r,\alpha 2} + \tilde{B}_{r,\alpha 4} - \tilde{B}_{\vartheta,\alpha 2} + \tilde{B}_{\vartheta,\alpha 4} \\
R_{x,\beta} &= \tilde{B}_{\vartheta,\beta 2} - \tilde{B}_{\vartheta,\beta 4} - \tilde{B}_{r,\beta 2} - \tilde{B}_{r,\beta 4} \\
T_{x,\beta} &= \tilde{B}_{r,\beta 2} - \tilde{B}_{r,\beta 4} - \tilde{B}_{\vartheta,\beta 2} - \tilde{B}_{\vartheta,\beta 4} \\
R_{y,\beta} &= \tilde{B}_{\vartheta,\beta 2} + \tilde{B}_{\vartheta,\beta 4} - \tilde{B}_{r,\beta 2} + \tilde{B}_{r,\beta 4} \\
T_{y,\beta} &= \tilde{B}_{r,\beta 2} + \tilde{B}_{r,\beta 4} - \tilde{B}_{\vartheta,\beta 2} + \tilde{B}_{\vartheta,\beta 4}
\end{aligned} \tag{3.47}$$

$\tilde{B}_{r,PM}$, $\tilde{B}_{\vartheta,PM}$ are the magnitudes of the radial and tangential 3^{rd} spatial harmonic of the PM magnetic field respectively, while $\tilde{B}_{r,\times 2}$, $\tilde{B}_{\vartheta,\times 2}$ and $\tilde{B}_{r,\times 4}$, $\tilde{B}_{\vartheta,\times 4}$ are the magnitudes of the radial and tangential 2^{nd} and 4^{th} spatial harmonic of the armature magnetic field, respectively. Their values can be calculated following the procedure described in Appendix B. In Table 3.5 the values of the amplitudes (3.46) evaluated for the machine under investigation are reported.

Table 3.5: Force Coefficients

	$x-\alpha$	$x-\beta$	$y-\alpha$	$y-\beta$
$K_{*,\times}$ [N/A]	8.28	8.91	0.92	4.37
$\varphi_{*,\times}$ [rad]	π	$\pi/2$	$-\pi/2$	π

Figure 3.8 shows the harmonic spectrum calculated by means the fast Fourier transform of the force coefficients obtained with FE simulations. It can be observed that the high order harmonic content is very small compared to the first harmonic, hence it can be neglected justifying the approximated expression reported in (3.45).

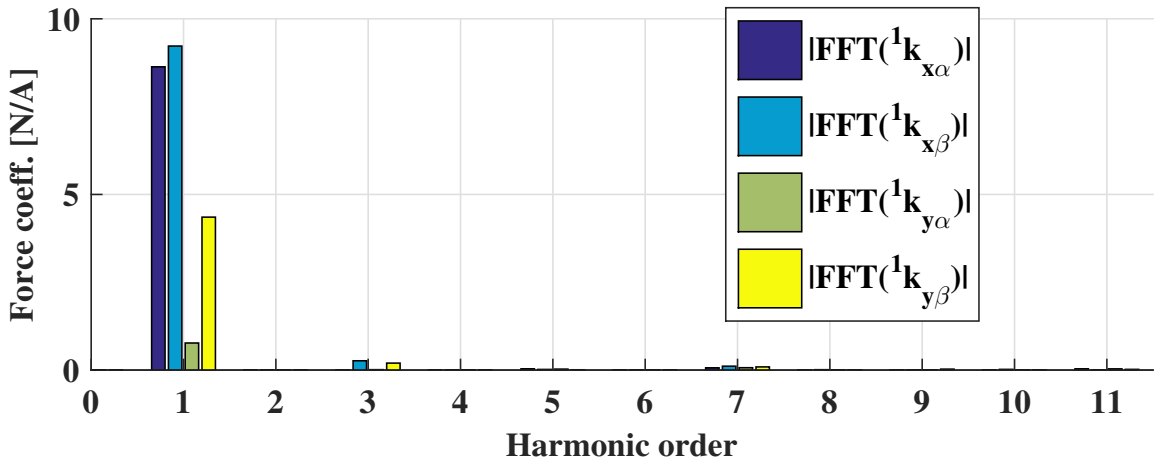


Figure 3.8: Amplitude of harmonic decomposition of the force coefficients obtained with FEA.

The effect of the machine saturation on the force coefficients can be appreciated observing Figure 3.9. The latter shows the amplitudes of the four force coefficients as a function of the related current. The current values varies from 0 to 25 A. The rated machine current is highlighted in red in the Figure. The analytical trend is compared with both the linear and non-linear FE simulation results. It can be observed that the analytical and linear trends match in all the Figures. The effect of the saturation can be observed in the non-linear trend. In particular, ${}^1K_{x\alpha}$ presents the highest saturation level as it can be observed in Figure 3.9 a) with a reduction of around 9.55 % in the coefficient amplitude at the rated current. Indeed, ${}^1K_{x\alpha}$ is obtained feeding sector 1 with $\alpha-$ axis current while the rotor magnetic axis is aligned with the one of phase u_1. Therefore, the winding magnetic flux is added to the PM one saturating the iron core.

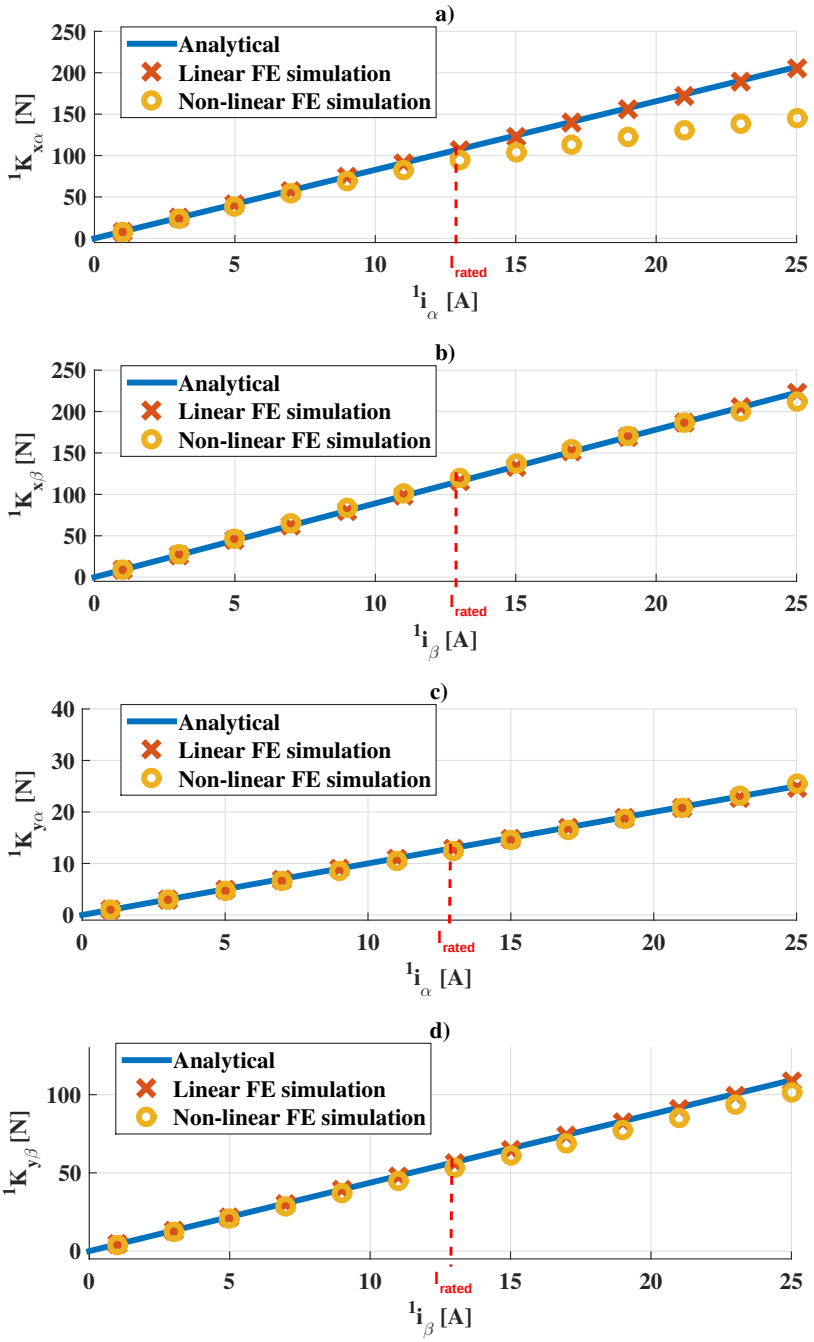


Figure 3.9: Magnitude of the force coefficients as a function of the current: a) ${}^1K_{x\alpha}$ vs i_α; b) ${}^1K_{x\beta}$ vs i_β; c) ${}^1K_{y\alpha}$ vs i_α; d) ${}^1K_{y\beta}$ vs i_β. The picture shows the analytical and both linear and non-linear FE trends.

The saturation effect can be appreciated observing the flux density distribution in the machine in Figure 3.10. The left hand side picture shows the no-load flux density. As it can be seen, the flux density distribution is uniform when no current is flowing in the windings. On the other hand, the central and the right hand side pictures are obtained feeding sector 1 with ${}^{1}\bar{i}_{\alpha\beta} = \begin{bmatrix} I_{rated} & 0 \end{bmatrix}^T$ A and ${}^{1}\bar{i}_{\alpha\beta} = \begin{bmatrix} 25 & 0 \end{bmatrix}^T$ A and aligning the PM axis with the one of phase ${}^{1}i_u$. It can be observed that the flux density is now unbalanced and that the iron in correspondence of sector 1 is heavily saturated. This phenomena justifies the saturation of the non-linear trend observed in Figure 3.9 a).

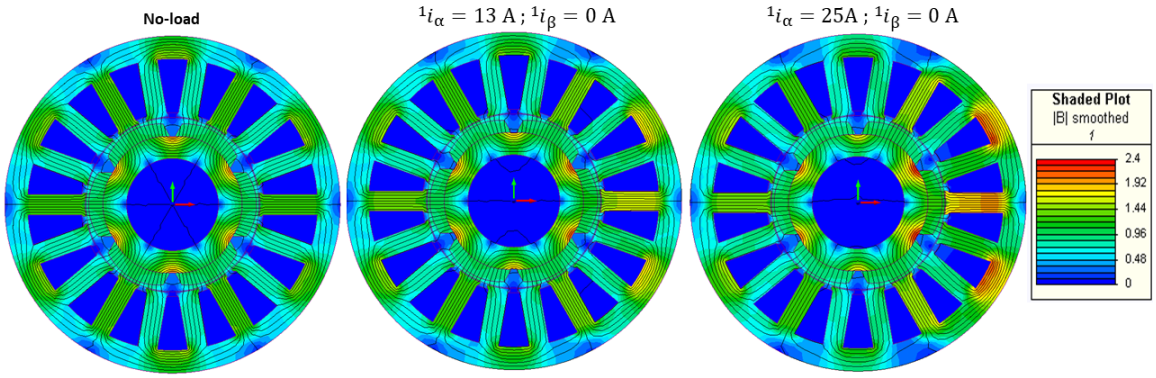


Figure 3.10: Flux density at no-load operating condition and at I_{rated} and 25 A $\alpha-$axis current supplied to sector 1.

In the next paragraph, the rotor displacement will be taken into account in the expression of the force components and torque given in (3.34). It will be shown that the force and torque coefficients in matrix ${}^{s}\mathbf{K}_E$ are not considerably affected by the rotor displacement if the latter is kept within the mechanical limits imposed by the backup bearing. On the other hand, even a very small rotor eccentricity gives raise to a large magnetic force that tends to attract the rotor to the machine stator. This phenomena can be taken into account introducing the negative magnetic stiffness vector function of the displacement information in the matrix formulation (3.34).

3.3.4 Matrix formulation considering the rotor radial displacement

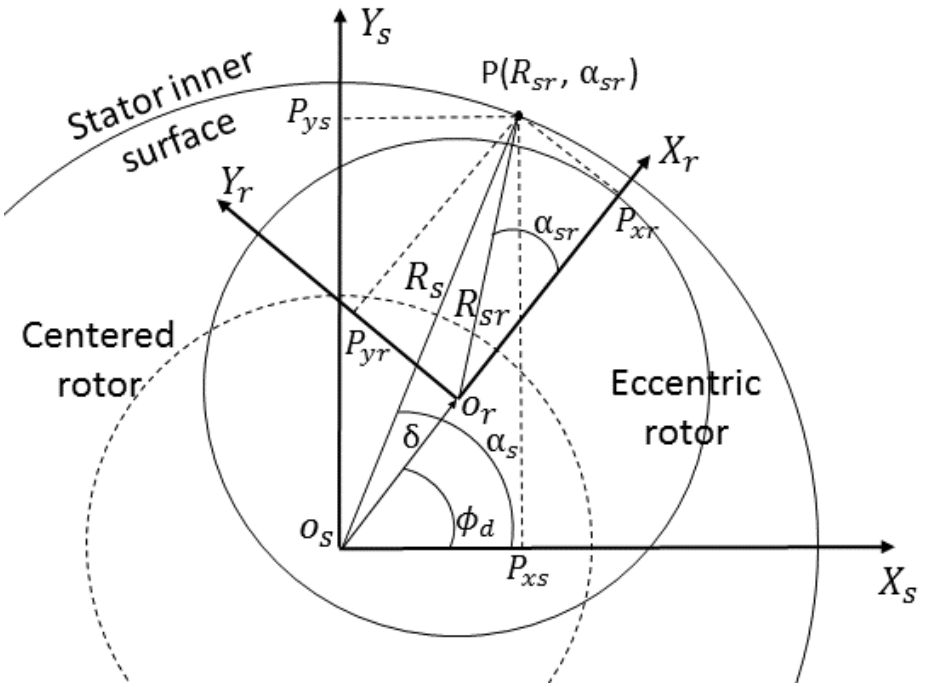


Figure 3.11: Cross-section of the eccentric rotor with stator and rotor reference frames.

The rotor radial displacement is defined by the translation δ and angle ϕ_d of the rotor centre from the rectangular $x-y$ reference frame origin of the stator O_s as depicted in Figure 3.11. The rotor is allowed to move radially within the maximum displacement δ_{max} given by the clearance of the backup bearing. δ_{max}=0.15 mm (15% of the airgap g_0) has being chosen in order to fulfil the force capability of the motor. As a matter of fact, the amplitude of the open circuit force generated by magnetic stiffness reaction at δ_{max} is around 100 N, corresponding to almost 50% of the motor force capability. The open-circuit forces $F_{x,ecc}(\delta, \phi_d)$ and $F_{y,ecc}(\delta, \phi_d)$ produced by the rotor displacement can be calculated with the Maxwell equations (3.28) and (3.29) considering only the contribution of the PMs flux density $B_{r,PM}(\alpha_s, \vartheta_e, \delta, \phi_d)$ and $B_{\vartheta,PM}(\alpha_s, \vartheta_e, \delta, \phi_d)$ as a function of the rotor displacement. $B_{r,PM}(\alpha_s, \vartheta_e, \delta, \phi_d)$ and $B_{\vartheta,PM}(\alpha_s, \vartheta_e, \delta, \phi_d)$

can be calculated following the procedure of paragraph B.2 in Appendix B. The analytical and FE trends of $F_{x,ecc}$ and $F_{y,ecc}$ versus δ and ϕ_d are shown in Figure 3.12. It allows to define the stiffness vector $\bar{K}_m(\phi_d)$ as follow:

$$\bar{K}_m(\phi_d) = \begin{bmatrix} k_m \cos(\phi_d) \\ k_m \sin(\phi_d) \\ t_\delta(\delta, \phi_d) \end{bmatrix} \tag{3.48}$$

where $k_m = 655$ [kN/m] is the magnetic stiffness constant and $t_\delta(\delta, \phi_d)$ represents the displacement dependent torque.

Figure 3.13 shows the FE simulation result for rated torque production (T_{rated}=5 Nm) for both zero and maximum rotor displacement. It can be observed that the torque production is almost the same, only a small difference in the torque ripple can be appreciated. The coefficient $t_\delta(\delta, \phi_d)$ can be therefore considered null.

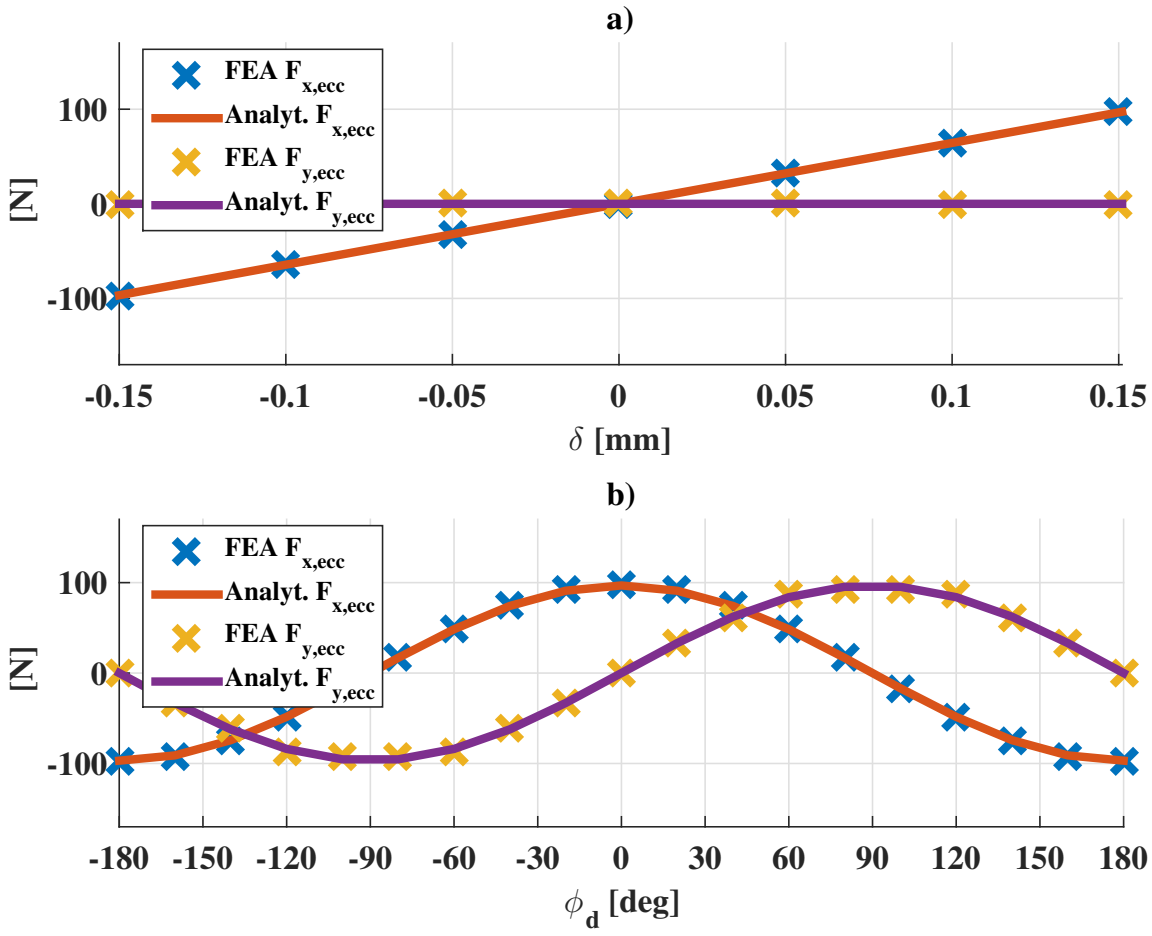


Figure 3.12: Open-circuit $x-y$ force components $F_{x,ecc}$ and $F_{y,ecc}$ as a function of the rotor eccentricity: a) varying δ at $\phi_d = 0$; b) varying ϕ_d at $\delta = \delta_{max}$.

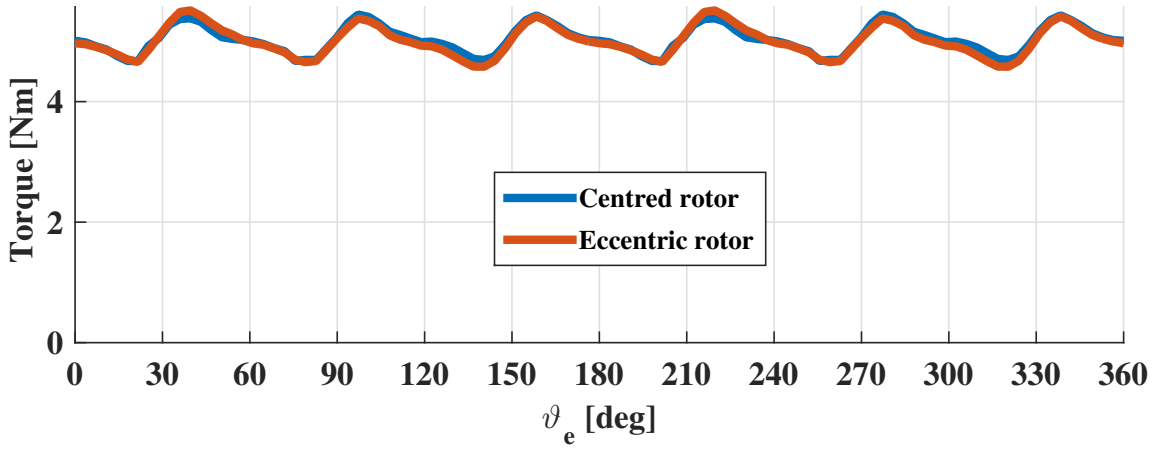


Figure 3.13: Torque production for centred and eccentric rotor ($\delta = \delta_{max}$).

Figure 3.14 shows the amplitude of the force coefficients against the rotor displacement δ obtained through FEA. A maximum variation of 5.5% can be appreciated in ${}^1K_{x,\alpha}$ justifying the assumption of neglecting the displacement in the force coefficients expression.

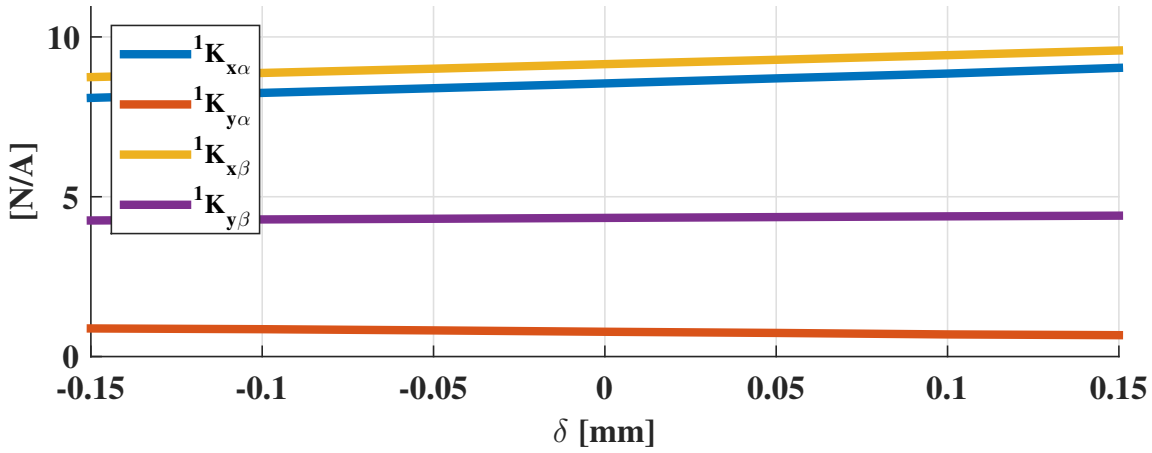


Figure 3.14: Variation of the force coefficients amplitudes against the rotor displacement δ.

Thanks to the approximations introduced, the rotor displacement effect can be neglected in the force and torque coefficients. Hence, matrix ${}^s\mathbf{K}_E(\vartheta_e, {}^s\gamma)$, defined in

(3.37), can still be used provided that $\delta \leq \delta_{max}$.
The mathematical expression that takes into account the rotor displacement can be now presented. In (3.34) the matrix formulation of the mechanical outputs as a function of the $\alpha - \beta$ currents was given assuming a centred rotor. In order to include the rotor displacement, the stiffness term has to be added in the formulation. The new matrix formulation of the force and torque production of the generic sector s is given in (3.49).

$$ {}^{s}\bar{W}_E = {}^{s}\mathbf{K}_E(\vartheta_e, {}^{s}\gamma)\ {}^{s}\bar{i}_{\alpha\beta} + \bar{K}_m(\phi_d)\delta \tag{3.49} $$

3.4 Reference Current Calculation Technique

3.4.1 Problem formulation

The current commands required to control the $x - y$ force and torque can be determined by evaluating the inverse of matrix $\mathbf{K}_E$ that characterizes the overall electro-magneto-mechanical output of the machine. The matrix formulation, written in (3.34), can be extended as in (3.50) in order to include all motor sectors.

$$ \bar{W}_E = \mathbf{K}_E(\vartheta_e, \bar{\gamma})\bar{i}_{\alpha\beta} + \bar{K}_m(\phi_d)\delta \tag{3.50} $$

where the elements are defined as

$$ \begin{aligned} \bar{W}_E &= \begin{bmatrix} F_{E,x} & F_{E,y} & T_E \end{bmatrix}^T \\ \bar{i}_{\alpha\beta} &= \begin{bmatrix} {}^{1}i_\alpha & {}^{1}i_\beta & \cdots & {}^{s}i_\alpha & {}^{s}i_\beta & \cdots & {}^{3}i_\beta & {}^{3}i_\beta \end{bmatrix}^T \\ \bar{\gamma} &= \begin{bmatrix} {}^{1}\gamma & \cdots & {}^{s}\gamma & \cdots & {}^{3}\gamma \end{bmatrix} \\ \mathbf{K}_E(\vartheta_e, \bar{\gamma}) &= \begin{bmatrix} {}^{1}\mathbf{K}_E(\vartheta_e, {}^{1}\gamma) & \cdots & {}^{s}\mathbf{K}_E(\vartheta_e, {}^{s}\gamma) & \cdots & {}^{3}\mathbf{K}_E(\vartheta_e, {}^{3}\gamma) \end{bmatrix} \end{aligned} \tag{3.51} $$

In general, the matrix of the generalized wrench is defined as $\mathbf{K}_E(\vartheta_e, \bar{\gamma}) \in \mathbb{R}^{n_m \times 2n_s}$ which results in a square matrix only if $2n_s = n_m$. The dimension of the output

electromagnetic wrench vector is smaller than the number of state variables ($n_m = 3 < 2n_s$), hence a proper strategy has to be adopted to obtain the phase current reference signals. The total current injected in the windings has an impact on the magnetic load distribution in the machine as well as on the total Joule losses which are the major source of heat in electrical machines [131]. The minimization of the copper losses can have a beneficial effect on the overall efficiency of the system, avoiding de-rating due to hotspots as well as reducing the impact of possible magnetic core saturation [131].
The compact expression of the total heat losses is given in (3.52).

$$P_{cu} = \bar{i}_{\alpha\beta}^{T}\, \mathbf{R}\, \bar{i}_{\alpha\beta} \tag{3.52}$$

where $\mathbf{R} \in \mathbb{R}^{2n_s \times 2n_s}$ is the matrix of electrical resistances. Under the assumption of identical electrical resistance of the phases, $\mathbf{R} = diag(R_{ph})$ and therefore (3.52) reduces to

$$P_{cu} = R_{ph}\, \bar{i}_{\alpha\beta}^{T}\, \bar{i}_{\alpha\beta} \tag{3.53}$$

3.4.2 Problem solution

The rectangular matrix $\mathbf{K}_E(\vartheta_e, \bar{\gamma})$ introduced in (3.50) cannot be inverted. The Moore-Penrose pseudo inverse is considered as the generalization of the inverse matrix and is commonly applied to compute the solution of under- and over-determined system of linear equations. In the specific configuration considered in this work $n_s = 3$ implying that the system in (3.50) is under-determined with an infinite number of solutions. The minimization of the copper losses has been chosen as strategy, leading to the calculation of the pseudo inverse of $\mathbf{K}_E$. The function that has to be minimized is (3.53) subjected to the constraint (3.50). The Lagrangian function (3.54) is constructed in order to solve the minimization problem.

$$\mathbb{L} = R_{ph}\bar{i}_{\alpha\beta}^{T}\, \bar{i}_{\alpha\beta} + \bar{\lambda}\big(\mathbf{K}_E(\vartheta_e, \bar{\gamma})\bar{i}_{\alpha\beta} + \bar{K}_m(\phi_d)\delta - \bar{W}_E^*\big) \tag{3.54}$$

where $\bar{\lambda} = \begin{bmatrix} \lambda_1 & \lambda_2 & \lambda_3 \end{bmatrix}$ is the Lagrangian multiplier vector and $\bar{W}_E^*$ is the reference wrench vector. System (3.55) can be now written with the partial derivatives of $\mathbb{L}$ with respects to $\bar{i}_{\alpha\beta}$ and $\bar{\lambda}$.

$$\begin{cases} \frac{\partial \mathbb{L}}{\partial \bar{i}_{\alpha\beta}} = 2R_{ph}\bar{i}_{\alpha\beta}^T + \bar{\lambda}\mathbf{K}_E(\vartheta_e, \bar{\gamma}) = 0 \\ \frac{\partial \mathbb{L}}{\partial \bar{\lambda}} = \mathbf{K}_E(\vartheta_e, \bar{\gamma})\bar{i}_{\alpha\beta} + \bar{K}_m(\phi_d)\delta - \bar{W}_E^* = 0 \end{cases} \tag{3.55}$$

(3.55) can be re-written as

$$\begin{cases} 2\bar{i}_{\alpha\beta} + R_{ph}^{-1}\mathbf{K}_E^T(\vartheta_e, \bar{\gamma})\bar{\lambda}^T = 0 \\ \mathbf{K}_E(\vartheta_e, \bar{\gamma})\bar{i}_{\alpha\beta} + \bar{K}_m(\phi_d)\delta = \bar{W}_E^* \end{cases} \tag{3.56}$$

hence

$$\begin{cases} \bar{i}_{\alpha\beta} = -\frac{1}{2}R_{ph}^{-1}\mathbf{K}_E^T(\vartheta_e, \bar{\gamma})\bar{\lambda}^T \\ \mathbf{K}_E(\vartheta_e, \bar{\gamma})\bar{i}_{\alpha\beta} + \bar{K}_m(\phi_d)\delta = \bar{W}_E^* \end{cases} \tag{3.57}$$

Multiplying from the left the first equation in (3.56) with $-(1/2)\mathbf{K}_E(\vartheta_e, \bar{\gamma})$ and adding the second equation leads to

$$-\frac{1}{2}R_{ph}^{-1}\mathbf{K}_E(\vartheta_e, \bar{\gamma})\mathbf{K}_E^T(\vartheta_e, \bar{\gamma})\bar{\lambda}^T + \bar{K}_m(\phi_d)\delta = \bar{W}_E^* \tag{3.58}$$

hence, considering that $\big(\mathbf{K}_E(\vartheta_e, \bar{\gamma})\mathbf{K}_E^T(\vartheta_e, \bar{\gamma})\big)$ is invertible $\forall\vartheta_e$ (see Appendix A), it is possible to explicate $\bar{\lambda}^T$

$$\bar{\lambda}^T = -2R_{ph}\big(\mathbf{K}_E(\vartheta_e, \bar{\gamma})\mathbf{K}_E^T(\vartheta_e, \bar{\gamma})\big)^{-1}\Big[\bar{W}_E^* - \bar{K}_m(\phi_d)\delta\Big] \tag{3.59}$$

that in turn can be substituted into the first equation of (3.57) giving the desired reference current vector $\bar{i}^*_{\alpha\beta}$ as a function of the reference wrench vector $\bar{W}^*_E$.

$$\bar{i}^*_{\alpha\beta} = \left[\mathbf{K}^T_E(\vartheta_e,\bar{\gamma})\left(\mathbf{K}_E(\vartheta_e,\bar{\gamma})\mathbf{K}^T_E(\vartheta_e,\bar{\gamma})\right)^{-1}\right]\left[\bar{W}^*_E - \bar{K}_m(\phi_d)\delta\right] = \\ = \mathbf{K}^+_E(\vartheta_e,\bar{\gamma})\left[\bar{W}^*_E - \bar{K}_m(\phi_d)\delta\right] \quad (3.60)$$

where

$$\mathbf{K}^+_E(\vartheta_e,\bar{\gamma}) = \mathbf{K}^T_E(\vartheta_e,\bar{\gamma})\left[\mathbf{K}_E(\vartheta_e,\bar{\gamma})\,\mathbf{K}^T_E(\vartheta_e,\bar{\gamma})\right]^{-1} \in \mathbb{R}^{2n_s\times 3} \quad (3.61)$$

is the pseudo inverse of $\mathbf{K}_E(\vartheta_e,\bar{\gamma})$. The resulting reference current vector calculated according to (3.60) results in that quantity which minimizes the overall copper losses. The online computation of the pseudo inverse matrix $\mathbf{K}^+_E(\vartheta_e,\bar{\gamma})$ is a difficult task mainly due to the large amount of operations required. Taking advantage of the full characterization of the machine, each element of matrix $\mathbf{K}_E(\vartheta_e,\bar{\gamma})$ results known and here approximated with their fundamental harmonic waveform as stated in paragraph 3.3.3.2. The elements of the pseudo inverse matrix $\mathbf{K}^+_E(\vartheta_e,\bar{\gamma})$ is therefore evaluated numerically off-line using equation (3.61) $\forall\,\vartheta_e$. The approximated sinusoidal expressions obtained are shown in Figure 3.15 and they are digitalised in the control platform enabling a drastic reduction of the online computational effort needed. The harmonic spectrum of the coefficients of $\mathbf{K}^+_E(\vartheta_e,\bar{\gamma})$ is presented in the next paragraph justifying the sinusoidal approximation.

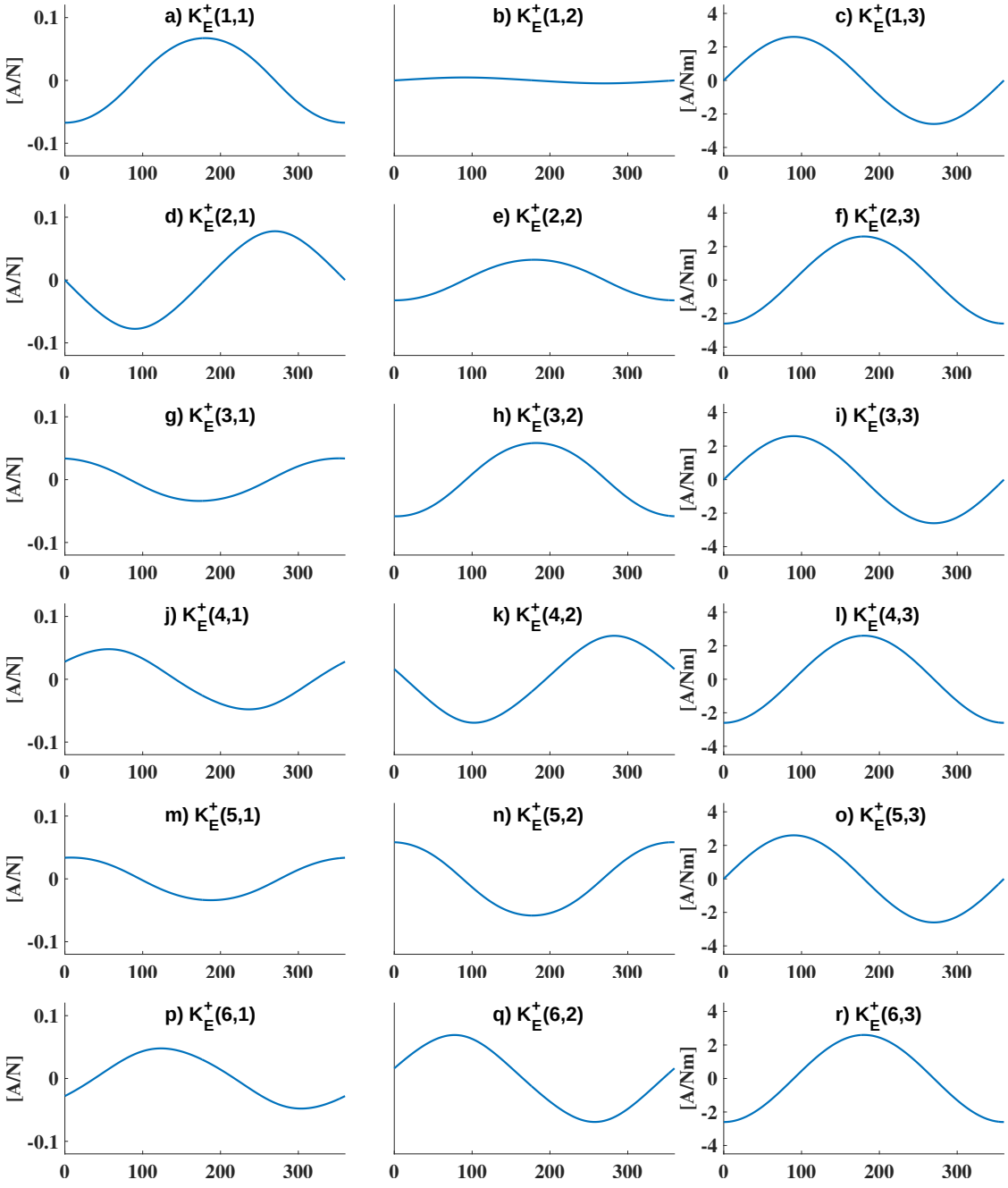


Figure 3.15: Coefficients of the pseudo inverse matrix. $\mathbf{K}_E^+(r,c)$ *stands for the coefficient in the* r^{th} *row and* c^{th} *column.*

The reference currents obtained in (3.60) are in the $\alpha-\beta$ stationary reference frame, however the current control loops of each sector relies on standard PI controllers operating in the $d-q$ synchronous reference frame. The transformation from static to rotating reference frame is obtained as

$$\bar{i}^*_{dq} = \mathbf{T}_R(\vartheta_e)\,\bar{i}^*_{\alpha\beta} = \mathbf{T}_R(\vartheta_e)\mathbf{K}^+_E(\vartheta_e,\bar{\gamma})\left[\bar{W}^*_E - \bar{K}_m(\phi_d)\delta\right] = \\ = \mathbf{K}^+_{E,dq}(\vartheta_e,\bar{\gamma})\left[\bar{W}^*_E - \bar{K}_m(\phi_d)\delta\right] \quad (3.62)$$

where $\mathbf{K}^+_{E,dq}$ is the pseudo inverse matrix in the rotor synchronous reference frame and $\mathbf{T}_R(\vartheta_e) \in \mathbb{R}^{2n_s\times 2n_s}$ is the rotation matrix written as

$$\mathbf{T}_R(\vartheta_e) = \begin{bmatrix} \mathbf{R}_{dq}(\vartheta_e) & \mathbf{0}_2 & \mathbf{0}_2 \\ \mathbf{0}_2 & \mathbf{R}_{dq}(\vartheta_e) & \mathbf{0}_2 \\ \mathbf{0}_2 & \mathbf{0}_2 & \mathbf{R}_{dq}(\vartheta_e) \end{bmatrix} \quad (3.63)$$

having $\mathbf{R}_{dq}(\vartheta_e) \in \mathbb{R}^{2\times 2}$ defined as

$$\mathbf{R}_{dq}(\vartheta_e) = \begin{bmatrix} \cos(\vartheta_e) & \sin(\vartheta_e) \\ -\sin(\vartheta_e) & \cos(\vartheta_e) \end{bmatrix} \quad (3.64)$$

The computation of matrix $\mathbf{K}^+_{E,dq}$ is carried out in Appendix C.1. Furthermore, the expressions of each $d-q$ axis current component as a function of the reference force, torque and rotor displacement is calculated in the Appendix.

3.4.3 Open-circuit fault of one sector

When an open-circuit fault occurs in one motor sector the correspondent $d-q$ axis current vector goes to zero eliminating its contribution to the radial force and torque

production. Therefore, the sub-matrix related to the open-circuited sector will disappear in $\mathbf{K}_E$ and the new matrices expression can be written as

$$\begin{aligned}
\mathbf{K}_{E,f1} &= \begin{bmatrix} {}^2\mathbf{K}_E(\vartheta_e, {}^2\gamma) & {}^3\mathbf{K}_E(\vartheta_e, {}^3\gamma) \end{bmatrix} \in \mathbb{R}^{n_m \times (2n_s-2)} \\
\mathbf{K}_{E,f2} &= \begin{bmatrix} {}^1\mathbf{K}_E(\vartheta_e, {}^1\gamma) & {}^3\mathbf{K}_E(\vartheta_e, {}^3\gamma) \end{bmatrix} \in \mathbb{R}^{n_m \times (2n_s-2)} \\
\mathbf{K}_{E,f3} &= \begin{bmatrix} {}^1\mathbf{K}_E(\vartheta_e, {}^1\gamma) & {}^2\mathbf{K}_E(\vartheta_e, {}^2\gamma) \end{bmatrix} \in \mathbb{R}^{n_m \times (2n_s-2)}
\end{aligned} \tag{3.65}$$

for open-circuit in sector 1, 2, 3, respectively. It can be noticed that matrices $\mathbf{K}_{E,f1}$, $\mathbf{K}_{E,f2}$ and $\mathbf{K}_{E,f3}$ are also rectangular. Therefore, in order to obtain the reference current signals in the case of open-circuit fault conditions, they can be substituted into (3.61) obtaining $\mathbf{K}^+_{E,f1}$, $\mathbf{K}^+_{E,f2}$ and $\mathbf{K}^+_{E,f3} \in \mathbb{R}^{(2n_s-2)\times n_m}$ respectively that in turn can be used in place of $\mathbf{K}^+_E$ in (3.60) to calculate the $\alpha-\beta$ reference current vectors. The $d-q$ reference current values are then calculated as follow

$$\begin{aligned}
\bar{i}^*_{dq,f1} &= \mathbf{T}_{R,f}(\vartheta_e)\mathbf{K}^+_{E,f1}\left[\bar{W}^*_E - \bar{K}_m(\phi_d)\delta\right] \\
\bar{i}^*_{dq,f2} &= \mathbf{T}_{R,f}(\vartheta_e)\mathbf{K}^+_{E,f2}\left[\bar{W}^*_E - \bar{K}_m(\phi_d)\delta\right] \\
\bar{i}^*_{dq,f3} &= \mathbf{T}_{R,f}(\vartheta_e)\mathbf{K}^+_{E,f3}\left[\bar{W}^*_E - \bar{K}_m(\phi_d)\delta\right]
\end{aligned} \tag{3.66}$$

where

$$\begin{aligned}
\bar{i}^*_{dq,f1} &= \begin{bmatrix} {}^2i_d & {}^2i_q & {}^3i_d & {}^3i_q \end{bmatrix}^T \\
\bar{i}^*_{dq,f2} &= \begin{bmatrix} {}^1i_d & {}^1i_q & {}^3i_d & {}^3i_q \end{bmatrix}^T \\
\bar{i}^*_{dq,f3} &= \begin{bmatrix} {}^1i_d & {}^1i_q & {}^2i_d & {}^2i_q \end{bmatrix}^T
\end{aligned} \tag{3.67}$$

and $\mathbf{T}_{R,f}(\vartheta_e) = \begin{bmatrix} \mathbf{R}_{dq}(\vartheta_e) & \mathbf{0}_2 \\ \mathbf{0}_2 & \mathbf{R}_{dq}(\vartheta_e) \end{bmatrix}$.
The expressions of each element of vectors $\bar{i}^*_{dq,f1}$, $\bar{i}^*_{dq,f2}$ and $\bar{i}^*_{dq,f3}$ is reported in Appendix C.2.

Figure 3.16 shows the harmonic content of the coefficients of matrix $\mathbf{K}_E^+ \in \mathbb{R}^{6\times3}$, for healthy operating condition and of matrices $\mathbf{K}_{E,f1}$, $\mathbf{K}_{E,f2}$ and $\mathbf{K}_{E,f3} \in \mathbb{R}^{4\times3}$ for an open-circuit fault in sector 1, 2 and 3, respectively. The magnitudes of the harmonics have been obtained through the fast Fourier transform of the aforementioned coefficients waveforms. Comparing the different harmonic contents it can be observed that a non negligible third harmonic appears in the terms of matrices $\mathbf{K}_{E,f1}$, $\mathbf{K}_{E,f2}$ and $\mathbf{K}_{E,f3}$, while the ones of $\mathbf{K}_E$ are essentially sinusoidal. Their waveforms were reported in Figure 3.15 and they can be easily implemented in a DSP reducing the computational efforts. On the other hand, the third harmonic has to be considered in the coefficients of $\mathbf{K}_{E,f1}$, $\mathbf{K}_{E,f2}$ and $\mathbf{K}_{E,f3}$ in order to produce the required suspension force and motoring torque complicating the control algorithm.

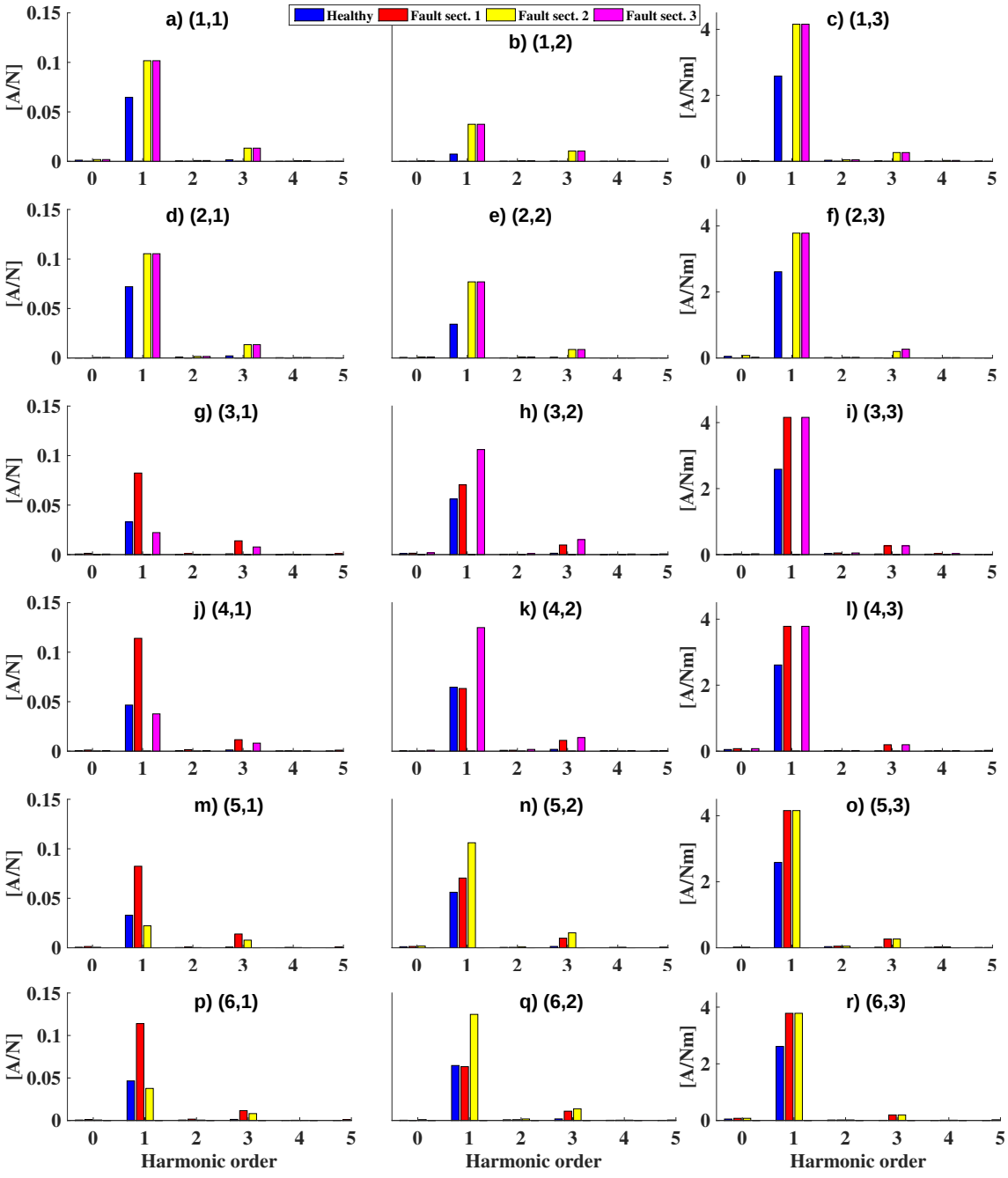


Figure 3.16: Comparison in terms of harmonic content between the coefficients of matrix $\mathbf{K}_E^+$ *(healthy machine), matrix* $\mathbf{K}_{E,f1}^+$ *(fault in sector 1), matrix* $\mathbf{K}_{E,f2}^+$ *(fault in sector 2) and matrix* $\mathbf{K}_{E,f3}^+$ *(fault in sector 3).*

3.5 Chapter Summary

The first part of this Chapter provides a detailed description of the electrical model of the machine considered. In particular, the $d-q$ axis voltage equations have been determined and expressed in state space form. In Chapter 5 the analytical model will be validated with FE simulations and will be employed in a Simulink function in order to replicate the electrical behaviour of the machine. The $d-q$ axis inductance matrix is presented and its elements obtained by means analytical calculation and verified with FEA. The main electrical parameters such as back-EMF, phase resistance and inductances will be experimentally evaluated in Chapter 6.

Then, the electromagnetic model that describes the torque and force production of a generic MSPM machine has been presented. It has been shown that a proper strategy has to be adopted to calculate the reference currents in order to generate the required torque and radial force. The minimization of the Joule losses has been chosen as objective leading to the calculation of the pseudo inverse matrix. The coefficients of the latter results in sinusoidal waveforms which can be digitalized in the control platform.

The open-circuit fault of one winding sector is also considered and the model of the MSPM machine is adapted accordingly. Again, the pseudo inverse matrix guarantees the calculation of those reference currents that minimize the Joule losses even in the case of one three-phase winding open-circuited.

The presented force control method will be experimentally validated exploiting it to damp selected vibration harmonics detected while the motor is spinning. Furthermore, the radial force will be controlled to suspend the rotor and realise then a 2-DOF bearingless drive.

Chapter 4

Radial Position Control Design

4.1 Introduction

This Chapter deals with the design and tuning of the $x - y$ axis radial position controller. The model of the mechanical plant is described highlighting the presence of an unstable pole that needs to be stabilized by the controller.

A transfer function-based method is considered in the first place for the controller synthesis. In particular, the closed loop transfer function of the overall system (controller and mechanical system) is analysed and the closed loop poles are placed at the desired position.

A more advanced controller is then derived in state space form. The so called standard controller is derived in two steps: at first a basic controller is introduced in order to stabilize the system; then a low-pass filter is included in the basic controller to improve the suspension performance. In both cases the LQR theory has been applied to determine the controller gains.

The robustness of the suspension control is investigated in a dedicated section. In particular, the LQR together with the LMI theory are used to calculate the standard

controller parameters in order to guarantee robustness and stability properties in the rotor suspension.

Finally, a multi-resonant controller (MRC) is introduced and synthesized using the state space method and applying again the LQR and LMI theories. The purpose of the MRC is the compensation of the multi-frequency position oscillations caused by periodic force disturbances.

4.2 Transfer Function-Based Design Method

4.2.1 The rotor dynamic system

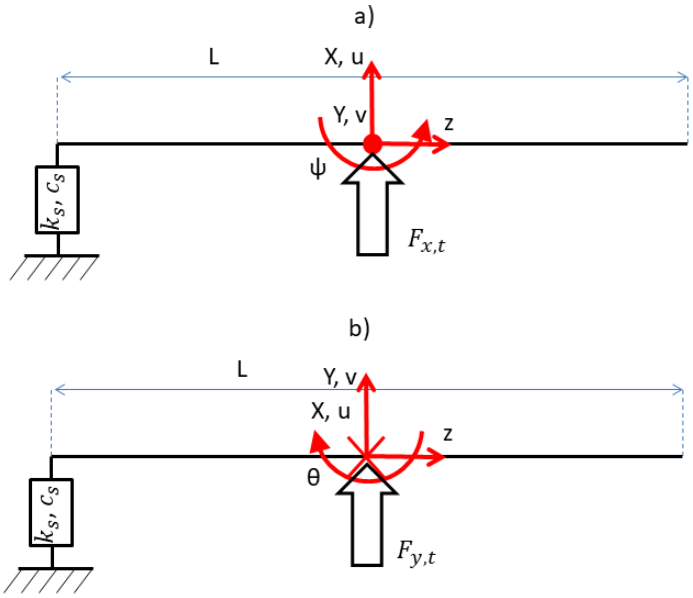


Figure 4.1: Schematic representation of the rotor fixed to the self-alignment bearing and geometrical reference frame representation: a) $x-$ axis rotor view; b) $y-$ axis rotor view.

In order to control 2-DOF the tilting movement and the axial displacement must be constrained by a self-alignment bearing mounted on one side of the shaft. The other

side is free to move along the $x-y$ axis only. Figure 4.1 presents a schematic of the rotor system model showing the overall force acting on the mass centre and the $x-y$ axis reference frame positioned on it. The self-alignment bearing is modelled as a spring of stiffness k_s and a viscous damper c_s. Hence, assuming the rotor a rigid cylinder and considering small radial displacements, the suspension rotor dynamic system can be written in matrix form as follow [132]:

$$M\ddot{q} + G\dot{q} + Kq = F \tag{4.1}$$

where

$$\begin{aligned} q &= \begin{bmatrix} u & v & \vartheta & \psi \end{bmatrix}^T \\ M &= diag(m, m, J_d, J_d) \\ G &= \begin{bmatrix} c_s & 0 & 0 & c_{s,c} \\ 0 & c_s & -c_{s,c} & 0 \\ 0 & -c_s & c_{s,r} & \omega_m J_p \\ c_s & 0 & -\omega_m J_p & c_{s,r} \end{bmatrix} \\ K &= \begin{bmatrix} k_s & 0 & 0 & k_{s,c} \\ 0 & k_s & -k_{s,c} & 0 \\ 0 & -k_{s,c} & k_{s,r} & 0 \\ k_{s,c} & 0 & 0 & k_{s,r} \end{bmatrix} \\ F &= \begin{bmatrix} F_{x,t} & F_{y,t} & 0 & 0 \end{bmatrix}^T \end{aligned} \tag{4.2}$$

$c_{s,c} = -Lc_s$, $k_{s,c} = -Lk_s$, $c_{s,r} = L^2 c_s$, $k_{s,r} = L^2 k_s$. $F_{x,t}$ and $F_{y,t}$ are the total $x-y$ forces described in (3.50) including a possible disturbance and, only in the $y-$axis, the rotor weight force. ϑ and ψ are the angular rotation angles around the $x-$ and $y-$ axis, respectively. Their signs are chosen according to the conventions taken in Figure 4.1. ω_m is the angular speed around the $z-$ axis. J_p and J_d are the polar and

diametral moment of inertia of the rotor defined as

$$\begin{aligned} J_p &= m\frac{R_m^2}{8} \\ J_d &= \frac{J_p}{2} + m\frac{l^2}{12} \end{aligned} \tag{4.3}$$

Being the ratio $J_p/J_d = 0.097$ and the maximum angular speed relatively low, the gyroscopic effect can be neglected. Furthermore, typical values of stiffness coefficients for ball bearings are $k_s = 110 \div 190$ [N/μm] therefore, the self-alignment bearing can by considered stiff. After the approximations introduced, the four equations of system (4.1) are decoupled and, for the position control purpose, only the first two are considered and written in (4.4).

$$\begin{bmatrix} m & 0 \\ 0 & m \end{bmatrix} \begin{bmatrix} \ddot{u} \\ \ddot{v} \end{bmatrix} - \begin{bmatrix} k_m & 0 \\ 0 & k_m \end{bmatrix} \begin{bmatrix} u \\ v \end{bmatrix} = \begin{bmatrix} F_{x,c} + F_{x,d} \\ F_{y,c} + F_{y,d} - mg \end{bmatrix} \tag{4.4}$$

$F_{x,c}$, $F_{y,c}$ and $F_{x,d}$, $F_{y,d}$ are the $x - y$ components of the forces generated by the controller and due to the disturbance, respectively. Finally, the negative term $-mg$ is the rotor weight force, treated as a disturbance in this analysis.
The transfer function $G(s)$ of the mechanical plant can be written, considering one axis, as follow:

$$G(s) = \frac{1}{ms^2 - k_m} \tag{4.5}$$

$G(s)$ has two poles in $\pm\sqrt{k_m/m}$ [rad/s]. It is worth noting that one of the pole has positive real part, hence it is unstable. The phenomena can be physically explained by the presence of the magnetic stiffness constant that produces a force that tend to attract the rotor to the stator core.

4.2.2 Standard Controller Designed with a Transfer Function-Based Method

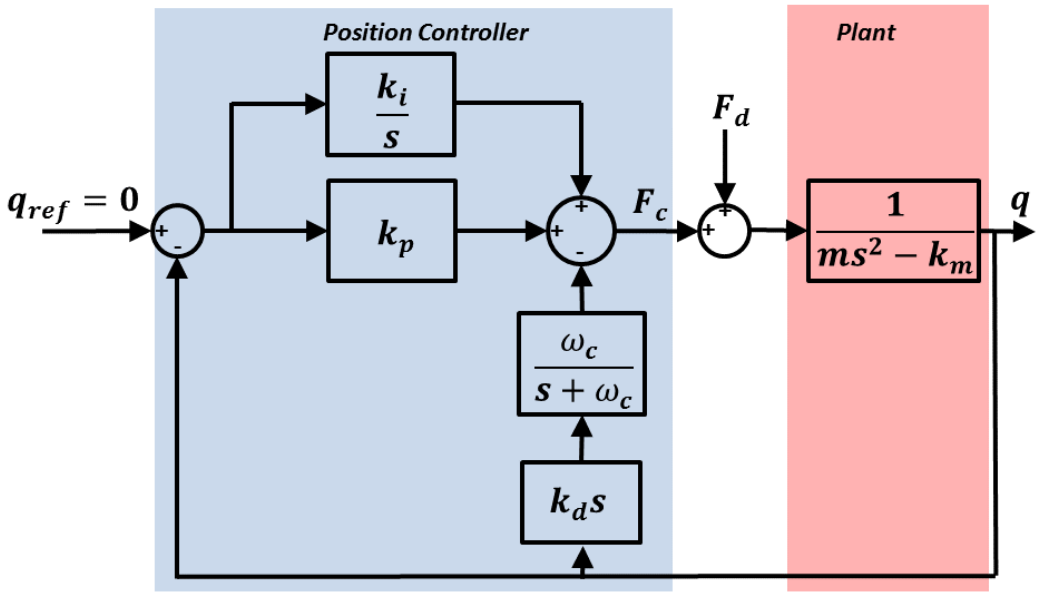


Figure 4.2: Structure of the radial position controller.

Since system (4.4) is decoupled, the position controller can be designed separately for the two axis. Furthermore, being the controller bandwidth around two orders of dimension smaller than the switching frequency the tuning can be carried out in the continuous domain. Indeed, the one sample time delay introduced by the controller can be neglected in the synthesis.

Figure 4.2 shows the block scheme of the position controller structure chosen for both axis. q_{ref} and q stand for either $x-$ or $y-$ axis position reference and measurement, respectively. The controller consists of a PID regulator where the output of the derivative term has been filtered with a first-order low pass filter. In fact, the discrete implementation of the position derivation produces high frequency noise that would deteriorate the performance of the position controller.

Since the position controller main goal is to reject disturbances and keep the shaft centred, the closed loop transfer function from F_d to q has been analysed. The latter

can be written as

$$T_{dq}(s) = \frac{1}{m} \frac{s^2 + \omega_c s}{s^4 + \omega_c s^3 + \frac{k_p + k_d \omega_c - k_m}{m} s^2 + \frac{k_i + k_p \omega_c - k_m \omega_c}{m} s + \frac{k_i \omega_c}{m}} \tag{4.6}$$

where k_p, k_i and k_d are the proportional, the integral and the derivative gain respectively and ω_c is the low-pass filter cut-off frequency. The roots of the denominator of $T_{dq}(s)$ are the poles of the closed loop system of Figure 4.2. Therefore, the transfer function-based technique consists of placing the poles of (4.6) in the desired position comparing the dominator of $T_{dq}(s)$ with a reference polynomial expression.
As a first simplified approach, the four poles are placed coincident at the pulsation ω_0. The corresponding reference polynomial is

$$(s + \omega_0)^4 = s^4 + 4\omega_0 s^3 + 6\omega_0^2 s^2 + 4\omega_0^3 s + \omega_0^4 \tag{4.7}$$

Equating the coefficients of the denominator of $T_{dq}(s)$ with the coefficients of (4.7) system (4.8) can be written.

$$\begin{cases} w_c = 4\omega_0 \\ \frac{k_p + k_d \omega_c - k_m}{m} = 6\omega_0^2 \\ \frac{k_i + k_p \omega_c - k_m \omega_c}{m} = 4\omega_0^3 \\ \frac{k_i \omega_c}{m} = \omega_0^4 \end{cases} \tag{4.8}$$

The solution of the above system gives the expression of the controller parameters as a function of the desired pulsation ω_0 of the final closed loop poles:

$$\begin{cases} w_c = 4\omega_0 \\ k_d = \frac{81}{64} m\omega_0 \\ k_p = \frac{15}{16} m\omega_0^2 + k_m \\ k_i = \frac{1}{4} m\omega_0^3 \end{cases} \tag{4.9}$$

A different solution that has been considered to tune the controller parameters consists of choosing the forth order Butterworth filter (4.10) instead of the polynomial expression (4.8).

$$\begin{aligned} (s^2 + 0.7654\omega_0 s + \omega_0^2)(s^2 + 1.8478\omega_0 s + \omega_0^2) = \\ = s^4 + 2.6132\omega_0 s^3 + 3.4143\omega_0^2 s^2 + 2.6132\omega_0^3 s + \omega_0^4 \end{aligned} \tag{4.10}$$

The motivation for choosing polynomial (4.10) is due to the fact that the poles of (4.6) calculated with the optimal Linear Quadratic Regulation (LQR) tend asymptotically to those of a Butterworth filter of the same order as the state weights in the cost function increase. The last statement will be better explained and demonstrated later in this Chapter.

The resulting system of equations (4.11) has to be solved for the controller parameters.

$$\begin{cases} w_c = 2.6132\omega_0 \\ \frac{k_p + k_d\omega_c - k_m}{m} = 3.4143\omega_0^2 \\ \frac{k_i + k_p\omega_c - k_m\omega_c}{m} = 2.613\omega_0^3 \\ \frac{k_i\omega_c}{m} = \omega_0^4 \end{cases} \tag{4.11}$$

The calculated parameters as a function of the rotor mass m and pulsation ω_0 are

listed as follow

$$\begin{cases} w_c = 2.6132\omega_0 \\ k_d = 0.9798m\omega_0 \\ k_p = 0.8535m\omega_0^2 + k_m \\ k_i = 0.3827m\omega_0^3 \end{cases} \tag{4.12}$$

k_m is considered as a known quantity and it is included in the proportional gain k_p expression leading to the compensation to the PM force attraction. Furthermore, ω_0 is the actual bandwidth of the closed loop system since, by definition, the amplitude response of a $n-$order Butterworth filter is equal to $1/\sqrt{2}$ (-3 dB) at the pulsation ω_0.

4.2.3 Numerical values of the controller gains

The choice of the poles pulsation ω_0 is a trade off between having a fast reacting controller and not exceeding the intrinsic limits given by the current control bandwidth. Indeed, the PMs produce big attraction forces between the stator and the rotor as soon as the latter has a small radial displacement. The phenomena is described by the magnetic stiffness constant k_m multiplied by the radial position information. Therefore, the controller should stabilize the rotor position in the case of unavoidable small displacements. In this work, after different attempts, the poles pulsation ω_0 has been chosen equal to $2\pi170$ rad/s leading to the controller gains values reported in table 4.1 and 4.2 for the coincident and Butterworth poles configuration, respectively.

Table 4.1: Controller Gains for Coincident Poles Config.

Gain	**Value**
ω_c	4.27e3
k_p	4.44e6
k_d	4.73e3
k_i	1.07e9

Table 4.2: Controller Gains for Butterworth Poles Config.

Gain	**Value**
ω_c	2.79e3
k_p	4.11e9
k_d	3.66e3
k_i	1.63e9

Figure 4.3 shows the poles position for the two tuning choices in the complex plane. As expected, the coincident poles configuration approach places the four poles in the same position on the real axis (no imaginary part), therefore, the poles damping is 1. On the other hands, two pairs of complex conjugate poles are obtained with the Butterworth configuration approach. Their damping is quite small leading to a big overshoot in the step response shown in Figure 4.4.

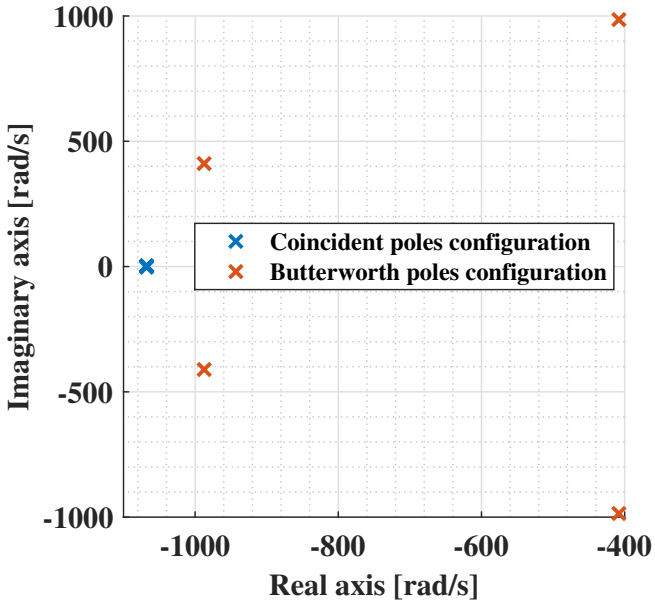


Figure 4.3: Poles map of the overall system (controller together with mechanical plant) for coincident and Butterworth pole configuration.

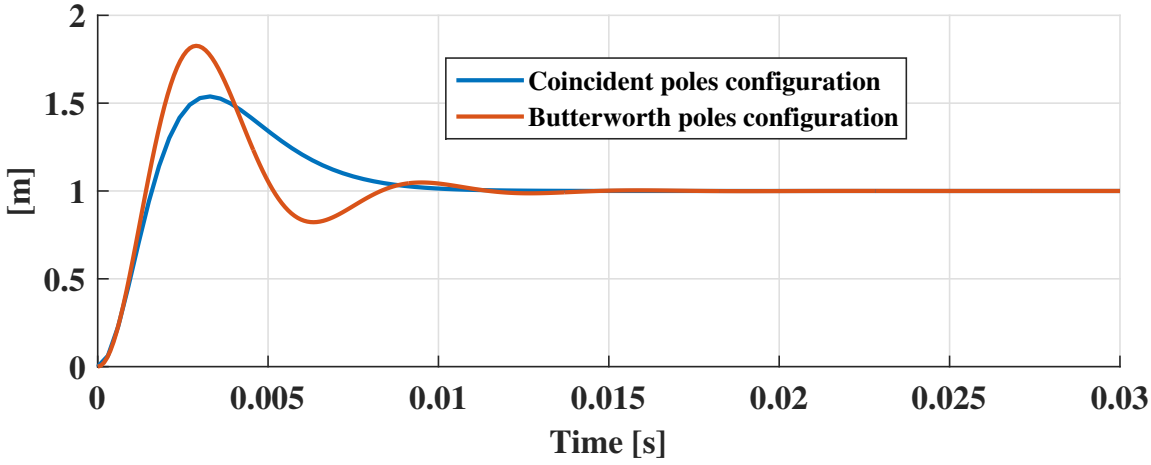


Figure 4.4: Step response of the overall system (controller together with mechanical plant) for coincident and Butterworth pole configuration.

Finally, observing the frequency response of the transfer function from force disturb to output ($T_{dq}(s)$) in Figure 4.5 it is straightforward to notice that the Butterworth

poles configuration performs a better disturbance rejection at low frequency while the remarkable peak suggests that at around ω_0 the disturbance rejection is smaller than the one achieved by the coincident poles configuration. At high frequency the two bode diagrams match, hence the two approaches presents same disturbance rejection. In this work the Butterworth pole configuration has been chosen and the gains used are the ones in table 4.2.

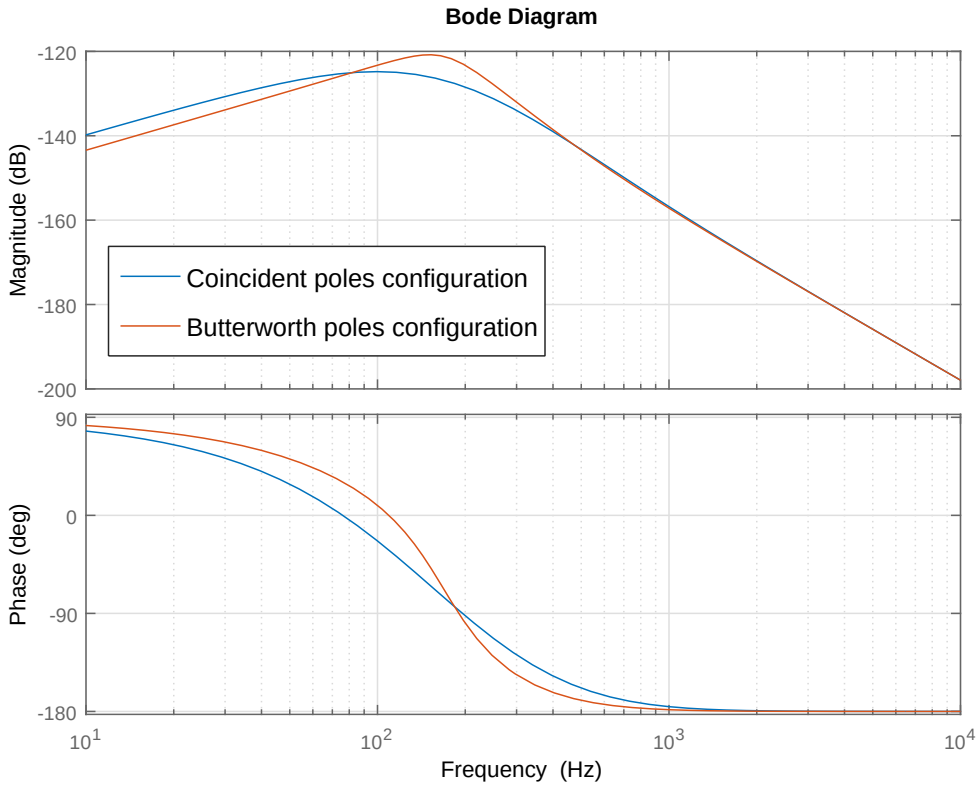


Figure 4.5: Bode diagram of the closed loop transfer function $T_{dq}(s)$ for coincident and Butterworth pole configuration.

4.3 State Space Design

The state space design technique allows to synthesize a dynamic compensation by working directly with the state variables of the system. Although the state space approach has been in use for more than 100 years it has been often referred to as modern control design, while transfer function-based methods such root locus and frequency response are considered classical control designs. Advantages in the state space approach are particularly evident when complex controllers have to be designed because it allows treating the overall system as a whole, hence the controller gains that guarantee stability and good performance can be easily calculated. As a matter of fact, the transfer function-based approach used in 4.2.2, based on the transfer function of the closed loop system, results difficult to apply when the controller presents more than 4 gains. In addition, for high order systems, the selection of a good closed loop poles location is not a simple task.

4.3.1 State Space Rotor-Dynamic Model of the Mechanical Plant

As stated in 4.2.1, the equation along the $x-$ axis can be considered decoupled from the one along the $y-$ axis. Hereafter, only one axis is considered. The state space system of the mechanical plant can be written as

$$\begin{cases} \dot{x}_p = A_p x_p + B_p u_p \\ y_p = C_p x_p \end{cases} \tag{4.13}$$

with

$$A_p = \begin{bmatrix} 0 & 1 \\ \frac{k_m}{m} & 0 \end{bmatrix}; B_p = \begin{bmatrix} 0 \\ \frac{1}{m} \end{bmatrix}; C_p = \begin{bmatrix} 1 & 0 \end{bmatrix} \tag{4.14}$$

$x_p = \begin{bmatrix} q & \dot{q} \end{bmatrix}^T$ is the state vector defined as the rotor displacement q and the rotor radial speed $\dot{q}$, u_p is the input force and y_p is the output position. Figure 4.6 shows the diagram of the mechanical plant given by the state space system (4.13).

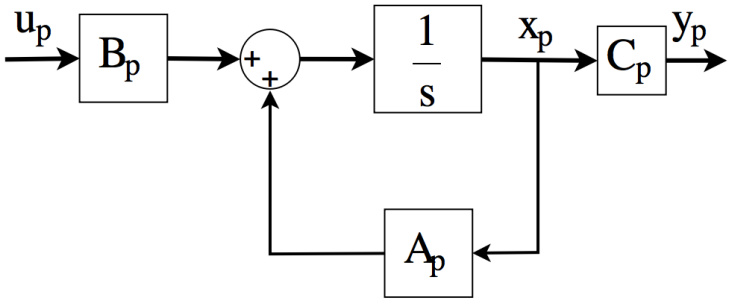


Figure 4.6: Representation of the mechanical plant.

It is worth to notice that the mechanical plant described by (4.13) is inherent unstable, hence the controller has to guarantee the stability of the overall closed loop system. The following derivations are carried out with the assumption that system (4.13) is controllable. In fact, the concepts of controllability plays an important role in the design of control systems in state space. A system is said to be controllable at time t_0 if it is possible to transfer the system from any initial state to any other state in a finite interval of time by means of a controller.
The continuous-time system

$$\dot{x} = Ax + Bu \tag{4.15}$$

where $A \in \mathbb{R}^{n \times n}$ and $B \in \mathbb{R}^{n \times 1}$, is completely state controllable if the rank of

$$\begin{bmatrix} B & AB & \cdots & A^{n-1}B \end{bmatrix} \quad \in \mathbb{R}^{n \times n} \tag{4.16}$$

is n [133].
Considering the mechanical plant system (4.14), the controllability condition requires that the rank of matrix

$$\begin{bmatrix} B_p & A_p B_p \end{bmatrix} \quad \in \mathbb{R}^{2\times 2} \tag{4.17}$$

be 2. Substituting A_p and B_p into (4.17) matrix (4.18) is obtained.

$$\begin{bmatrix} 0 & \frac{1}{m} \\ \frac{1}{m} & \frac{k_m}{m} \end{bmatrix} \tag{4.18}$$

It is straightforward that the rank of (4.18) is 2, hence system (4.14) is completely state controllable.

4.3.2 Standard position controller

The design of the standard position controller that has been implemented in the bearnigless drive is obtained in two stages. To start with, a basic controller is realized in order to stabilize the mechanical plant considered. Then, a low-pass filter has been included in the basic controller in order to improve the position control performance.

4.3.2.1 Basic controller

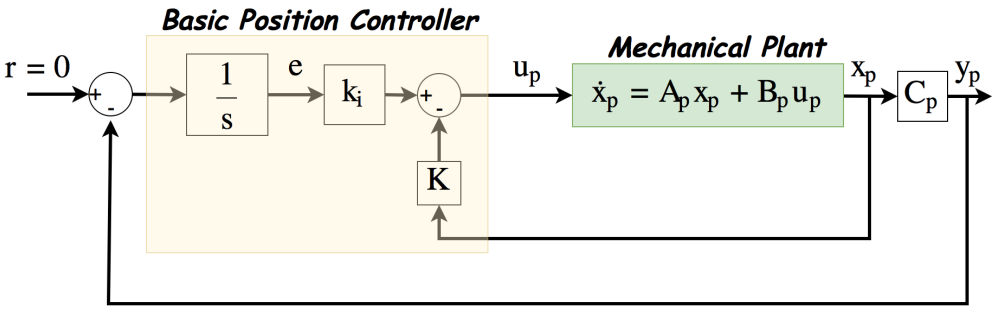


Figure 4.7: Block scheme of the basic position controller.

A convenient control structure to adopt for regulating the described mechanical plant is the full state feedback. Since the plant has no integrator, a basic approach to design the controller is to insert an integrator between the error comparator and the plant in order to obtain a zero steady state error [134]. The resultant controller block scheme is shown in Figure 4.7. Observing the diagram it is possible to write the following equalities:

$$\begin{aligned} \dot{x}_p &= A_p x_p + B_p u_p \\ y_p &= C_p x_p \\ u_p &= -K x_p + k_i e \\ \dot{e} &= r - y_p = r - C_p x_p \end{aligned} \tag{4.19}$$

where u_p is the control signal, e is the output of the integrator and r is the step function reference input signal. The plant state space system can be extended adding the integrator as in (4.20).

$$\dot{x}_B = A_B x_B + B_B u_B \tag{4.20}$$

$x_B = \begin{bmatrix} x_p & e \end{bmatrix}^T$ is the augmented state vector, A_B and B_B are the augmented state and input matrix respectively, defined as

$$A_B = \begin{bmatrix} A_p & \mathbf{0}_{2,1} \\ -C_p & 0 \end{bmatrix}; \quad B_B = \begin{bmatrix} B_p \\ 0 \end{bmatrix} \tag{4.21}$$

while

$$u_B = -Kx_p + k_i e = -K_B x_B = -\begin{bmatrix} K & -k_i \end{bmatrix} \begin{bmatrix} x_p \\ e \end{bmatrix} \tag{4.22}$$

$\mathbf{0}_{m,n} \in \mathbb{R}^{m \times n}$ is a null matrix.

An elegant approach to compute the feedback gain vector K_B is to use the LQR technique. With this approach it is possible to compute a state feedback gain that minimizes the cost function

$$J_{LQR} = \int_0^\infty [x_B^T Q_B x_B + u_B^T R_B u_B] dt \tag{4.23}$$

where Q_B and R_B are state and input weight matrices respectively [135].

4.3.2.2 Improved controller

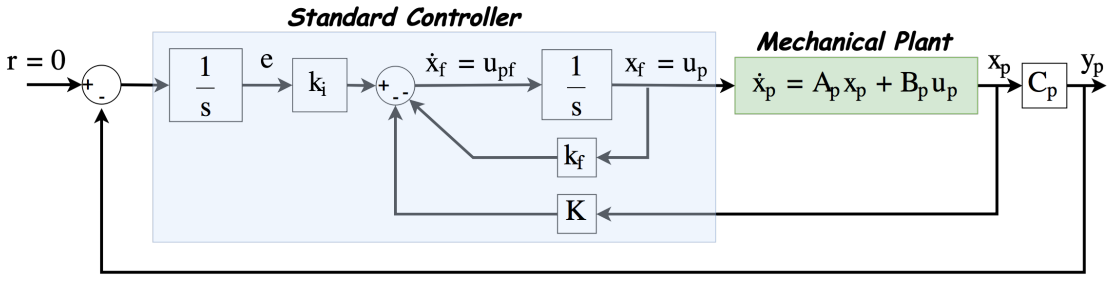


Figure 4.8: Block scheme of the standard position controller including the low-pass filter.

The rotor speed measurement $\dot{q}$ is not available in practise. Its calculation through discrete derivative of rotor position introduces noise in the feedback path. To handle this, the plant input can be extended with an integrator to filter out high frequency noise. As it will be better explained later, this extension will result in a low-pass filter in the plant input. Figure (4.8) shows the block diagram of the basic controller with the aforementioned low-pass filter. Observing the diagram it is possible to write the following equalities:

$$\begin{aligned} \dot{x}_p &= A_p x_p + B_p x_f \\ \dot{x}_f &= 0 \cdot x_f + u_{pf} \end{aligned} \tag{4.24}$$

where x_f and u_{pf} represent the filter state and input variables, respectively. The filter can be included in the mechanical plant augmenting its order. Defining the augmented state vector of the plant-filter system as $x_{pf} = \begin{bmatrix} x_f \\ x_p \end{bmatrix}$ and writing the new state space system matrices as

$$A_{pf} = \begin{bmatrix} 0 & \mathbf{0}_{1,2} \\ B_p & A_p \end{bmatrix}; B_{pf} = \begin{bmatrix} 1 \\ \mathbf{0}_{2,1} \end{bmatrix}; C_{pf} = \begin{bmatrix} 0 & 1 & 0 \end{bmatrix} \tag{4.25}$$

the state space formulation of the extended mechanical plant can be written as in (4.26).

$$\begin{cases} \dot{x}_{pf} = A_{pf} x_{pf} + B_{pf} u_{pf} \\ y_{pf} = y_p = C_{pf} x_{pf} \end{cases} \tag{4.26}$$

The input u_{pf} is now defined as

$$u_{pf} = -K_{pf} x_{pf} + k_i e = -\begin{bmatrix} k_f & K \end{bmatrix} \begin{bmatrix} x_f \\ x_p \end{bmatrix} + k_i e \tag{4.27}$$

The resultant block diagram is shown in Figure 4.9. It is straightforward to notice

that the diagram is equal to the one shown in Figure 4.7 where the mechanical plant has been replaced with the extended one.

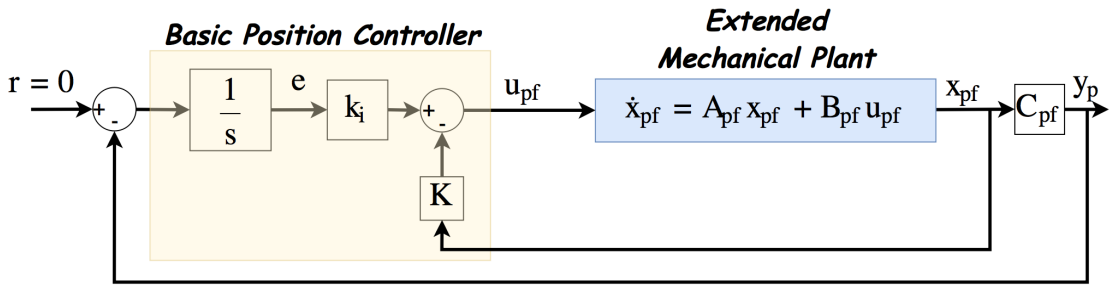


Figure 4.9: Block scheme of the standard position controller where the mechanical plant has been extended with the low-pass filter.

It is now possible to further extend the plant-filter system with the integrator as in the previous paragraph. The resulting extended system is

$$\begin{cases} \dot{x} = Ax + B_2 u \\ y_p = Cx \end{cases} \tag{4.28}$$

where the state matrices are defined as follow

$$A = \begin{bmatrix} A_{pf} & \mathbf{0}_{3,1} \\ -C_{pf} & 0 \end{bmatrix}; B_2 = \begin{bmatrix} B_{pf} \\ 0 \end{bmatrix}; C = \begin{bmatrix} C_{pf} & 0 \end{bmatrix}. \tag{4.29}$$

A full state feedback control law in the form

$$u = -K_e x = -\begin{bmatrix} k_f & K & -k_I \end{bmatrix} \begin{bmatrix} x_f \\ x_p \\ e \end{bmatrix} \tag{4.30}$$

can then be computed. The resulting control scheme is reported in Figure 4.8. From Figure 4.8 it can be noted how the feedback loop around the filter integrator moves

the pole depending on the value of k_f changing the low-pass cut off frequency.
The cost function that has to be minimized is still (4.23) where x_B and u_B have to be replaced with x and u. The state and input weight matrices have to be updated with Q and R. The resultant new cost function is defined in (4.31).

$$J_{LQR} = \int_0^\infty [x^T Q x + u^T R u] dt \tag{4.31}$$

4.4 Robustness Analysis

4.4.1 Generalities of the robustness analysis

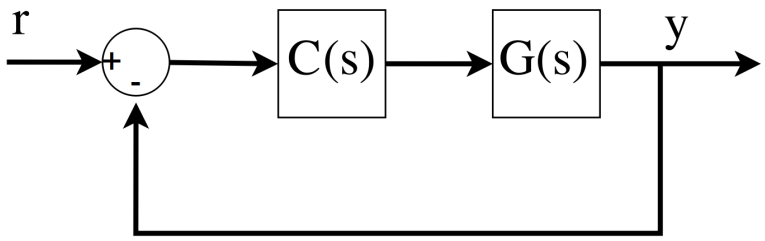


Figure 4.10: Basic closed loop control system.

LQR tuning method offers good robustness performance, guaranteeing at least 60 deg phase margin, infinite positive gain margin and 0.5 negative gain margin. The above listed features are obtained analysing the peak M_s of the sensitivity function $S(s)$ defined as

$$M_s = \max(|S(j\omega)|) = \max\left(\frac{1}{1 + L(j\omega)}\right); \quad 0 \leq \omega < \infty \tag{4.32}$$

where $L(s)$ is the open loop transfer function defined just before the plant. For the basic closed loop control scheme of Figure 4.10 it results that

$$L(s) = G(s)C(s) \tag{4.33}$$

where $G(s)$ and $C(s)$ are the plant and the controller, respectively. In order to obtain a robust closed loop system, it is important that the maximum value of the sensitivity function is limited. A common requirement is to make M_s be in a range of 1.3 to 2. As a matter of fact, the quantity $1/M_s$ is the inverse of the shortest distance from the Nyquist curve of the open loop transfer function to the critical point -1. For instance, a sensitivity $M_s < \xi_0$ guarantees that the distance from the critical point to the Nyquist curve is always greater than $1/\xi_0$ and that the Nyquist curve of the loop transfer function is always outside a circle of radius $\frac{1}{M_s}$ around the critical point -1, known as the sensitivity circle. The LQR method guarantees that the inverse of the sensitivity function peak is smaller than 2 resulting in a 60 [deg] phase margin and 0.5 negative gain margin.

However, if an extended system is used (like the filter-plant one depicted in 4.3.2.2), the margins are ensured at the extended plant input, and not at the original plant one [136]. To overcome this limitation, it is useful to reformulate the LQR problem as the minimization of an H_2 system norm limiting M_s to the desired value ξ_0. In the next two paragraphs the problem will be reformulated to keep into account the above considerations. In particular it will be shown that the LQ optimal regulator problem can be derived in terms of H_2 system norm. Furthermore, the constraint of the sensitivity function peak will be taken into account analysis the H_∞ norm of the sensitivity function.

4.4.2 H_2 optimal control

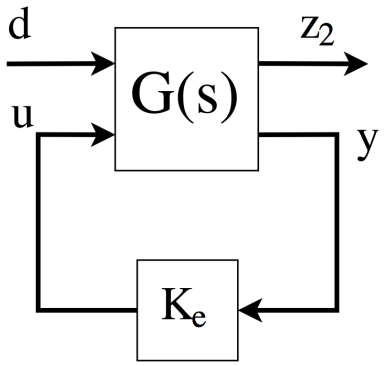


Figure 4.11: Basic closed loop control system.

Observing Figure 4.11, it is possible to write the following formulation:

$$\begin{cases} \begin{bmatrix} z_2 \\ y \end{bmatrix} = \begin{bmatrix} G_{11} & G_{12} \\ G_{21} & G_{22} \end{bmatrix} \begin{bmatrix} d \\ u \end{bmatrix} \\ u = K_e y \end{cases} \tag{4.34}$$

The two inputs d and u are the disturb and control signals respectively while the two outputs z_2 and y are the error (to be kept small) and measured signal, respectively. It is then possible to express z_2 as a function of the disturb signal d as

$$z_2 = F(G, K_e)d = \big(G_{11} + G_{12}(I - K_e G_{22})^{-1} K_e G_{21}\big)d \tag{4.35}$$

The H_2-optimal control problem consists of finding a causal controller K_e that stabilizes the plant $G(s)$ and minimizes the cost function

$$J_2 = \|F(G, K)\|_2^2 \tag{4.36}$$

where $\|F(G, K)\|_2$ is the H_2 norm.

The H_2 optimal control problem is more easily solved in the time-domain. System (4.34) can be written in state space form as in (4.37).

$$\begin{cases} \dot{x}(t) = Ax(t) + B_1 d(t) + B_2 u(t) \\ z_2(t) = C_2 x(t) + D_{22} u(t) \end{cases} \tag{4.37}$$

where A and B_2 were already defined for the considered position controller in the previous section, $B_1 = \begin{bmatrix} 0 \\ B_p \\ 0 \end{bmatrix}$ and C_2, D_{22} are hereafter defined.
It is convenient to write the cost function J_2 in the time-domain as in (4.38) in order to derive the solution of the H_2 optimal controller problem in a conventional way.

$$J_2 = \int_0^\infty [z_2(t)^T z_2(t)]dt = \int_0^\infty [(C_2 x(t) + D_{22} u(t))^T (C_2 x(t) + D_{22} u(t))]dt \tag{4.38}$$

Imposing $C_2 = \begin{bmatrix} \sqrt{Q} \\ \mathbf{0}_{1,4} \end{bmatrix}$ and $D_{22} = \begin{bmatrix} \mathbf{0}_{4,1} \\ \sqrt{R} \end{bmatrix}$ the cost function (4.38) is equivalent to the one of the LQ optimal regulator J_{LQR} defined in (4.31) [135]. The LQR problem can then be stated as: find a state feedback control law (4.30) that minimize the H_2 norm defined in (4.38).

4.4.3 H_∞ method

The problem reformulation introduced in the previous paragraph can be cast to an LMI problem offering a more flexible resolution of the controller syntheses. For example, it is possible to set a constraint on the H_∞ norm of the sensitivity function $S(s)$ allowing to increase closed loop robustness. The H_∞ norm of the sensitivity function $S(s)$ is defined as follow

$$\|S(s)\|_\infty = \max(|S(j\omega)|); \quad 0 \leq \omega < \infty \tag{4.39}$$

It is important ot notice that the above expression corresponds to the definition of the sensitivity function peak M_s given in (4.32). It was highlighted that M_s is directly related to gain and phase margin and limiting it to values typically smaller than $\xi_0 = 2$ ensures good robustness of the closed loop system [137]. In order to formulate the H_∞ problem, it is convenient to express the sensitivity function as

$$y_s = S(s)u_s = \frac{1}{1 + L(s)}u_s \tag{4.40}$$

$L(s)$ was already defined in (4.33) for a basic closed loop control scheme.
Figure 4.12 represents schematically the considered position controller including the low-pass filter and an eventual disturbance.

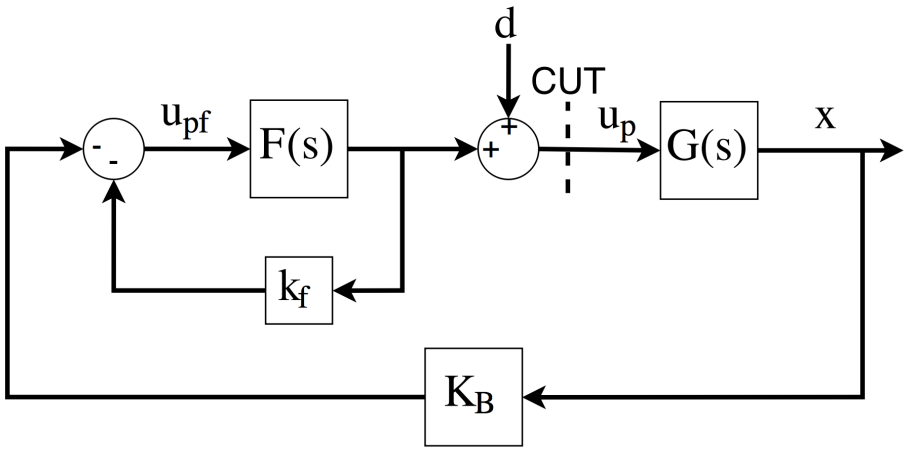


Figure 4.12: Schematic representation of the position control scheme with the low-pass filter and the disturbance signal.

$L(s)$ is then defined cutting the loop just before the plant $G(s)$ and it can be written as follow

$$L(s) = \frac{F(s)}{1 + k_f F(s)} K_B G(s) \tag{4.41}$$

where $F(s)$ is the transfer function of the low-pass filter. It is now necessary to identify an appropriate input and output in the diagram shown in Figure 4.12 in order

to obtain an expression of the transfer function equal to (4.40) with $L(s)$ defined as in (4.41). It has been found that the desired transfer function is obtained having as input and output d and u_p, respectively. Indeed, observing Figure 4.12 it is possible to write

$$u_p = \frac{1}{1 + \frac{F(s)}{1+k_f F(s)} K_B G(s)} d = \frac{1}{1 + L(s)} d \tag{4.42}$$

It is now possible to rewrite the state space formulation (4.37) to take into consideration the H_∞ problem:

$$\begin{cases} \dot{x} = Ax + B_1 d + B_2 u \\ z_2 = C_2 x + D_{22} u \\ z_\infty = C_1 x + D_{11} d \end{cases} \tag{4.43}$$

where $z_\infty = u_p$. Defining matrices C_1 and D_{11} in (4.43) as

$$C_1 = \begin{bmatrix} 1 & 0 & 0 & 0 \end{bmatrix}; D_{11} = 1 \tag{4.44}$$

the closed loop transfer function from d to z_∞ is equal to $S(s)$ defined in (4.40). It is now possible to set an upper bound to M_s during the optimal controller syntheses in order to increase the overall system robustness.

The calculation of the controller parameters can be obtained numerically by means the Matlab function "msfsyn". Indeed, "msfsyn" computes a state-feedback control (4.30) that minimizes the H_2 norm defined in (4.38) and that maintains the H_∞ norm of the transfer function from d to z_∞ (equal to $S(s)$ in (4.43)) below the prescribed value $\xi_0 > 0$.

4.5 Integration of MRC in the standard position control

In order to compensate the position oscillation, the relevant system state portion can be filtered by means of a dynamic system presenting high gain at the frequencies to be damped. A multi-frequency force disturbance causes a multi-frequency position oscillation, hence a set of dynamic systems, each of them designed to have high gain at a specific frequency, is required in this work. For this reason a set of filters is used, forming the MRC [120]. The state space equation of the n^{th} filter is

$$\begin{cases} \dot{x}_{r,n} = A_{r,n}x_{r,n} + B_{r,n}u_r \\ y_{r,n} = C_{r,n}x_{r,n} \end{cases} \tag{4.45}$$

where $x_{r,n}$ is the state vector and $A_{r,n}$, $B_{r,n}$, $C_{r,n}$ are defined as

$$A_{r,n} = \begin{bmatrix} 0 & 1 \\ -\omega_n^2 & 0 \end{bmatrix}; B_{r,n} = \begin{bmatrix} 0 \\ \omega_n^2 \end{bmatrix}; C_{r,n} = \begin{bmatrix} 1 & 0 \end{bmatrix} \tag{4.46}$$

with $\omega_n = 2\pi f_n$ the resonant pulsation.

In the proposed work the first 4 harmonics of the rotating pulsation are compensated. Hence, defining ω_m the rotating speed in [rad/s], the $n = 4$ resonant pulsations are: $\omega_1 = \omega_m$, $\omega_2 = 2\omega_1$, $\omega_3 = 3\omega_1$ and $\omega_4 = 4\omega_1$. Equation (4.47) shows the state space formulation of the MRC.

$$\begin{cases} \dot{x}_r = A_r x_r + B_r u_r \\ y_r = C_r x_r \end{cases} \tag{4.47}$$

where $A_r = \begin{bmatrix} A_{r,1} & \mathbf{0}_{2,2} & \mathbf{0}_{2,2} \\ \mathbf{0}_{2,2} & \ddots & \mathbf{0}_{2,2} \\ \mathbf{0}_{2,2} & \mathbf{0}_{2,2} & A_{r,4} \end{bmatrix}$, $B_r = \begin{bmatrix} B_{r,1} \\ \vdots \\ B_{r,4} \end{bmatrix}$ and $C_r = \begin{bmatrix} C_{r,1} & \mathbf{0}_{1,2} & \mathbf{0}_{1,2} \\ \mathbf{0}_{1,2} & \ddots & \mathbf{0}_{1,2} \\ \mathbf{0}_{1,2} & \mathbf{0}_{1,2} & C_{r,4} \end{bmatrix}$.

The output y_r can now be inserted in the cost function (4.31) obtaining

$$J_{LQR} = \int_0^\infty [x^T Q x + y_r^T Q_r y_r + u^T R u] dt = \int_0^\infty [x^T Q x + x_r^T C_r^T Q_r C_r x_r + u^T R u] dt \tag{4.48}$$

where Q_r is the state weight matrix of the MRC that will be defined in the next section. Defining the augmented state $\hat{x} = \begin{bmatrix} x & x_r \end{bmatrix}^T$, (4.48) becomes

$$J_{LQR} = \int_0^\infty [\hat{x}^T \hat{Q} \hat{x} + u^T R u] dt \tag{4.49}$$

where $\hat{Q} = \begin{bmatrix} Q & \mathbf{0}_{4,8} \\ \mathbf{0}_{8,4} & C_r^T Q_r C_r \end{bmatrix}$. (4.49) is the conventional LQR cost function for the augmented system

$$\dot{\hat{x}} = \hat{A}\hat{x} + \hat{B}_2 \hat{u} \tag{4.50}$$

$\hat{A}$ and $\hat{B}_2$ are defined as follow

$$\hat{A} = \begin{bmatrix} A & \mathbf{0}_{4,8} \\ W_r & A_r \end{bmatrix}; W_r = -B_r C; \hat{B}_2 = \begin{bmatrix} B_2 \\ \mathbf{0}_{8,1} \end{bmatrix} \tag{4.51}$$

System (4.50) is obtained merging systems (4.43) and (4.47) and assuming the rotor position as input of the MRC (4.47). Minimizing the cost function (4.49) results in a state feedback control law of the form

$$\hat{u} = -\hat{K}\hat{x} = -\begin{bmatrix} K & -K_r \end{bmatrix} \begin{bmatrix} x \\ x_r \end{bmatrix} \tag{4.52}$$

The resulting control structure is depicted in Figure 4.13.

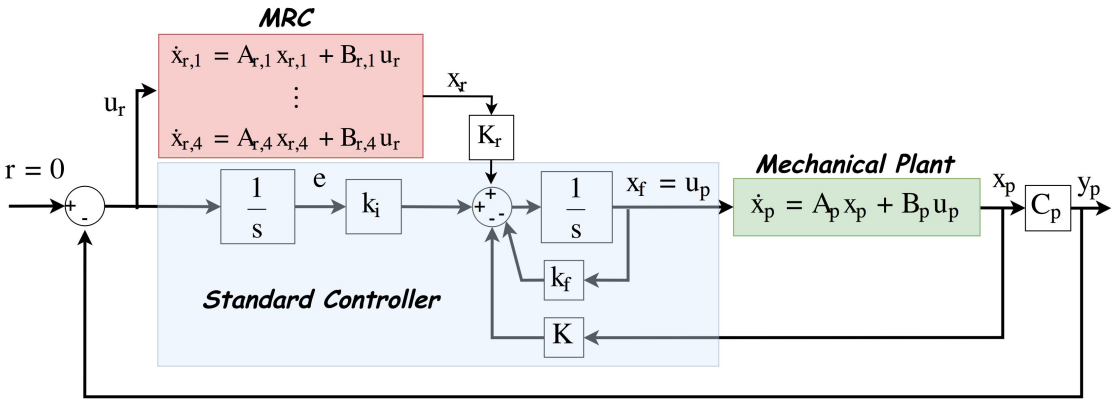


Figure 4.13: Block scheme of the MR position controller.

The presented controller has been designed to compensate 4 specific frequencies, however it is straightforward to customize (4.47) for any order n.

The synthesis of the optimal controller can be done following the formulation presented in the previous paragraph once matrices A and B_2 are replaced with $\hat{A}$ and $\hat{B}_2$ in (4.43). Furthermore, C_1, B_1, C_2 and D_{22} have to be re-written taking into account the considered MRC as follow

$$\hat{C}_1 = \begin{bmatrix} C_1 & \mathbf{0}_{1,8} \end{bmatrix}; \hat{B}_1 = \begin{bmatrix} B_1 \\ \mathbf{0}_{8,1} \end{bmatrix}; \hat{C}_2 = \begin{bmatrix} \sqrt{\hat{Q}} \\ \mathbf{0}_{1,12} \end{bmatrix}; \hat{D}_{22} = \begin{bmatrix} \mathbf{0}_{12,1} \\ \sqrt{R} \end{bmatrix} \tag{4.53}$$

while D_{11} remains unchanged.

4.6 Gain Calculation

4.6.1 Gain calculation in the whole frequency range

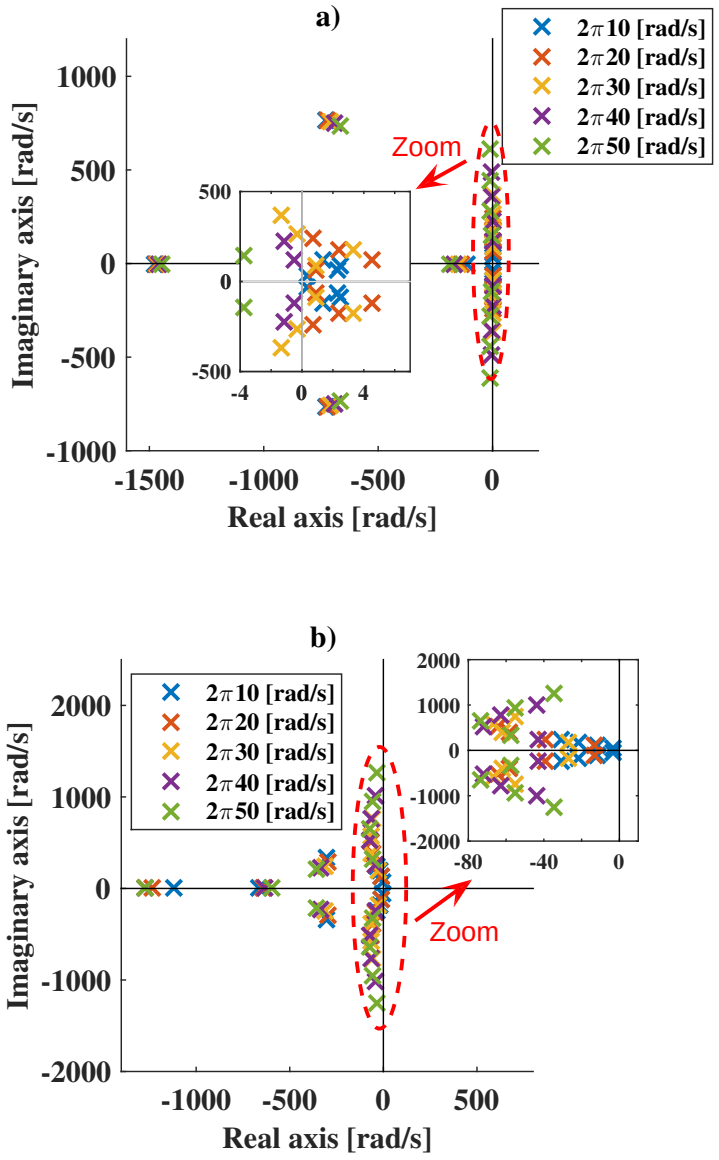


Figure 4.14: Poles map of the MRC controller: a) tuning with a single speed value; b) tuning with different speed values to cover the whole speed range.

Since the frequency of the disturbances to be compensated changes with the motor rotational speed, also the MR controller parameters will change accordingly. This makes the system time varying. Figure 4.14 a) shows how the closed loop poles move on the complex plane changing the rotational speed but keeping the controller gains constant. The latter have been calculated assuming $\omega_m = \omega_m^{max}$. It can be noticed that, for a certain speed range, some of the poles cross the imaginary axis making the system unstable. Therefore, the controller gains are calculated for ten different ω_m ranging from 0 to ω_{max}. A linear interpolation is then performed on-line in the controller to obtain the optimal gains in the whole speed range. Figure 4.14 b) shows that the closed loop poles stay in the left hand side of the complex plane for all the operating speed range considered.

The numerical values of the controllers gains as well as the weighting matrices will be reported in the next paragraph.

4.6.2 Numerical values of the controllers gains

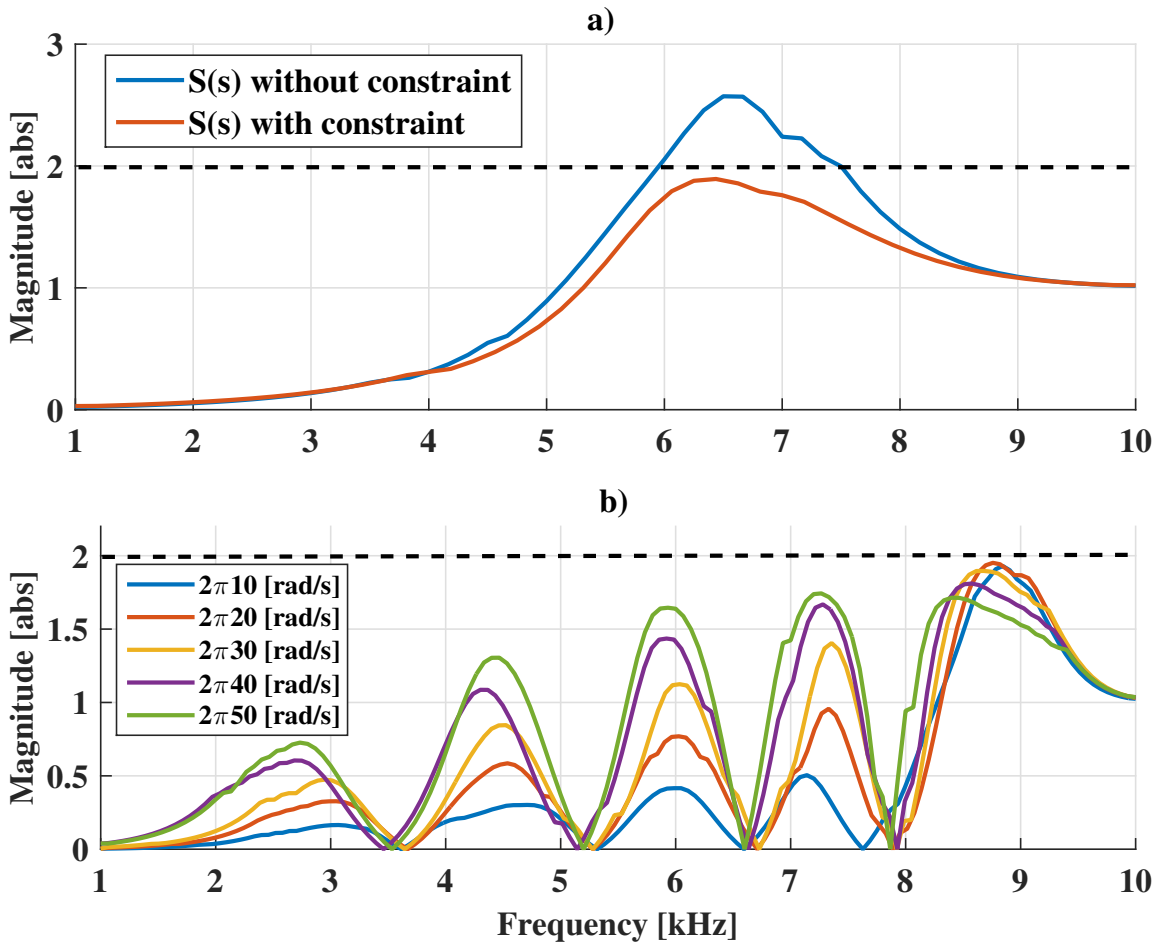


Figure 4.15: Sensitivity functions: a) standard controller; b) MRC in the whole speed range.

The feedback vector K_e of the standard controller can be obtained setting the weighting matrices Q and R. Their choice is the key problem in the design of optimal controllers with the LQR method and it is often based on the designer experience. Indeed, iterative and trial and error approaches are conventionally used to determine those values of Q and R that provide the desired system response. The same has been done for the considered position controller. In particular, both sides of (4.31)

have been divided by R, defined as a scalar quantity for this controller. The operation scales the cost function J_{LQR} but does not change its shape. Therefore, only the weights of matrix Q have to be defined. Increasing the integral weight produces a fast reference signal response while increasing the states weights produces the opposite effect, hence Q has been set equal to $diag(0, 0, 0, q_i)$. The integral weight q_i is chosen equal to $3e23$ in order to guarantee a good system dynamic.
In order to guarantee a good robustness, the sensitivity function is constrained setting the value ξ_0 equal to 2. The controller gains obtained are reported in Table 4.3. Figure 4.15 reports a comparison between the sensitivity function of the LQR controller described in section 4.3.2 and the constrained one (LMI method) described in section 4.4. As can be noted, in the second case, the sensitivity function does not exceed the setting value ξ_0 increasing the system robustness.
Figure 4.16 presents the closed loop poles of the standard controller obtained employing the LQR method and varying q_i from $3e17$ to $3e25$ showing that the poles tend asymptotically to the ones of a Butterworth filter of equal order. Furthermore, the poles obtained using the LMI method (setting $q_i = 3e23$) can be observed in the Figure. It can be noticed that the LMI method produces two real poles and one pair of complex conjugate ones while the LQR technique generates two pairs of complex conjugate poles.

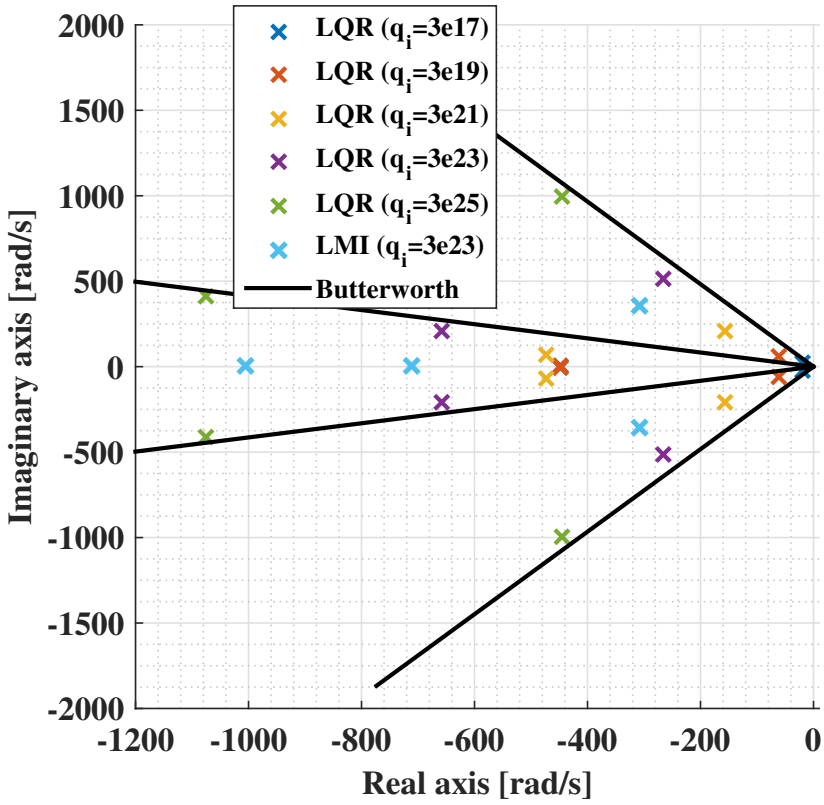


Figure 4.16: Poles map of the standard controller tuned with the LQR method for different values of q_i and with the LMI method with $q_i = 3e23$.

In the MRC considered in this work n is equal 4 hence the size of the feedback vector $\hat{K}$ is 12, where the first four elements correspond to K_e while the last eight are the resonant state vector gains. R and ξ_0 remain unchanged while $\hat{Q}$ has to be used as weighting matrix including Q, previously defined, and $Q_r = diag(10q_r, 8q_r, 6q_r, 4q_r)$ where q_r is set equal to $1e17$. The MR controller weights were chosen with a trial and error method in order to obtain a stable system and an effective rejection of the position oscillation for the four harmonics considered. Table 4.4 shows the gain values for the ten operating speeds considered, covering the whole frequency range. Furthermore, Figure 4.15 b) shows that the sensitivity function is maintained below ξ_0 for the all speed range.

Table 4.3: Standard Controller Gains

Gains	**Value**
k_f	2.33e3
k_p	4.48e9
k_d	7.66e6
k_i	5.48e11

Table 4.4: MR Controller Gains

Gains	$2\pi5$	$2\pi10$	$2\pi15$	$2\pi20$	$2\pi25$	$2\pi30$	$2\pi35$	$2\pi40$	$2\pi45$	$2\pi50$
k_f	2.39e3	2.53e3	2.67e3	2.81e3	2.9e3	2.96e3	3e3	3.02e3	3.02e3	3.03e3
k_p	4.81e9	5.67e9	6.71e9	7.63e9	8.31e9	8.76e9	9.01e9	9.12e9	9.09e9	9.01e9
k_d	0.80e7	0.90e7	1.01e7	1.12e7	1.19e7	1.24e7	1.28e7	1.3e7	1.31e7	1.31e7
k_i	5.5e11	5.5e11	5.5e11	5.5e11	5.5e11	5.5e11	5.5e11	5.5e11	5.6e11	5.5e11
${}^1k_{r,1}$	8.66e8	7.96e8	6.4e8	4.56e8	2.83e8	1.21e8	-0.28e8	-1.64e8	-2.87e8	-4e8
${}^2k_{r,1}$	8.85e6	8.86e6	8e6	6.99e6	6.04e6	5.23e6	4.52e6	3.91e6	3.37e6	2.9e6
${}^1k_{r,2}$	7.54e8	4.71e8	1.48e8	-1.35e8	-3.59e8	-5.34e8	-6.66e8	-7.64e8	-8.31e8	-8.71e8
${}^2k_{r,2}$	7.1e6	6e6	4.67e6	3.51e6	2.6e6	1.9e6	1.35e6	0.91e6	0.56e6	0.28e6
${}^1k_{r,3}$	6.41e8	3.4e8	-0.03e8	-2.97e8	-5.14e8	-6.58e8	-7.4e8	-7.7e8	-7.57e8	-7.15e8
${}^2k_{r,3}$	4.48e6	3.68e6	2.74e6	1.89e6	1.22e6	0.71e6	0.33e6	0.05e6	-0.16e6	-0.3e6
${}^1k_{r,4}$	5.82e8	4.01e8	0.87e8	-2.33e8	-4.66e8	-5.94e8	-6.3e8	-6.01e8	-5.31e8	-4.43e8
${}^2k_{r,4}$	1.88e6	1.94e6	1.66e6	1.17e6	0.68e6	0.28e6	-1.6e3	-0.19e6	-0.3e6	-0.35e6

Finally, Figure 4.17 shows the frequency response of the transfer function from force disturb to output for the standard and the MR position controller. It is straightforward to notice from the negative peaks at 50, 100, 150 and 200 Hz that the MR controller is able to completely reject the multi-frequency force disturbance.

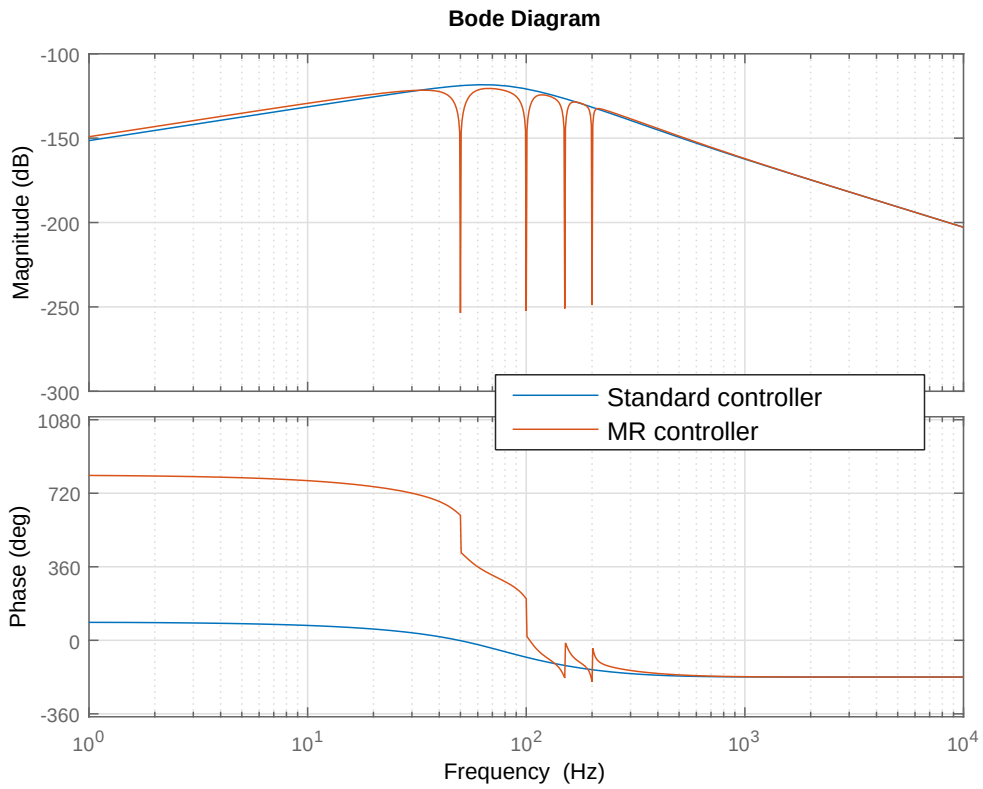


Figure 4.17: Bode diagram of the closed loop transfer function from disturb to output for standard controller and MR controller with $\omega_m = 50$ Hz.

4.7 Conclusions

In this Chapter the radial position control of the bearingless drive has been examined and different tuning approaches have been proposed. At first a transfer function-based method has been employed to place the closed loop system poles in the desired positions. Two possibilities have been investigated: coincident poles and Butterworth pole configuration. The latter has been chosen leading to the calculation of the controller gains.

Then, a state space approach has been used to syntheses the controller. The LQ optimal regulator method was at first chosen to compute the controller gains. It was explained that a low-pass filter was necessary in order to get good controller performance. The low-pass filter was included in the so called extended plant and a new state space formulation has been carried out. The robustness of the controller is affected by the presence of the filter, therefore the LMI theory has been applied to carry out the controller tuning. In particular, the LQR method has been reformulated in terms of H_2 optimal control limiting the peak value of the sensitivity function (H_∞ norm) in order to enhance the control robustness.

Finally, a MR controller was designed with the aim of rejecting the multi-frequency position oscillation caused by the periodic force disturbance. In fact, it will be shown in the experimental result Chapter that the latter remarkably affects the radial position control since the standard controller cannot perform a periodic disturbance rejection. The MRC has been designed with a state space approach allowing to treat the system as a whole. The H_2 optimal control theory together with the H_∞ norm constraint have being employed to guarantee an optimal and robust position controller.

In the last section, the numerical values of the standard and MR controllers gains designed in state space have been provided. The speed variation has been also taken into account for the MRC gains calculation in order to assure the system stability in the whole speed operating range.

Chapter 5

Simulation Results

5.1 Introduction

This Chapter presents the simulation results of the radial force and torque control and of the bearingless operations. In particular, the machine analytical model described in Chapter 3 is validated through FE simulations in the first part of this Chapter. As a matter of fact, the radial force and torque generation has been verified for the considered machine looking at three different case studies: healthy operating condition, open-circuit of one three-phase winding and rotor eccentricity (both static and dynamic). It will be demonstrated that the radial force and torque can be successfully controlled in all the above mentioned operating conditions. Furthermore, the presented force and torque control method is compared with the methods or strategies proposed in literature.

In the second part, the simulation results for bearingless operations are displayed. The overall control scheme of the bearingless drive is presented and the structure of the simulation model is depicted in the first part of the Chapter. The results obtained with the standard position controller designed with a pole placement method in 4.2

are then shown for both healthy and open-circuit operating conditions. Finally, a comparison between standard and MR controllers designed with a state space method in 4.3, 4.4 and 4.5 respectively is presented. Indeed, the MRC will result particularly effective for suppressing a multi-frequency force disturbance.

5.2 FE Simulation Results

The case study machine is modelled in the computational environment (MagNet) and FEA are performed in order to validate the predicted performances. Two-dimensional simulations are employed since the machine is assumed axially uniform. Furthermore, the complete motor section has been included in the FE model, therefore no boundary conditions have been imposed. Hereafter, all the FE simulations have been performed setting a non-linear solver in order to take into account the iron saturation and aligning the magnetic axis of sector 1 with the $x-$axis ($\gamma_0 = 0$) at $\vartheta_e = 0$.

5.2.1 Healthy operating condition and centred rotor

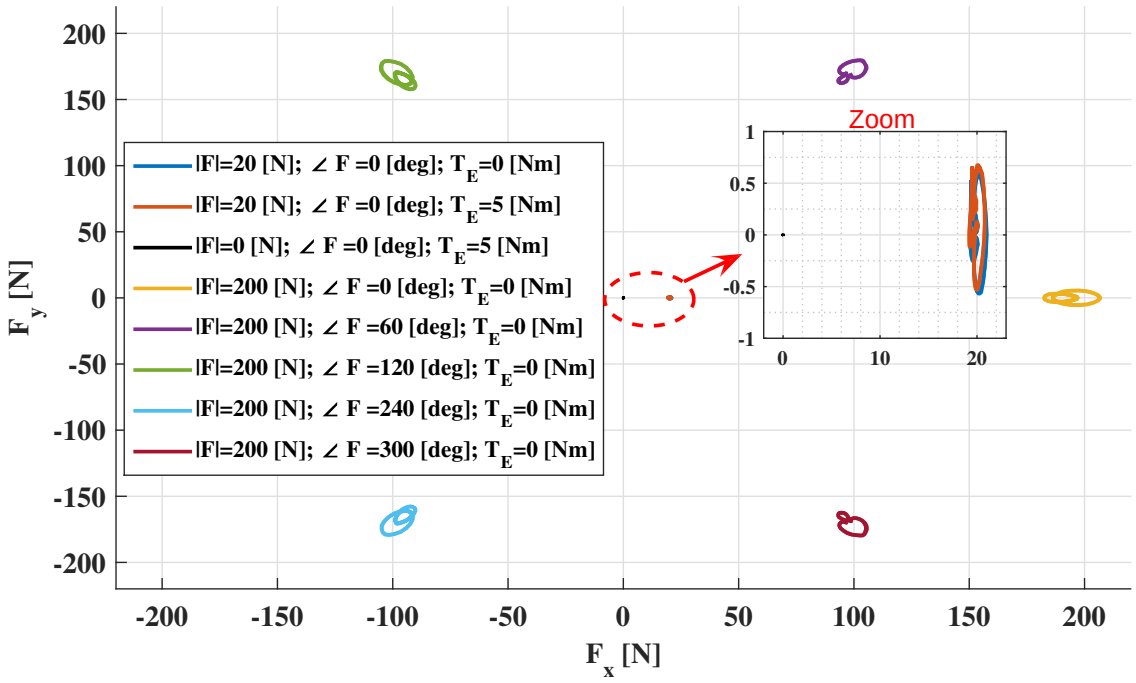


Figure 5.1: Force generation in healthy operating condition. Different force reference magnitudes $|F_E|$ and directions $\angle F_E$ are used. Zero and rated torque operating conditions are considered.

The FE simulation results for healthy operating conditions and centred rotor are illustrated in this paragraph. The reference currents to be supplied in the FE model of the motor are calculated with equation (3.60) once the mechanical reference vector $\bar{W}_E^*$ is defined. The displacement information δ in (3.60) is set equal to zero. The radial force production result can be appreciated in Figure 5.1. Each result shown in the picture has been obtained running a multi-static FE simulation varying ϑ_e from 0 to 2π (one electrical period) with steps of 1 deg.

Different force reference magnitudes $|F_E|$ and direction $\angle F_E$ have been considered as well as zero and rated torque operating conditions. Vector $\bar{W}_E^*$ is then computed as

$$\bar{W}_E^* = \begin{bmatrix} F_{E,x}^* \\ F_{E,y}^* \\ T_E^* \end{bmatrix} = \begin{bmatrix} |F_E|^* \cos(\angle F_E^*) \\ |F_E|^* \sin(\angle F_E^*) \\ T_E^* \end{bmatrix} \tag{5.1}$$

A maximum reference magnitude of 200 N was chosen to fulfil the machine current limit. It can be appreciated in the Figure how the radial forces can be effectively controlled in any desired direction with a small force ripple. The small dot that can be observed in (0,0) then, shows that no force is generated by the torque control.
The force generation results for $|F_E|^* = 20$ N (corresponding to the rotor weight force) at zero and rated torque (zoom detail in Figure 5.1) demonstrate that the force generation is very little affected by the torque generation. This can be further confirmed observing the $x - y$ axis force waveforms in Figure 5.2 and their Fast Fourier Transform (FFT) in Figure 5.3. Indeed, the harmonic content of the force components with and without force generation is almost identical.

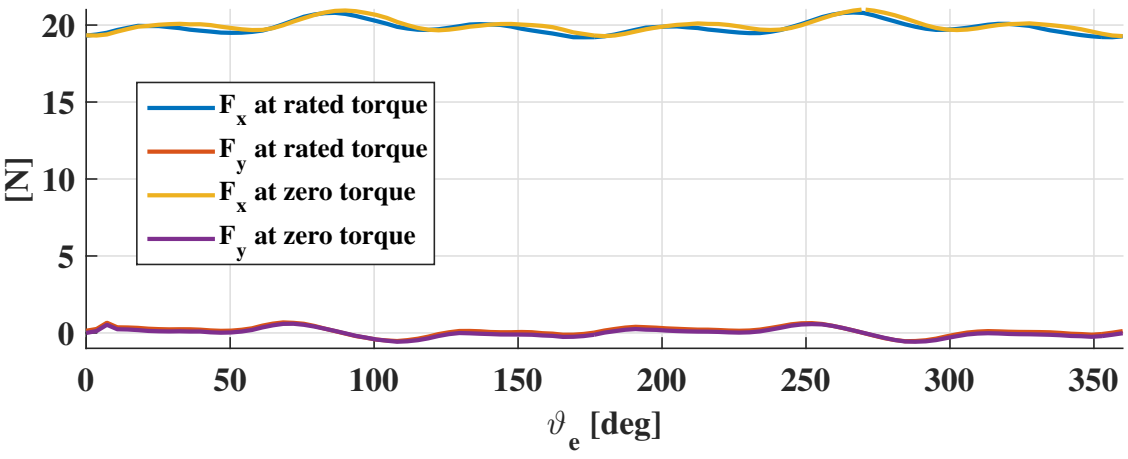


Figure 5.2: 20 N force generation at zero and at rated torque.

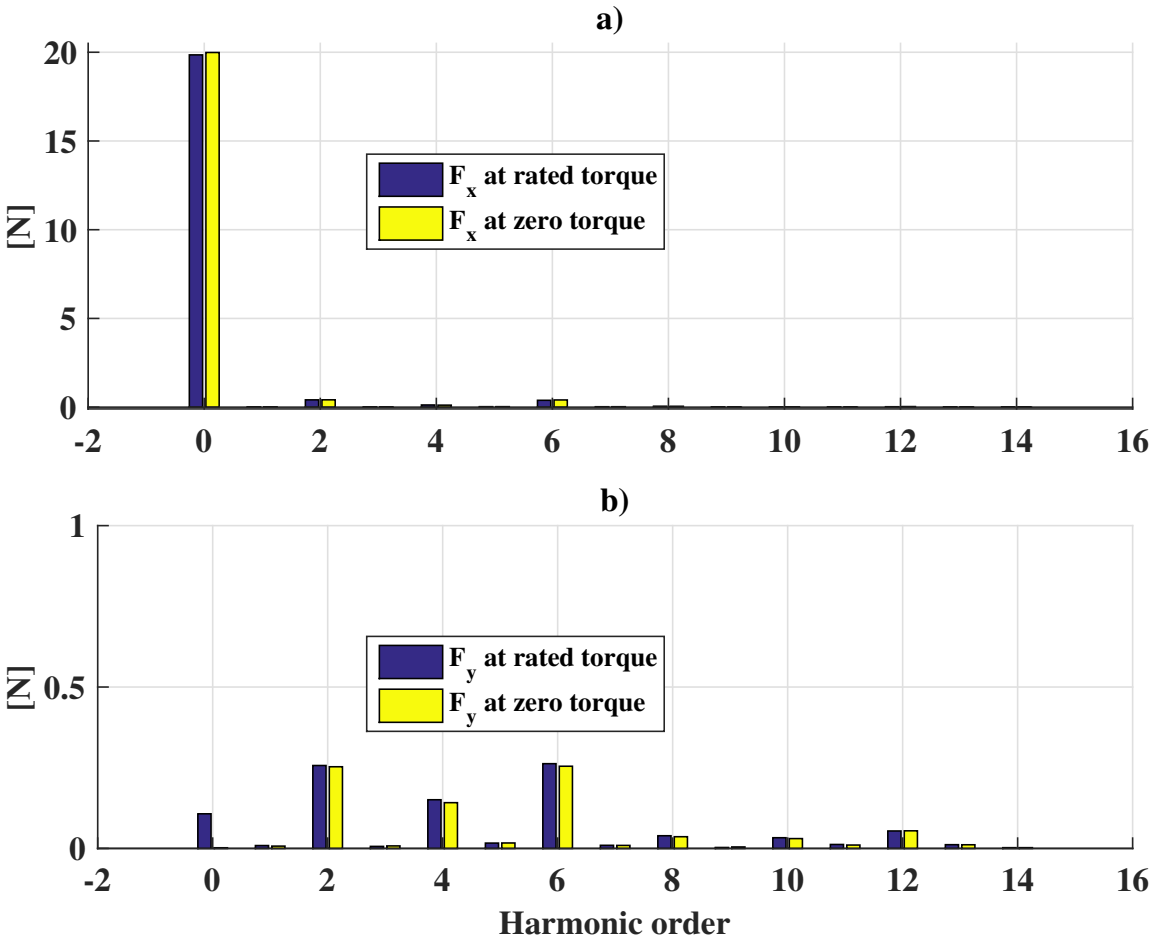


Figure 5.3: Harmonic content of F_x and F_y with and without torque production: a) FFT of F_x; b) FFT of F_y

Figure 5.4 shows the torque generation for zero and 20 N force production. It can be observed that the torque waveforms of both case studies result identical confirming the capability of the proposed control technique to produce radial force and torque simultaneously and without mutual interaction.

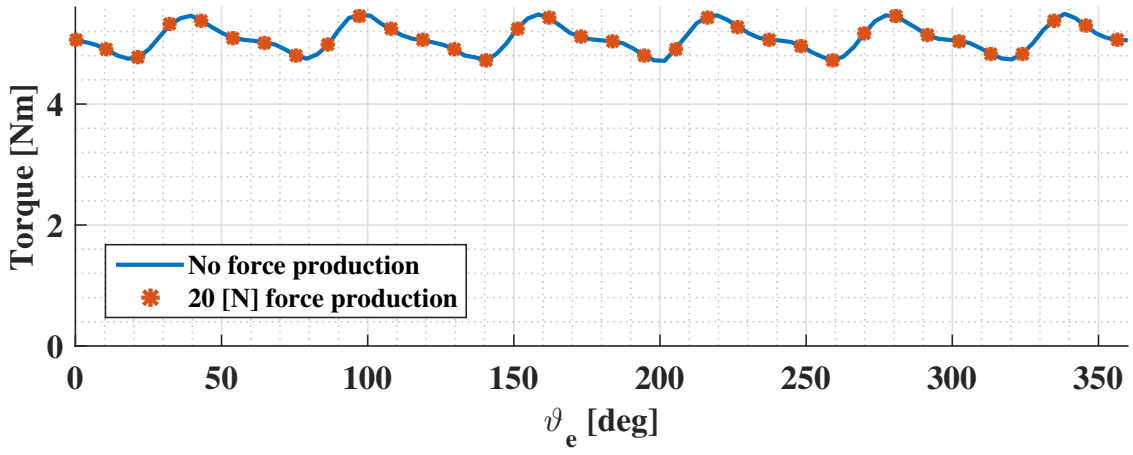


Figure 5.4: Torque generation in healthy operating condition for zero and 20 N force production.

Figure 5.5 shows the phase currents in each of the three-phase winding supplied in the FE machine model to generate 200 N in the $x-$axis direction without torque. It can be observed that the rated current (13 [A]) is needed to produce the desired force. Furthermore, it is interesting to notice that the resultant three-phase current pattern is unbalanced. This phenomena could be predicted observing the analytical expression of the $d-q$ axis reference currents presented in Appendix C. As a matter of fact, a significant sinusoidal component is found in their expressions producing asymmetric phase currents.

Finally, Figure 5.6 presents the machine nine phase currents supplied to the FE model in order to generate 20 N in the $x-$axis direction for zero (left hand side) and rated (right hand side) torque production. It can be appreciated how the current needed to suspend the rotor is just above 10% of the rated current. It is worth reminding that the machine considered is a conventional PM synchronous motor, hence its design was not optimized for the radial force production. Therefore, even better force capabilities could be obtained when the maximization of the radial force production is taken into account in the machine design stage.

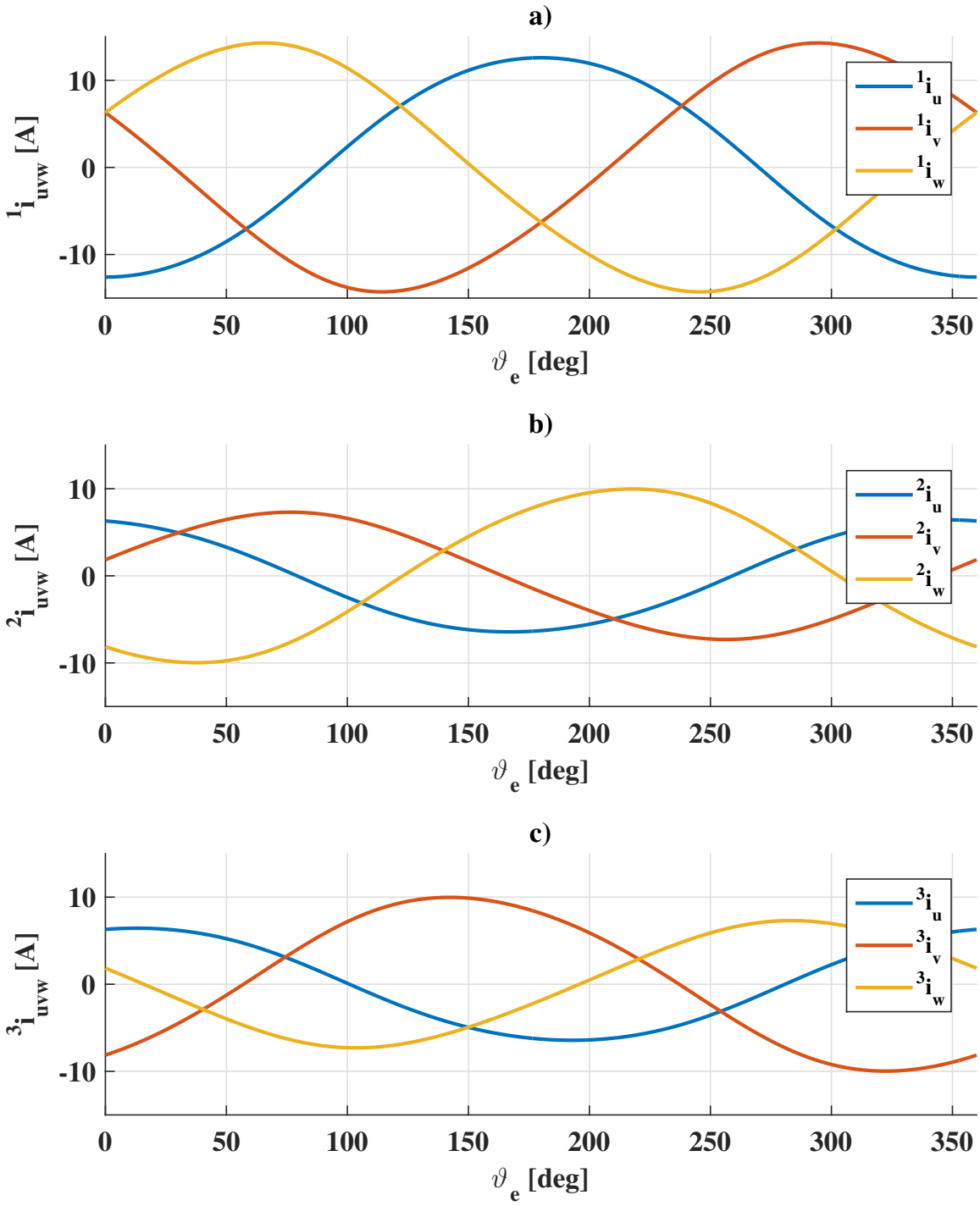


Figure 5.5: Phase current required to generate $|F_E| = 200$ N in the $\angle F_E = 0$ direction and $T_E = 0$: a) phase current of sector 1; b) phase current of sector 2; c) phase current of sector 3.

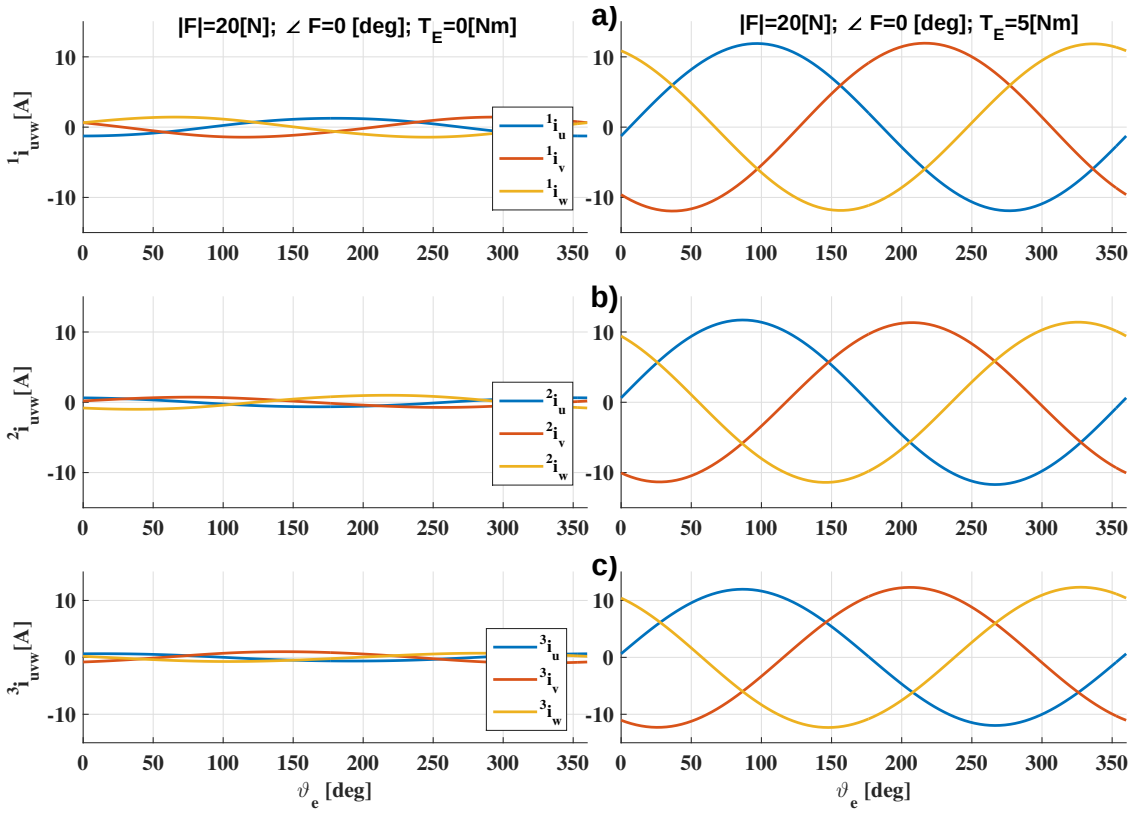


Figure 5.6: Phase current required to generate $|F_E| = 20$ N in the $\angle F_E = 0$ direction at $T_E = 0$ and $T_E = T_{rated}$: a) phase current of sector 1; b) phase current of sector 2; c) phase current of sector 3.

5.2.2 Open-circuit operating condition

In this paragraph the FE validation of the mathematical model written for open-circuit faults in sector 1, 2 and 3 is presented. The reference current necessary to produce the desired radial force and torque can be calculated according to paragraph 3.4.3.

Figures 5.7, 5.8 and 5.9 a)-b) show the force production for healthy and open-circuit fault in sector 1, 2 and 3 respectively considering two case studies: a) setting $T_E^* = 0$;

b) setting $T_E^* = 2.7[Nm]$.

In the simulations the rotor is rotated of two whole mechanical revolutions (720 deg), while the force reference magnitude $|F_E|^*$ is kept constant and the direction $\angle F_E^*$ varies from 0 to 360 deg with steps of 120 deg as it is possible to observe in the Figures. In order to satisfy the current limit of the machine the force reference magnitude $|F_E|^* = 100$ N is halved when torque is also produced.

It is possible to observe from Figures 5.7, 5.8 and 5.9 a) that the force ripple remains about the same when a fault occurs and no torque is produced. On the other hand, when torque is simultaneously generated the ripple slightly increases as depicted in Figures 5.7, 5.8 and 5.9 b). The above observations can be quantified in terms of Total Harmonic Distortion (THD) of the $x - y$ axis force components and summarized in table 5.1 for all the considered case studies. It is straightforward to see that the highest THD occurs for an open-circuit fault in sector 3 for $T_E = 2.7$ N. The THD obtained is 7.42 % which is only 3 % higher than the one obtained at no-load.

Finally, the torque generated during healthy and faulty conditions can be examined in Figures 5.7, 5.8 and 5.9 c) showing that the torque ripple is not significantly affected by the open-circuit faults.

Figure 5.10 shows the nine phase currents supplied to the FE model to generate the 100 N in the $x-$axis direction in the case of healthy operating condition (left hand side) and open-circuit fault in sector 1 (right hand side). Being the winding of sector 1 open-circuited, the related phase currents are zero as shown in the top right Figure. It can be notice that when the fault occurs the magnitude of the currents become greater and a third harmonic appears in their waveform. The latter can be observed in the harmonic spectrum of current i_{u2} represented in Figure 5.11. In particular, it is straightforward to notice that i_{u2} in case of fault presents a greater fundamental component and a remarkable third harmonic if compared with the harmonic content of the same phase current in healthy condition. The presence of the third harmonic was predicted in the open-circuit fault model described in 3.4.3 and in particular in Figure 3.16.

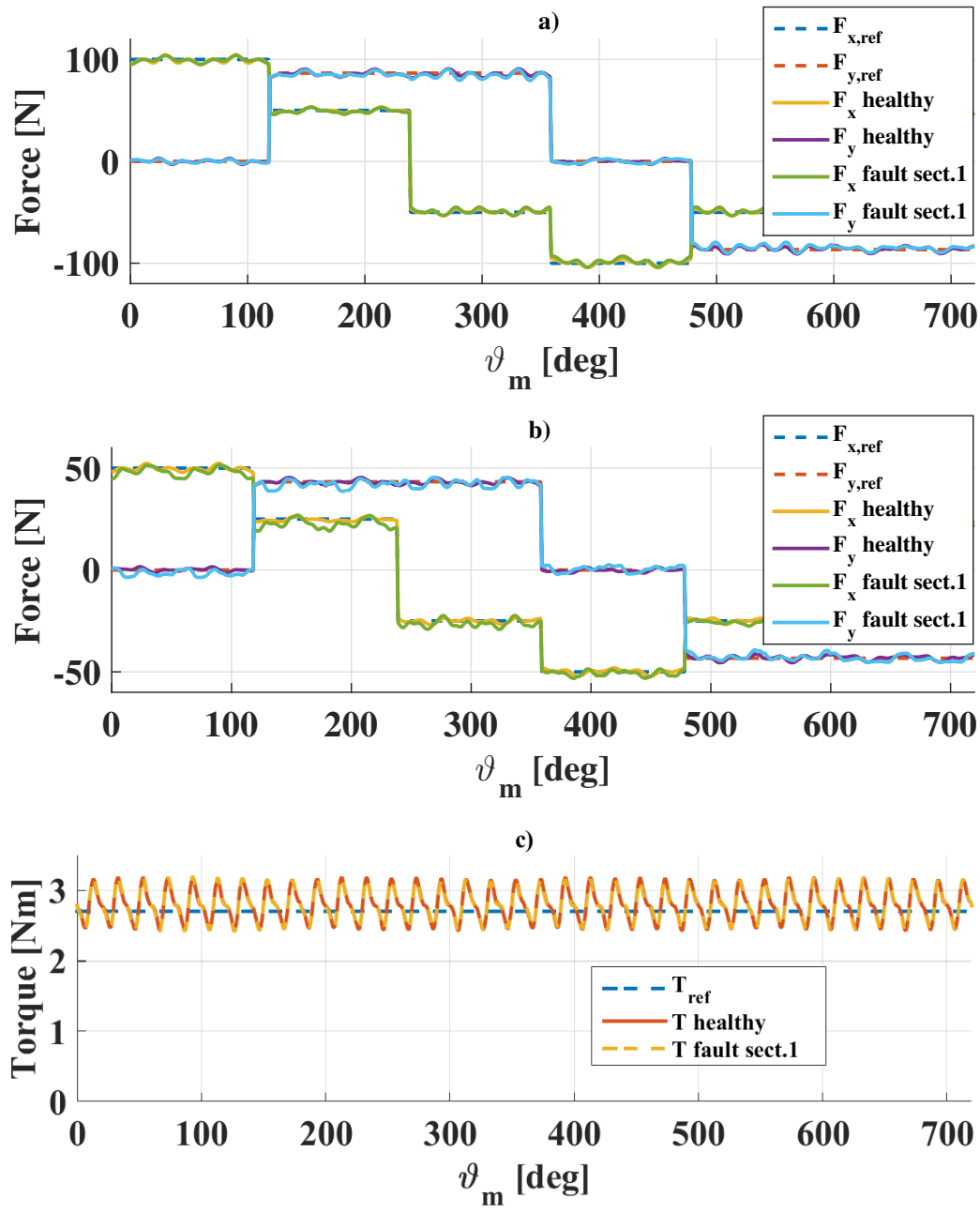


Figure 5.7: Force and torque generation with open-circuit fault in sector 1: a) $x-y$ axis force production for $T_{ref}=0$; b) $x-y$ axis force production for $T_{ref}=2.7[Nm]$; c) torque production setting $T_{ref}=2.7[Nm]$.

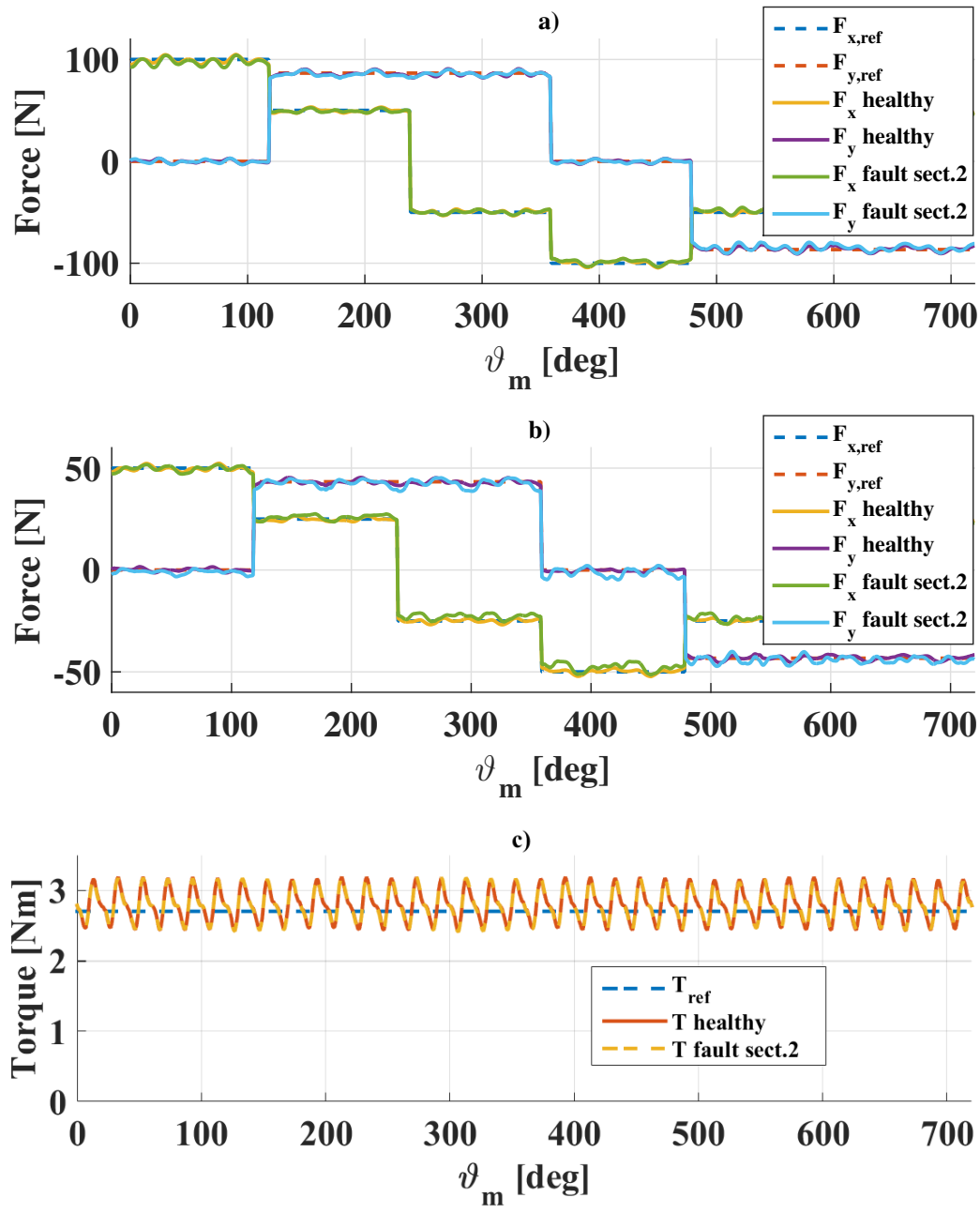


Figure 5.8: Force and torque generation with open-circuit fault in sector 2: a) $x-y$ axis force production for $T_{ref}=0$; b) $x-y$ axis force production for $T_{ref}=2.7[Nm]$; c) torque production setting $T_{ref}=2.7[Nm]$.

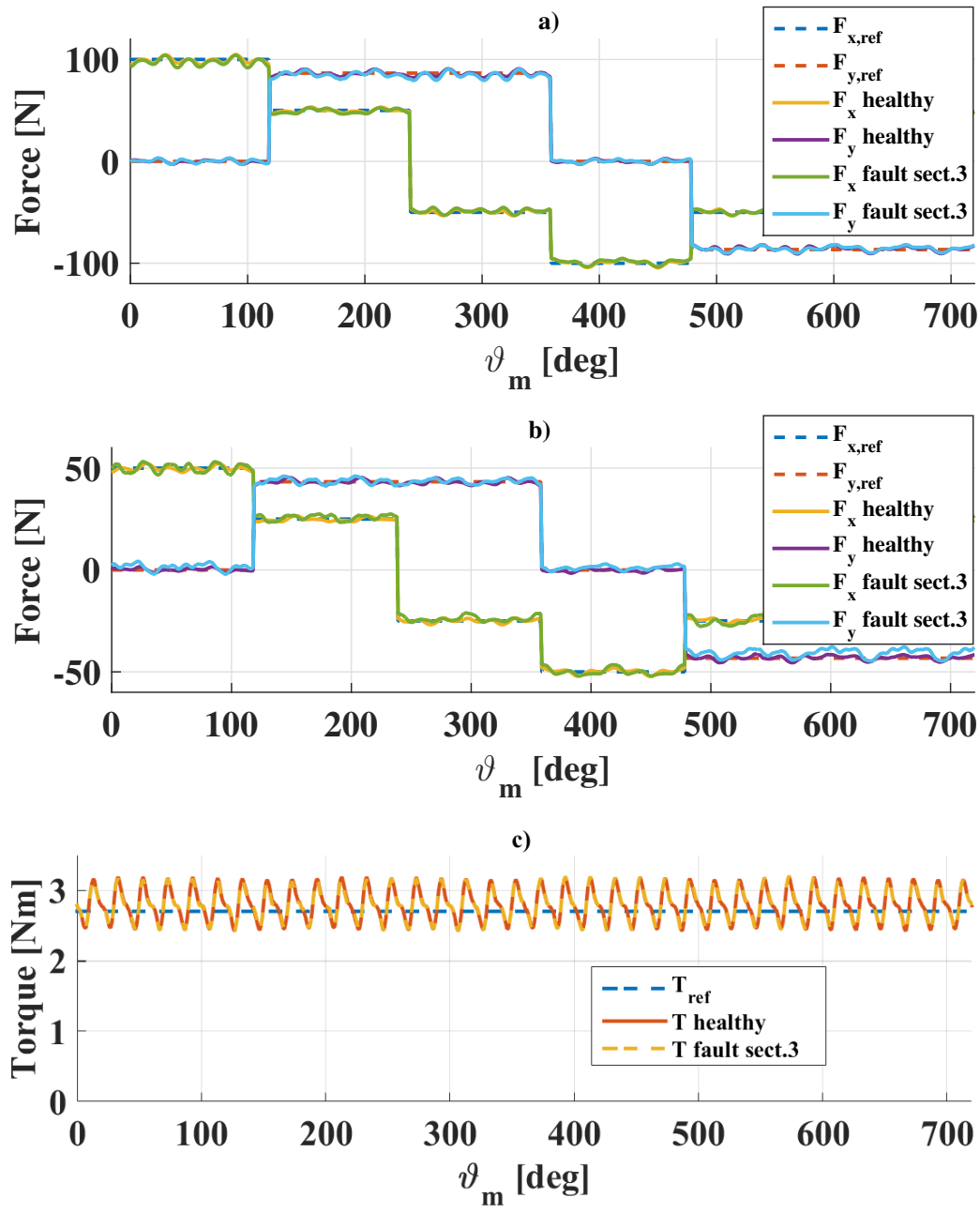


Figure 5.9: Force and torque generation with open-circuit fault in sector 3: a) $x-y$ axis force production for $T_{ref}=0$; b) $x-y$ axis force production for $T_{ref}=2.7[Nm]$; c) torque production setting $T_{ref}=2.7[Nm]$.

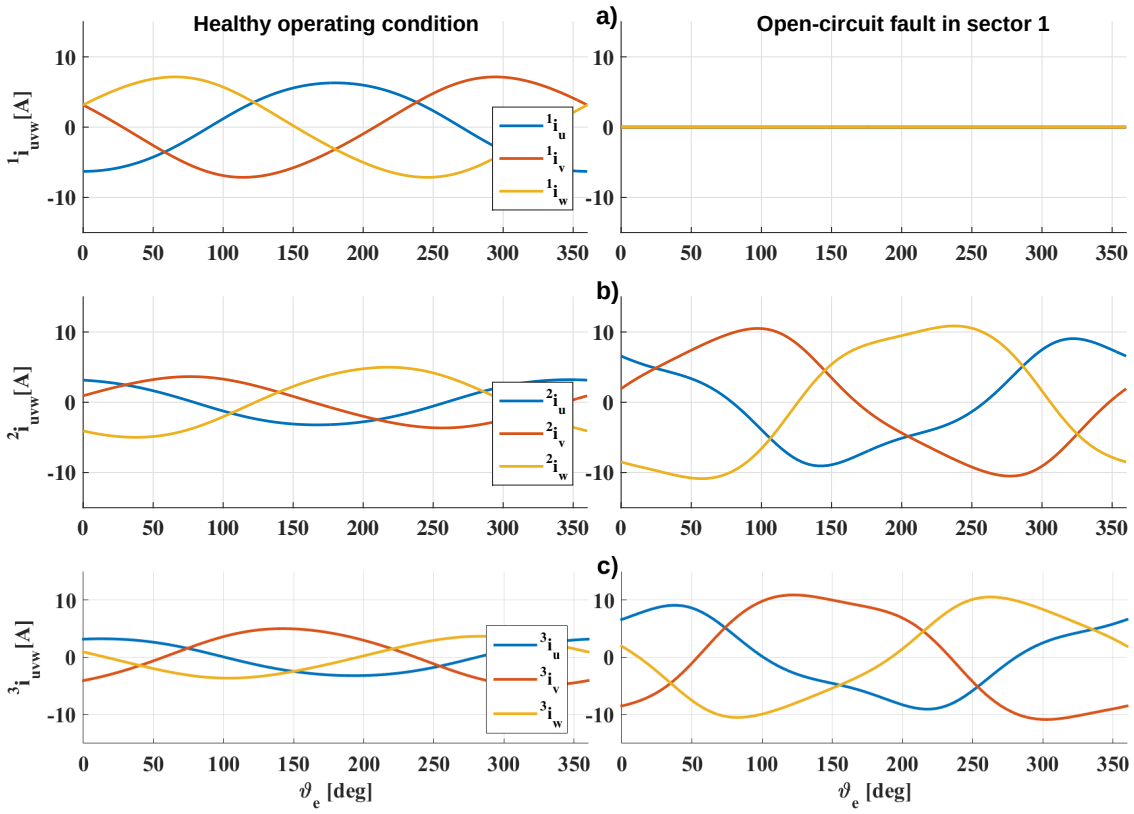


Figure 5.10: Phase current required to generate $|F_E| = 100$ N in the $\angle F_E = 0$ direction at $T_E = 0$ for healthy condition and open-circuit in sector 1: a) phase current of sector 1; b) phase current of sector 2; c) phase current of sector 3.

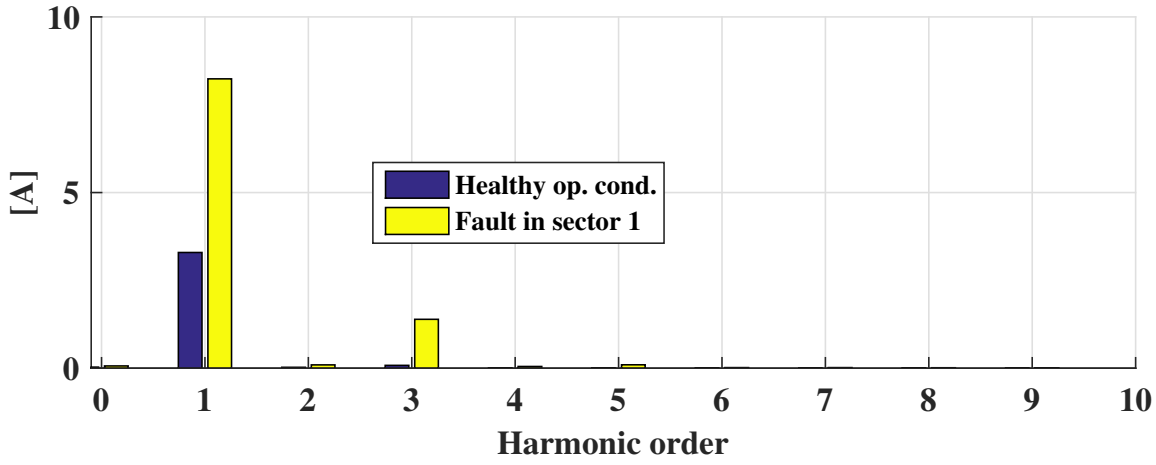


Figure 5.11: Harmonic content of the phase current i_{u2} in healthy condition and with fault in sector 1.

Table 5.1: THD of the force generation

	$T_E = 0Nm$				$T_E = 2.7Nm$			
	Healthy	Fault 1	Fault 2	Fault 3	Healthy	Fault 1	Fault 2	Fault 3
F_x	4.31	5.1	4.58	4.56	4.05	7.22	6.64	7.42
F_y	3.56	3.77	4.04	4.02	3.25	5.27	5.52	5.11

5.2.3 Eccentric rotor

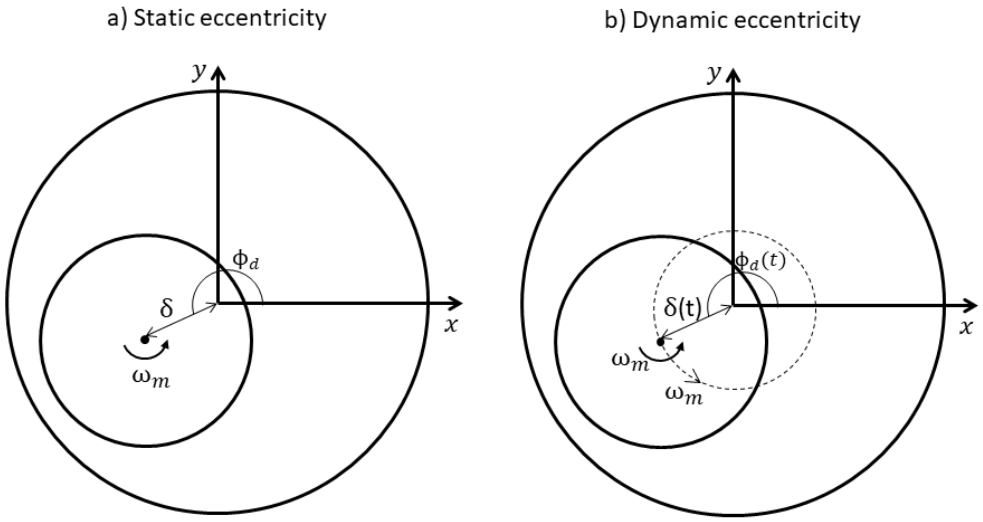


Figure 5.12: Difference between static and dynamic rotor eccentricity.

The expression of the force and torque production in the case of rotor displacement (or eccentricity) was described in paragraph 3.3.4. The rotor eccentricity can be either static or dynamic depending on whether the displacement between the rotor and stator centres is constant or whether it is moving (usually in an orbit of some description). Usually, in the dynamic eccentricity the off-centre axis of rotation spin along a circular path with the same speed of the rotor. Figure 5.12 shows the difference between static and dynamic eccentricity.

The static eccentricity can be caused by a not perfect rotor centring during the manufacturing process, a not accurate rotor balancing, bearing tolerances, stator ovality, by a misalignment introduced in the assembly process. Typical causes of dynamic eccentricity are also manufacturing tolerances and bearings wear.

The rotor eccentricity can result in a reduced lifetime of the machine due to bearings wear and additional mechanical stresses on the rotating components.

The next two paragraphs present the FE results relative to the analysis of force damping for static and dynamic eccentricity. The model described in 3.3.4 is used to

compensate the imbalanced forces generated by the rotor eccentricity.

5.2.3.1 Static eccentricity

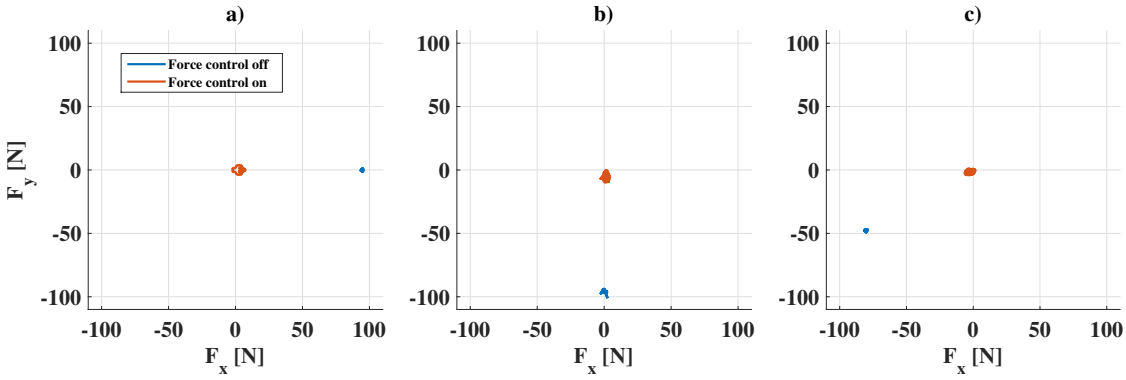


Figure 5.13: Force generation for static eccentricity with and without the force control: a) $\delta = 0.15$ mm, $\Phi_d = 0$ deg; b) $\delta = 0.15$ mm, $\Phi_d = 270$ deg; c) $\delta = 0.15$ mm, $\Phi_d = 150$ deg.

Figure 5.13 shows the force generated on the rotor element in case of static eccentricity. The rotor translation δ is fixed to its maximum value δ_{max} while the eccentricity angle Φ_d is equal to 0, 270 and 150 deg for Figure 5.13 a), b) and c), respectively. Each FE simulation has been performed rotating the rotor of one electrical period. It can be noticed that the eccentricity force magnitude is around 100 N and it changes its direction according to the eccentricity angle. Figures 5.13 a), b) and c) also report the results for force damping obtained adopting the proposed radial force control. In particular, the $x - y$ force reference components have been set to zero in order to reduce the stress of the bearing elements. The reference current necessary to achieve the force compensation are calculated with equation (3.60) taking into account the rotor displacement informations. It is straightforward to see from the Figures that the proposed force control method effectively suppress the big unbalanced forces in all the eccentricity conditions. The torque production in case of eccentricity was already presented in Figure 3.13 showing that the torque production is not significantly affected by the rotor displacement given that $\delta < \delta_{max}$.

5.2.3.2 Dynamic eccentricity

Figure 5.14 a) shows the $x-y$ components of the force caused by a dynamic eccentricity. Indeed, during FE simulation the rotor element, while spinning on its axis of one electrical period, moves along an orbit described in Cartesian coordinates as

$$\begin{aligned} x_r &= \delta_{max}\cos(\Phi_d) \\ y_r &= \delta_{max}\sin(\Phi_d) \end{aligned} \tag{5.2}$$

where Φ_d varies from 0 to 360 deg. It can be observed that, if the force control is deactivated, a rotating unbalanced force is generated. Therefore, it is desirable to suppress the latter in order to reduce the overall vibrations and avoid mechanical faults on the bearings. In the Figure, it can be appreciated how the force control technique suppresses the unbalanced rotating force. The reference current are still calculated with equation (3.60), where the angle Φ_d varies from 0 to 360 deg.
Figure 5.14 b) presents the torque production for dynamic eccentricity and it shows that the torque can be still controlled to a desired value (5 Nm in the picture).

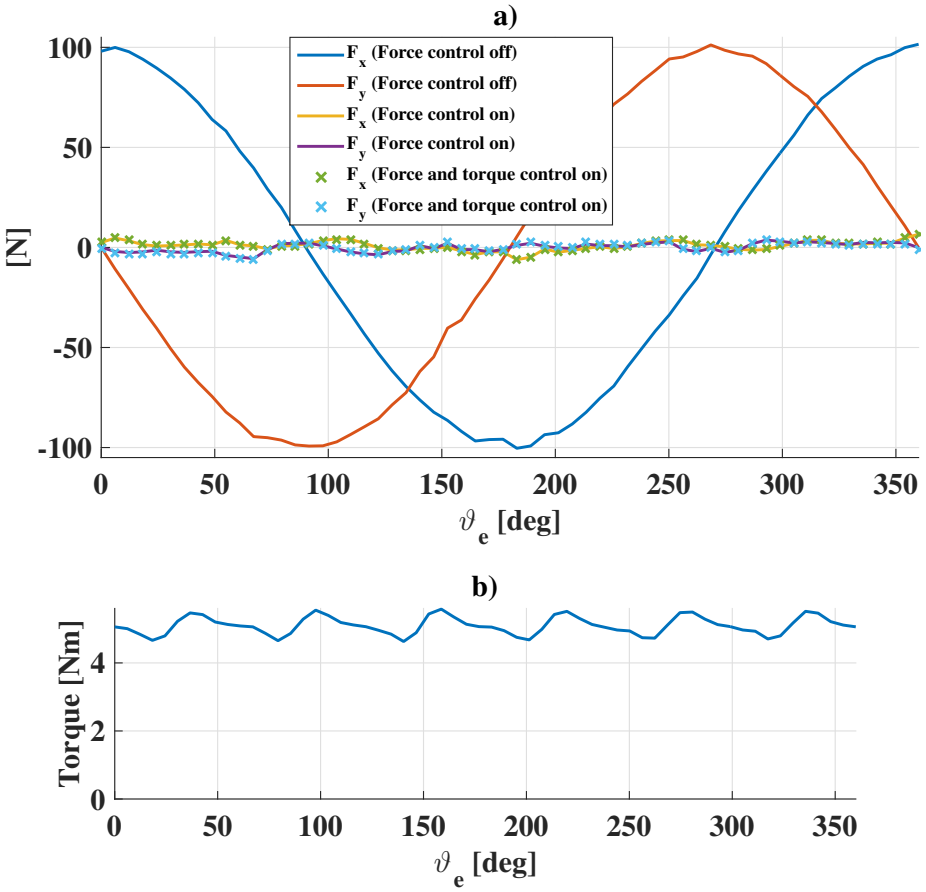


Figure 5.14: Force and torque generation for dynamic eccentricity with and without the force control: a) force generation; b) torque generation.

5.2.4 Comparison with different force and torque generation techniques

In this paragraph the performance and capabilities of the control strategy proposed are compared with the more conventional ones. The strategies compared are listed below:

- The force-torque decoupled (FTD).

- The FTD including the harmonic compensation technique (HFTD).
- The Pseudo Inverse matrix technique (PIM) presented in this thesis.

The FTD technique was described in 2.4.5. It consists of decoupling the force and torque production using only $d-$axis current to control the force (equation (2.19)) and $q-$axis current to control the torque (equation (2.18)). The force ripple resulting with the FTD technique can be compensated with an harmonic compensator (HFTD) as described in 2.4.5. Once the amplitude gain k_h and the direction angle error Φ_h are computed by means of FEA (Figure 5.15), the model relative to the HFTD technique can be written as in equation (2.21).

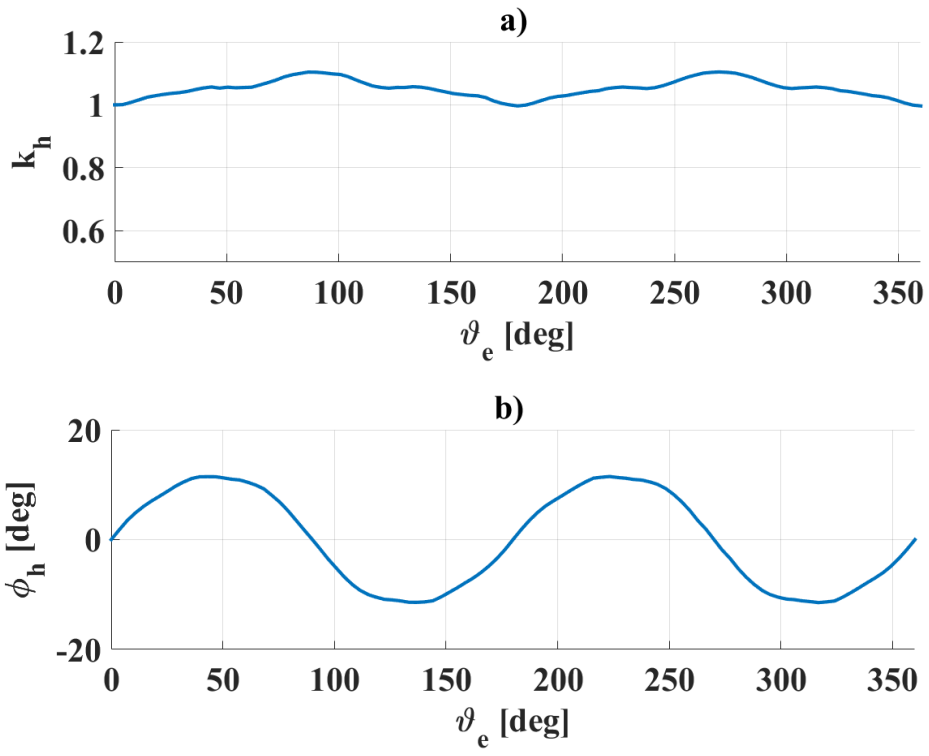


Figure 5.15: Amplitude gain k_h and direction angle error Φ_h: a) $k_h(\vartheta_e)$; b) $\Phi_h(\vartheta_e)$.

Figure 5.16 a) and b) present the resultant radial force produced by the three control strategies considered under no-load operating condition ($T_E = 0$). Figure 5.16 a) and

b) show the $x-y$ force components obtained commanding $|F_E| = 100$ N, $\angle F_E = 0$ deg and $|F_E| = 100$ N, $\angle F_E = 60$ deg as force references, respectively. It is straightforward to notice that both HFTD and PIM strategies perform an effective damping against the force ripple while generating the commanded radial force compared with the FDT technique. The results show that the proposed PIM technique achieves a constant force production without the adoption of a compensation stage or a lookup table, while relying only on analytical solutions that can be easily implemented.

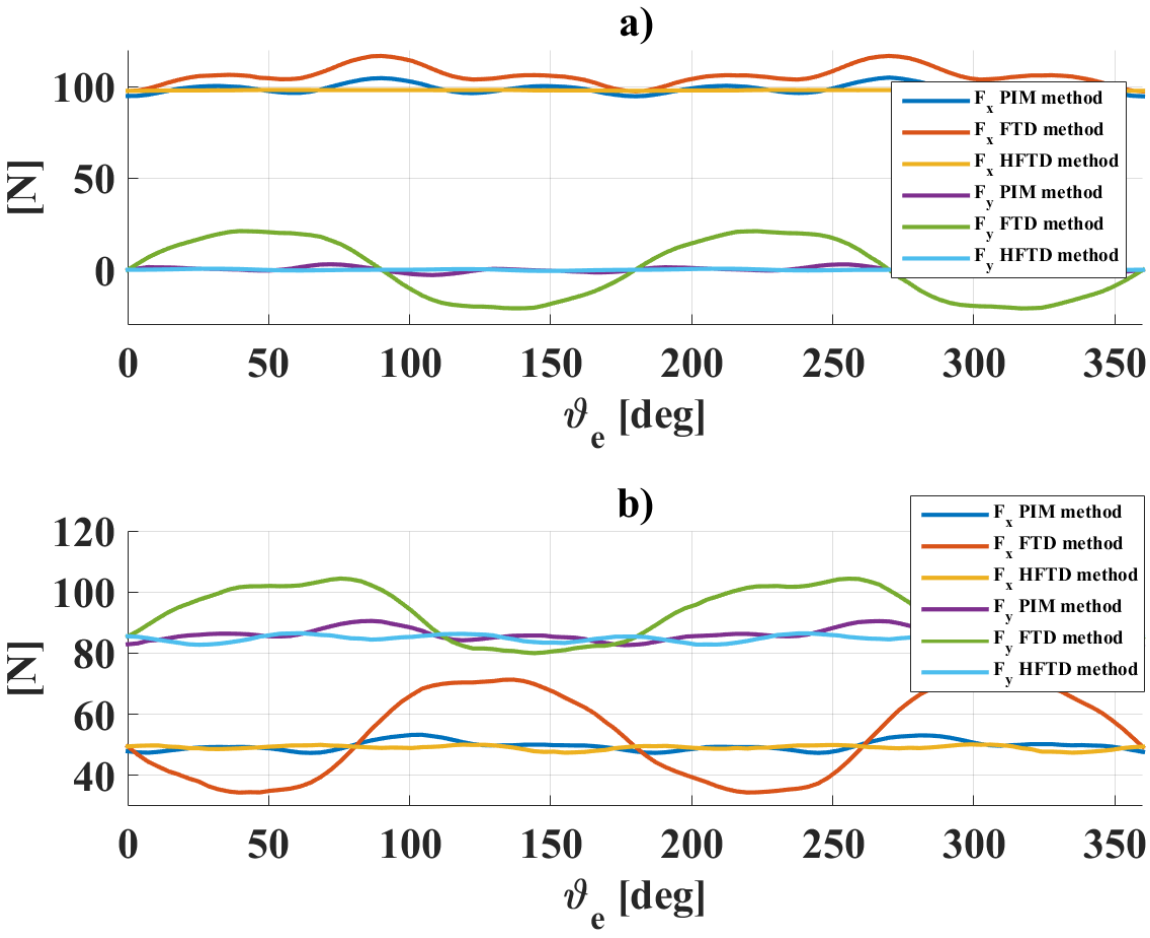


Figure 5.16: Comparison of the force generation with the PIM, FTD and HFTD methods: a) $|F_E| = 100$ N, $\angle(F) = 0$ deg ; b) $|F_E| = 100$ N, $\angle(F) = 60$ deg.

The effect of commanding $|F_E| = 20$ N, $\angle(F) = 0$ deg as force reference of the three techniques is presented in Figure 5.17 a) under rated load condition ($T_{ref} = 5$ Nm). The developed torque is presented in Figure 5.17 b). It can be noticed that the FTD technique still presents a remarkable force ripple while the torque trend of the three techniques is identical.

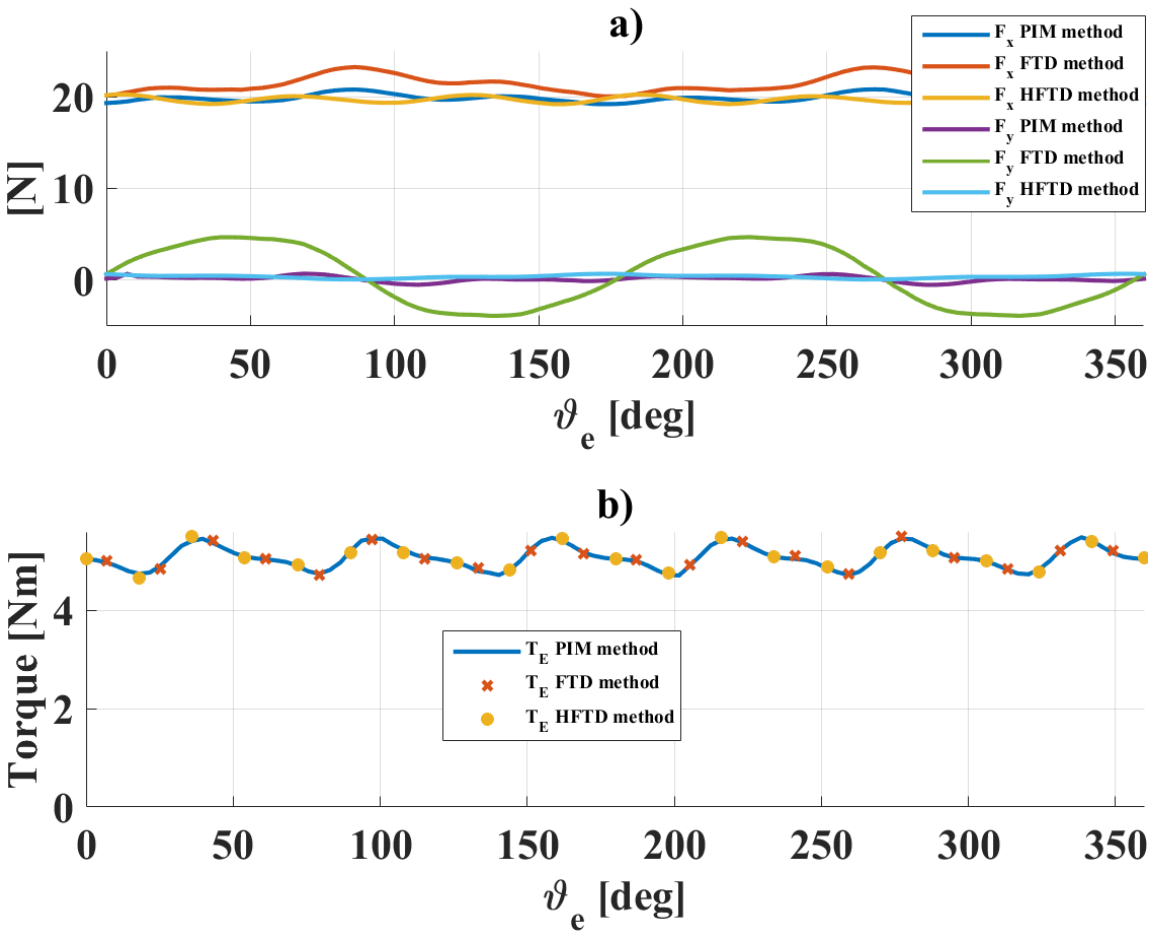


Figure 5.17: Comparison of the force and torque generation with the PIM, FTD and HFTD methods for $|F_E| = 20$ N, $\angle(F) = 0$ deg, $T_{ref} = 5$ Nm: a) force generation; b) torque generation.

The quality of the suspension force produced is appreciated observing the THD of

the magnitude $|F_E|$ and the maximum error of the force direction

$$\angle F_E = \frac{\left(\max\left(\angle F_E\right) - \left(\angle F_E\right)_{ref}\right)}{360} 100 \tag{5.3}$$

In Figure 5.18 the three techniques are compared using the aforementioned parameters. The operating condition reported in Figure 5.16 (no-load,$|F_E| = 100$ N, $\angle(F) = 0$ deg) has been selected for this analysis.

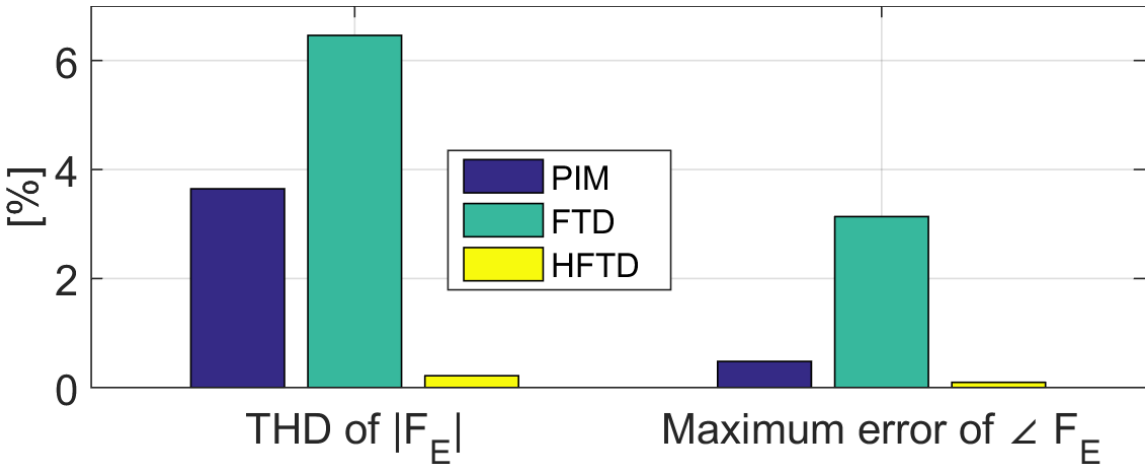


Figure 5.18: Comparison of the magnitude THD and phase error between the PIM, FTD and HFTD methods for $|F_E| = 100$ N, $\angle(F) = 0$ deg.

From the analysis performed, it can be noticed that both the HFTD and PIM enables to considerably reduce the magnitude THD and the maximum direction error with respect to the FTD. The HFDT technique presents the smallest THD in the force magnitude since it relies on a lookup table that enables to perform a point by point compensation. The PIM technique seats in between the FDT and HFDT control strategies in terms of overall THD while performing comparably with respect the HFTD method for what concerns the maximum error in the force phase angle. However, the lower on-line computational effort required adopting the proposed PIM technique results in a considerable advantage for what concerns direct implementa-

tion and generalization compared with HFTD. The influence of the torque production on the suspension force generation is also accounted in the PIM whereas the FDT technique requires the additional compensation technique (HFDT) to be evaluated. To summarize, the main features of the radial force control techniques under investigation are qualitatively compared in Table 5.2.

Table 5.2: Qualitative comparison

	PIM	**FTD**	**HFTD**
Force magnitude	+	+	+
Force quality	+	-	+
Efficiency	+	-	-
Computational simplicity	+	+	-

5.2.5 Joule losses calculation

In this paragraph the machine Joule losses calculation is considered for different operating conditions. The expression of the Joule losses is given by (3.53) where the phase resistance R_{ph} has a value of 0.23 Ohm, which has been experimentally identified (see section 6.3).

Figure 5.19 shows the computed Joule losses for rated torque operating conditions with and without force generation. In particular, a 20 N force magnitude has been set as reference value in order to simulate a bearingless operation. It can be noticed that the Joule losses generated for only torque production is a constant value due to the symmetrical distribution of the three-phase currents in the machine sectors. On the other hand, when the force is generated, an oscillation appears because of the asymmetrical three-phase current distribution. It is also interesting to observe that the Joule losses increment necessary to suspend the rotor is very little, only 0.76 %. This makes the bearingless machine an efficient device especially suitable for high speed application. In fact, the power losses of the ball bearing elements are

proportional to the rotational speed. An expression of the bearings power losses has being provided by the bearing manufacturer SKF and is reported as follow:

$$P_{loss,b} = 1.05 \times 10^{-4} Mn \tag{5.4}$$

where n is the rotational speed in [rpm] and M is the total frictional moment in [Nmm]. The latter is strongly affected by the bearing condition and the lubricant quality.

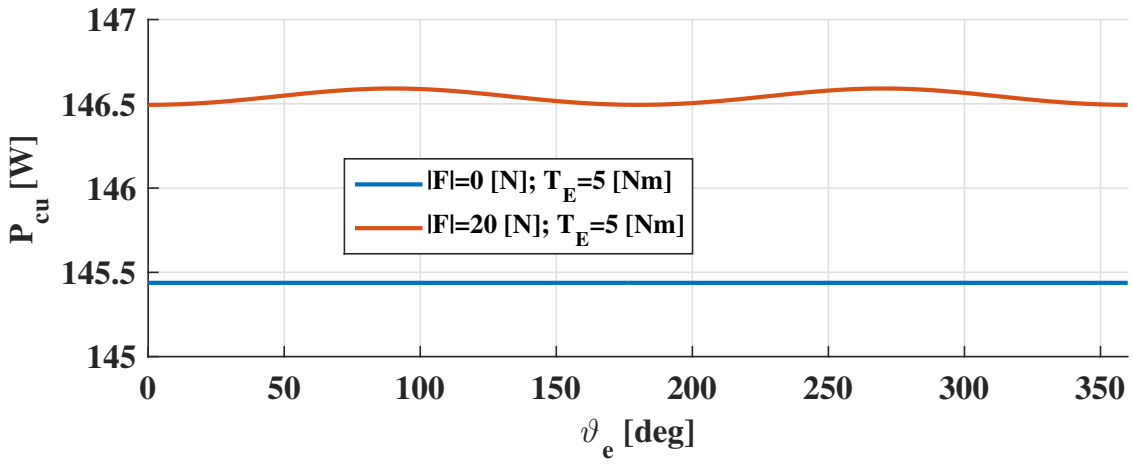


Figure 5.19: Joule losses at rated torque operating condition with and without the 20 N force generation for the PIM method.

Figure 5.20 shows the difference in Joule losses generation between healthy and open-circuit fault operating conditions. A force and torque production of 100 N and 0 Nm respectively are considered for the test. It can be observed that the Joule losses significantly increase if a fault occurs. However, it is worth reminding that faults are occasional events and a degradation of the machine performance and efficiency can be accepted. Indeed, the priority is to guarantee the essential drive functionality until it can be safely turned off in the shortest time possible.

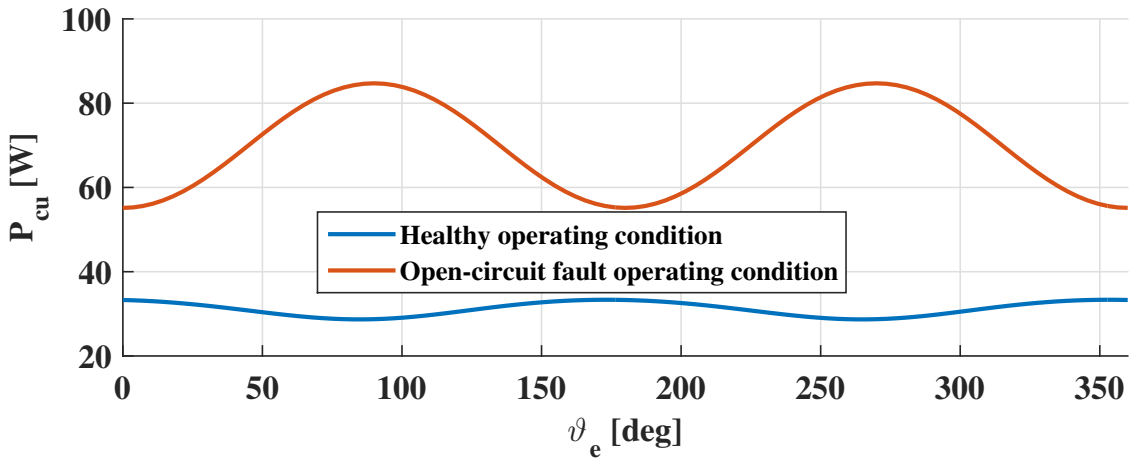


Figure 5.20: Joule losses at no-load with 100 N force generation for healthy and open-circuit fault operating conditions for the PIM method.

Figure 5.21 presents a comparison for the Joule losses generation between the three force control techniques presented in the previous paragraph. Same operating conditions are considered: no-load and 100 N force generation. It is straightforward to notice that the proposed method achieves the lowest average Joule losses generation.

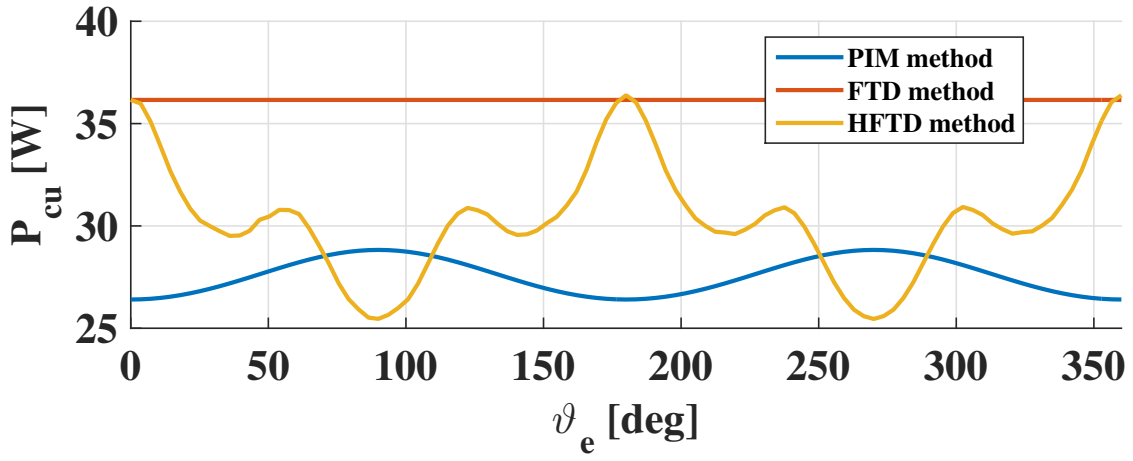


Figure 5.21: Joule losses at no-load with 100 N force generation for PIM, FTD and HFTD methods.

5.3 Numerical Simulation Results

5.3.1 Structure of the Simulation Model

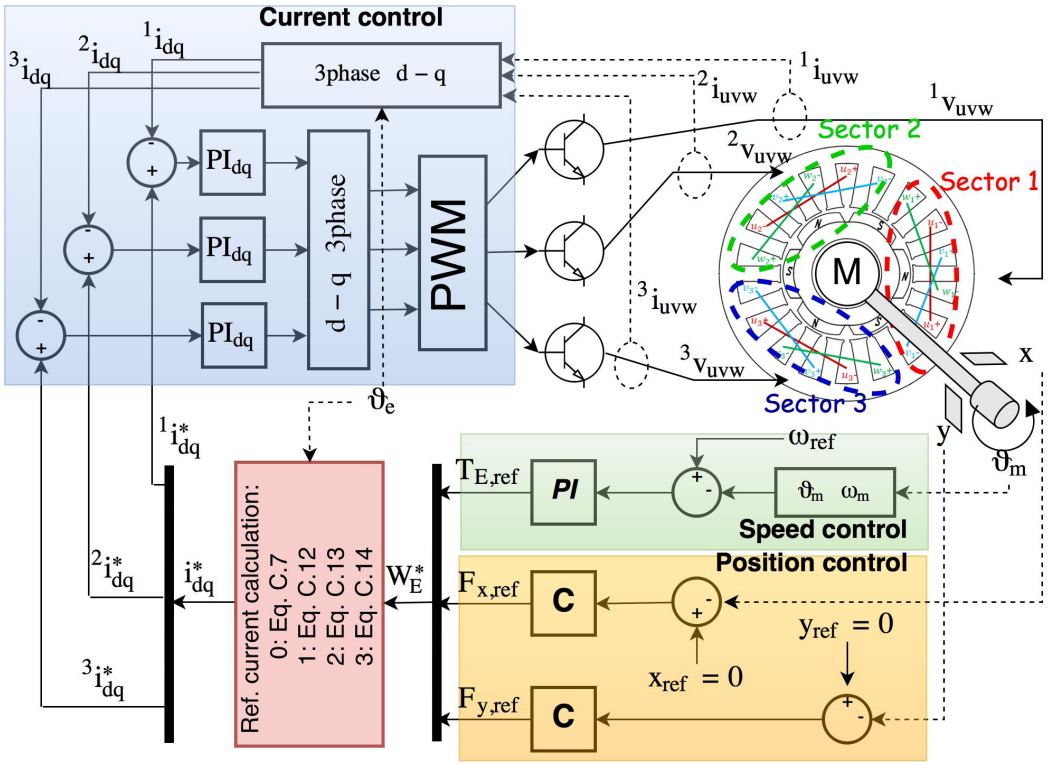


Figure 5.22: Overall control scheme of the bearingless MSPMSM.

The simulation results that are going to be presented were obtained in the Matlab-Simulink environment.

A simulation model has been built following the control scheme shown in Figure 5.22. In the Figure it is possible to identify the $x-y$ position controller designed in the previous Chapter and a standard PI controller for the speed loop. Their outputs are the reference force components $F_{x,ref}$, $F_{y,ref}$ and the reference torque $T_{E,ref}$. The three quantities compose the vector $\bar{W}_E^*$ of the mechanical references that, together with the angular position ϑ_e, is the input of the mathematical model. A fault selector

has been included in the latter allowing to switch from healthy operating condition to open-circuit fault in sector 1, 2 or 3 depending on its input. As a matter of fact, the $d-q$ axis reference currents needed in healthy operating condition are obtained with equation (C.4) while the ones needed in case of open-circuit fault in sector 1, 2 and 3 are calculated with equations (C.9), (C.10) and (C.11). The fault selector logic can be represented as follow:

- $0 \longrightarrow$ healthy operating condition.
- $1 \longrightarrow$ open-circuit fault in sector 1.
- $2 \longrightarrow$ open-circuit fault in sector 2.
- $3 \longrightarrow$ open-circuit fault in sector 3.

The $d-q$ axis current references can then be used in the six $d-q$ axis PI regulators. The current regulators outputs are the $d-q$ axis voltages of the three sectors (six quantities in total) that are transformed by means of the inverse nine-phase Park transformation matrix (3.6) into the three three-phase voltages. The latter compose the phase voltage vector $\bar{v}$ that is used to calculate the machine phase current vector $\bar{i}$ exploiting the analytical model described in (3.2).
The truthfulness of the analytical model can be appreciated from Figure 5.23 where the analytical phase currents are compared with the ones obtained with transient-with-motion FE simulations. In particular, three different operating conditions have been considered for the comparison: stand still operation with DC voltage supply (Figure 5.23 a)); stand still operation with sinusoidal (50 Hz) voltage supply Figure 5.23 b)); 1000 [rpm] operating speed with sinusoidal (50 Hz) voltage supply Figure 5.23 c)).

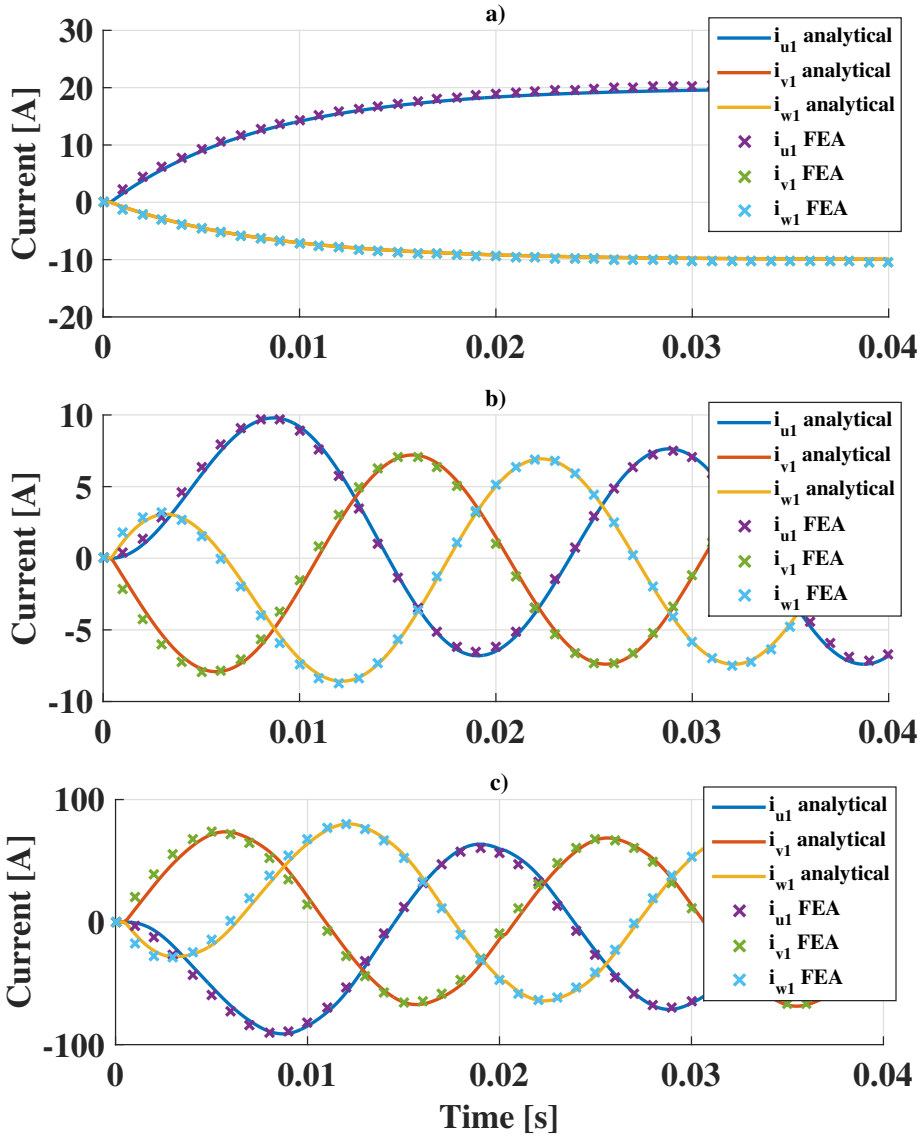


Figure 5.23: Comparison of the current waveforms obtained with the analytical and FE models: a) stand still operation and DC voltage supply of the three sectors: $v_u = 1$ *V,* $v_v = -0.5$ *V,* $v_w = -0.5$ *V; b) stand still operation and sinusoidal voltage supply of the three sectors:* $v_u = \cos(2\pi 50t)$ *V,* $v_v = -\frac{1}{2}\cos(2\pi 50t - \frac{2\pi}{3})$ *V,* $v_w = -\frac{1}{2}\cos(2\pi 50t - \frac{4\pi}{3})$ *V; c) 1000 [rpm] operating speed and sinusoidal voltage supply of the three sectors:* $v_u = \cos(2\pi 50t)$ *V,* $v_v = -\frac{1}{2}\cos(2\pi 50t - \frac{2\pi}{3})$ *V,* $v_w = -\frac{1}{2}\cos(2\pi 50t - \frac{4\pi}{3})$ *V.*

The resultant nine phase current signals are used in the simulation model as feedbacks for the current controllers. Furthermore, the current signals feed the electro-mechanical model of the machine, stored in the form of lookup table. The latter provides the machine mechanical outputs such as overall $x-y$ axis force components and torque having as input the $2n_s$ $d-q$ axis currents. The lookup table has been carried out by mean "multi-static" non-linear FE simulations to take into account the iron saturation. In particular, for each angular rotor position the FE model of the motor has been fed with $d-$ axis and $q-$ axis currents ranging between $-I_{rated}$ and I_{rated} with steps of 1 A. Then, the matrix obtained has been imported in the Matlab-Simulink model where a linear method has been employed for the interpolation of the lookup table elements. Finally, the $x-y$ axis force components feed the rotor-dynamic model of the motor written in form of state space system in (4.13).
The position, the speed and the current controllers are implemented in the simulation in a discrete form, choosing as sample time value $T_s = 100[\mu s]$ while the electro-mechanical model (lookup table) and the electrical model of the phase voltage equation are simulated in the continuous domain.

5.3.2 2-DOF levitation the standard controller designed with the transfer function-based method

The simulation results presented in this paragraph are carried out employing the position controller designed in 4.2.2. In the first part, the bearingless drive operates in healthy condition while in the second one the open-circuit faults in the three sectors are simulated.

5.3.2.1 Healthy operating condition

The fault selector input is set equal to 0 to examine the healthy operating condition. The simulation time considered is 0.5 s. The results shown are: $x-y$ rotor position and force in Figure 5.24, rotating speed and torque in Figure 5.25 and $d-q$ axis currents supplied to the three motor sectors in Figure 5.26.

At $t = 0$ s the position controller is activated and the rotor is brought from its resting position ([0,$-\delta_{max}$]) to the stator centre ([0,0]) after a short transient as depicted in Figure 5.24 a). Figure 5.24 b) shows the correspondent $x-y$ axis force initial transient. It can be observed that only $y-$axis force is necessary to suspend the rotor and that its steady state value is equal to the rotor weight force (20 N). The resultant $d-q$ axis currents are shown in Figure 5.26. It can be noticed that the main contribution to the start up force generation is provided by the $d-$axis currents of sector 2 and 3 and in a smaller amount by the $q-$axis current of the three sectors. After the initial position transient is over, the rotor is accelerated to its rated speed as shown in Figure 5.25 a). The speed control requires a torque step of around 6 Nm (Figure 5.25 b)) and consequently a step in the $q-$axis currents of the three sectors (Figures 5.26 a), b) and c)).

At 0.05 s a constant force disturb $F_d = 110$ N is applied in the negative $y-$axis direction for 0.02 s. It can be observed that the position controller is capable of maintaining the rotor centred after a short position transient. At 0.1 s another force disturbance of magnitude 200 N is applied for 0.03 s causing the rotor to drop on the backup bearing. As a matter of fact, the total force necessary to suspend the rotor is now $F_d + mg = 220$ N exceeding the machine force capability. The rotor is again suspended as soon as the force disturbance is removed. In Figure 5.26, it can be appreciated how the $d-q$ axis currents of the three sectors change according to the required suspension force.

Finally, a load torque of 5 Nm is commanded as a step at 0.25 s causing the rotation speed to slightly drop before the speed control manages to bring it to the reference value. Consequently, the $q-$axis currents demand of the three sectors is remarkably

increased due to the torque production as can be seen in Figure 5.26. It is interesting to notice in Figure 5.24 a) that the rotor radial is not significantly affected by the torque generation.

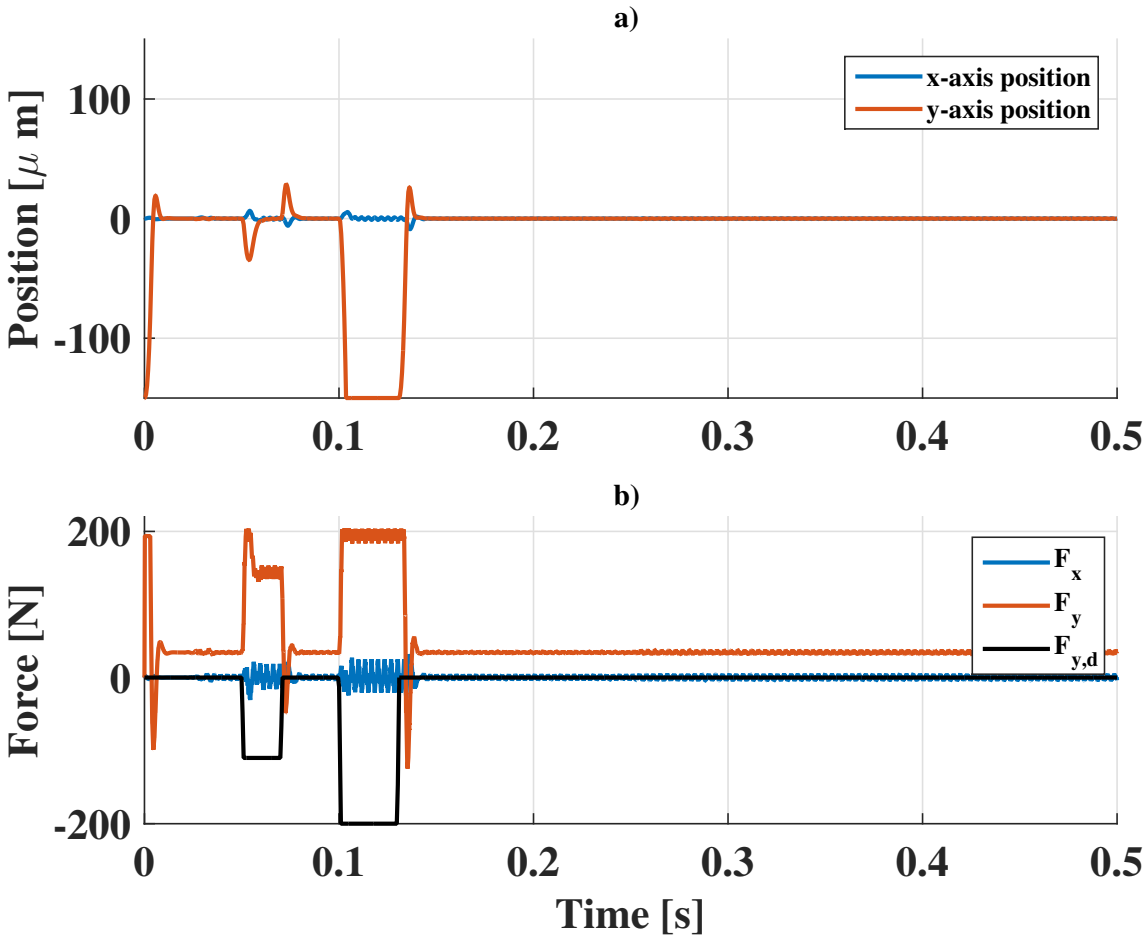


Figure 5.24: Result of the numerical simulation for bearingless operation in healthy condition: a) $x-y$ axis rotor position; b) $x-y$ axis generated forces and $y-$axis force disturb.

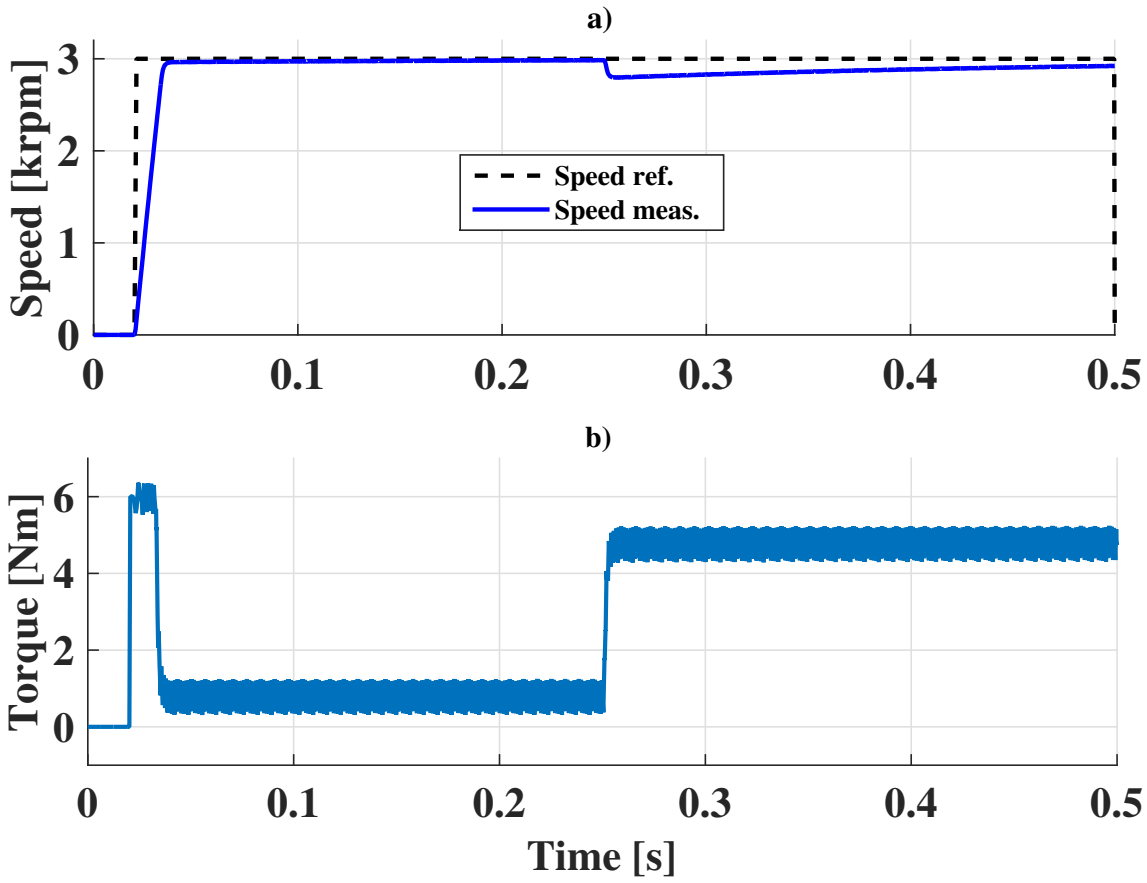


Figure 5.25: Result of the numerical simulation for bearingless operation in healthy condition: a)rotor speed; b) generated torque.

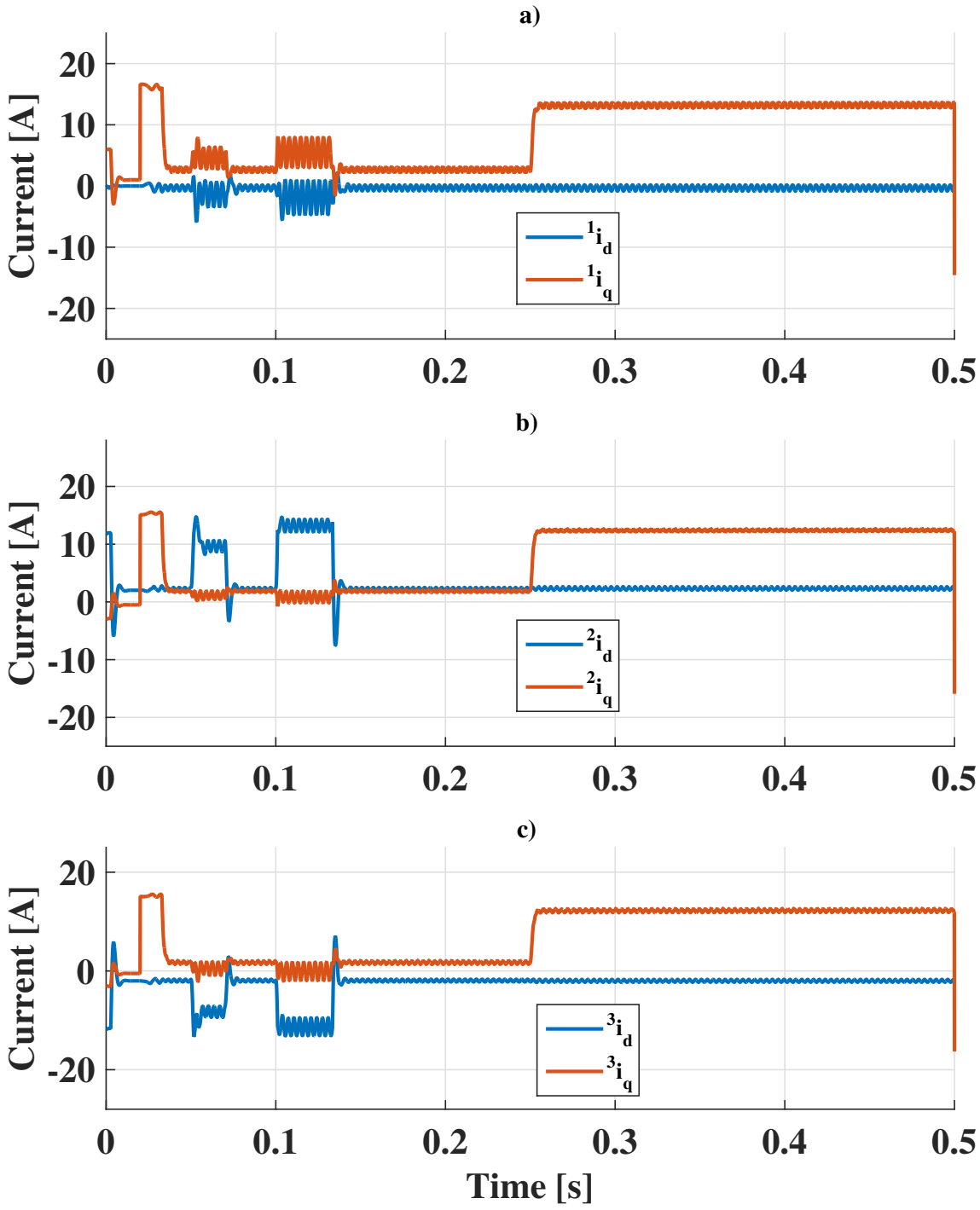


Figure 5.26: Result of the numerical simulation for bearingless operation in healthy condition: :a) $d-q$ axis currents sect. 1; b) $d-q$ axis currents sect. 2; c) $d-q$ axis currents sect. 3.

5.3.2.2 Open-circuit fault

The results of the simulation for open-circuit faults are displayed in Figures 5.27, 5.28 and 5.29. A simulation time of 1 s is considered.

At first, the fault selector is set to 0 and the rotor is positioned in the stator centre after an initial short transient (Figure 5.27 a)). Then at 0.02 and 0.04 s the rotor speed is commanded to its rated value (Figure 5.28 a)) and force disturbance is applied in the $y-$ axis (Figure 5.27 b)) respectively justifying the first perturbation in the rotor position observed in Figure 5.27 a) and the increase of the $d-q$ axis currents in the motor sectors observed in Figure 5.29 a)-c). The aforementioned force disturbance $F_{y,d} = -100$ N has a duration of 0.02 s. At 0.1 s, then, the load torque is set equal to 3 Nm (Figure 5.28 b)) justifying the increment of the $q-$axis currents of the three sectors (Figure 5.29).

While the simulation is running the fault selector is manually set to 1 in order to simulate a sudden open-circuit fault in sector 1. It can be observed from Figure 5.27 a) that the position controller manages to maintain the rotor centred after a very small position transient. Figure 5.29 a) shows that, for the duration of the fault, the $d-q$ currents of sector 1 is zero while Figures 5.29 b) and c) show that the ones of sectors 2 and 3 increase their magnitudes to compensate the loss of the contribution of sector 1 to the force generation. From Figure 5.29 b) and c) it can also be noticed that the current ripple of the healthy sectors is remarkably increased after the fault occurs. This phenomena could be predicted observing the expressions of the $d-q$ axis reference current signals written in (C.9) written for an open-circuit fault in sector 1. In fact, not only the second harmonic in the current is increased but also a forth harmonic appears when the open-circuit fault occurs. The previously described force disturbance is applied during the fault (Figure 5.27 b)) in order to verify the disturbance rejection capability of the faulty bearingless drive.

The same procedure is followed to simulate the open-circuit fault in sectors 2 and 3 showing a similar behaviour.

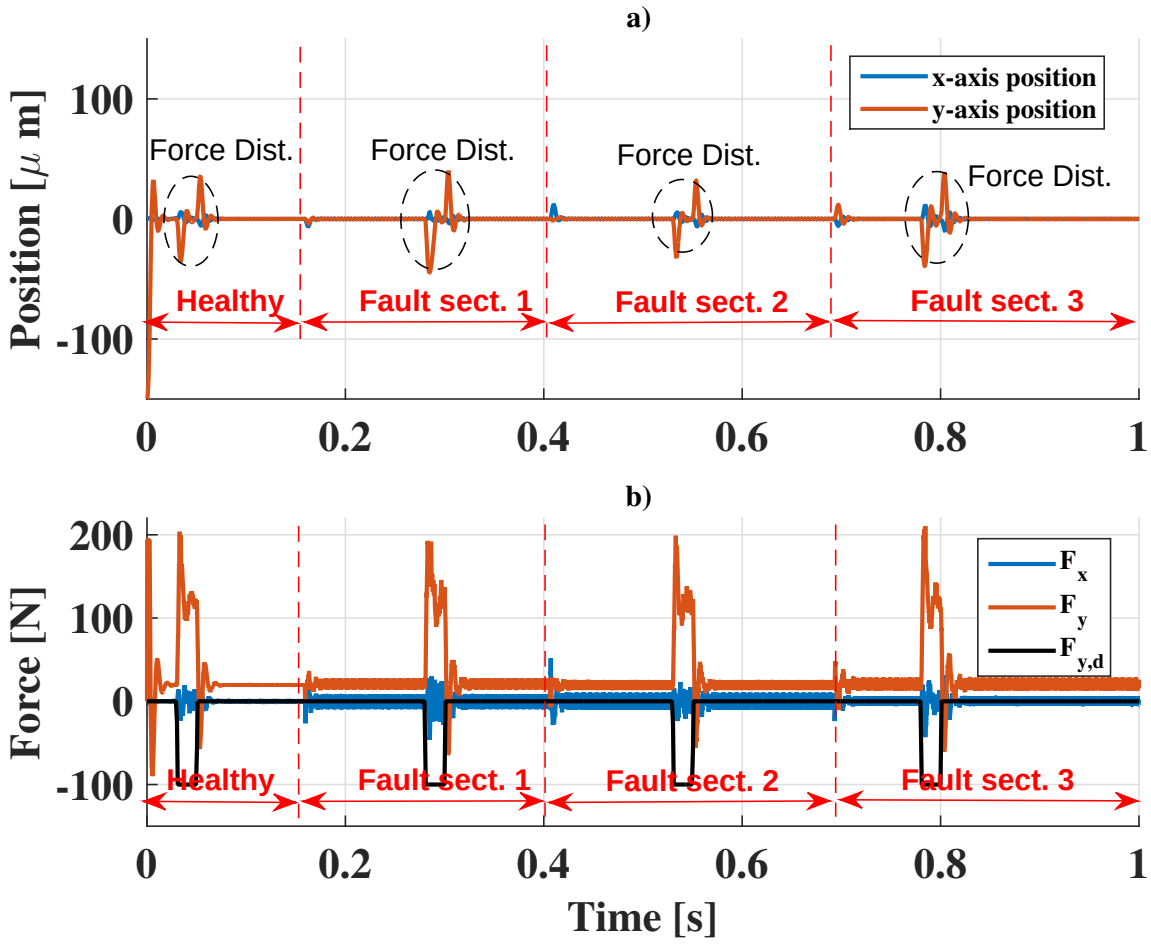


Figure 5.27: Result of the numerical simulation for bearingless operation in open-circuit fault condition: a) $x-y$ axis rotor position; b) $x-y$ axis generated forces and $y-$axis force disturb.

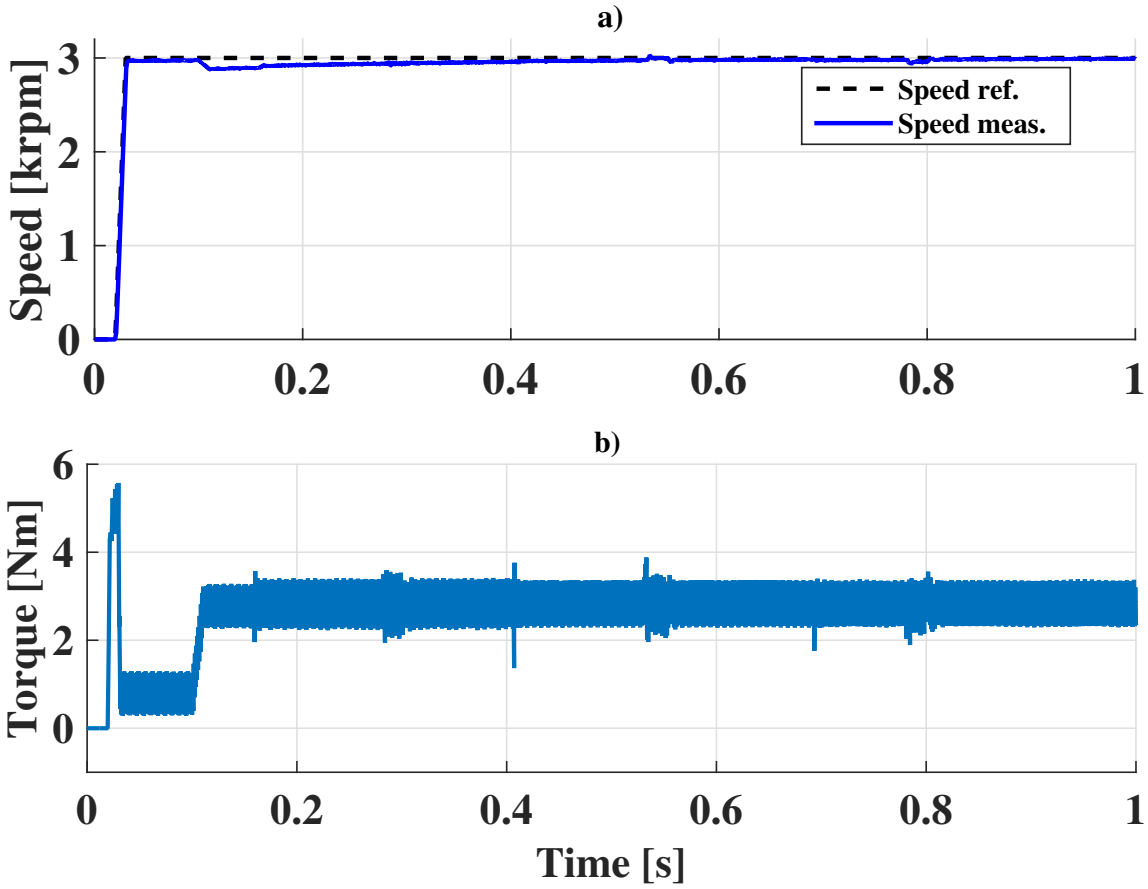


Figure 5.28: Result of the numerical simulation for bearingless operation in open-circuit fault condition: a)rotor speed; b) generated torque.

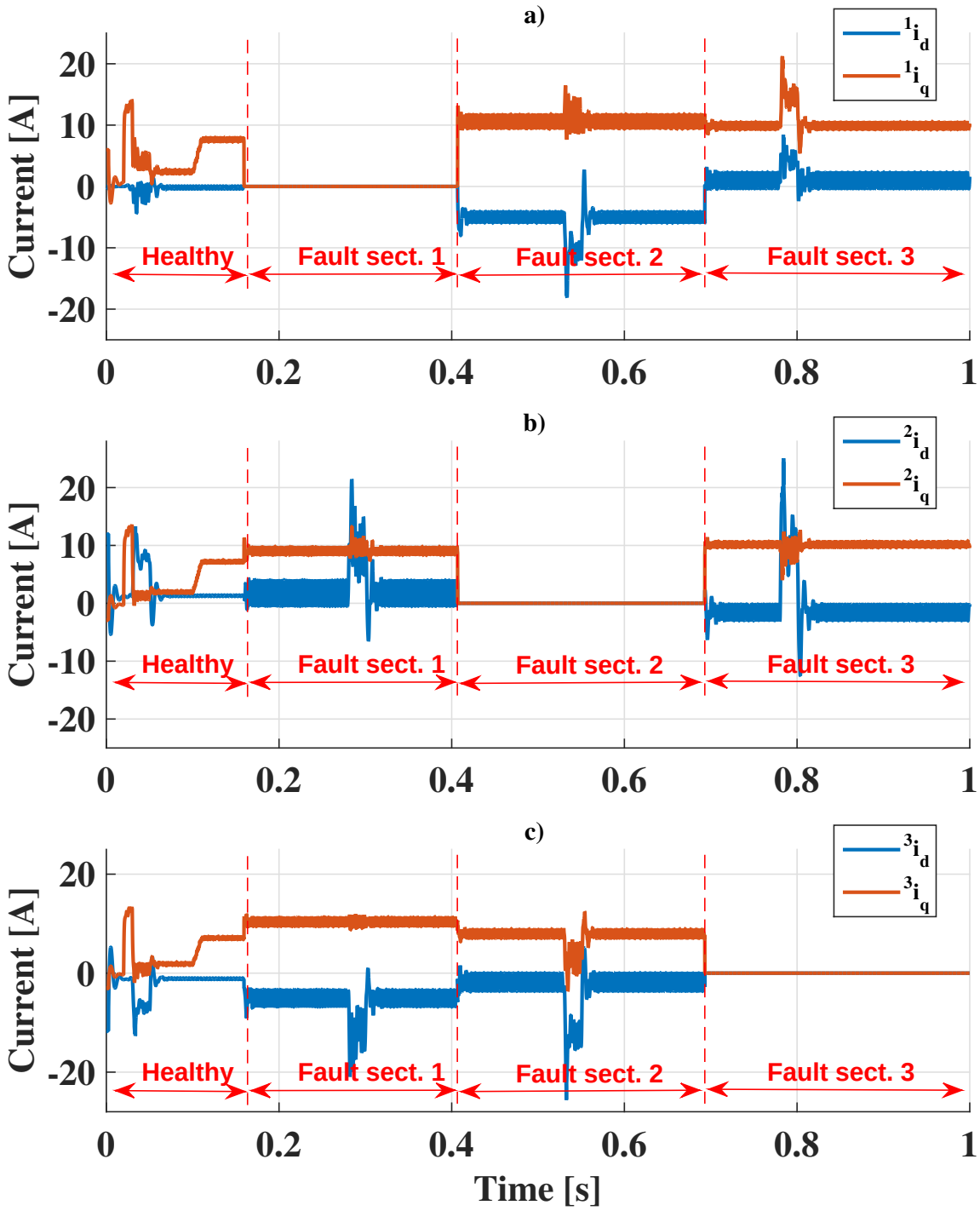


Figure 5.29: Result of the numerical simulation for bearingless operation in open-circuit fault condition: :a) $d-q$ axis currents sect. 1; b) $d-q$ axis currents sect. 2; c) $d-q$ axis currents sect. 3.

5.3.3 2-DOF levitation using standard and MR controllers designed in state space

A multi-frequency force disturbance of the form of equation (5.5) is injected in the simulation model in order to produce the position oscillation.

$$\begin{cases} F_{x,d}(t) = \sum |F_k(\omega_m)| \cos(k\omega_m t) \\ F_{y,d}(t) = \sum |F_k(\omega_m)| \sin(k\omega_m t) \end{cases} ; k = 1, ..., 4 \tag{5.5}$$

The force magnitudes $|F_1(\omega_m)|$, $|F_2(\omega_m)|$, $|F_3(\omega_m)|$ and $|F_4(\omega_m)|$ increase linearly with the rotation speed ω_m reaching their maximum values (40, 30, 20, 10 N respectively) at ω_{max}.

Figure 5.30 shows the comparative results between position control performances considering the standard and the MR controller for a transient simulation. In particular, the rotation speed ω_m has been varied from zero to $2\pi30$, $2\pi40$ and $2\pi50$ with slopes as presented in Figure 5.30 a). The $x-y$ axis components $F_{x,d}$ and $F_{y,d}$ of the force disturbance injected in the model are calculated with (5.5) and shown in Figure 5.30 b). Finally, Figure 5.30 c)-d) show the $x-y$ axis rotor position obtained employing the standard and MR controllers, respectively. It can be observed that both controllers present similar performances at start-up, with the rotor being lifted from the touch down position ([0,$-\delta_{max}$]) and reaching the reference position ([0,0]) with a small overshoot in about 15 [ms]. However, the performance of the standard controller significantly deteriorates as soon as the rotor speeds up and the force disturbance arises. This can be detected in Figure 5.30 c) where the rotor position reaches a maximum displacement of around 90 μm when the rotation speed is $2\pi50$ rad/s and the force disturbance presents its maximum magnitude and frequency. Therefore, a MRC is required to guarantee a stable bearingless operation. Fig. 5.30 d) shows that the MRC introduced effectively suppresses the multi-frequency oscillation after a short transient in the whole operating speed range.

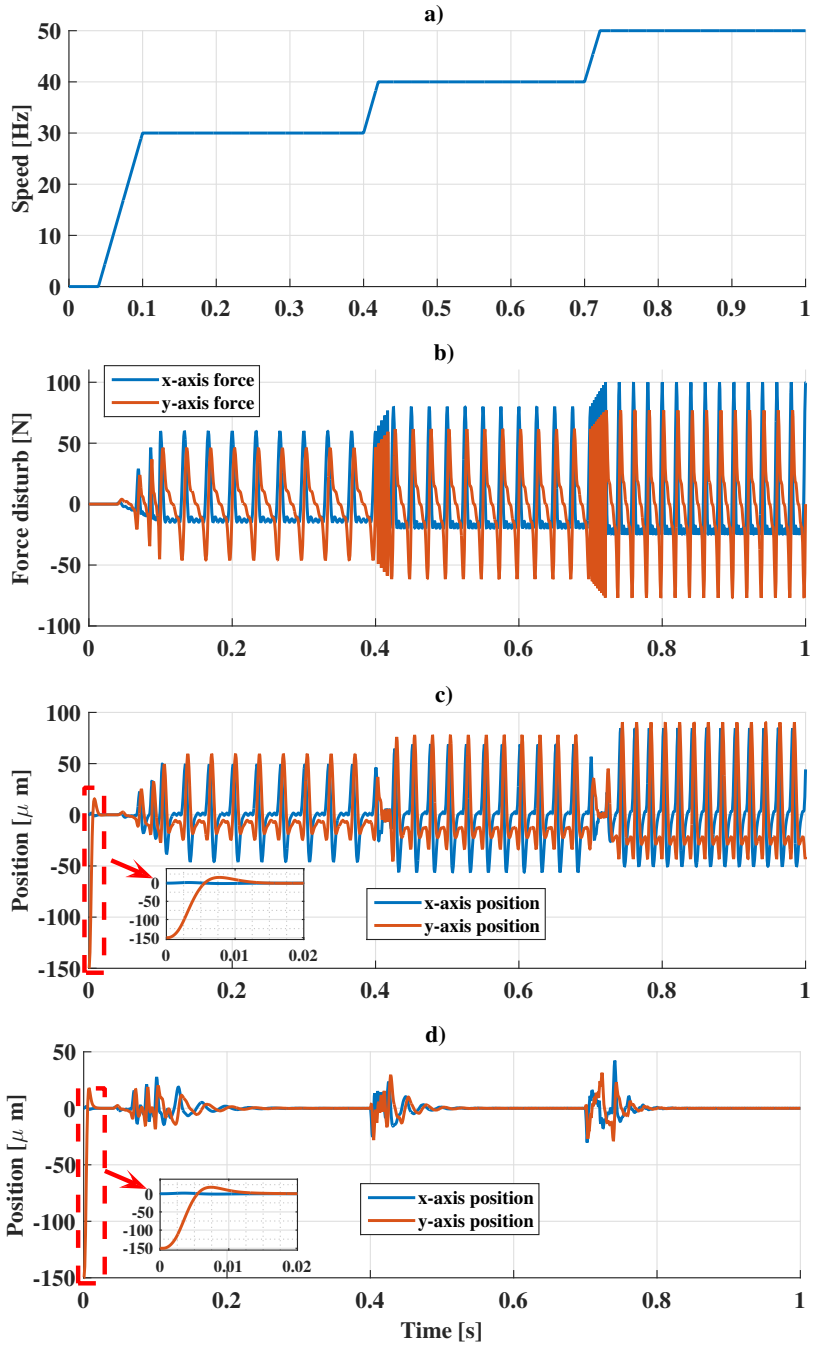


Figure 5.30: Simulative comparison between standard and MR controllers during a speed transient: a) rotating speed; b) force disturbance; c) $x-y$ axis position with standard controller; d) $x-y$ axis position with MRC.

5.4 Conclusions

In this Chapter, the radial force and torque generation method presented in Chapter 3 has been validated by means of FEA. In particular, it has been shown that a controllable force can be produced in any desired direction and magnitude within the machine force capability. The torque can be produced simultaneously without significantly affecting the quality of the force generation. The same can be claimed for the force and torque generation when an open-circuit fault occurs in one of the machine sectors. As a matter of fact, the THD of the $x-y$ force components changes very little from healthy to faulty operating conditions, even when the a torque load is required. The force control has been also employed to suppress unbalanced forces caused by the rotor eccentricity. At first, the static eccentricity was considered and the rotor was translated of a fixed displacement $\delta = \delta_{max}$ and Φ_d and rotated. A big constant force rises from the static eccentricity tending to further push the rotor toward the stator if the force control is deactivated. On the other hand, if the force control is activated, the force acting on the rotor is remarkably reduced. The same can be said in the case of dynamic eccentricity. The latter causes a rotating force that is effectively compensated by the introduced force control method.

The presented force and torque control technique has been benchmarked with more conventional ones. It has been shown that the proposed control achieves better force production performance than the FTD technique and presents similar quality of the generated force if compared with the HFTD technique. However, the greater advantage consists in the more accurate analytical model that allows to generate the desired force without the help of a lookup table. In general, this will lead to a reduction of the computational effort required.

In the second part of the Chapter the numerical simulation results have been presented. The simulation model was at first detailed and the overall control algorithm presented. Then, the results for 2-DOF levitation control in case of healthy and open-circuit operations have been displayed. The position controller considered was designed in the previous Chapter (section 4.2.2) with a transfer function-based

method. The position controller has been found capable to stably suspend the rotor when a constant force disturb of 110 N is introduced. However, the rotor touchdown occurs when the magnitude of the force disturb is 200 N (rated force). During the simulation the rotor speed is commanded to its rated value and rated torque is generated. It has been shown that the radial rotor position is very little affected by the speed control and by the torque generation.

Good results have been also obtained in case of open-circuit fault of one motor three-phase winding. In the simulation the bearginless drive is activated in healthy condition and the faults in the different sectors are induced by means of external inputs. It has been verified that the position controller manages to maintain the rotor suspended after a small position transient. Different force disturbs have been introduced to prove the robustness of the position control even in fault conditions.

Finally, the standard and MR controllers designed in state space in sections 4.3, 4.4 and 4.5 have been compared. A multi-frequency force disturbance has been injected in the simulation model to generate a periodic position oscillation. It has been observed that a remarkable oscillation can be appreciated in the position if the standard position controller is employed. On the other hand, the position oscillation is completely compensated and the periodic force disturb rejected if the MR controller is introduced.

Chapter 6

Experimental Results

6.1 Introduction

This Chapter presents the experimental validation of the proposed force and torque control technique. The Chapter is divided into four sections. At first the experimental rig is described in all its parts. Furthermore, the procedure to switch from normal motor operation to bearingless operation is defined.
Then, the electrical parameters have been experimentally identified and compared to the analytical prediction and to the FE results.
In the third section, the radial force control has been exploited to suppress selected vibrations at different rotor speeds. Normal motor operations with the shaft equipped with standard ball bearings were considered and two acceleration transducers were employed for the tests.
Finally, the last section presents the experimental results for the bearingless operations. The 2-DOF position controllers designed in Chapter 4 have been employed and validated in this section. Two proximity transducers measure the feedback $x-y$ axis rotor position. In the same section the open-circuit fault tolerant capabilities of the

MSPM machine are also verified.

6.2 Experimental Rig Design

6.2.1 Mechanical Structure

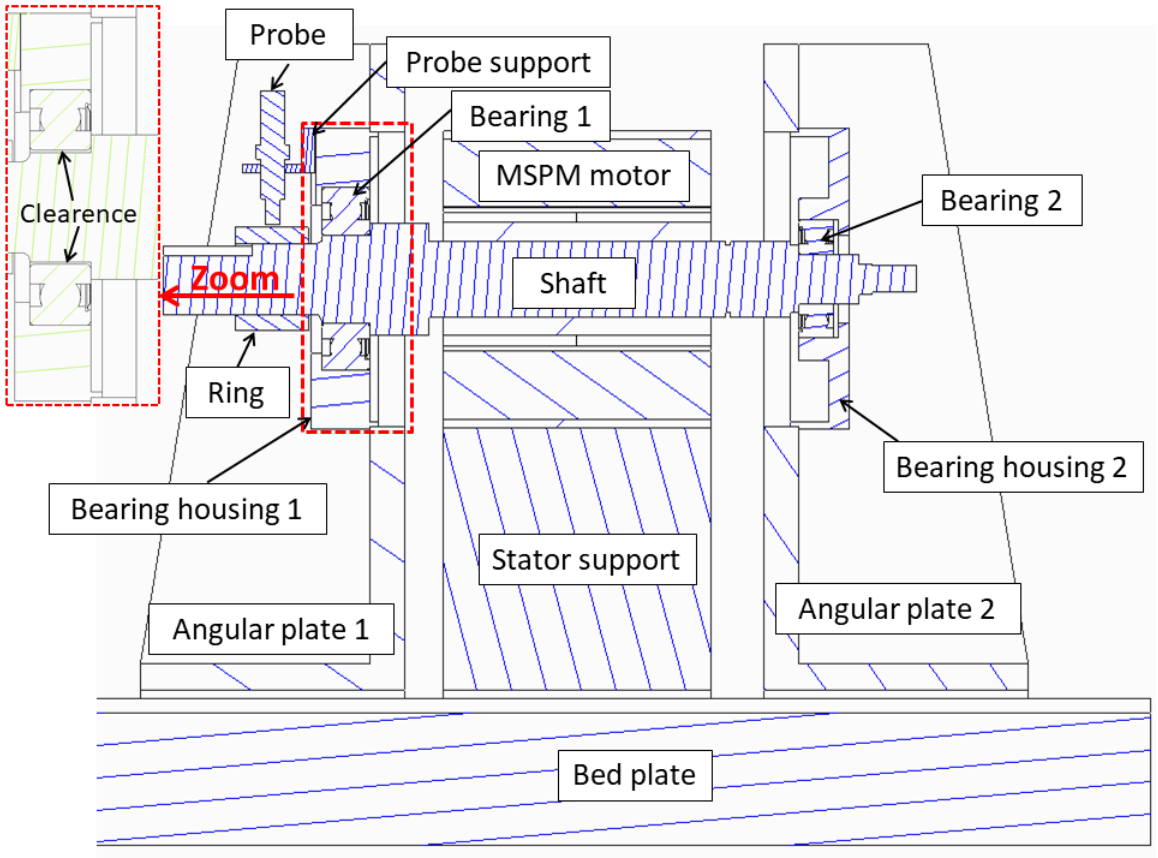


Figure 6.1: Axial section of the mechanical parts of the rig.

The pursued design criterion consisted of realizing a flexible mechanical structure that could be used for a normal motor operation as well as for a bearingless operation. In particular, the shaft is supported by two conventional ball bearings (bearing 1 and 2

in Figure 6.1) when normal motor operations are required. On the other hand, the 2-DOF levitation tests could be performed substituting the shaft-rotor part equipped with standard ball bearings with an other one presenting an identical rotor element, but with a self-aligning bearing in place of bearing 2. Furthermore, the portion of shaft in correspondence of bearing 2 has been machined in order to create a clearance between the shaft and bearing 1 (now called backup bearing) to allow for the shaft-rotor part movement.

The drawings of all the mechanical parts have been realised using Creo Parametric 3.0. The overall mechanical structure is displayed in Figure 6.1 where all the parts have been labelled. The dashed frame on the top right of the Figure shows the zoom of the clearance between the backup bearing and the machined portion of the shaft. The bed plate has been designed with a slotted precision guide running for all its length (Figure 6.2) that guarantees the alignment of the two angular plates and stator support with a very small mechanical tolerance.

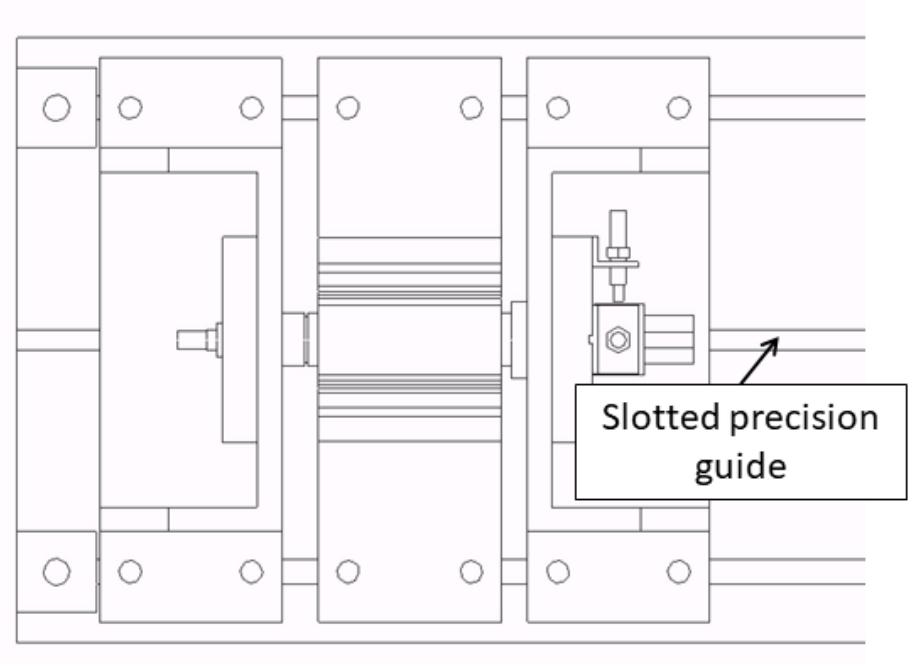


Figure 6.2: Top view of the rig mechanical assembly.

Figure 6.3 a) shows the assembled mechanical rig. A DC load has been coupled through a universal joint to the MSPM motor to perform the no-load and load tests. It features the same rated speed of the MSPM motor and 15 Nm rated torque. A four-quadrant DC servo drive is installed to control the DC machine as a motor or as a generator when no-load or load tests on the MSPM motor are required. The universal joint (see detail in Figure 6.3 b) permits to mechanically decouple the two machines so that the MSPM motor shaft is free to radially translate during bearingless operations.

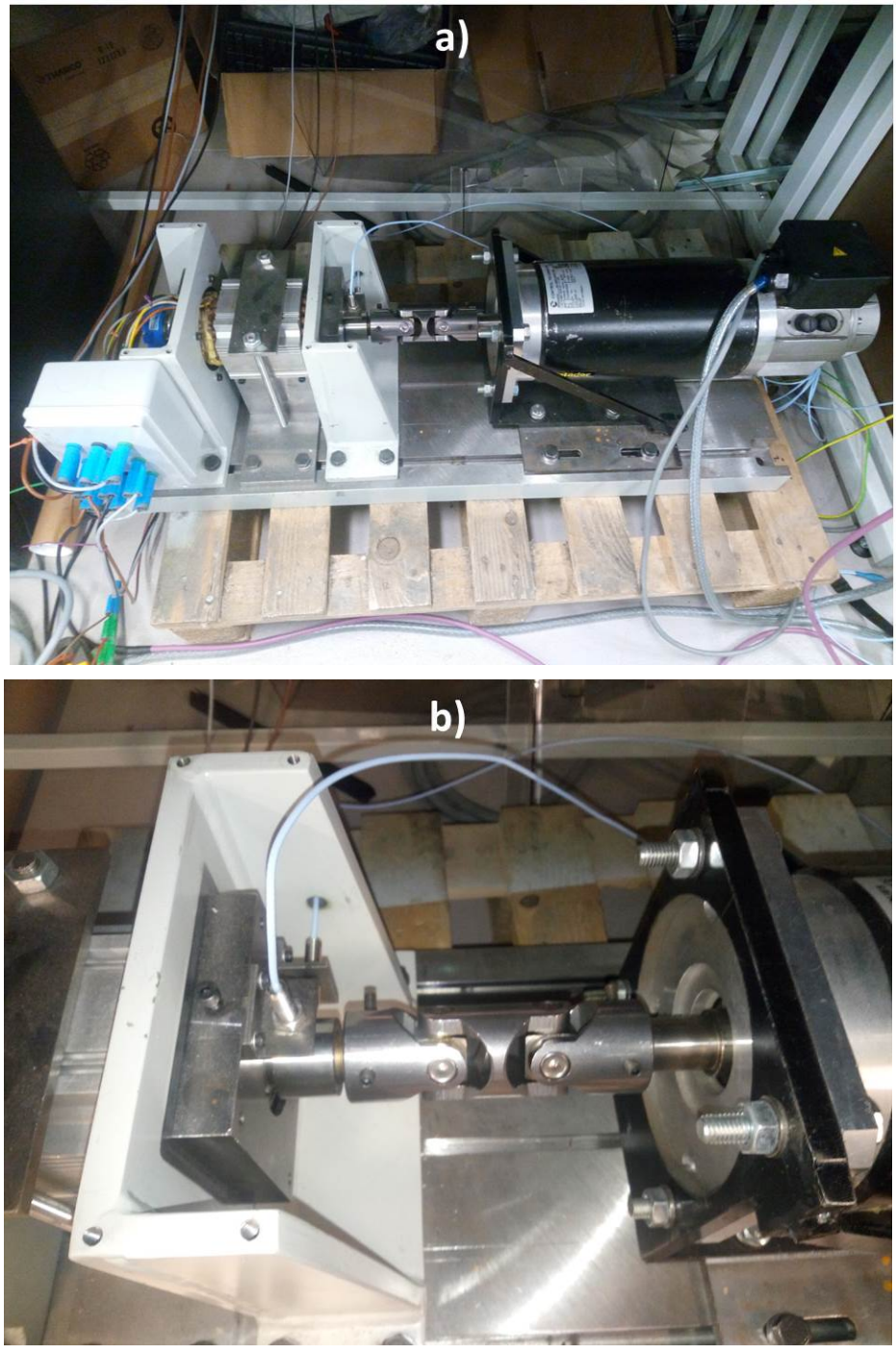


Figure 6.3: Assembled mechanical rig: a) MSPM machine coupled with the DC load; b) detail of the coupling realized by means a universal joint.

6.2.2 Power converters and control platform

Each of the three three-phase inverters with rated power 2 kW feeds one of the MSPM motor winding sets. The three inverters are shown in picture 6.4 a). The power module of the single inverter is a "dual-in-line package intelligent power module (PS21A79)" manufactured by Mitsubishi Semiconductor. The switching frequency and dead time of the transistors are set equal to 10 kHz and 2.2 μs, respectively. The DC links of the three converters are connected in parallel and supplied by a Variac through a passive rectifier. As a matter of fact, the rated voltage of the DC link capacitors is 400 V, hence the inverters cannot be connected directly to the three-phase grid.

The industrial control boards mounted on each inverter have been removed and substituted by one centralized control platform that communicates with the power modules gate drives by means of fibre optics cables. The custom made control platform (uCube) shown in Figure 6.4 b) has been designed by Dr. Giovanni Lo Calzo, Dr. Adrea Formentini and Dr. Alessandro Galassini and it is based on the off-the-shelf Microzed board from Avnet, a low-cost development board based on the Xilinx Zynq-7000 All Programmable SoC [138]. The Zynq integrates in a single device a dual-core ARM CortexA9 based Processing System (PS) and a Field Programmable Gate Array (FPGA) Programmable Logic (PL) [138]. An interface board has been then realized with the main function of converting the fibre optic light signals into voltage signals suitable for the power modules gate drives.

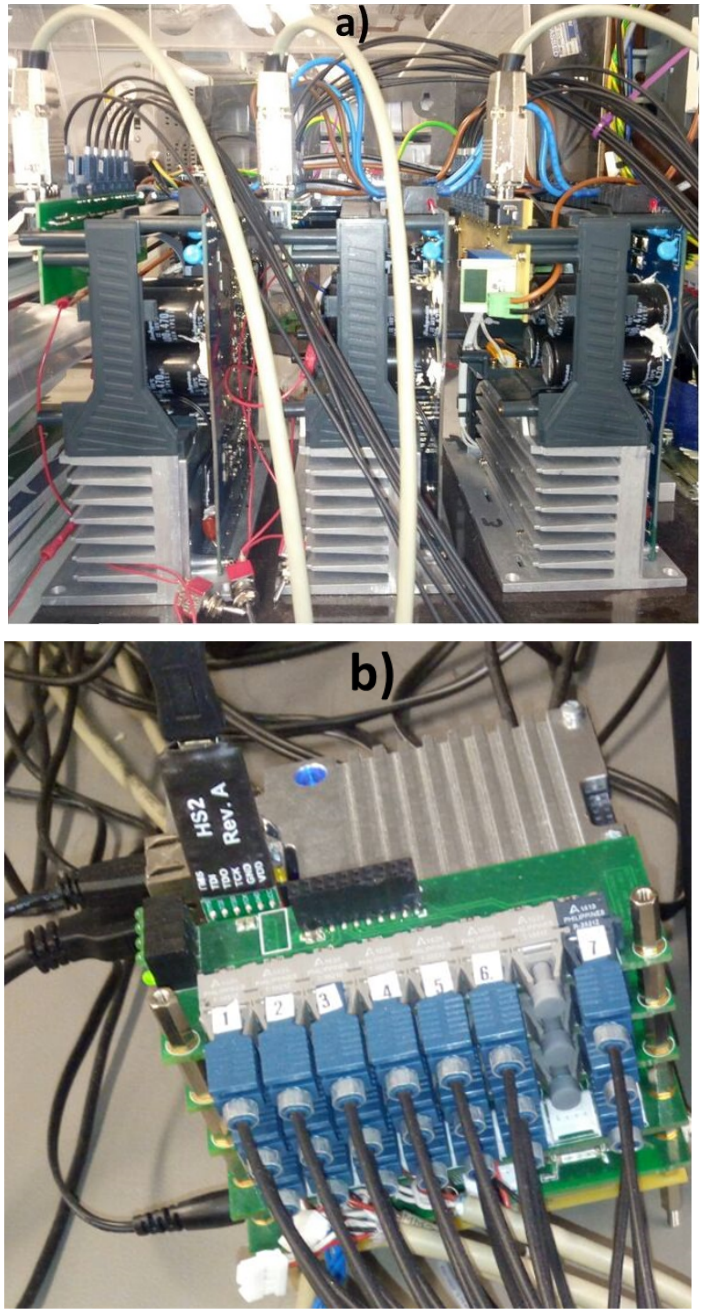


Figure 6.4: a) Three three-phase inverters; b) uCube control board.

6.2.3 Vibration Transducer System

The level of vibration is measured by means of accelerometers and dedicated signal processing tools. The vibration transducer system employed is the SKF Microlog MX vibration kit composed by two acceleration transducers and a vibration analyser module. The latter is shown in Figure 6.5. The two acceleration transducers are fixed by means of magnets on the angular plate 1 as shown in Figure 6.6 in order to detect the vibrations on the x- and y-axis.



Figure 6.5: Vibration analyser module.

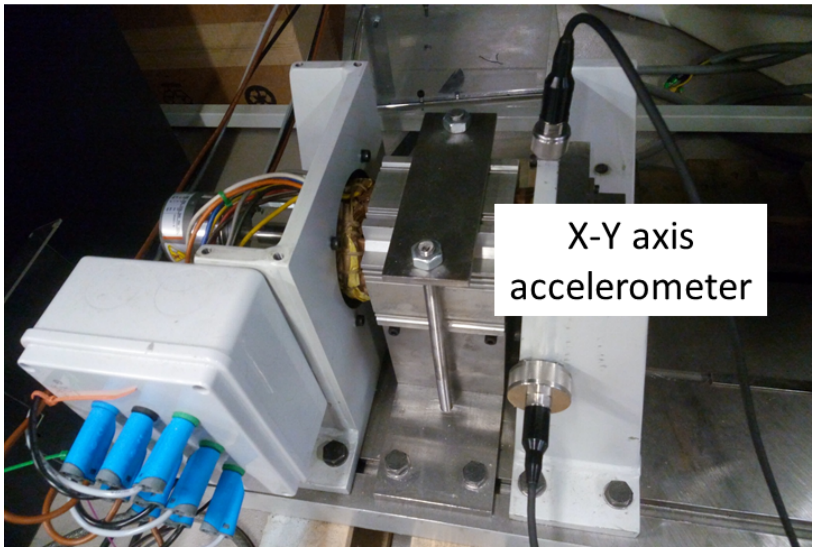


Figure 6.6: Detail of the MSPM motor with the $x-y$ axis acceleration transducers mounted on one of the angular plates.

6.2.4 Proximity Transducer System

Proximity sensors, also called displacement sensors, possess the ability of detecting the instantaneous position of an object (target) during the movement without a mechanical contact. They are divided mainly into three categories: capacitive, laser and electromagnetic. The first type exploits the dependency of the isolation length on the capacitance. Therefore, good isolation between the sensor probe and the shaft is necessary. The second type detects the target position by reflecting the laser light on the target surface that should be as smooth as possible to avoid noise. The two above described sensor types can be used in a bearingless application, however the electromagnetic type is certainly the most popular.

Electromagnetic sensors can be divided into two subcategories: inductive and eddy current. The target for an inductive sensor is made of a ferromagnetic laminated material with high permeability. A coil is wound around a ferromagnetic core and excited with high frequency voltage in the range of 20-100 kHz. The displacement

information can be extracted by measuring the position dependent input impedance at the coil terminals. In fact, a small displacement results in a big inductance, hence in a high input impedance and vice-versa. On the other hand, the target of an eddy current sensor should be made of conductive material. The excitation voltage that supplies the coil is very high (around 2 MHz) so that eddy currents are induced in the target. The magnetic flux produced by the eddy currents opposes to the magnetic flux generated by the coil current. Therefore, if the displacement is small, the flux is reduced and consequently the inductance and the input impedance are small and vice-versa.

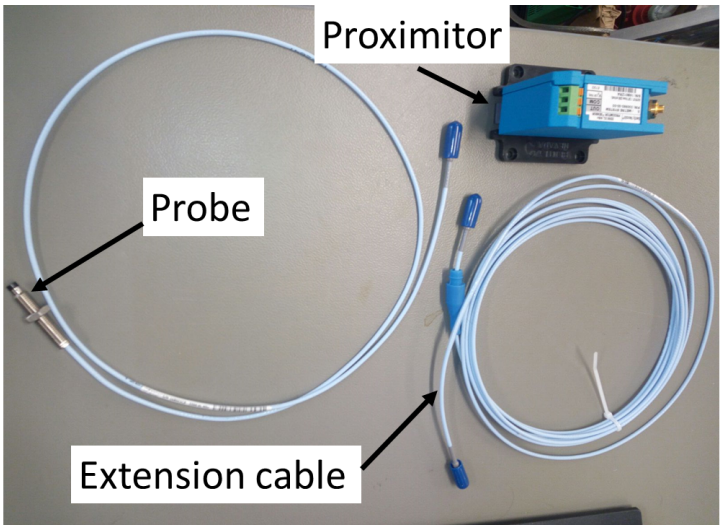


Figure 6.7: Elements composing the proximity transducer system.

The proximity sensor type chosen for this PhD project is the eddy current one. The main reason is the greater availability of eddy current sensors on the market. The second reason is that the target has to be laminated if a inductive sensor is employed. Therefore, two 3300 XL NSv proximity transducer systems, one for the $x-$ and one for the $y-$axis displacement, have been purchased from Bently Nevada. Each of them consists of a probe, an extension cable and a proximitor that has the function of signal conditioning and probe supply. The proximitor provides a DC output voltage

function of the target position. The three elements are shown in Figure 6.7. The main features of the 3300 XL NSv proximity transducer system are 10 kHz bandwidth, a linear range from 0.25 to 1.75 mm and an Incremental Scale Factor (ISF) of 7.87 V/mm. The target material on which the sensors are calibrated in the factory is steel AISI 4140, therefore a ring of the same material has been manufactured within the facility of the University of Nottingham and mounted on the shaft. Since eddy current sensors are very sensitive to target surface imperfections, the outer ring surface was machined in order to make it as smooth as possible.

Each proximity transducer system has been connected to the control platform through an interface board represented by the circuit in Figure 6.8. Table 6.1 reports the commercial resistance values used in the circuit. From the circuit schematic it is possible to observe that the board has two inputs given by the proximitor output DC voltage signal and the power supply and one output that goes straight to the ADC in the control platform. Two operational amplifiers with unity gain guarantee the isolation between the input stages and the differential amplifier circuit. The latter provides the following output voltage:

$$v_{diff} = \frac{R_3}{R_1}(v_1 - v_2) \tag{6.1}$$

where $v_1 = 14$ V is a constant DC voltage signal provided by the power supply 24 V after the voltage dividing stage. v_2 instead is the displacement dependent proximitor output DC voltage which ranges between 14 and 20 V for the maximum displacement allowed by the backup bearing. Therefore, $v_1 - v_2 = 0 \div 6$ V, hence $v_{diff} = 0 \div 18$ V. Since the voltage range accepted by the ADC is 0 to 4.096 V, a second voltage divider is employed in the board output stage.

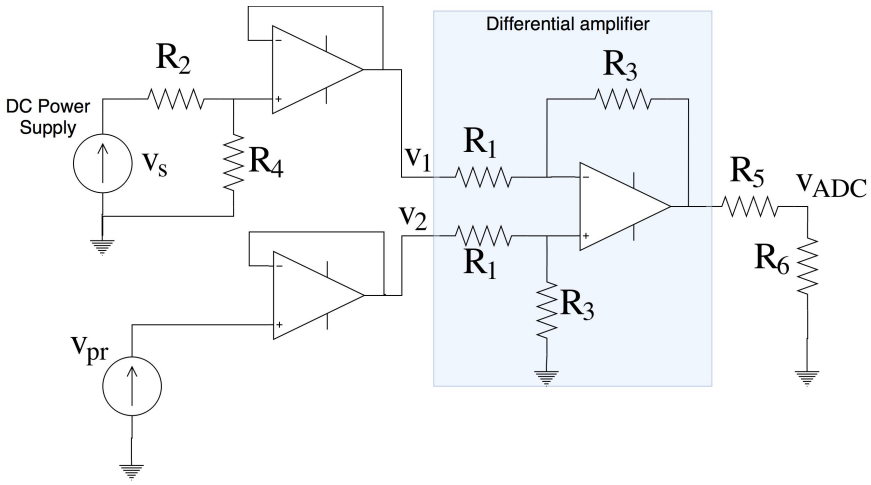


Figure 6.8: Circuit schematic of one of the two channels (the other is identical) of the interface board.

Table 6.1: Resistor values

Name	**Value [kohm]**
R_1	3
R_2	4.22
R_3	9.09
R_4	5.9
R_5	7.87
R_6	2.26

6.3 Electrical Parameters Identification

In this section the electrical machine parameters such as back-EMF and inductances are calculated analytically and validated with FEA and experimentally.

6.3.1 Back-EMF

The back-EMF validation is performed comparing the analytical, FEA and experimental results in open-circuit condition. The latter has been obtained driving the machine at various rotational speed (within the machine operative range) by means of an external load and measuring the voltage between consecutive phases with an oscilloscope. Figure 6.9 presents the experimental line to line back-EMF waveforms of the three motor sectors at the rated motor speed ω_{rated}.

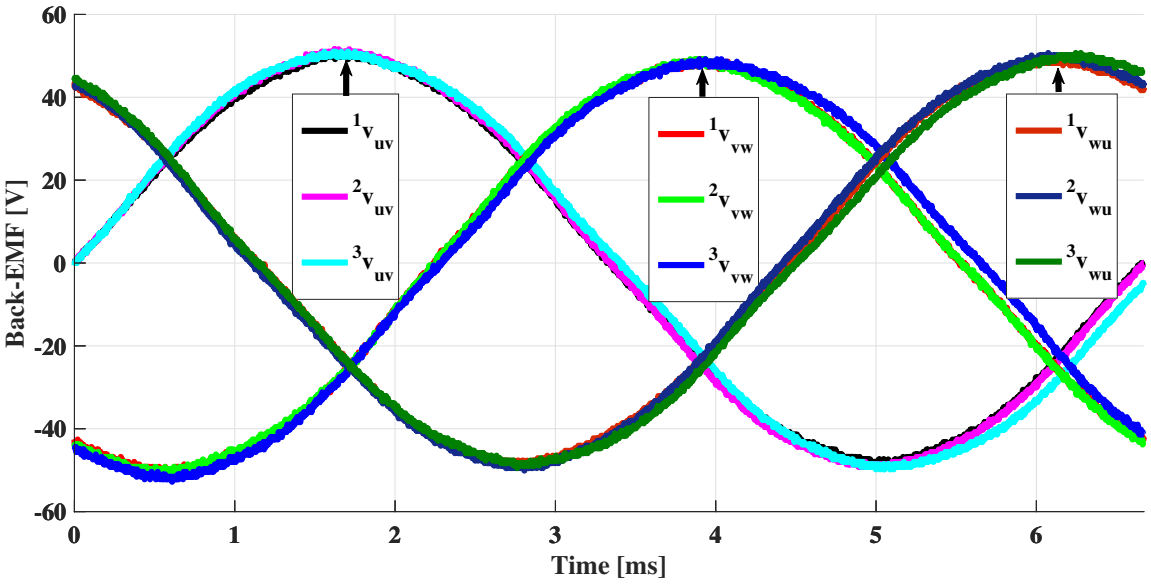


Figure 6.9: Experimental line to line back-EMF waveforms of the three sectors of the MSPM motor at ω_{rated}.

It can be noticed that same phases in different sectors presents identical back-EMF waveforms since they are located in equivalent electrical position.
The analytical expression of the back-EMF waveform is obtained calculating the line to line voltage constant as

$$k_V = \sqrt{3}\,\frac{\omega_{rated}\, p\ {}^{s}\Lambda_{PM}}{v_{rated}}\ [V/rpm] \tag{6.2}$$

where ω_{rated} and v_{rated} are the rated rotation speed in rad/s and rpm, respectively. It

results in a good prediction if compared with respect to the experimental and FEA values presented in Figure 6.10. The FEA are computed through transient-with-motion simulations considering the machine in open-circuit condition at different mechanical rotational speed.

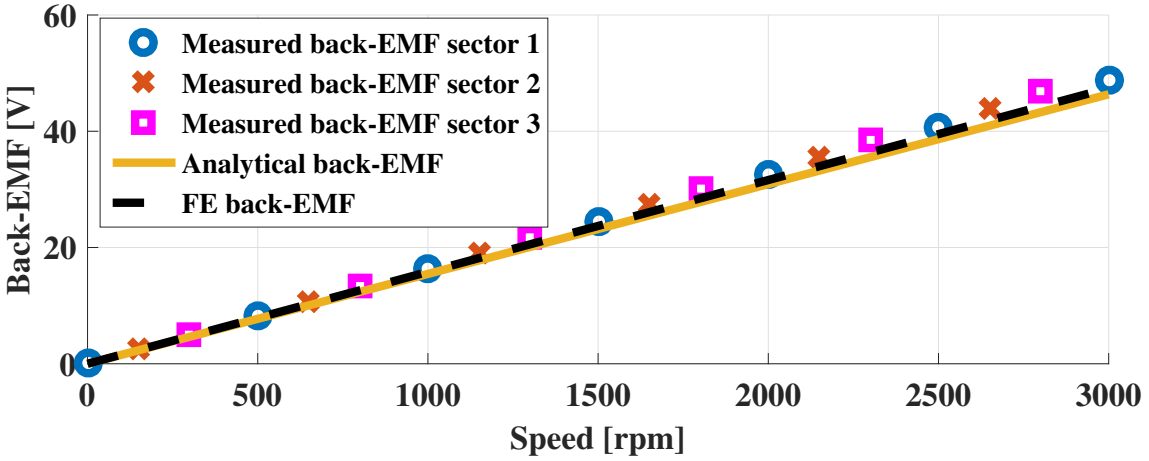


Figure 6.10: Comparison between the experimental, FE and analytical back-EMF trends against the rotation speed. The back-EMF between phase u and v of each motor sector has been included in the graph.

Figure 6.11 shows the harmonic spectrum of the experimental, FEA and analytical waveform of the back-EMF of one motor phase. The analytical prediction results accurate if considered that the harmonic content of the experimental and FEA waveforms is negligible as it can be observed.

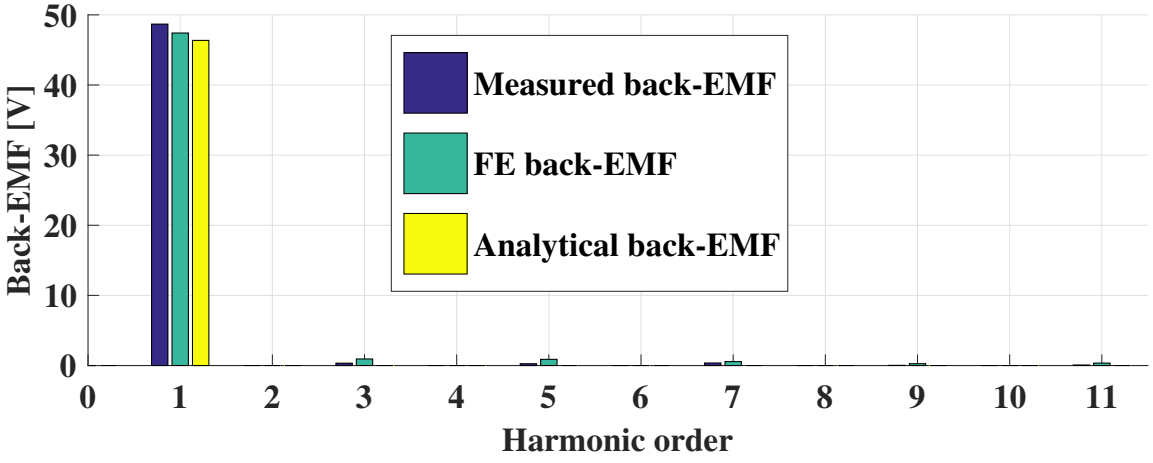


Figure 6.11: Comparison of the harmonic spectrum between measured, FE and analytical back-EMFs between phase u_1 and v_1.

6.3.2 Machine inductances

The $d-q$ axis inductance matrix has been characterized in Chapter 3 through analytical calculations and FE linear simulations. In this paragraph the effect of the iron saturation on the inductance elements is considered and both non linear FE simulation and experimental results will be presented.

The FE computation of the inductance values of $\mathbf{L}_{dq,t}(\vartheta_e)$ can be performed supplying one machine sector with alternatively $d-$axis current and $q-$axis current. Figure 6.12 shows the trend of $L_d(i_d)$ and $L_q(i_q)$ (main diagonal inductances) for $\vartheta_e = 0$ against the $d-$ and $q-$ axis current, respectively. Furthermore, the FE curve of $L_d(i_d)$ is compared with the experimental one validating the result obtained.

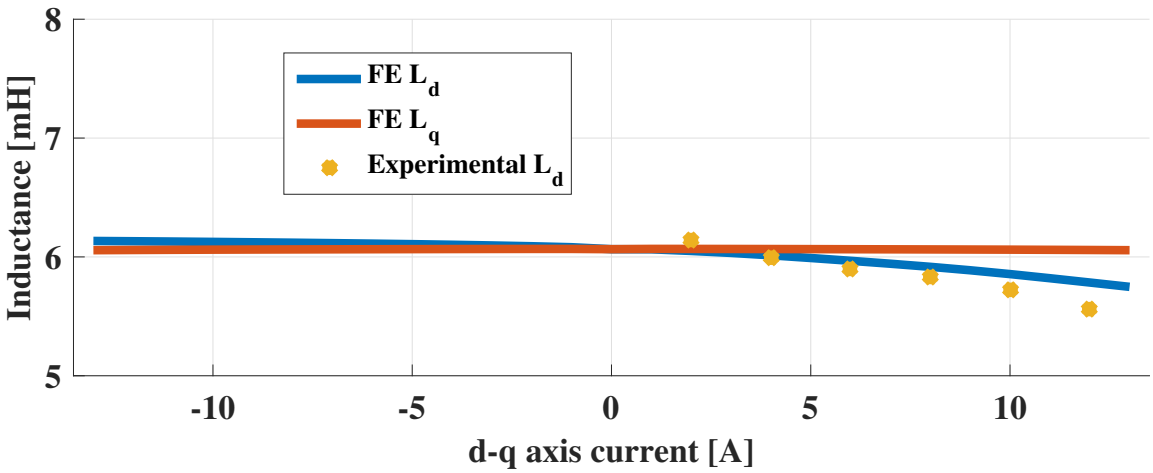


Figure 6.12: $d-q$ axis inductances as a function of the current.

The inductance L_d was obtained experimentally feeding the following current vector to the three-phase winding of sector 1: ${}^{1}\bar{i} = \begin{bmatrix} i & -i/2 & -i/2 \end{bmatrix}^T$, with i ranging from 0 to I_{rated}. The rotor will then automatically align its magnetic axis with the one of the supplied winding. Inductance L_q was not experimentally identified since a mechanical clamp or a load motor controlled in position would have been necessary to avoid the rotor to start spinning when the $q-$ axis current was supplied to the winding. At that time they were not available, hence only the L_d inductance could be experimentally identified.

The experimental identification of L_d was carried out performing a closed loop current control and recording input and output values of the system: $d-$axis reference and measured currents $i_{d,ref}$ and i_d, respectively. In a post-processing stage, the particle swarm optimization technique has been employed to identify the unknown parameters of the system such as the phase resistance R_{ph}, the inductance L_d and constant voltage drop on the switches and diodes V_c. The identification process has been implemented in Matlab where the function "particleswarm" has been exploited to obtain the above mentioned electrical parameters. As a matter of facts, after a defined number of iterations, the function "particleswarm" returns those parameters that minimize the error between the real output i_d and the simulation output $i_{d,sim}$ of the discretized

system. The latter is reported in (6.3) and it includes the PI current controller and the electrical plant.

$$\begin{cases} e(k) = i_{d,ref}(k) - i_{d,sim}(k) \\ I(k) = e(k)T_s + I(k-1) \\ u_d(k) = k_I I(k) + k_p e(k) \\ i_{d,sim}(k+1) = \frac{\left(e^{\frac{R_{ph}T_s}{L_d}} - 1\right)u_d(k-1) + \left(e^{\frac{R_{ph}T_s}{L_d}} - 1\right)V_c + R_{ph} i_d(k)}{R_{ph} e^{\frac{R_{ph}T_s}{L_d}}} \end{cases} \tag{6.3}$$

where T_s is the sample time, $k = 1, ..., \frac{T_f}{T_s}$ with T_f the time length of the test, e is the input error of the PI current controller, $i_{d,ref}$ is the $d-$axis reference current, I is the discrete integral of e, k_I and k_p are the integral and proportional gains respectively, V_c is the constant voltage drop on the component and finally $i_{d,sim}$ is the output of the simulated discretized system. The sample time T_s and time length T_f are equal to 50 μs and 0.1 s, respectively.

Figure 6.13 shows the comparison between i_d and $i_{d,sim}$. The reference current chosen presents a triangular waveform plus a constant value in order to be able to well identify the electrical parameters. It can be noticed that the output $i_{d,sim}$ of system (6.3) matches the real current output i_d meaning that, in a good approximation, the identified parameters can be considered correct. The identification gave as output 0.23 Ohm, 5.56e-04 H and -2.83 V for R_{ph}, L_d and V_c, respectively.

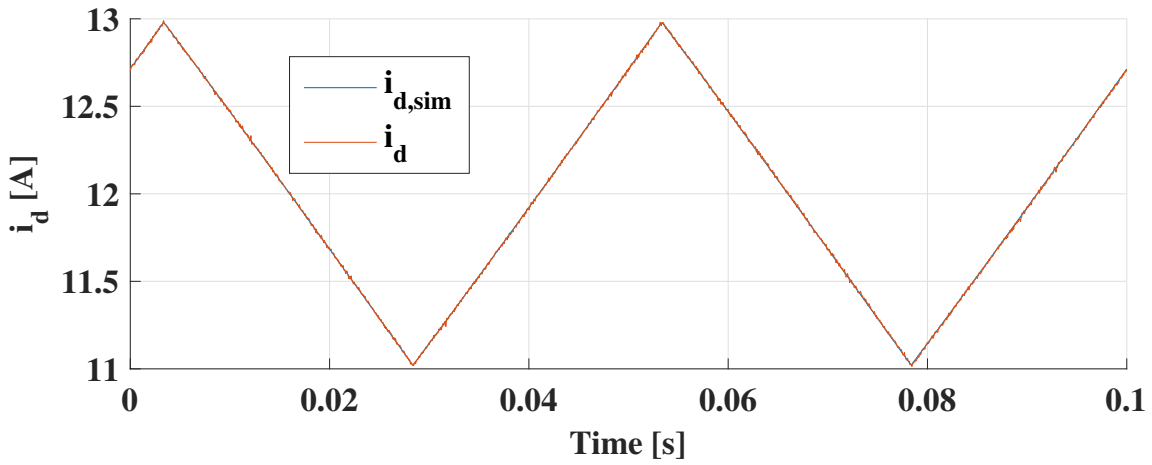


Figure 6.13: Comparison between the measured current i_d and the output of the simulated system $i_{d,sim}$.

6.4 Vibration Suppression Results

This section aims to demonstrate the feasibility of the radial force control method proposed. It has been mentioned in section 2.2 that the force control can be exploited for several purposes. The force control has been exploited for the suppression of specific vibrations that has been detected by means of the acceleration transducers during normal operation of the motor equipped with ball bearings. This section shows the experimental results obtained during the performed vibration suppression tests.

6.4.1 No load vibration spectrum

The no-load vibration characteristic of the rig is measured controlling the MSPM motor at different rotational speed by means the speed loop and recording the harmonic spectrum of the signal from the accelerometer probes using the vibration analyser module.

Figure 6.14 shows the spectrum of the accelerations for several rotor speeds varying from 200 rpm up to 3000 rpm. It can be noticed that the harmonic spectrum presents a peak related with the fundamental rotating frequency followed by peaks of higher harmonic order. The source of the vibrations are related with the mechanical ball bearing reaction, UMP due to rotor misalignment, encoder mechanical coupling, ripple in the currents, non-symmetric airgap flux density distribution under each motor sector.

Considering the harmonic decomposition of a general disturbance force, (6.4) defines the general formulation of the vibration source that is aimed to be minimized featuring $|F_k|$ and φ_k as the unbalanced force amplitude and phase angle, respectively.

$$\begin{cases} F_{x,k} = |F_k| \cos(k\vartheta_m + \varphi_k) \\ F_{y,k} = |F_k| \sin(k\vartheta_m + \varphi_k) \end{cases} ; k = 1, 2, 3, ..., \infty \tag{6.4}$$

Unbalanced forces rotating at k times the rotor mechanical speed are considered and the main harmonics for different orders k are highlighted with red continuous lines in Figure 6.14.

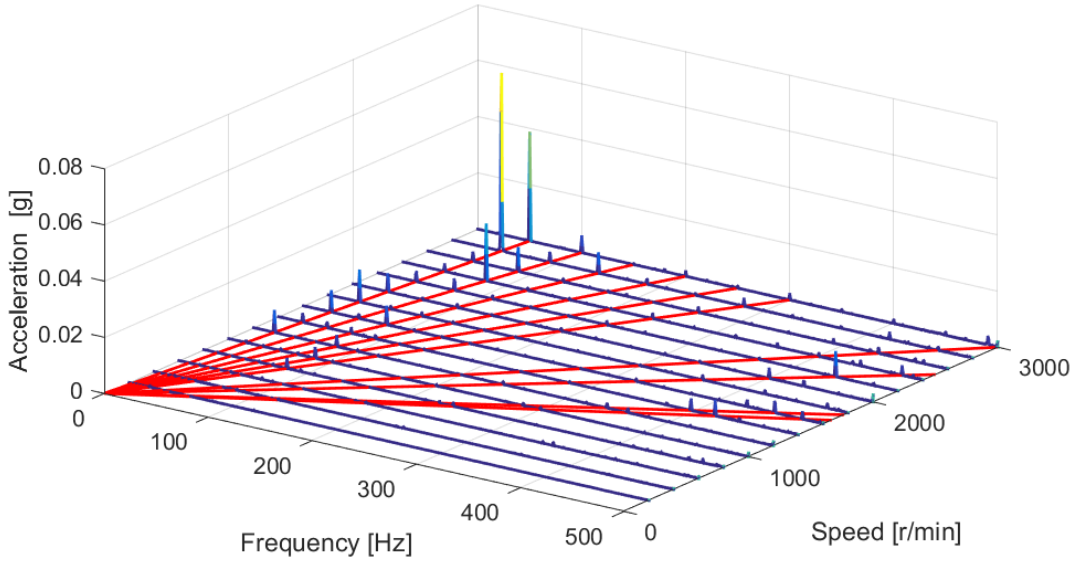


Figure 6.14: No-load vibrations waterfall plot.

6.4.2 Vibration suppression

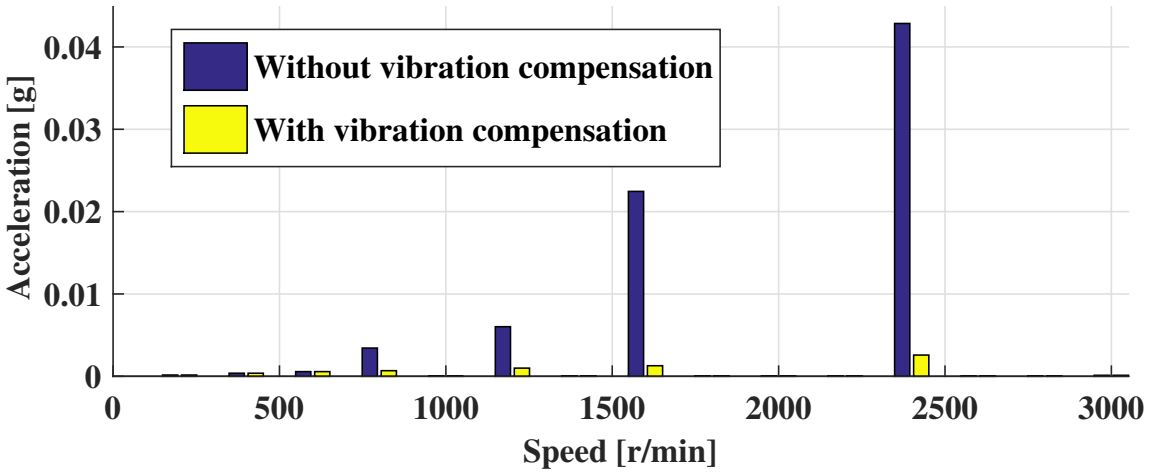


Figure 6.15: 80 Hz vibration harmonic amplitudes for different speeds with and without vibration suppression.

In this paragraph the force control has been exploited to suppress specific harmonics of the vibration spectrum. In particular, Figure 6.15 shows that the 80 Hz vibration harmonic features high peaks for several rotating speeds. The four highest peaks have been chosen as target of the vibration suppression. The selected unbalanced force to compensate are defined by means of (6.4) where k is equal to 6, 4, 3, 2 for 800 rpm, 1200 rpm, 1600 rpm and 2400 rpm, respectively. Hence, the amplitude $|F_k|$ and the phase angle φ_k are the two parameters required to define the force components of the reference vector $\bar{W}_E^*$. They are manually identified observing the changes in the vibration harmonic spectrum amplitude provided by the SKF Microlog vibration analyser. In fact, once k is defined, an arbitrary amplitude value of $|F_k|$ has to be chosen (preferably not too big). Then, φ_k is changed till the selected vibration harmonic reaches its minimum value. At this point $|F_k|$ is increased till the selected vibration harmonic is completely suppressed. Figure 6.15 and Figure 6.16 presents the compensation results achieved while in Table 6.2, the parameters used for the vibration suppression are listed.

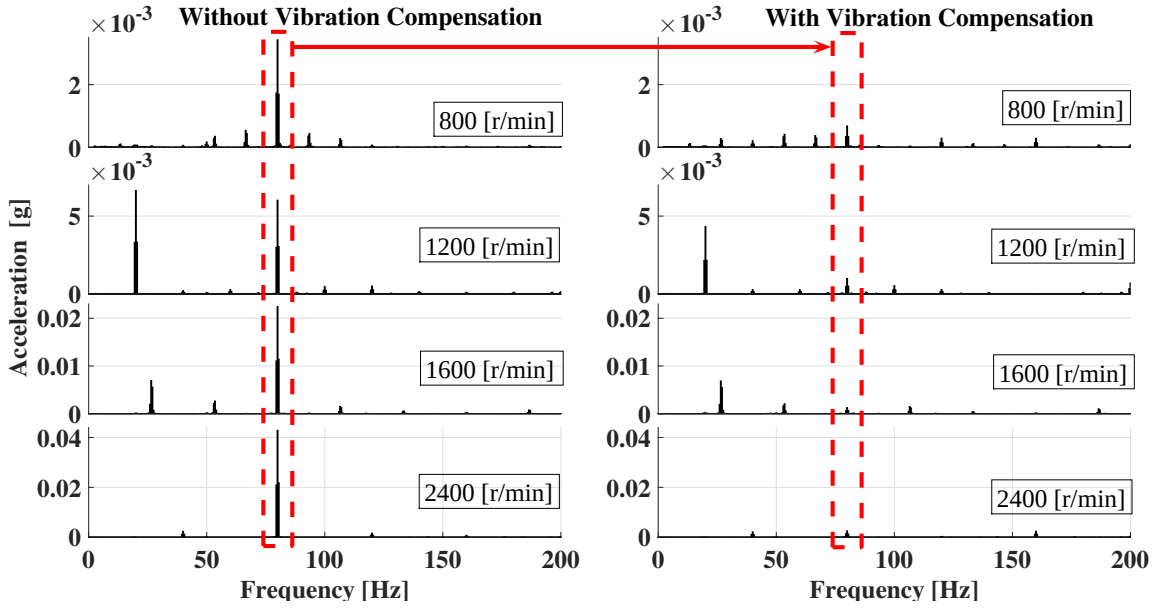


Figure 6.16: Suppression of the 80 Hz vibration at 800 rpm, 1200 rpm, 1600 rpm and 2400 rpm.

Table 6.2: Vibration Suppression Parameters

ω_m [rpm]	800	1200	1600	2400
$\|F\|[N]$	35	55	47	120
φ [deg]	220	230	80	100

Two higher vibration peaks can be found in Figure 6.14 at 425 and 440 Hz for 1500 and 2200 rpm rotating speed, respectively. An attempt to suppress the two peaks has been done and the results are shown in Figure 6.17 and 6.18.

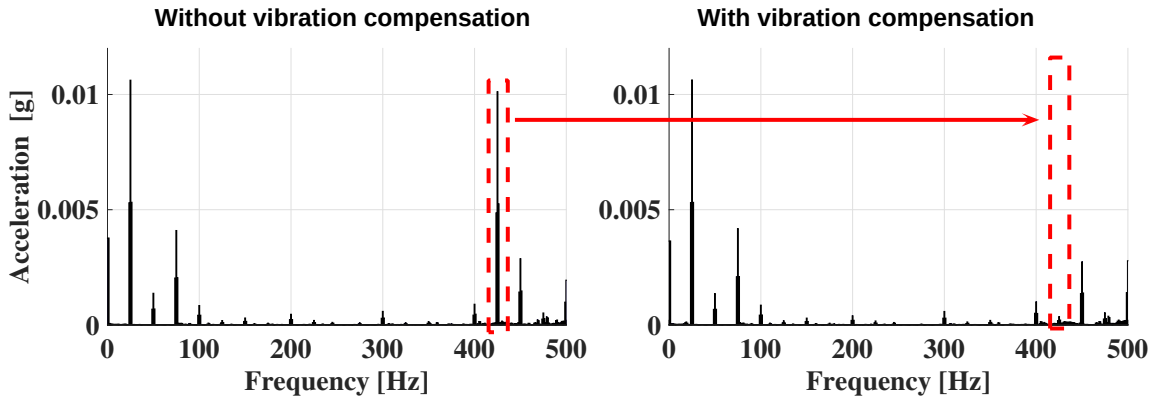


Figure 6.17: Suppression of the 425 Hz vibration at 1500 rpm.

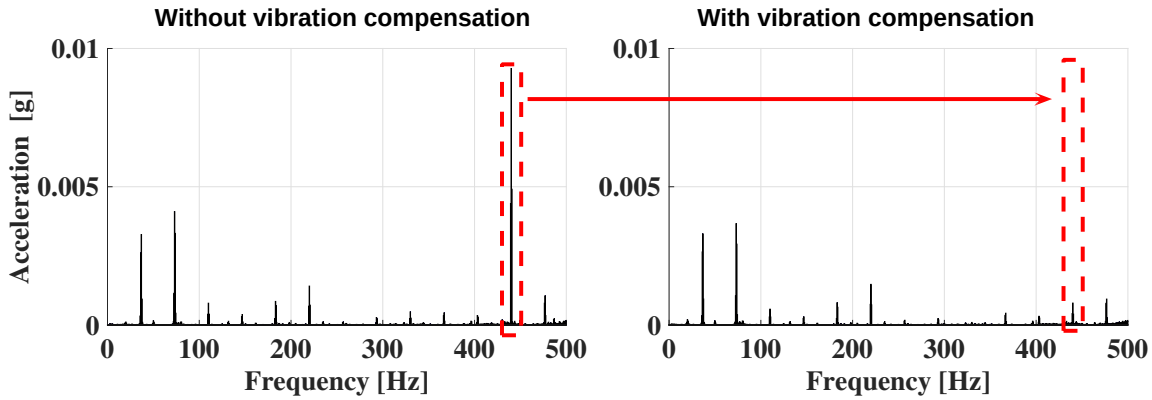


Figure 6.18: Suppression of the 440 Hz vibration at 2200 rpm.

6.4.3 Post-processing analysis

The measured $d-q$ axis current waveforms supplied to the three motor sectors to perform the 80 Hz vibration suppression at 800, 1200 1600 and 2400 rpm are shown in Figures 6.19, 6.20, 6.21 and 6.22, respectively.

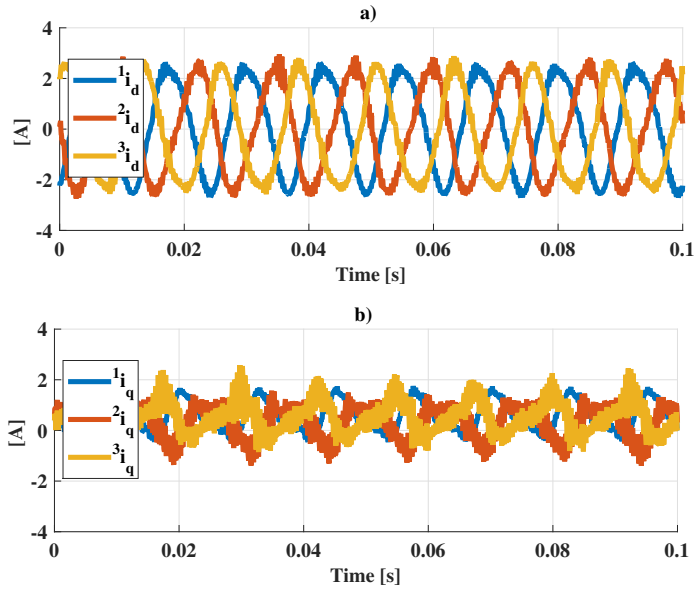


Figure 6.19: Measured d−q axis currents absorbed by the three sectors for the 80 Hz vibration compensation at 800 rpm: a) d− axis current; b) q− axis current

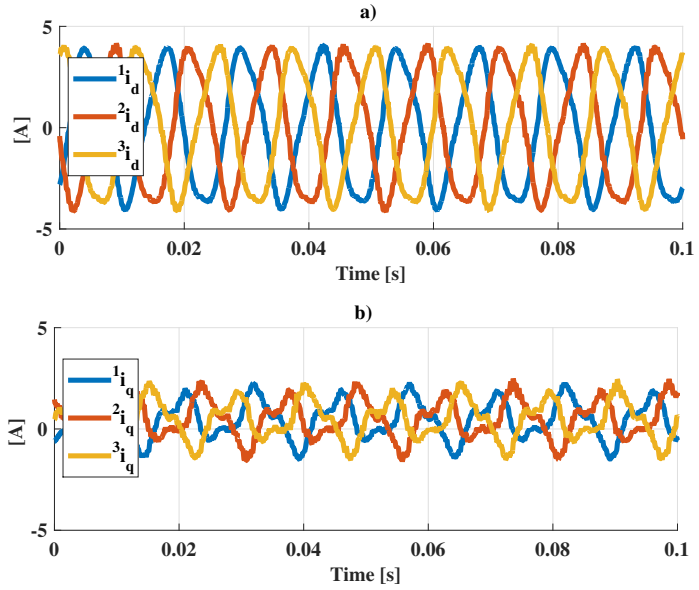


Figure 6.20: Measured d−q axis currents absorbed by the three sectors for the 80 Hz vibration compensation at 1200 rpm: a) d− axis current; b) q− axis current

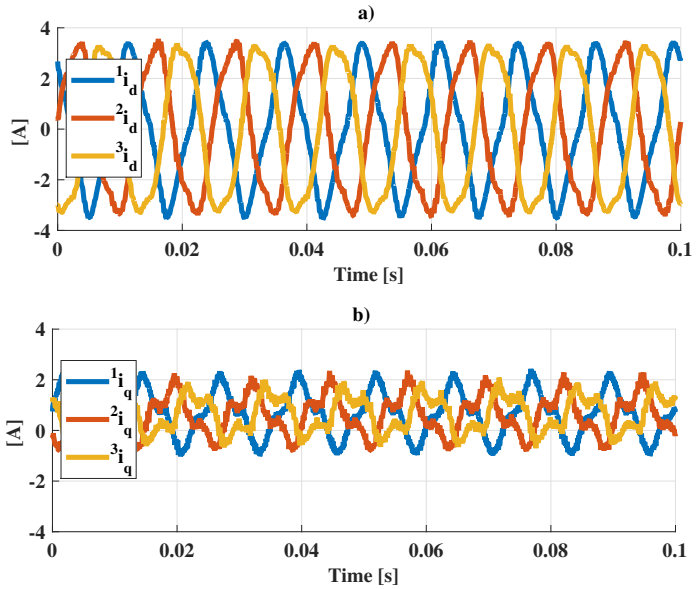


Figure 6.21: Measured d−q axis currents absorbed by the three sectors for the 80 Hz vibration compensation at 1600 rpm: a) d− axis current; b) q− axis current

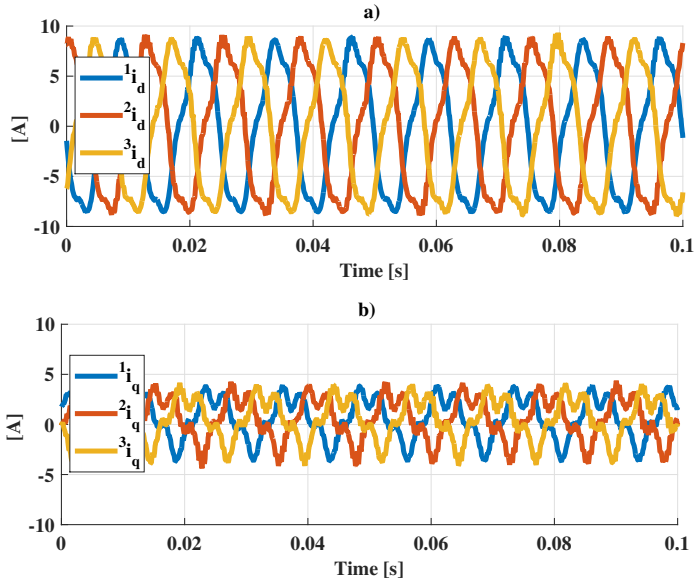


Figure 6.22: Measured d−q axis currents absorbed by the three sectors for the 80 Hz vibration compensation at 2400 rpm: a) d− axis current; b) q− axis current

It can be noticed that the current waveforms are distorted. Their main harmonic component is at the same frequency of the produced rotating force (80 Hz). Figure 6.23 a)-h) shows the harmonic spectrum of the measured, reference and analytical $d-q$ axis currents of sector 1 carried out with the FFT. It can be observed that the $d-q$ axis currents required to produce the rotating force consist of a main harmonic at the desired frequency kf_{rot} and two secondary harmonics. The explanation for this phenomena can be found in the analytical expression of the $d-q$ axis reference currents as a function of $|F_k|$ and φ_k. The latter can be easily obtained with (3.62) (setting $\delta = 0$) replacing $\bar{W}_E^*$ with the expressions of the rotating force references given in (6.4) and the torque reference T_{ref}. For the sake of brevity only the analytical expression of the reference $d-q$ axis current of sector 1 is reported in (6.5).

$$\begin{cases} i_{d1} = \Big[k_d(\varphi_k) + k_{d+}(\varphi_k) + k_{d-}(\varphi_k)\Big]|F_k| \\ i_{q1} = \Big[k_q(\varphi_k) + k_{q+}(\varphi_k) + k_{q-}(\varphi_k)\Big]|F_k| - k'_T\, T_{ref} \end{cases} \tag{6.5}$$

The coefficients k_d, k_{d+} and k_{d-} are reported in (6.6)

$$\begin{cases} k_d(\varphi_k) = \frac{(k_1+k_3)}{2}\cos\left(\vartheta_e\,\frac{k}{p} + \varphi_k\right) \\ k_{d+}(\varphi_k) = \frac{(k_1-k_2-k_3-k_4)}{4}\cos\left(\vartheta_e\left[\frac{k}{p}+2\right] + \varphi_k\right) \\ k_{d-}(\varphi_k) = \frac{(k_1+k_2-k_3+k_4)}{4}\cos\left(\vartheta_e\left[\frac{k}{p}-2\right] + \varphi_k\right) \end{cases} \tag{6.6}$$

while coefficients k_q, k_{q+} and k_{q-} are detailed in (6.7)

$$\begin{cases} k_q(\varphi_k) = \frac{(k_4-k_2)}{2}\sin\left(\vartheta_e\,\frac{k}{p} + \varphi_k\right) \\ k_{q+}(\varphi_k) = \frac{(-k_1+k_2+k_3+k_4)}{4}\sin\left(\vartheta_e\left[\frac{k}{p}+2\right] + \varphi_k\right) \\ k_{q-}(\varphi_k) = \frac{(k_1+k_2-k_3+k_4)}{4}\sin\left(\vartheta_e\left[\frac{k}{p}-2\right] + \varphi_k\right) \end{cases} \tag{6.7}$$

Finally, k_1, k_2, k_3 and k_4 are the amplitudes of the coefficients of $\mathbf{K}_E^+(\vartheta_e)$ related to sector 1 only. In fact, the sub-matrix $\mathbf{K}_{E,1}^+(\vartheta_e)$ extracted from $\mathbf{K}_E^+(\vartheta_e)$ considering

only sector 1 is expressed as follow

$$\mathbf{K}^{+}_{E,1}(\vartheta_e) = \begin{bmatrix} k_1\cos(\vartheta_e) & k_2\sin(\vartheta_e) & k'_T\sin(\vartheta_e) \\ k_3\sin(\vartheta_e) & k_4\cos(\vartheta_e) & -k'_T\cos(\vartheta_e) \end{bmatrix} \tag{6.8}$$

where $k'_T = 1/(n_s k_T)$ A/Nm.

In equations (6.6) and (6.7) the amplitudes and frequencies of the aforementioned harmonics are presented. The same calculations can be done for sector 2 and 3 obtaining an expressions of the $d-q$ axis reference current with identical harmonic orders content but with different amplitudes and phase angles.

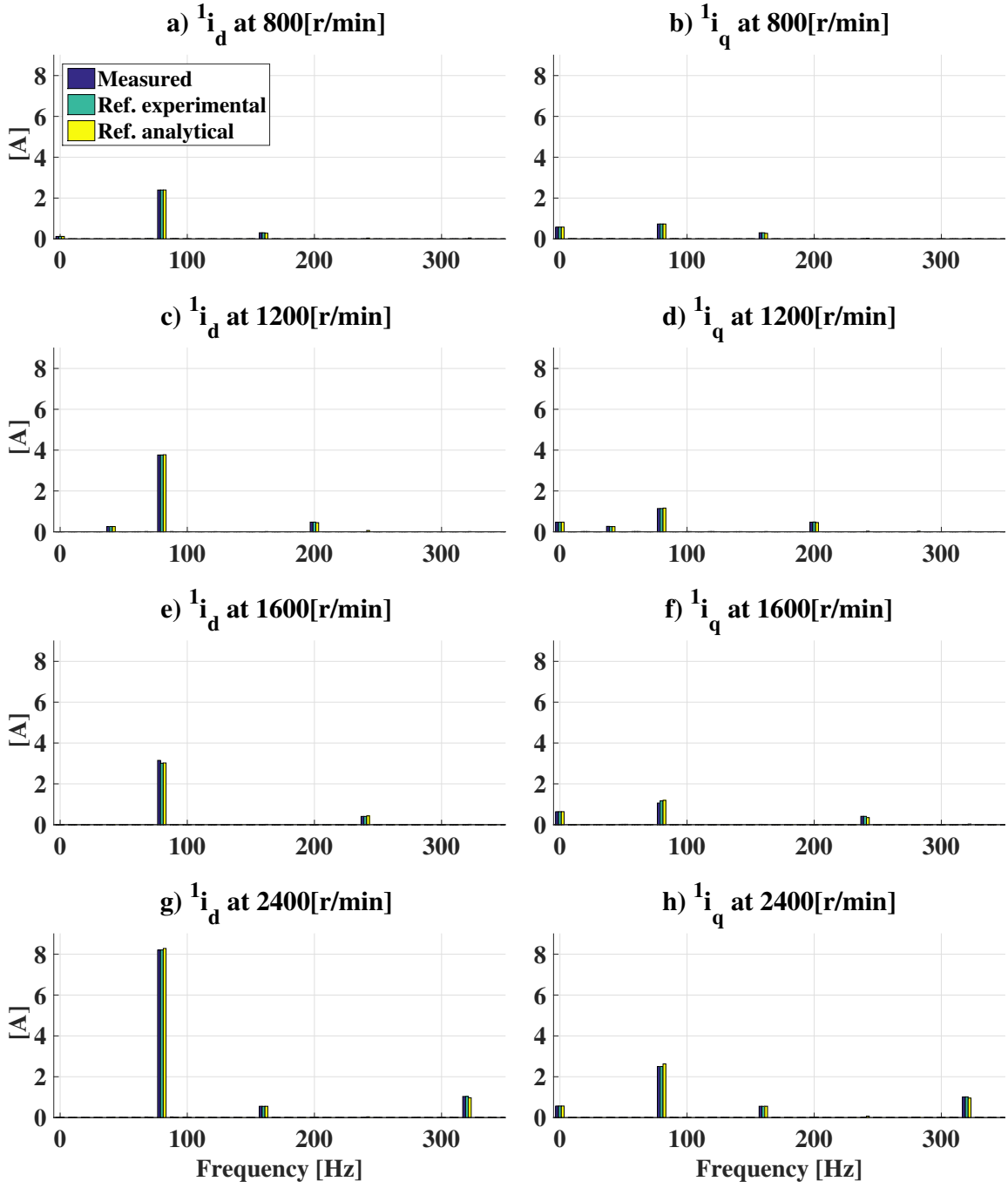


Figure 6.23: FFT amplitudes of the measured, reference and analytical $d-q$ axis currents absorbed by sector 1 for the 80 Hz vibration compensations.

6.5 Bearingless Operation

This section presents the experimental results obtained performing the tests for bearingless operations. In the first paragraph a detailed description of the procedure followed to achieve the 2-DOF levitation is proposed. Then, several experimental results of the 2-DOF levitation are displayed in the second paragraph. The standard position controller designed with a transfer function-based method in section 4.2 is employed and different torque operating conditions were considered. Both healthy and open-circuit fault of one motor sector are investigated. Finally, the third paragraph presents the experimental validation of the standard and MR controller designed with a state space method considering both the LQR and the LMI theory in sections 4.3, 4.4 and 4.5.

6.5.1 Preliminary tests

The $x - y$ axis position sensors were connected through the extension cables to the proximitors and mounted on the probe supports as shown in Figure 6.24. Then, they have been positioned 1 mm far from the ring inserted on the shaft equipped with standard ball bearings on both sides. The threaded surface of the probe allowed a convenient regulation of the gap between the sensor tip and the ring. The exact distance could be obtained knowing that the proximitor output DC voltage with 1 mm displacement is 7 V.

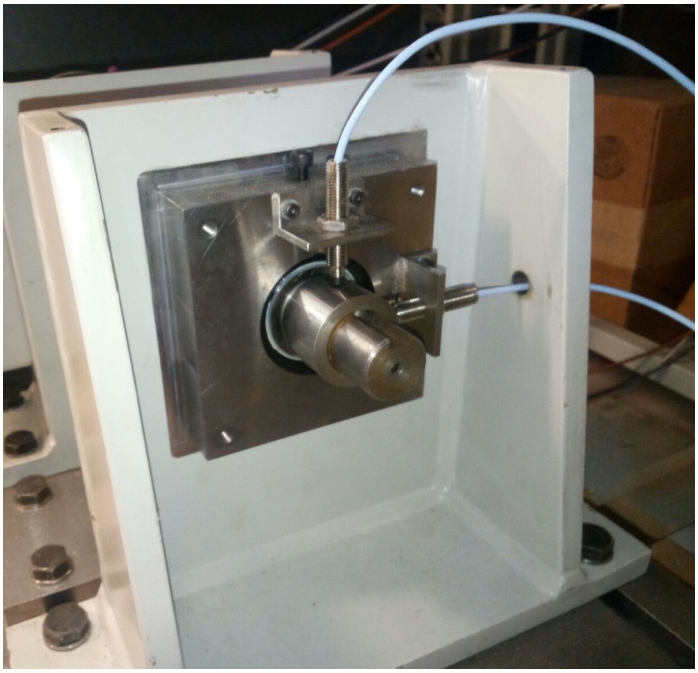


Figure 6.24: Proximity sensors mounted on the probe supports.

At this point, the shaft-rotor part for normal motor operations was removed and substituted with the one arranged for bearingless operations, paying attention not to move the proximity sensors. The angle γ_0 had to be measured with precision in order to calculate the force coefficients as illustrated in Chapter 3. Figure 6.25 shows the machine stator with the multi-phase sectored winding. Each motor sector has been labelled in the Figure so that it can be observed that sector 1 has been assigned to the three-phase winding at the bottom. Therefore, γ_0 could be established being -97.54 deg for the considered machine. The $d-q$ axis reference currents could then be obtained as in Appendix C.

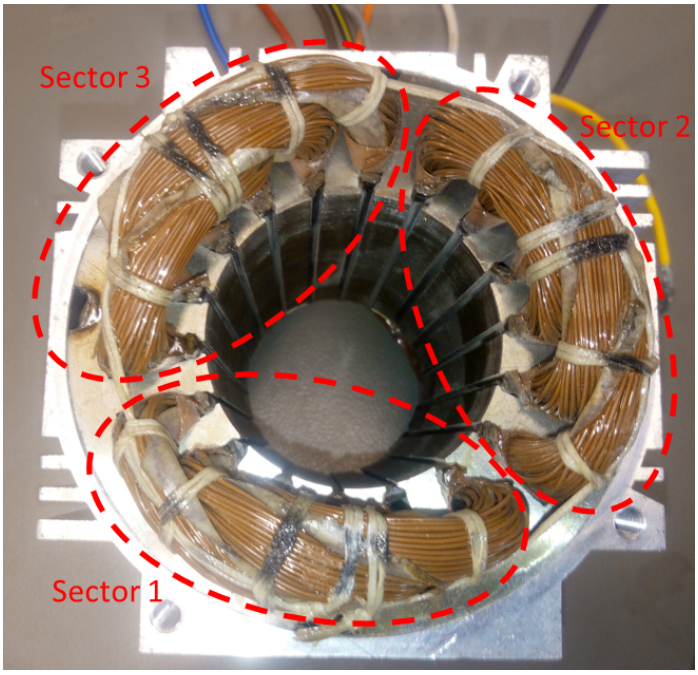


Figure 6.25: View of the MSPM machine stator and of the multi-phase sectored winding.

A preliminary test has been performed in order to verify that the direction of the generated radial force was appropriate. At stand still, a rotating force of magnitude $|F| = 150$ N and frequency 0.5 Hz has been commanded in open loop in order to check that the $x - y$ axis reference force components were in phase with the $x - y$ axis rotor position. The recorded $x - y$ rotor position and the reference rotating force is presented in Figure 6.26 showing that the commanded force push the rotor against the backup bearing in the expected position.

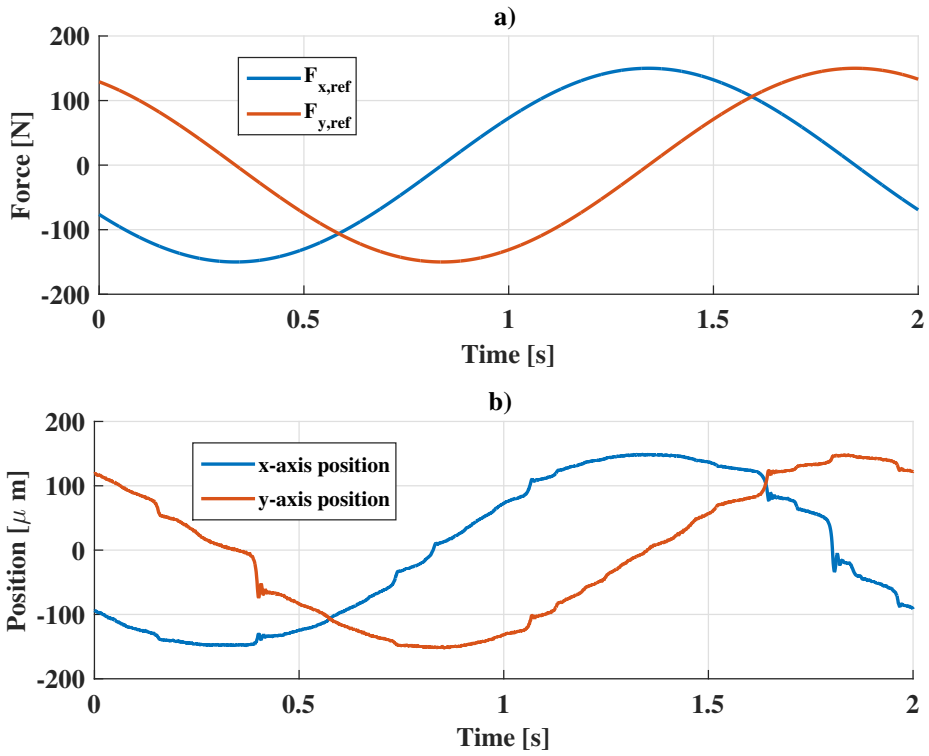


Figure 6.26: Open loop force control: a) rotating force reference; b) measured rotor position.

Exploiting the above mentioned test it is possible to verify whether the backup bearing centre coincides with the [(0,0)] of the proximity sensors. The easiest way was to compare the circular rotor trajectory with the circle which describes the backup bearing inner surface as depicted in Figure 6.27. It can be noticed in the Figure that the blue circular line, representing the rotor path, is translated with respect to the dashed line of the backup bearing. The correction could be easily implemented at software level adding 5 and 10 μm in the $x-$ and $y-$ axis position measures, respectively. The corrected rotor trajectory (red line in the Figure) matches very well the backup bearing line.

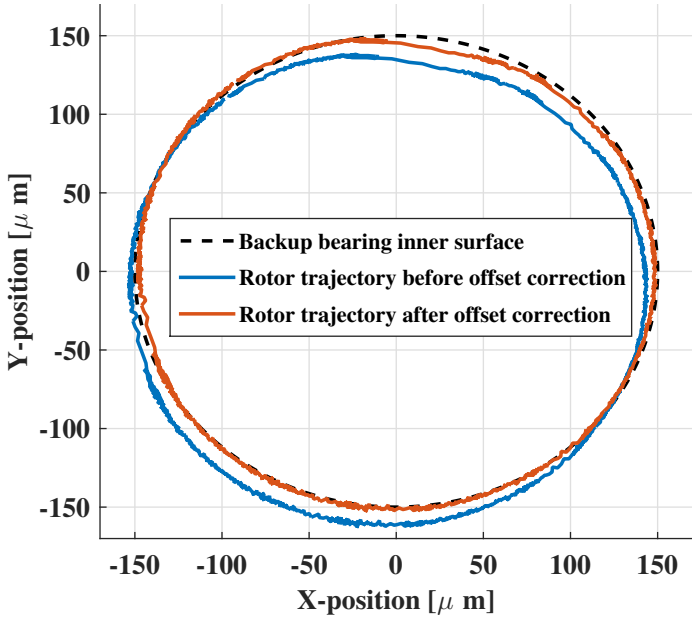


Figure 6.27: Rotor trajectory before and after the offset correction.

Finally, it is important to establish whether the stator and the sensors centre coincide. The verification could be done at stand still commanding a rotating reference radial position as shown in Figure 6.28 a). The chosen reference displacement was 100 μm. Observing the $x - y$ axis position controller output force in 6.28 b) it can be noticed that if the two above mentioned centres do not coincide the circular force trajectory is not centred in [(0,0)]. Therefore, small shims could be added on the one side of the housing in order to move the stator centre in the required direction.

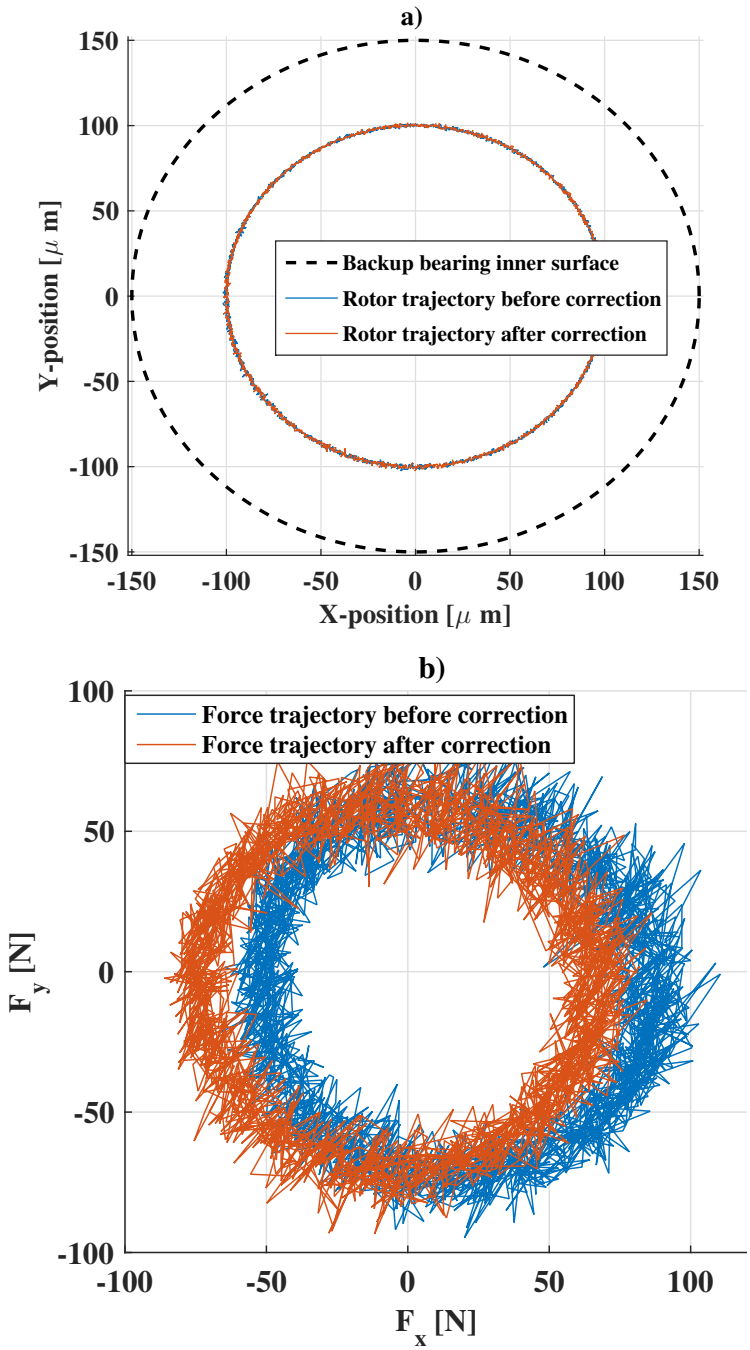


Figure 6.28: Closed loop radial rotor position control with a rotating position reference: a) rotor trajectory before and after the correction; b) force trajectory before and after the correction.

6.5.2 Levitation results for the standard controller designed with pole placement method

6.5.2.1 Healthy operation

Once the experimental set up has been prepared for the 2-DOF levitation the position control can be activated setting the $x-y$ axis position reference at [(0,0)]. To start with, the 2-DOF position control designed in section 4.2.2 is verified at stand still. Figure 6.29 a) shows the initial position transient after the position controller is activated at $t = 0.01$ s. It can be noticed that the rotor is brought to its central position after a short transient of around 0.15 s. Furthermore, the $x-y$ axis force output of the position controller presented in Figure 6.29 b) shows that after the initial transient the steady state force is equal to the rotor weight force. The result is obtained choosing the pulsation equal to $\omega_0 = 2\pi 170$ rad/s leading to the gains values reported in Table 4.1. On the other hand, Figure 6.30 displays the result of an identical test where ω_0 is set equal to $2\pi 20$ rad/s. It is straightforward that the position controller is not capable to maintain the rotor centred in [(0,0)].
It can be noticed that the initial rotor position is different in the two tests. This is due to the large attraction force between rotor and stator generated by the PMs that tends to push the rotor in the displacement direction as soon as the radial position control is disabled. Therefore, the initial position can change performing different tests.

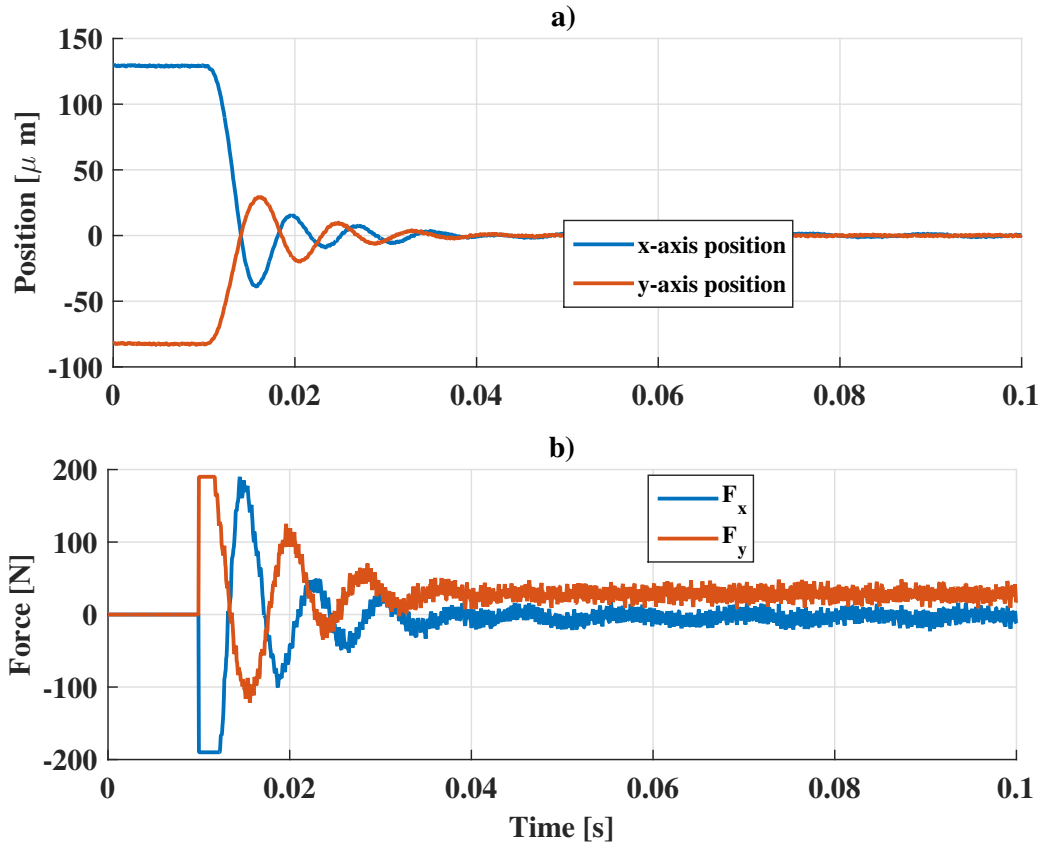


Figure 6.29: Start up of the 2-DOF levitation setting $\omega_0 = 2\pi 170$ rad/s: a) $x-y$ axis position; b) $x-y$ axis force output of the position controller

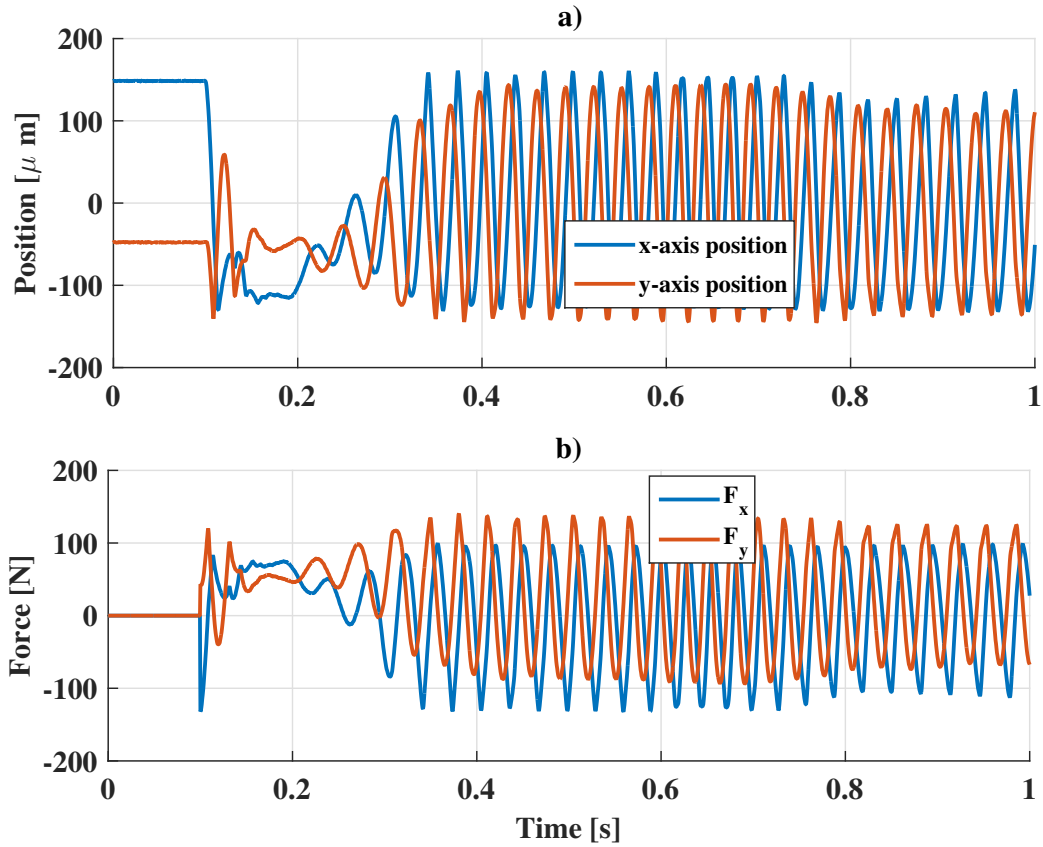


Figure 6.30: Start up of the 2-DOF levitation setting $\omega_0 = 2\pi 20$ rad/sz: a) $x-y$ axis position; b) $x-y$ axis force output of the position controller

Hereafter the experimental results shown are obtained for $\omega_0 = 2\pi 170$ rad/s. A speed transient test has been performed in order to verify the 2-DOF levitation while the rotor accelerates from 0 to the rated speed. The position control is activated after 0.2 s as shown in Figure 6.31 a) while at 0.6 s a reference speed ramp is commanded. The rotor reaches the rated speed in less than 0.4 s as depicted in 6.31 b). It can be noticed that a position oscillation arises as soon as the rotor starts spinning. However, the position controller maintains the rotor centred with a maximum displacement of about 30 μm (30 % of clearance given by the backup bearing). The aforementioned oscillation can be completely rejected by the MR controller designed in section 4.5 as it will be demonstrated in the following section.

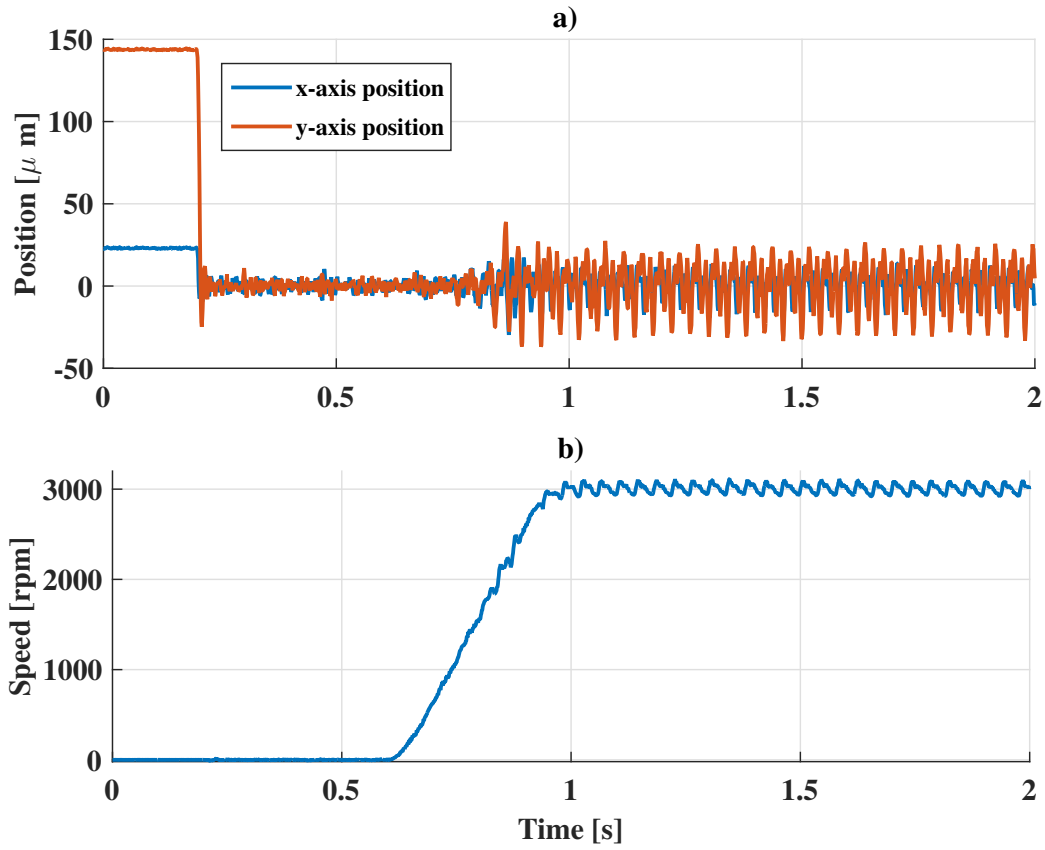


Figure 6.31: Bearingless operation test for a speed transient from 0 to 3000 rpm: a) $x-y$ position; b) rotor angular speed.

The test at full load could be performed controlling the MSPM machine as a motor and the DC load as a generator. In Figure 6.32 a), b) and c) the comparison of levitation performance between zero torque and rated torque operating conditions is presented. Three operating speeds were considered: 1000 rpm, 2000 rpm and 3000 rpm. It can be noticed that the rotor radial position is very little affected by the load conditions. Figure 6.33 shows the measured $d-q$ axis current of the three sectors at zero and rated torque operating conditions for 3000 rpm rotating speed. It can be noticed that in both load conditions the $d-$axis currents of the three sectors present

large spikes due to the position oscillation. Furthermore, when torque is produced with the MSPM machine the $q-$axis current increases from 0 to about 13 A.

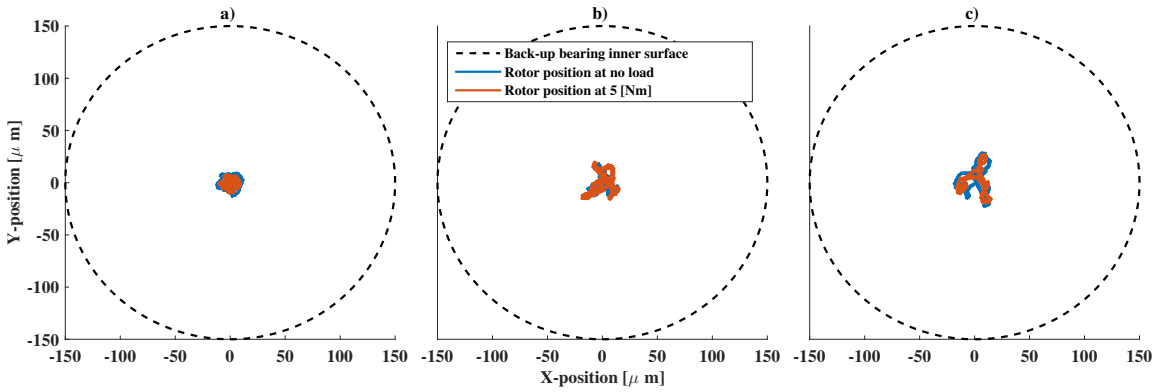


Figure 6.32: Rotor trajectory obtained at no load and load ($T_E = T_{rated}$) operating conditions at different rotating speeds: a) 1000 rpm; b) 2000 rpm; c) 3000 rpm.

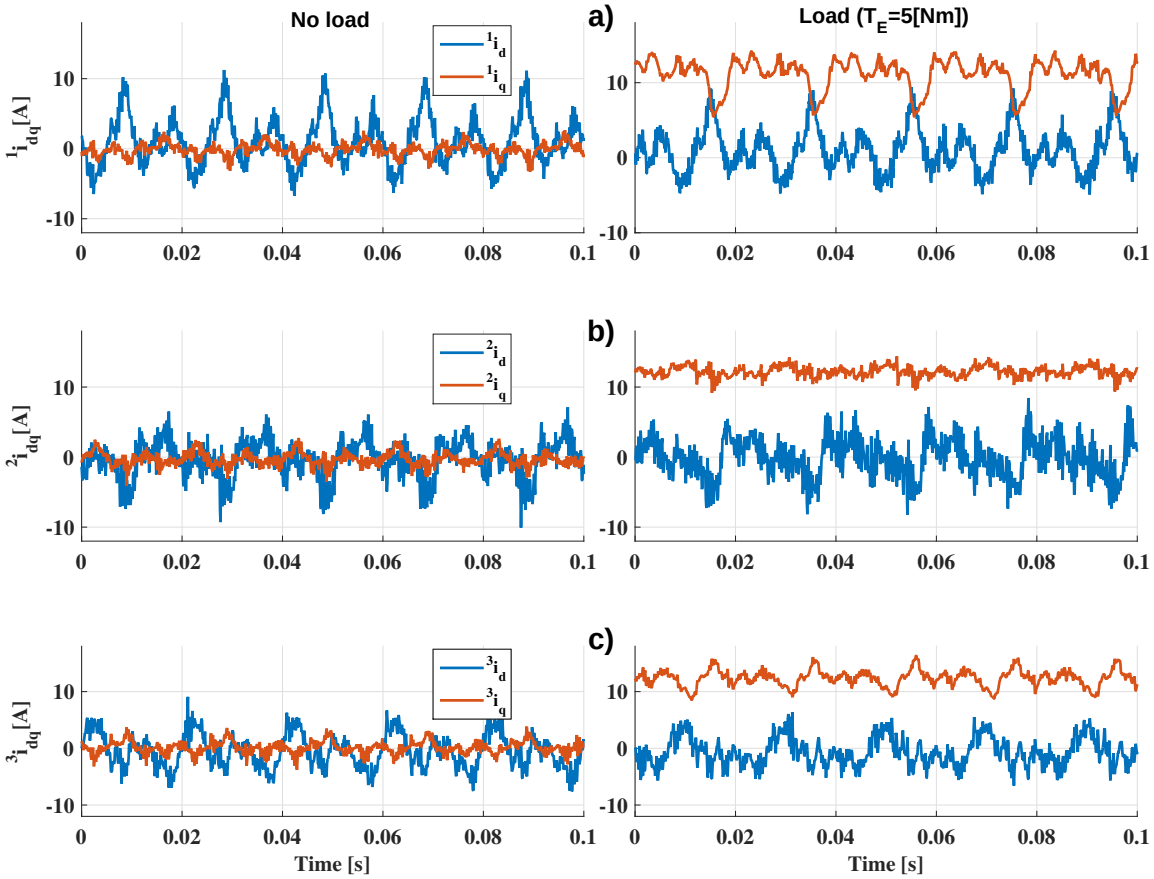


Figure 6.33: Measured $d-q$ axis current of the three sector during bearingless operation at 3000 rpm for no load and load ($T_E = T_{rated}$) operating conditions: a) sector 1; b) sector 2; c) sector 3.

6.5.2.2 Open-circuit fault

This paragraph presents the experimental validation of the open-circuit fault tolerant capability of the bearingless MSPM machine. In the first test, the position control is activated in healthy condition and the motor is dragged by the DC load at 2000 rpm. Then, a torque step of 3 Nm is commanded. A time period of 0.1 s has been recorded

and shown in Figure 6.34. After 0.02 s from the trigger time the inverter connected to sector 1 has been disabled (all the IGBTs opened) in order to cause a three-phase open-circuit fault in the related winding sector. In fact, as can be seen in Figure 6.34 b), the three-phase currents of sector 1 go to zero loosing the sector contribution to the force and torque generation. At the same time, the $d-q$ axis reference currents calculation switches from equation (C.4) to (C.9). It can be noticed in Figure 6.34 b) and c) that the current demand on the healthy sectors increases. Furthermore, the resultant phase current waveforms are more distorted due to the presence of the third harmonic as it was depicted in paragraph 3.4.3. As it can be appreciated from Figure 6.34 a) the rotor $x-y$ position does not present any remarkable perturbation after the open-circuit fault of one sector.

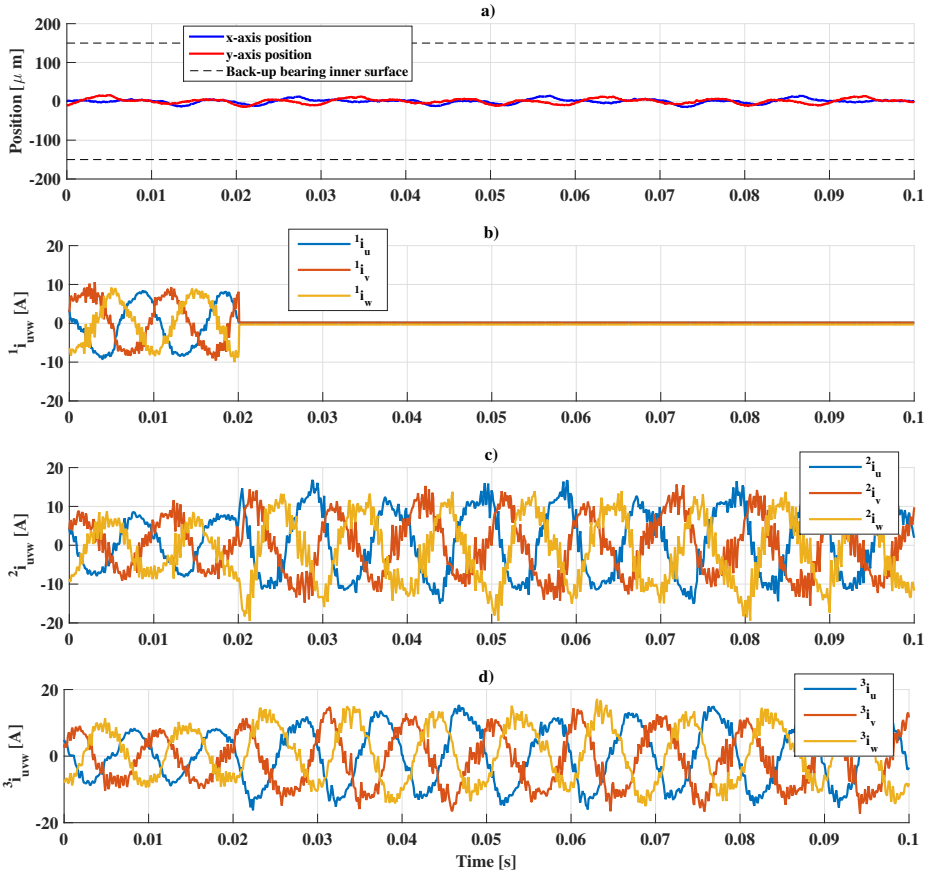


Figure 6.34: Simulation results for open-circuit fault in sector 1 at 2000 rpm operating speed and $T_E = 3$ Nm: a) $x - y$ axis position b) phase currents of sector 1; c) phase currents of sector 2; d) phase currents of sector 3.

The results of a similar test, where the rotating speed is 3000 rpm and the torque 2 Nm, is shown in Figure 6.35. Again the rotor radial position is not sensibly affected by the open-circuit fault of one sector.

An attempt to command a torque step of 3 Nm has been done and the result is shown in Figure 6.36. However, a short time after the fault in sector 1 was induced, the current ^3i_v exceeded the limit given by the software protection and the inverters pulses were automatically disabled. Therefore, the rotor position is not controlled any more as can be seen in Figure 6.36 a).

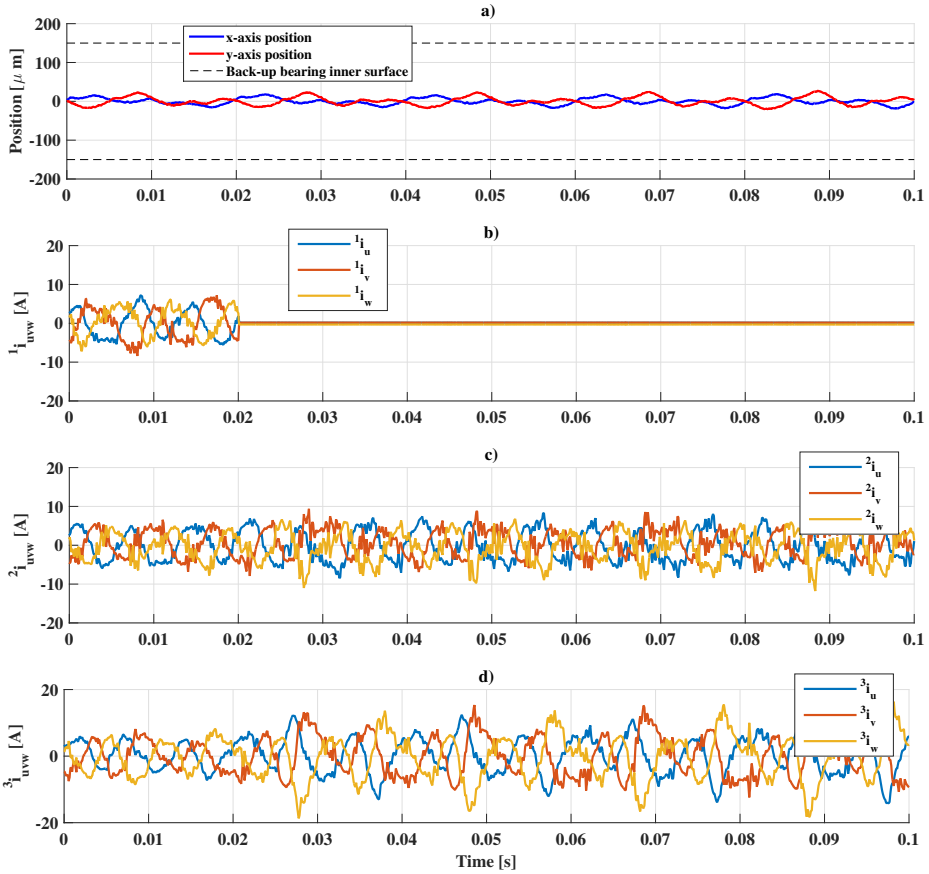


Figure 6.35: Simulation results for open-circuit fault in sector 1 at 3000 rpm operating speed and $T_E = 2$ Nm: a) $x - y$ axis position b) phase currents of sector 1; c) phase currents of sector 2; d) phase currents of sector 3.

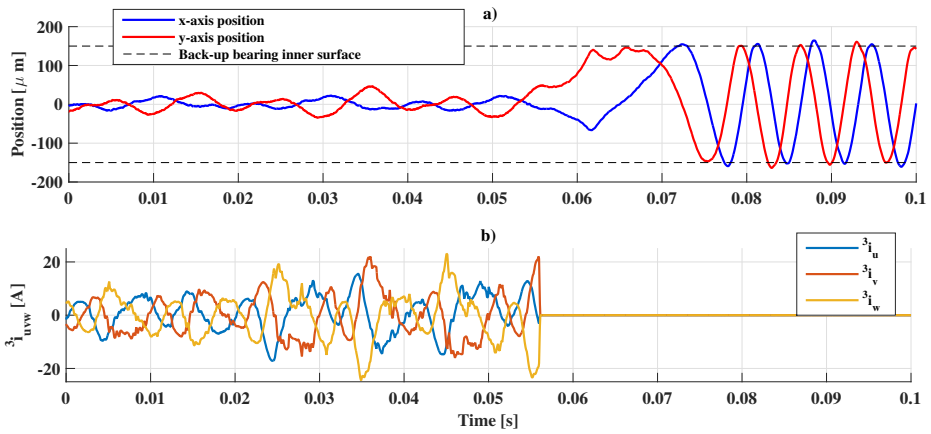


Figure 6.36: Simulation results for open-circuit fault in sector 1 at 3000 rpm operating speed and $T_E = 3$ Nm: a) $x - y$ axis position b) phase currents of sector 3.

6.5.3 Levitation results for the standard and the MR controller designed in state space

The suppression of the multi-frequency position oscillation has been tested for three different operating speeds ($\omega_m = 2\pi 30, 2\pi 40, 2\pi 50$ Hz) in order to experimentally validate the stability of the position controllers in a wide speed range. Figure 6.37 a)-c) shows the rotor trajectory in a $x - y$ plane. It can be noticed that both the standard and the MR controllers can achieve stable bearingless operations keeping the rotor element far from the backup bearing inner surface. From the Figures it can also be observed that the MR controller significantly improves the levitation performances maintaining the rotor displacement within 10 μm against the 40 μm achieved with the standard controller.

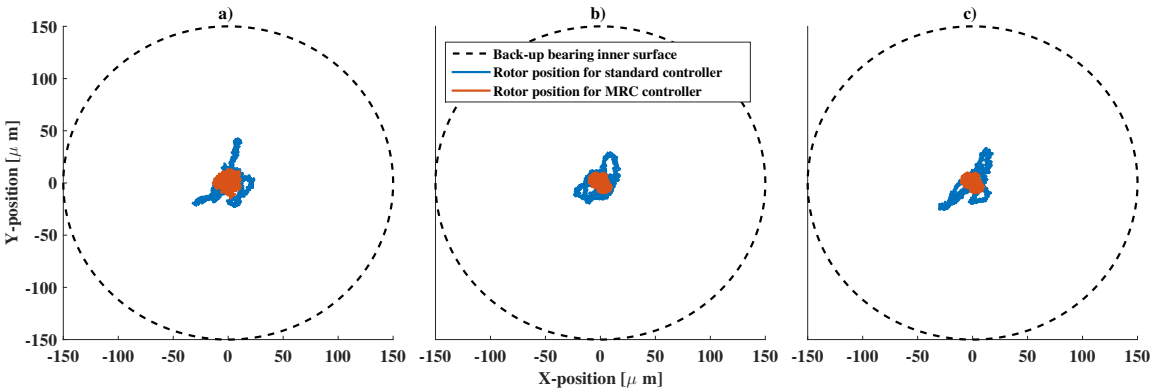


Figure 6.37: Rotor trajectory obtained with the standard and with the MR position controllers: a) 30 Hz rotating speed; b) 40 Hz rotating speed; c) 50 Hz rotating speed;

The harmonic spectrum of the $x-$axis position for the three rotation speeds considered is presented in Figure 6.38. It can be appreciated how the MRC manages to damp the first four position harmonics corresponding to the pulsations $\omega_1 = \omega_m$, $\omega_2 = 2\omega_1$, $\omega_3 = 3\omega_1$ and $\omega_4 = 4\omega_1$.

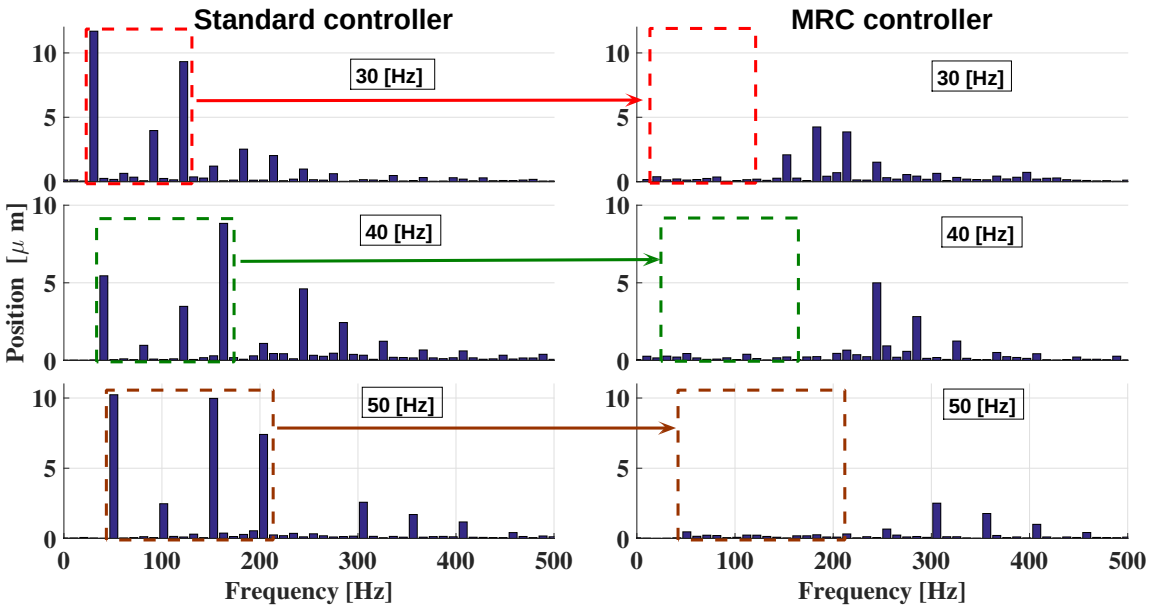


Figure 6.38: Harmonic spectrum carried out with the fast Fourier transform of the $x-$axis position measurement. The compensation of the multi-frequency position oscillation can be appreciated.

The previous experimental results prove the improvements in terms of levitation performances of the MRC respect to the standard controller in steady state operating conditions. However, the rapidity of damping the position oscillation should also be taken into account in the analysis, hence a transient test has been performed running the motor progressively from stand still to 30, 40 and 50 Hz within one second. The results are presented in Figure 6.39. In particular, the speed transient is shown in Figure 6.39 a) while Figure 6.39 b) and c) shows the $x-y$ axis position for standard and MR controllers, respectively. In both tests, the position controllers are activated after 10 ms and the rotor reaches the reference position in about 15 ms (Figure 6.39 b) and c)). Then the rotor is accelerated as shown in Figure 6.39 a) and the MRC quickly operates an effective damping of the position oscillation during the speed variations (Figure 6.39 c)). On the other hand, a remarkable position oscillation is present if the standard controller is employed in the test as shown in Figure 6.39 b).

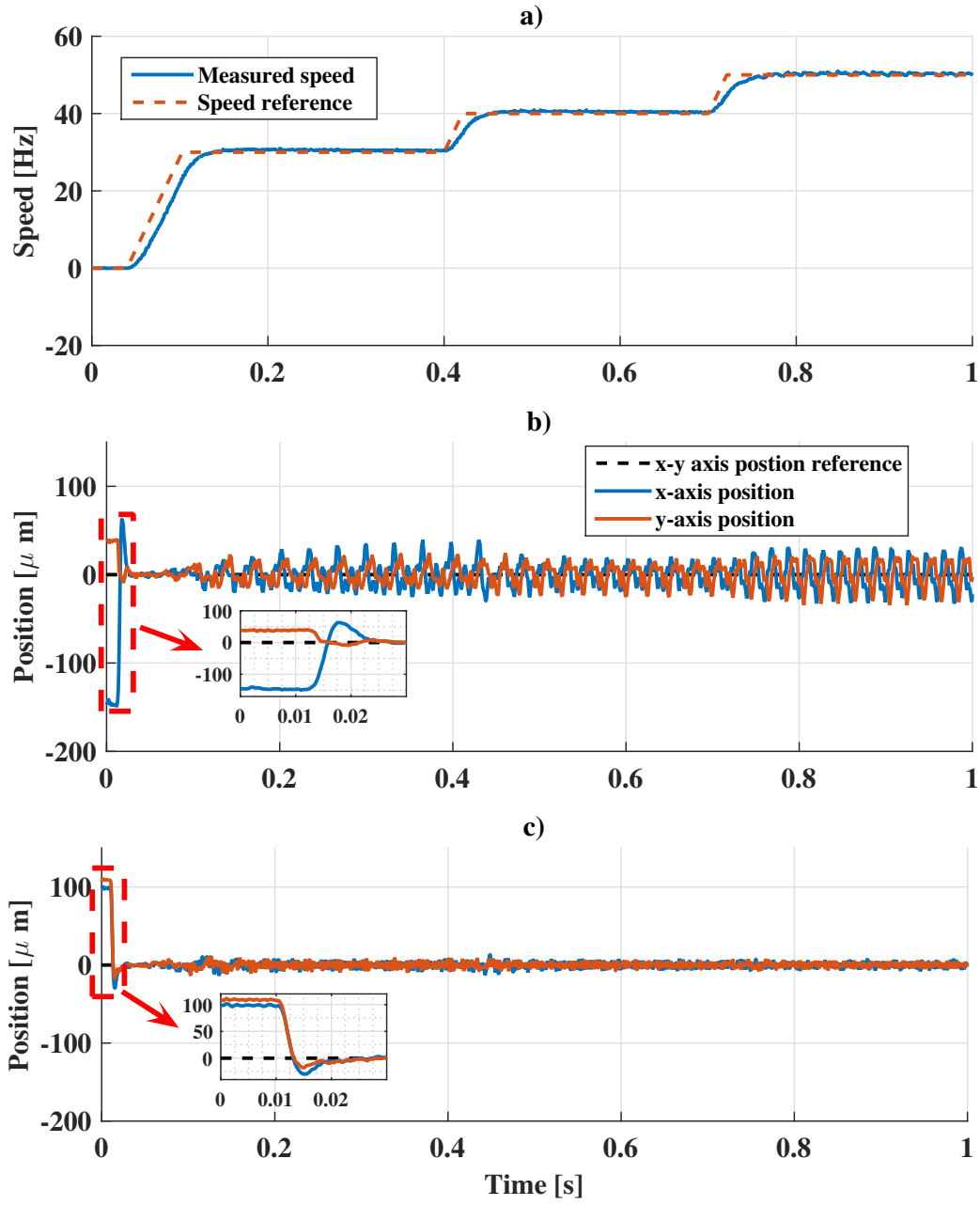


Figure 6.39: Transient bearingless operation results using the standard and the MR controllers: a) rotating speed; b) $x-y$ axis position obtained with the standard controller; c) $x-y$ axis position obtained with the MR controller.

6.6 Conclusions

This Chapter showed the experimental results obtained both for normal and bearingless operations. At first, a detailed description of the experimental set up has been provided. Then, the main electrical parameters such as back-EMF and inductances are computed with FE simulations and compared to the experimental results. The particle swarm optimization technique has been adopted to identify the inductance L_d for different current values together with the phase resistance R_{ph} and voltage drop of the switches and diodes V_c. It has been possible then to observe the impact of the saturation on the $d-$axis inductance value. The $q-$axis inductance could not be identified at the time, hence this task is postponed to a future investigation.

In the following section, the experimental results for the vibration suppression were displayed. Normal motor operations were considered for these tests. The main aim was to demonstrate the feasibility of the radial force control method proposed. It has been shown that a controllable radial force can be generated and exploited to suppress selected vibration harmonics. Although the presented results only aim to experimentally validate the proposed radial force control technique, the work presents a great potential. As a matter of facts, the same control strategy can be employed to damp the forces that occur when crossing critical frequencies, hence allowing the rotor to achieve high rotating speed, with the drawback of generating more distorted currents.

In the last section the results for bearingless operations have been shown. The procedure followed to achieve the 2-DOF levitation has been first described and some preliminary results have been presented. Then, the 2-DOF levitation results under different operating conditions were presented. As a matter of fact, zero and rated torque operating conditions together with healthy and faulty conditions have been considered. The 2-DOF position controller designed with a transfer function-based method has been employed for the tests. It could be observed that the position control achieves a stable rotor suspension in the whole operating speed, at rated torque and during a open-circuit fault of one winding sector. However, as the rotating speed

increases a remarkable position oscillation appears. Therefore, in the last paragraph the effectiveness of the MR controller could be experimentally validated showing a significant reduction of the periodic position oscillations.

Chapter 7

Conclusions

7.1 Summary of Achievements and Conclusion

The first part of the PhD project dealt with the radial force and torque generation technique of a multiphase sectored PM synchronous machine. In particular, a 18 slot-6 pole PMSM featuring a multi-sector multiphase winding arrangement has been considered. The machine has been analysed and an alternative mathematical model for the electromagnetic torque and radial force production has been developed analytically and verified by FEA. To start with, the rotor element was assumed rigid and fixed in the stator centre. Then, the rotor eccentricity has been analysed and the mathematical model reformulated to take into account its effect on the radial force and torque generation. Finally, the redundant degrees of freedom of the MSPM machine can be exploited to achieve an effective force and torque control during an open-circuit fault of one three-phase motor winding.

The torque and radial force models obtained result under-determined, hence the pseudo inverse matrix is introduced to define the optimal current reference signals that minimize the copper losses. The capabilities and performances of the proposed

method are validated through FEA, where several simulations were performed considering different operating conditions.

The final goal of the PhD project was the achievement of the 2-DOF levitation exploiting the force generation model carried out for the analysed MSPM machine. Therefore, a certain amount of time has been committed to design the radial position control. Two design approaches were considered: a transfer function-based approach and a state space approach. The former allowed to obtain a position controller that could stabilize the rotor position during bearingless operations while the latter permitted to synthesize an optimum and robust controller. Furthermore a multi-resonant controller was designed with the state space method with the aim of rejecting the multi-frequency position oscillations caused by periodic force disturbances. A simulation model was built in the Matlab-Simulink environment in order to verify the 2-DOF position controllers.

An experimental set-up has been built to corroborate the theoretical predictions. At first, the force control strategy could be employed to suppress selected vibration harmonics that were detected by means acceleration transducers during normal motor operations. Since force transducers were not available an actual measure of the generated force could not be performed. However, the results obtained from the vibration suppression clearly demonstrate that a controllable radial force could be produced.

Finally, experimental tests on the 2-DOF levitation could be performed using proximity sensors to measure the position feedback necessary for the position control loop. Both the radial position controllers designed with a transfer function-based method and with a state space method were tested. The results obtained validate the position controllers and the force control technique. The radial position measurement showed that a multi-frequency oscillation was present due to period force disturbances. Therefore, the MR controller was tuned with the state space approach and used to suppress the periodic force disturbance. Finally, the open-circuit fault tolerant capability has been experimentally verified achieving promising results. In particular, it could be seen that the radial position controller can maintain the rotor suspended after an open-circuit fault without significantly deteriorating the levitation

performance.
The PhD project achievements can be summarized as follow:

- Full characterization of the analysed MSPM machine in terms of force and torque generation and voltage equations.
- Development of a novel radial force and torque generation technique. The latter has been written in a generalized form and can be applied to any MSPM machines.
- Suppression of the machine vibrations detected by means of accelerometer transducers. The machine was equipped with both ball bearings for this test.
- Synthesis and tuning of a 2-degrees of freedom radial position controller considering stability and robustness issues. Furthermore, a multi-resonant controller has been developed to suppress the multi-frequency radial position oscillation. The rotor suspension has been validated both by means numerical simulation and experimental tests.
- The open-circuit fault of one machine sector has been analysed and tested.

7.2 Future Work

A list of tasks for future works that have been identified as promising and challenging is given as follow:

- Design of a machine that optimizes the force production. The MSPM considered in this PhD project is a conventional PMSM that has not been designed to maximize the force generation. Therefore, future work would include exploiting the experience gained during this project to maximize the force capability of

the machine in the design phase. Furthermore, the elimination of the sinusoidal term in the $d-q$ axis reference current should also be investigated to improve the force production performance of the machine.

- In order to perform the vibration suppression the force control has been implemented in open loop since the acceleration measurement was not available in a form suitable for the control platform. Future work could include the possibility of installing accelerometer transducers that can be connected directly to the control platform allowing the implementation of more complex force control algorithms (i.e. the repetitive control) to suppress multiple vibration peaks. Furthermore, the measurement of acoustic noise variation due to the vibration compensation will be considered for a future investigation.

- The short-circuit fault capabilities should also be examined and included in a future design requirement. Indeed, the machine considered is not fault tolerant, hence very large current values are expected if a short-circuit fault occurs.

- A short and open-circuit fault detection strategy should be implemented. Indeed, in this project, the open-circuit fault was tested commanding all the IGBTs of one converter to open and simultaneously switching from health control to open-circuit control strategy. In a real implementation the fault can occur at any time and the control algorithm has to be able to detect it and act accordingly.

- The levitation feasibility was demonstrated controlling 2-DOF of the rotor. Future work would consider the implementation of a full levitating system controlling the remaining degrees of freedom. The latter can be either actively controlled or passively compensated.

- Design and manufacture of an eddy current proximity system. The accurate position detection is of fundamental importance for the development of a bearingless machine and a custom made displacement detection system would certainly improve the levitation performance.

- The radial position control loop relies on proximity sensors for the feedback signals. These sensors are expensive and they affect considerably the overall bearingless drive cost. Therefore, a further future investigation would examine the possibility of performing sensorless bearingless operations exploiting the position dependent machine inductances.

- High and ultra-high speed operating conditions should be considered in order to reduce the size of the machine. When very high rotating speeds are considered the shaft bending modes cannot be neglected and, therefore the radial position controller should be capable of compensating them. Furthermore, the calculation of the efficiency for the machine equipped with both ball bearings and for the bearingless machine should be done in the whole speed range. This analysis should determine the operating speed at which the bearingless machine performs a better efficiency then the machine with ball bearings.

- Implement and compare different radial position controllers (PID, multi-resonant, repetitive, predictive, sliding mode and so on) in terms of levitation performance, computation effort, robustness and efficiency.

- Implement on the same machine structure the different winding topologies that can be employed to produce suspension force (two-winding topology, parallel and bridge winding configuration and so on) and determine one that performs the best levitation performance and efficiency.

Appendix A

Invertion Matrix Verification

In linear algebra, a square matrix $\mathbf{A} \in \mathbb{R}^{n \times n}$ is invertible if there exists a different square matrix $\mathbf{B} \in \mathbb{R}^{n \times n}$ that satisfies the following property:

$$\mathbf{AB} = \mathbf{BA} = \mathbf{I}_n \tag{A.1}$$

where $\mathbf{I}_n \in \mathbb{R}^{n \times n}$ is the identity matrix.
In order to verify the inversion property of matrix $\mathbf{A}$ it is sufficient to demonstrate that its determinant is different from 0. In the considered case matrix $\mathbf{A} \in \mathbb{R}^{3 \times 3}$ is expressed as

$$\mathbf{A}(\vartheta_e) = \mathbf{K}_E(\vartheta_e, \bar{\gamma})\mathbf{K}_E^T(\vartheta_e, \bar{\gamma}) \tag{A.2}$$

hence, $\mathbf{A}(\vartheta_e)$ is invertible only if $det(\mathbf{A}(\vartheta_e)) \neq 0 \; \forall \; \vartheta_e$. Matrix $\mathbf{K}_E(\vartheta_e, \bar{\gamma})$ can be written as

$$\mathbf{K}_E(\vartheta_e, \bar{\gamma}) = \begin{bmatrix} {}^1\mathbf{K}_{E,F}(\vartheta_e, {}^1\gamma) & \mathbf{R}_T({}^2\gamma)\,{}^1\mathbf{K}_{E,F}(\vartheta_e, {}^1\gamma) & \mathbf{R}_T({}^3\gamma)\,{}^1\mathbf{K}_{E,F}(\vartheta_e, {}^1\gamma) \\ \bar{K}_{E,T}(\vartheta_e) & \bar{K}_{E,T}(\vartheta_e) & \bar{K}_{E,T}(\vartheta_e) \end{bmatrix} \tag{A.3}$$

where ${}^1\mathbf{K}_{E,F}(\vartheta_e, {}^1\gamma)$ is written in (A.4) having set ${}^1\gamma = 0$

$${}^1\mathbf{K}_E(\vartheta_e, 0) = \begin{bmatrix} {}^1k_{x,\alpha}(\vartheta_e, 0) & {}^1k_{x,\beta}(\vartheta_e, 0) \\ {}^1k_{y,\alpha}(\vartheta_e, 0) & {}^1k_{y,\beta}(\vartheta_e, 0) \\ {}^1k_{T,\alpha}(\vartheta_e) & {}^1k_{T,\beta}(\vartheta_e) \end{bmatrix} \tag{A.4}$$

and $\bar{K}_{E,T}(\vartheta_e)$ is defined in (3.41).
The determinant of $\mathbf{A}(\vartheta_e)$ has been computed using the Matlab tool, MuPAD, obtaining

$$det\big(\mathbf{A}(\vartheta_e)\big) = \frac{27}{4}k_T^2\left(\widetilde{k}_{x,\alpha}^2\cos(\vartheta_e)^2 - \widetilde{k}_{x,\beta}^2\cos(\vartheta_e)^2 + \widetilde{k}_{x,\beta}^2 - \widetilde{k}_{y,\alpha}^2\cos(\vartheta_e)^2 + \widetilde{k}_{y,\alpha}^2 + \widetilde{k}_{y,\beta}^2\cos(\vartheta_e)^2\right)^2 \tag{A.5}$$

Figure A.1 shows the waveform of the function described in (A.5). It can be noticed that $det\big(\mathbf{A}(\vartheta_e)\big)$ does not cross 0, therefore, it is possible to conclude that $\mathbf{A}(\vartheta_e)$ is invertible $\forall\,\vartheta_e$.

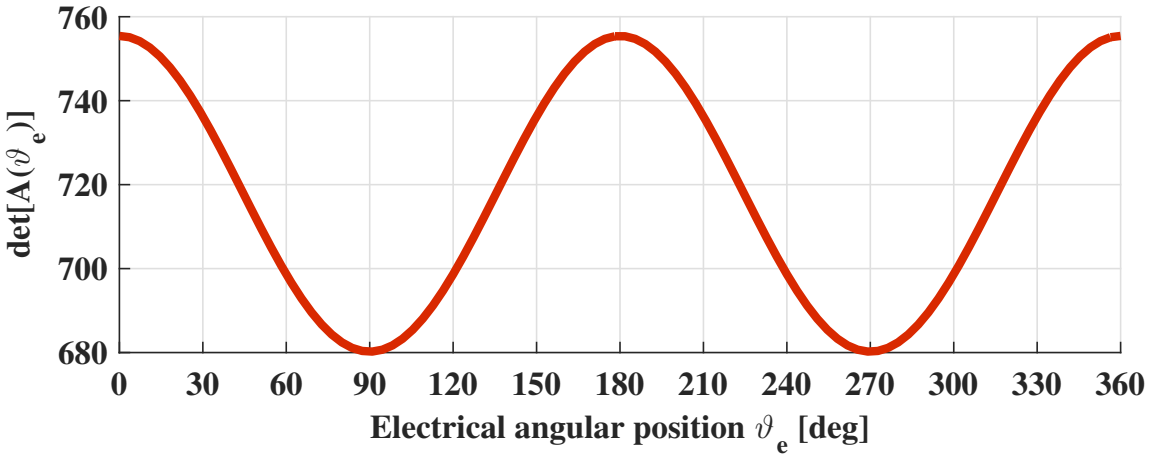


Figure A.1: Trend of $det\big(\mathbf{A}(\vartheta_e)\big)$ *against* ϑ_e.

Appendix B

Flux Density Prediction

The accurate prediction of the airgap flux density is of fundamental importance for the force and torque calculation in an electrical machine. In this Appendix, a mathematical model enabling to predict the flux density distribution at the airgap for a given input current in a MSPM machine is presented. The model is carried out considering the rotor centred at first and finally considering a rotor eventual radial displacement. A detailed airgap flux density prediction in PM machines was proposed in [139–143] for a centred rotor, taking into account the no-load and the armature flux density and the slotting effect.

The model presented hereafter is extracted in particular from [139, 140, 143] and it is generated assuming 2D flux density distribution. Under the assumption of linear magnetic behaviour of the soft magnetic materials, the superimposition principle can be applied. Therefore, the flux density at the mid-airgap can be written in polar coordinates as in (B.1) featuring the dependency with respect of the rotor angular position ϑ_e and stator angular coordinate α_s ($\alpha_s = 0$ corresponds to the axis of phase u_1).

$$\begin{aligned} B_r(\alpha_s, \vartheta_e) &= B_{r,PM}(\alpha_s, \vartheta_e) + B_{r,w}(\alpha_s, \vartheta_e) \\ B_\vartheta(\alpha_s, \vartheta_e) &= B_{\vartheta,PM}(\alpha_s, \vartheta_e) + B_{\vartheta,w}(\alpha_s, \vartheta_e) \end{aligned} \tag{B.1}$$

where B_r and B_ϑ are the radial and tangential components of the flux density at the mid-airgap respectively. $B_{r,PM}$, $B_{\vartheta,PM}$ and $B_{r,w}$, $B_{\vartheta,w}$ are the radial and tangential components of the open-circuit and armature-reaction flux density at the mid-airgap, respectively.

B.1 No rotor displacement

Table B.1: Machine geometrical parameters

Parameter	**Value**
Inner stator radius R_s	24.75 [mm]
Outer rotor PM radius R_m	23.75 [mm]
Outer rotor radius R_r	19.75 [mm]
Mid-airgap radius R_g	24.25 [mm]
Magnet pole-arc to pole-pitch ratio α_p	0.783
Coil pitch α_c	$\pi/3$ [rad]
Slot-opening b_0	2.1 [mm]
Magnets thickness h_m	4 [mm]

A comprehensive calculation of the open circuit flux density in the airgap for the case of perfectly centred rotor is carried out in [139]. The expression, in polar coordinate, is reported in (B.2).

$$B_{r,PM}(\alpha_s,\vartheta_e) = \sum_{n=1,3,5,\ldots}^{\infty} K_B(n) f_{Br} \cos\big(np(\alpha_s-\vartheta_e)\big)$$
$$B_{\vartheta,PM}(\alpha_s,\vartheta_e) = \sum_{n=1,3,5,\ldots}^{\infty} K_B(n) f_{B\vartheta} \sin\big(np(\alpha_s-\vartheta_e)\big) \tag{B.2}$$

Coefficients $K_B(n)$, f_{Br} and $f_{B\vartheta}$ take into account the main geometry features of the motor listed in Table 3.1 and Table B.1. Their expressions are written in (B.3).

$$K_B(n) = \frac{\mu_0 M_n}{\mu_r}\frac{np}{(np)^2-1}\left[\frac{(np-1)+2\left(\frac{R_r}{R_m}\right)^{np+1}-(np+1)\left(\frac{R_r}{R_m}\right)^{2np}}{\frac{\mu_r+1}{\mu_r}\left[1-\left(\frac{R_r}{R_s}\right)^{2np}\right]-\frac{\mu_r-1}{\mu_r}\left[\left(\frac{R_m}{R_s}^{2np}-\frac{R_r}{R_m}^{2np}\right)\right]}\right]$$
$$f_{Br}(n,r) = \left(\frac{r}{R_s}\right)^{np-1}\left(\frac{R_m}{R_s}\right)^{np+1}+\left(\frac{R_m}{r}\right)^{np+1} \tag{B.3}$$
$$f_{B\vartheta}(n,r) = -\left(\frac{r}{R_s}\right)^{np-1}\left(\frac{R_m}{R_s}\right)^{np+1}+\left(\frac{R_m}{r}\right)^{np+1}$$

and $M_n = 2\frac{B_{res}}{\mu_0}\alpha_p\frac{\sin(\frac{n\pi\alpha_p}{2})}{\frac{n\pi\alpha_p}{2}}$. The PM remanence flux density and relative permeability can be found in Table 3.1. The flux density is calculated at the mid-airgap radius $r = R_g$. In figure B.1 the flux density components obtained using equations (B.2) are compared with FEA for $\vartheta_e = 0$ and $n = 1$.

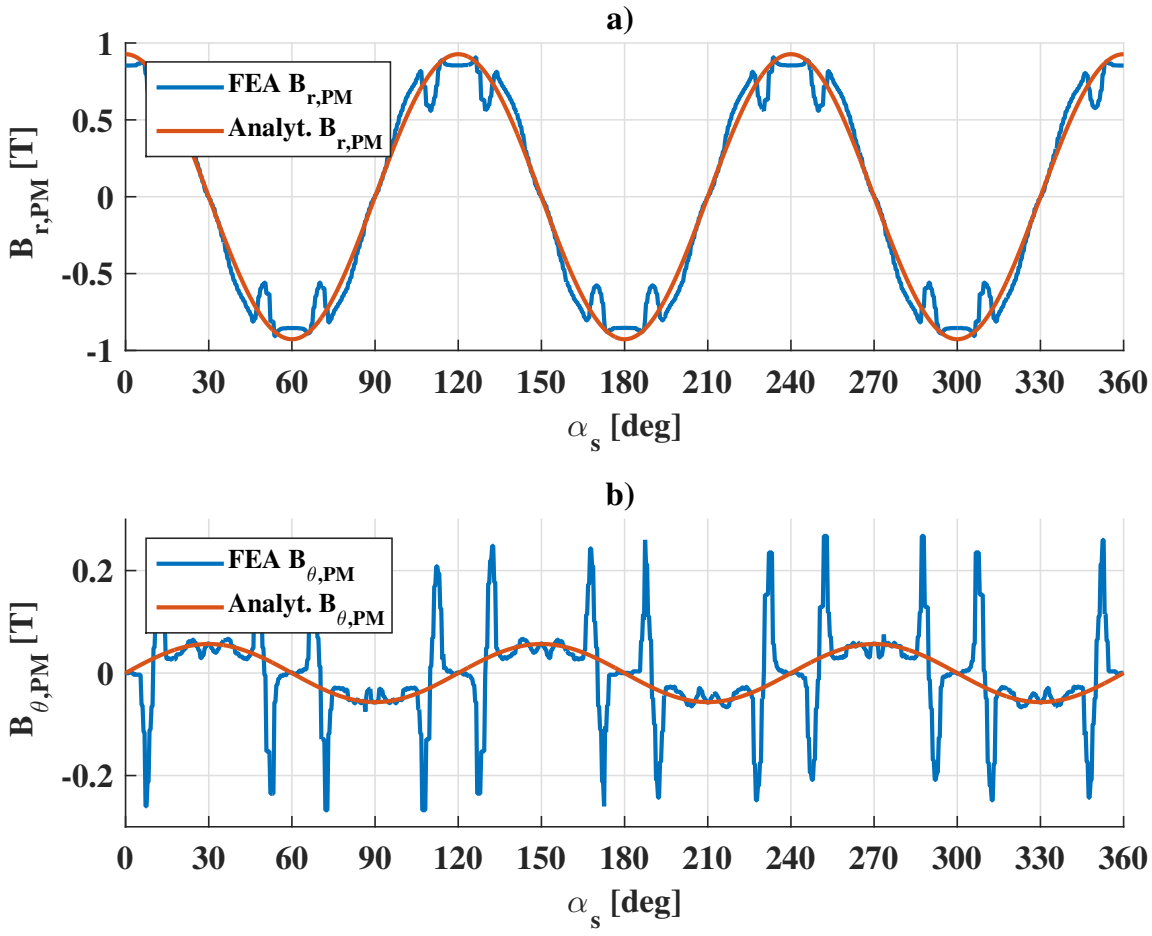


Figure B.1: Open-circuit airgap flux density for $\vartheta_e = 0$ [deg]: a) radial component; b) tangential component.

As far as the flux density due to the armature-reaction is concerned, the results of [140, 143], achieved considering a conventional three-phase winding, are adapted to the multi-sector motor presented. Equation (B.4) shows the radial and tangential components of the flux density produced by one motor phase.

$$B_{r,ph}(\alpha_s,\vartheta_e) = K \sum_{v=1,2,3,4,...}^{\infty} \tfrac{1}{v} K_{so}(v) K_p(v) F(v) I_r(\alpha_s,\vartheta_e)$$
$$B_{\vartheta,ph}(\alpha_s,\vartheta_e) = K \sum_{v=1,2,3,4,...}^{\infty} \tfrac{1}{v} K_{so}(v) K_p G(v) I_\vartheta(\alpha_s,\vartheta_e) \tag{B.4}$$

with

$$K = 2\tfrac{\mu_0}{\pi}\tfrac{N_c}{g_t}$$
$$I_r(\alpha_s,\vartheta_e) = i_{ph}(\vartheta_e)\cos(v\alpha_s+\varphi_{ph})$$
$$I_\vartheta(\alpha_s,\vartheta_e) = i_{ph}(\vartheta_e)\sin(v\alpha_s+\varphi_{ph})$$
$$K_{so}(v) = \tfrac{\sin(v\frac{b_0}{2R_s})}{v\frac{b_0}{2R_s}} \tag{B.5}$$
$$K_p(v) = \sin(v\tfrac{\alpha_c}{2})$$
$$F(v) = g_{tot}\tfrac{v}{r}\left(\tfrac{r}{R_s}\right)^v \tfrac{1+(\frac{R_r}{r})^{2v}}{1-(\frac{R_r}{R_s})^{2v}}$$
$$G(v) = g_{tot}\tfrac{v}{r}\left(\tfrac{r}{R_s}\right)^v \tfrac{1-(\frac{R_r}{r})^{2v}}{1-(\frac{R_r}{R_s})^{2v}}$$

$i_{ph}(t)$ is the phase current, $g_t = g_0 + h_m$ is the total airgap length (including the magnet thickness h_m and the physical air-gap clearance g_0) and φ_{ph} is the mechanical angular position of the phase axis with respect the $x-$axis (for instance, for sector 1, assuming ${}^1\gamma = 0$: $\varphi_{u_1} = 0$, $\varphi_{v_1} = 20$[deg], $\varphi_{w_1} = -20$[deg].

The radial and tangential flux density distributions of one winding sector (${}^sB_{r,\times}$ and ${}^sB_{\vartheta,\times}$) can be obtained summing up the contributions of the phases given by (B.4) and updating φ_{ph} according to the phase considered.

Only sub-matrix ${}^1\mathbf{K}_{E,F}(\vartheta_e, {}^1\gamma)$ is sufficient to characterize the force production of the machine, hence ${}^1B_{r,\times}$ and ${}^1B_{\vartheta,\times}$ need to be calculated as follow.

$$\begin{aligned} B_{r,\times}(\alpha_s) &= K \sum_{v=1,2,3,4,...}^{\infty} \tfrac{1}{v} K_{so}(v) K_p(v) F(v) I_{r,\times}(\alpha_s) \\ B_{\vartheta,\times}(\alpha_s) &= K \sum_{v=1,2,3,4,...}^{\infty} \tfrac{1}{v} K_{so}(v) K_p G(v) I_{\vartheta,\times}(\alpha_s) \end{aligned} \tag{B.6}$$

In particular, ${}^1B_{r,\alpha}$ and ${}^1B_{\vartheta,\alpha}$ are obtained with ${}^1\bar{i}_{\alpha\beta} = const. = \begin{bmatrix} 1 & 0 \end{bmatrix}^T$ [A], hence substituting $I_{r,\times}(\alpha_s)$ and $I_{\vartheta,\times}(\alpha_s)$ with the first two equations of (B.7). In the same way, ${}^1B_{r,\beta}$ and ${}^1B_{\vartheta,\beta}$ are obtained with ${}^1\bar{i}_{\alpha\beta} = const. = \begin{bmatrix} 0 & 1 \end{bmatrix}^T$ [A], hence $I_{r,\times}(\alpha_s)$ and $I_{\vartheta,\times}(\alpha_s)$ have to be substituted with the last two equations of (B.7).

$$\begin{aligned} I_{r,\alpha}(\alpha_s) &= \cos(v\alpha_s) - 0.5\cos(v\alpha_s + \pi/9) - 0.5\cos(v\alpha_s - \pi/9) \\ I_{\vartheta,\alpha}(\alpha_s) &= \sin(v\alpha_s) - 0.5\sin(v\alpha_s + \pi/9) - 0.5\sin(v\alpha_s - \pi/9) \\ I_{r,\beta}(\alpha_s) &= \tfrac{\sqrt{3}}{2}\cos(v\alpha_s + \pi/9) - \tfrac{\sqrt{3}}{2}\cos(v\alpha_s - \pi/9) \\ I_{\vartheta,\beta}(\alpha_s) &= \tfrac{\sqrt{3}}{2}\sin(v\alpha_s + \pi/9) - \tfrac{\sqrt{3}}{2}\sin(v\alpha_s - \pi/9) \end{aligned} \tag{B.7}$$

Figure B.2 and B.3 show the above calculated ${}^sB_{r,\alpha}$, ${}^sB_{\vartheta,\alpha}$ and ${}^sB_{r,\beta}$, ${}^sB_{\vartheta,\beta}$ respectively, for $v = 1, ..., 50$. The analytical waveforms are compared to the FE ones showing good agreements in the predicted flux densities.

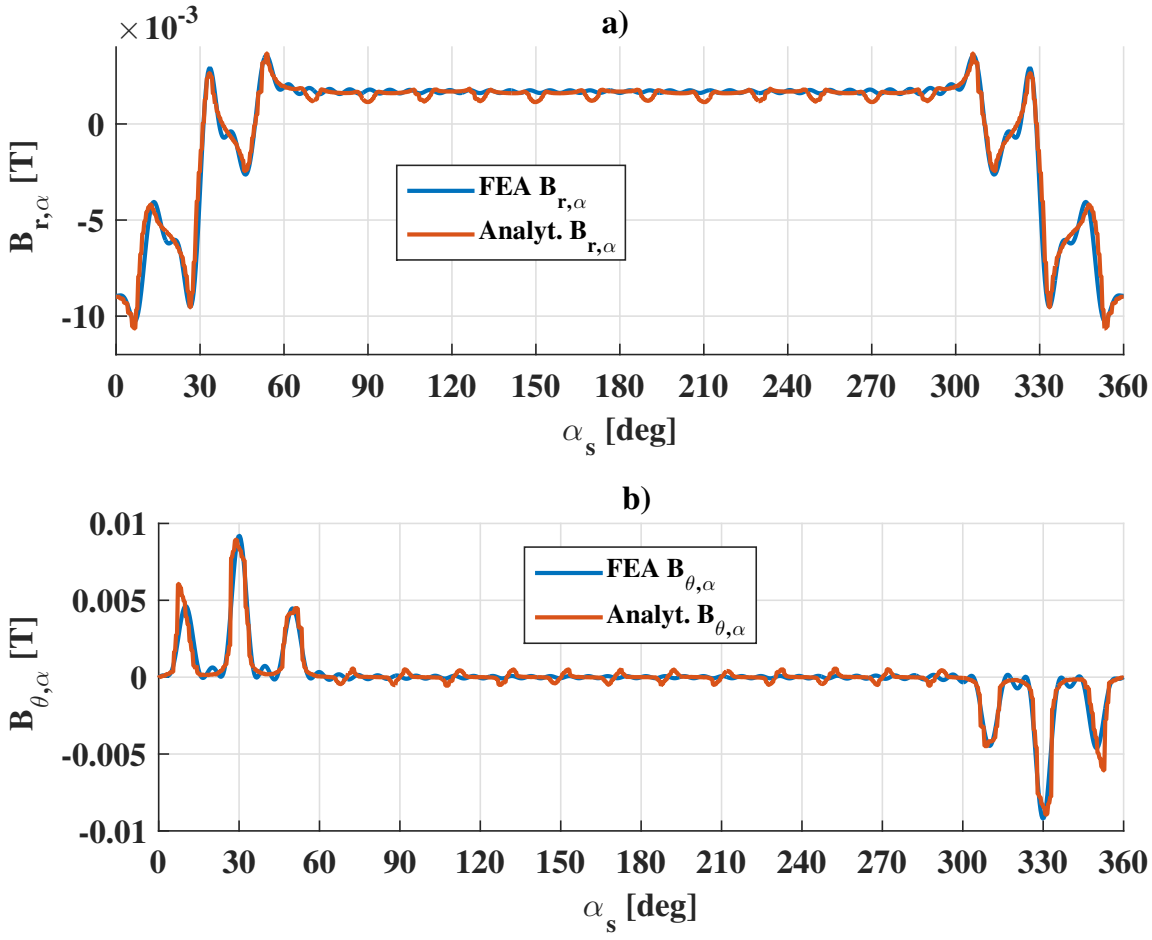


Figure B.2: Armature-reaction flux density at the airgap produced by ${}^1i_\alpha = const. = 1[A]$ *and* ${}^1i_\beta = 0[A]$*: a) radial component; b) tangential component.*

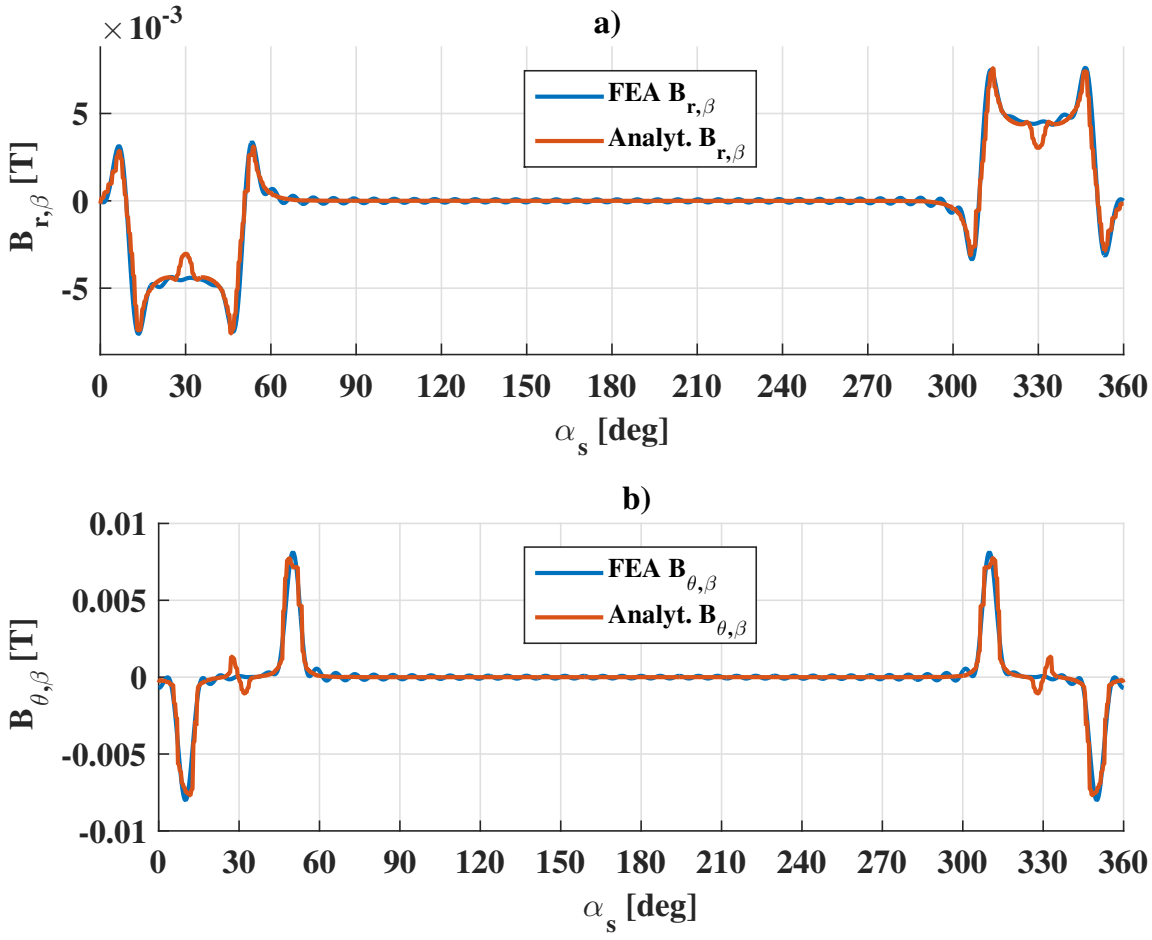


Figure B.3: Armature-reaction flux density at the airgap produced by ${}^1i_\alpha = 0[A]$ *and* ${}^1i_\beta = const. = 1[A]$*: a) radial component; b) tangential component.*

B.2 Rotor displacement

The flux density prediction in the airgap region in the case of static rotor eccentricity is the topic of this section. Figure 3.11 shows a geometrical description of the generic rotor displacement. The rotor axis O_r appears to be translated of the quantity δ and angle ϕ_d from the stator axis O_s.

In order to predict the flux density distribution in the airgap when rotor eccentricity occurs, the constant inner stator radius R_s and middle airgap radius R_g have to be replaced by variable distances R_{sr} and R_{gr}, respectively. Furthermore α_s has to be updated with α_{sr} [144,145]. This is the result of the coordinate transformation shown in figure 3.11 of a generic point P on the stator surface or at the mid-airgap from the stator to the rotor reference frame. The aforementioned transformation consists of a rotation (B.8) and a translation (B.9).

$$\begin{bmatrix} P'_{xr} \\ P'_{yr} \end{bmatrix} = \begin{bmatrix} \cos(\phi_d) & \sin(\phi_d) \\ -\sin(\phi_d) & \cos(\phi_d) \end{bmatrix} \begin{bmatrix} P_{xs} \\ P_{ys} \end{bmatrix} \tag{B.8}$$

$$\begin{aligned} P_{xr} &= P'_{xr} - \delta \\ P_{yr} &= P'_{yr} - \delta \end{aligned} \tag{B.9}$$

Where $P_{xs} = R_s \cos(\alpha_s)$ and $P_{ys} = R_s \sin(\alpha_s)$ are the Cartesian coordinates of the point P in the stator reference frame while P_{xr} and P_{yr} are the ones in the rotor reference frame. R_{sr} and α_{sr} can be now calculated in (B.10).

$$\begin{aligned} R_{sr} &= \sqrt{P_{xr}^2 + P_{yr}^2} \\ \alpha_{sr} &= \tan^{-1} \tfrac{P_{yr}}{P_{xr}} \end{aligned} \tag{B.10}$$

R_{gr} can be obtained in the same way using (B.8), (B.9), (B.10) and replacing the inner stator radius R_s with the mid-airgap radius R_g. From figure 3.11, the angle α_s can be written in (B.11) taking into account the transformation introduced.

$$\alpha_s \approx \alpha_{sr} + \phi_d \tag{B.11}$$

Finally, the non-uniform airgap length can be found in (B.12) [145].

$$g(\alpha_s) = g_0 + \delta \cos(\alpha_s - \phi_d) \tag{B.12}$$

Appendix C

$d-q$ Axis Reference Current Calculation

C.1 Healthy operating condition

The pseudo inverse matrix in the rotor synchronous reference frame was introduced in (3.62). It can be calculated as

$$\mathbf{K}^{+}_{E,dq}(\vartheta_e, \bar{\gamma}) = \mathbf{T}_R(\vartheta_e)\mathbf{K}^{+}_{E}(\vartheta_e, \bar{\gamma}) \tag{C.1}$$

and explicated as follow

$$\mathbf{K}^{+}_{E,dq}(\vartheta_e,\bar{\gamma}) = \begin{bmatrix} {}^{1}k^{+}_{xd}(\vartheta_e) & {}^{1}k^{+}_{yd}(\vartheta_e) & 0 \\ {}^{1}k^{+}_{xq}(\vartheta_e) & {}^{1}k^{+}_{yq}(\vartheta_e) & -k'_T \\ {}^{2}k^{+}_{xd}(\vartheta_e) & {}^{2}k^{+}_{yd}(\vartheta_e) & 0 \\ {}^{2}k^{+}_{xq}(\vartheta_e) & {}^{2}k^{+}_{yq}(\vartheta_e) & -k'_T \\ {}^{3}k^{+}_{xd}(\vartheta_e) & {}^{3}k^{+}_{yd}(\vartheta_e) & 0 \\ {}^{3}k^{+}_{xq}(\vartheta_e) & {}^{3}k^{+}_{yq}(\vartheta_e) & -k'_T \end{bmatrix} \tag{C.2}$$

where $k'_T = 1/3k_T$ [A/Nm] and the expression of the generic coefficient ${}^{s}k^{+}_{*\times}(\vartheta_e)$ is

$${}^{s}k^{+}_{*\times}(\vartheta_e) = {}^{s}c_{*\times} + {}^{s}s_{*\times}\cos(2\vartheta_e + {}^{s}\varphi_{*\times}) \tag{C.3}$$

It is possible to notice that ${}^{s}k^{+}_{*\times}(\vartheta_e)$ presents a constant and a sinusoidal term. The latter pulsates at twice the electrical frequency and produces non-constant $d-q$ axis current reference signals.

The angle γ_0 is required for the calculation of parameters ${}^{s}c_{*\times}$, ${}^{s}s_{*\times}$ and ${}^{s}\varphi_{*\times}$. As a matter of facts, γ_0 was defined in 3.2.1 as the angular position of the magnetic axis of the sector 1 with respect to the $x-$axis. As an example, Table C.1 reports the above mentioned parameters calculated for $\gamma_0 = 0$.

Table C.1: Parameters of force coefficients

	Sector 1				Sector 2				Sector 3			
	x,d	x,q	y,d	y,q	x,d	x,q	y,d	y,q	x,d	x,q	y,d	y,q
${}^{s}c_{*\times}$ [A/N]	0.068	0	0	0.021	0.034	0.018	0.058	0.01	0.034	0.018	0.058	0.01
${}^{s}s_{*\times}$ [A/N]	0.0055	0.0025	0.014	0.013	0.012	0.0112	0.0083	0.0068	0.0121	0.0121	0.0083	0.0068
${}^{s}\varphi_{*\times}$ [rad]	0.0622	1.63	1.63	-3.08	-1.74	-0.05	-0.9	0.39	1.86	-2.97	-2.12	-0.26

Finally, the expressions of the $d-q$ axis reference current signals to be digitalized in the force-torque control algorithm code are written as follow:

$$
\begin{aligned}
{}^1i_d^*(\vartheta_e) &= {}^1k_{xd}^+(\vartheta_e)F_{x,ref} + {}^1k_{yd}^+(\vartheta_e)F_{y,ref} \\
{}^1i_q^*(\vartheta_e) &= {}^1k_{xq}^+(\vartheta_e)F_{x,ref} + {}^1k_{yq}^+(\vartheta_e)F_{y,ref} - k'_T T_{ref} \\
{}^2i_d^*(\vartheta_e) &= {}^2k_{xd}^+(\vartheta_e)F_{x,ref} + {}^2k_{yd}^+(\vartheta_e)F_{y,ref} \\
{}^2i_q^*(\vartheta_e) &= {}^2k_{xq}^+(\vartheta_e)F_{x,ref} + {}^2k_{yq}^+(\vartheta_e)F_{y,ref} - k'_T T_{ref} \\
{}^3i_d^*(\vartheta_e) &= {}^3k_{xd}^+(\vartheta_e)F_{x,ref} + {}^3k_{yd}^+(\vartheta_e)F_{y,ref} \\
{}^3i_q^*(\vartheta_e) &= {}^3k_{xq}^+(\vartheta_e)F_{x,ref} + {}^3k_{yq}^+(\vartheta_e)F_{y,ref} - k'_T T_{ref}
\end{aligned}
\tag{C.4}
$$

C.2 Open-circuit operating condition

It has been shown in 3.4.3 that matrix $\mathbf{K}_E^+$ has to be replaced with $\mathbf{K}_{E,f1}^+$, $\mathbf{K}_{E,f2}^+$ and $\mathbf{K}_{E,f3}^+$ in case of open-circuit fault in sector 1,2 and 3, respectively. The above mentioned matrices are related to the $\alpha - \beta$ stationary reference frame. In order to describe the model in the rotor synchronous reference frame, matrices $\mathbf{K}_{E,f1}^+$, $\mathbf{K}_{E,f2}^+$ and $\mathbf{K}_{E,f3}^+$ have to be replaced with $\hat{\mathbf{K}}_{E,f1}^+$, $\hat{\mathbf{K}}_{E,f2}^+$ and $\hat{\mathbf{K}}_{E,f3}^+$ obtained as follow:

$$
\begin{aligned}
\hat{\mathbf{K}}_{E,f1}^+(\vartheta_e) &= \mathbf{T}_{R,f}(\vartheta_e)\mathbf{K}_{E,f1}^+(\vartheta_e) \\
\hat{\mathbf{K}}_{E,f2}^+(\vartheta_e) &= \mathbf{T}_{R,f}(\vartheta_e)\mathbf{K}_{E,f2}^+(\vartheta_e) \\
\hat{\mathbf{K}}_{E,f3}^+(\vartheta_e) &= \mathbf{T}_{R,f}(\vartheta_e)\mathbf{K}_{E,f3}^+(\vartheta_e)
\end{aligned}
\tag{C.5}
$$

The expressions of the pseudo inverse matrices $\hat{\mathbf{K}}_{E,f1}^+$, $\hat{\mathbf{K}}_{E,f2}^+$ and $\hat{\mathbf{K}}_{E,f3}^+$ ($\in \mathbb{R}^{4\times3}$) can be explicated as follow

$$
\hat{\mathbf{K}}_{E,f1}^+(\vartheta_e) = \begin{bmatrix}
{}^2k_{xd,f1}^+(\vartheta_e) & {}^2k_{yd,f1}^+(\vartheta_e) & {}^2k_{Td,f1}^+(\vartheta_e) \\
{}^2k_{xq,f1}^+(\vartheta_e) & {}^2k_{yq,f1}^+(\vartheta_e) & {}^2k_{Tq,f1}^+(\vartheta_e) \\
{}^3k_{xd,f1}^+(\vartheta_e) & {}^3k_{yd,f1}^+(\vartheta_e) & {}^3k_{Td,f1}^+(\vartheta_e) \\
{}^3k_{xq,f1}^+(\vartheta_e) & {}^3k_{yq,f1}^+(\vartheta_e) & {}^3k_{Tq,f1}^+(\vartheta_e)
\end{bmatrix}
\tag{C.6}
$$

$$\hat{\mathbf{K}}^{+}_{E,f2}(\vartheta_e) = \begin{bmatrix} {}^{1}k^{+}_{xd,f2}(\vartheta_e) & {}^{1}k^{+}_{yd,f2}(\vartheta_e) & {}^{1}k^{+}_{Td,f2}(\vartheta_e) \\ {}^{1}k^{+}_{xq,f2}(\vartheta_e) & {}^{1}k^{+}_{yq,f2}(\vartheta_e) & {}^{1}k^{+}_{Tq,f2}(\vartheta_e) \\ {}^{3}k^{+}_{xd,f2}(\vartheta_e) & {}^{3}k^{+}_{yd,f2}(\vartheta_e) & {}^{3}k^{+}_{Td,f2}(\vartheta_e) \\ {}^{3}k^{+}_{xq,f2}(\vartheta_e) & {}^{3}k^{+}_{yq,f2}(\vartheta_e) & {}^{3}k^{+}_{Tq,f2}(\vartheta_e) \end{bmatrix} \tag{C.7}$$

$$\hat{\mathbf{K}}^{+}_{E,f3}(\vartheta_e) = \begin{bmatrix} {}^{1}k^{+}_{xd,f3}(\vartheta_e) & {}^{1}k^{+}_{yd,f3}(\vartheta_e) & {}^{1}k^{+}_{Td,f3}(\vartheta_e) \\ {}^{1}k^{+}_{xq,f3}(\vartheta_e) & {}^{1}k^{+}_{yq,f3}(\vartheta_e) & {}^{1}k^{+}_{Tq,f3}(\vartheta_e) \\ {}^{2}k^{+}_{xd,f3}(\vartheta_e) & {}^{2}k^{+}_{yd,f3}(\vartheta_e) & {}^{2}k^{+}_{Td,f3}(\vartheta_e) \\ {}^{2}k^{+}_{xq,f3}(\vartheta_e) & {}^{2}k^{+}_{yq,f3}(\vartheta_e) & {}^{2}k^{+}_{Tq,f3}(\vartheta_e) \end{bmatrix} \tag{C.8}$$

leading to the calculation of the $d-q$ axis reference current signals in (C.9), (C.10) and (C.11) for open-circuit fault in sector 1, 2 and 3, respectively.

$$\begin{aligned} {}^{1}i^{*}_{d}(\vartheta_e) &= 0 \\ {}^{1}i^{*}_{q}(\vartheta_e) &= 0 \\ {}^{2}i^{*}_{d}(\vartheta_e) &= {}^{2}k^{+}_{xd,f1}F_{x,ref} + {}^{2}k^{+}_{yd,f1}F_{y,ref} + {}^{2}k^{+}_{Td,f1}(\vartheta_e)T_{ref} \\ {}^{2}i^{*}_{q}(\vartheta_e) &= {}^{2}k^{+}_{xq,f1}F_{x,ref} + {}^{2}k^{+}_{yq,f1}F_{y,ref} + {}^{2}k^{+}_{Tq,f1}(\vartheta_e)T_{ref} \\ {}^{3}i^{*}_{d}(\vartheta_e) &= {}^{3}k^{+}_{xd,f1}F_{x,ref} + {}^{3}k^{+}_{yd,f1}F_{y,ref} + {}^{3}k^{+}_{Td,f1}(\vartheta_e)T_{ref} \\ {}^{3}i^{*}_{q}(\vartheta_e) &= {}^{3}k^{+}_{xq,f1}F_{x,ref} + {}^{3}k^{+}_{yq,f1}F_{y,ref} + {}^{3}k^{+}_{Tq,f1}(\vartheta_e)T_{ref} \end{aligned} \tag{C.9}$$

$$\begin{aligned} {}^{1}i^{*}_{d}(\vartheta_e) &= {}^{1}k^{+}_{xd,f2}F_{x,ref} + {}^{1}k^{+}_{yd,f2}F_{y,ref} + {}^{1}k^{+}_{Td,f2}(\vartheta_e)T_{ref} \\ {}^{1}i^{*}_{q}(\vartheta_e) &= {}^{1}k^{+}_{xq,f2}F_{x,ref} + {}^{1}k^{+}_{yq,f2}F_{y,ref} + {}^{1}k^{+}_{Tq,f2}(\vartheta_e)T_{ref} \\ {}^{2}i^{*}_{d}(\vartheta_e) &= 0 \\ {}^{2}i^{*}_{q}(\vartheta_e) &= 0 \\ {}^{3}i^{*}_{d}(\vartheta_e) &= {}^{3}k^{+}_{xd,f2}F_{x,ref} + {}^{3}k^{+}_{yd,f2}F_{y,ref} + {}^{3}k^{+}_{Td,f2}(\vartheta_e)T_{ref} \\ {}^{3}i^{*}_{q}(\vartheta_e) &= {}^{3}k^{+}_{xq,f2}F_{x,ref} + {}^{3}k^{+}_{yq,f2}F_{y,ref} + {}^{3}k^{+}_{Tq,f2}(\vartheta_e)T_{ref} \end{aligned} \tag{C.10}$$

$$
\begin{aligned}
{}^{1}i_d^*(\vartheta_e) &= {}^{1}k^+_{xd,f3}F_{x,ref} + {}^{1}k^+_{yd,f3}F_{y,ref} + {}^{1}k^+_{Td,f3}(\vartheta_e)T_{ref} \\
{}^{1}i_q^*(\vartheta_e) &= {}^{1}k^+_{xq,f3}F_{x,ref} + {}^{1}k^+_{yq,f3}F_{y,ref} + {}^{1}k^+_{Tq,f3}(\vartheta_e)T_{ref} \\
{}^{2}i_d^*(\vartheta_e) &= {}^{2}k^+_{xd,f3}F_{x,ref} + {}^{2}k^+_{yd,f3}F_{y,ref} + {}^{2}k^+_{Td,f3}(\vartheta_e)T_{ref} \\
{}^{2}i_q^*(\vartheta_e) &= {}^{2}k^+_{xq,f3}F_{x,ref} + {}^{2}k^+_{yq,f3}F_{y,ref} + {}^{2}k^+_{Tq,f3}(\vartheta_e)T_{ref} \\
{}^{3}i_d^*(\vartheta_e) &= 0 \\
{}^{3}i_q^*(\vartheta_e) &= 0
\end{aligned}
\tag{C.11}
$$

where the generic force and torque coefficients can be calculated according to

$$
\begin{aligned}
{}^{s}k^+_{*\times,f1}(\vartheta_e) &= {}^{s}c_{*\times,f1} + {}^{s}s_{*\times,f1}\cos(2\vartheta_e + {}^{s}\varphi_{*\times,f1}) + {}^{s}r_{*\times,f1}\cos(4\vartheta_e + {}^{s}\psi_{*\times,f1}) \\
{}^{s}k^+_{*\times,f2}(\vartheta_e) &= {}^{s}c_{*\times,f2} + {}^{s}s_{*\times,f2}\cos(2\vartheta_e + {}^{s}\varphi_{*\times,f2}) + {}^{s}r_{*\times,f2}\cos(4\vartheta_e + {}^{s}\psi_{*\times,f2}) \\
{}^{s}k^+_{*\times,f3}(\vartheta_e) &= {}^{s}c_{*\times,f3} + {}^{s}s_{*\times,f3}\cos(2\vartheta_e + {}^{s}\varphi_{*\times,f3}) + {}^{s}r_{*\times,f3}\cos(4\vartheta_e + {}^{s}\psi_{*\times,f3})
\end{aligned}
$$

$$
\begin{aligned}
{}^{s}k^+_{T\times,f1}(\vartheta_e) &= {}^{s}c_{T\times,f1} + {}^{s}s_{T\times,f1}\cos(2\vartheta_e + {}^{s}\varphi_{T\times,f1}) + {}^{s}r_{T\times,f1}\cos(4\vartheta_e + {}^{s}\psi_{T\times,f1}) \\
{}^{s}k^+_{T\times,f2}(\vartheta_e) &= {}^{s}c_{T\times,f2} + {}^{s}s_{T\times,f2}\cos(2\vartheta_e + {}^{s}\varphi_{T\times,f2}) + {}^{s}r_{T\times,f2}\cos(4\vartheta_e + {}^{s}\psi_{T\times,f2}) \\
{}^{s}k^+_{T\times,f3}(\vartheta_e) &= {}^{s}c_{T\times,f3} + {}^{s}s_{T\times,f3}\cos(2\vartheta_e + {}^{s}\varphi_{T\times,f3}) + {}^{s}r_{T\times,f3}\cos(4\vartheta_e + {}^{s}\psi_{T\times,f3})
\end{aligned}
\tag{C.12}
$$

The parameters in the above expressions can be easily calculated once γ_0 is defined. As an example, the parameters of the force and torque coefficients for fault in sector 1 have been calculated for $\gamma_0 = 0$ and they have been reported in Table C.2 and C.3.

Table C.2: Parameters of force coefficients for fault in sect. 1

	Sector 1				Sector 2				Sector 3			
	x,d	x,q	y,d	y,q	x,d	x,q	y,d	y,q	x,d	x,q	y,d	y,q
${}^{s}c_{*\times,f1}$[A/N]	/	/	/	/	0.088	0.0427	0.0661	0	0.088	0.0427	0.0661	0
${}^{s}s_{*\times,f1}$[A/N]	/	/	/	/	0.0234	0.0204	0.0205	0.0039	0.0234	0.0204	0.0205	0.0039
${}^{s}r_{*\times,f1}$[A/N]	/	/	/	/	0.0018	0.003	0.0015	0.0016	0.0018	0.003	0.0015	0.0016
${}^{s}\varphi_{*\times,f1}$[deg]	/	/	/	/	-2.7	0.062	-1.63	-1.51	2.83	-3.1	-1.38	1.63
${}^{s}\psi_{*\times,f1}$[deg]	/	/	/	/	2.16	-3.02	2.55	-1.45	-1.91	0.12	0.84	1.7

Table C.3: Parameters of torque coefficients for fault in sect. 1

	Sector 1		Sector 2		Sector 3	
	T, d	T, q	T, d	T, q	T, d	T, q
${}^{s}c_{T\times,f1}$[A/N]	/	/	0.627	3.55	0.627	3.55
${}^{s}s_{T\times,f1}$[A/N]	/	/	0.523	0.0915	0.523	0.0915
${}^{s}r_{T\times,f1}$[A/N]	/	/	0.0442	0.0373	0.0442	0.0373
${}^{s}\varphi_{T\times,f1}$[deg]	/	/	-2.5	-1.51	-0.52	1.63
${}^{s}\psi_{T\times,f1}$[deg]	/	/	-1.93	-1.45	-0.96	1.7

Appendix D

Published Papers

The following papers were published with material directly related to this thesis:

G. Valente, L. Papini, A. Formentini, C. Gerada and P. Zanchetta, "Radial force control of multi-sector permanent magnet machines," 2016 XXII International Conference on Electrical Machines (ICEM), Lausanne, 2016, pp. 2595-2601.

G. Valente, L. Papini, A. Formentini, C. Gerada and P. Zanchetta, "Radial force control of Multi-Sector Permanent Magnet machines considering radial rotor displacement," 2017 IEEE Workshop on Electrical Machines Design, Control and Diagnosis (WEMDCD), Nottingham, 2017, pp. 140-145.

G. Valente, A. Formentini, L. Papini, P. Zanchetta and C. Gerada, "Position control study of a bearingless multi-sector permanent magnet machine," IECON 2017 - 43rd Annual Conference of the IEEE Industrial Electronics Society, Beijing, 2017, pp. 8808-8813.

G. Valente, L. Papini, A. Formentini, C. Gerada and P. Zanchetta, "Radial Force Control of Multi-Sector Permanent Magnet Machines for Vibration Suppression," in IEEE Transactions on Industrial Electronics, vol. PP, no. 99, pp. 1-1.

G. Sala, G. Valente, A. Formentini, L. Papini, D. Gerada, P. Zanchetta, A. Tani, C. Gerada, "Space Vectors and Pseudo Inverse Matrix Methods for the Radial Force Control in Bearingless Multi-Sector Permanent Magnet Machines," in IEEE Transactions on Industrial Electronics, vol. PP, no. 99, pp. 1-1.

Bibliography

[1] S. Zhou and J. Shi, "Active balancing and vibration control of rotating machinery: a survey," *Shock and Vibration Digest*, vol. 33, no. 5, pp. 361–371, 2001.

[2] X. Sun, L. Chen, and Z. Yang, "Overview of bearingless permanent-magnet synchronous motors," *IEEE Transactions on Industrial Electronics*, vol. 60, pp. 5528–5538, Dec 2013.

[3] R. Oishi, S. Horima, H. Sugimoto, and A. Chiba, "A novel parallel motor winding structure for bearingless motors," *IEEE Transactions on Magnetics*, vol. 49, pp. 2287–2290, May 2013.

[4] X. L. Wang, Q. C. Zhong, Z. Q. Deng, and S. Z. Yue, "Current-controlled multiphase slice permanent magnetic bearingless motors with open-circuited phases: Fault-tolerant controllability and its verification," *IEEE Transactions on Industrial Electronics*, vol. 59, pp. 2059–2072, May 2012.

[5] S. Kobayashi, M. Ooshima, and M. N. Uddin, "A radial position control method of bearingless motor based on d - q- axis current control," *IEEE Transactions on Industry Applications*, vol. 49, pp. 1827–1835, July 2013.

[6] H. Mitterhofer, W. Gruber, and W. Amrhein, "On the high speed capacity of bearingless drives," *IEEE Transactions on Industrial Electronics*, vol. 61, pp. 3119–3126, June 2014.

[7] T. Baumgartner, R. M. Burkart, and J. W. Kolar, "Analysis and design of a 300-w 500000-r/min slotless self-bearing permanent-magnet motor," *IEEE Transactions on Industrial Electronics*, vol. 61, pp. 4326–4336, Aug 2014.

[8] J. Asama, D. Kanehara, T. Oiwa, and A. Chiba, "Development of a compact centrifugal pump with a two-axis actively positioned consequent-pole bearingless motor," *IEEE Transactions on Industry Applications*, vol. 50, pp. 288–295, Jan 2014.

[9] J. Asama, T. Fukao, A. Chiba, A. Rahman, and T. Oiwa, "A design consideration of a novel bearingless disk motor for artificial hearts," in *2009 IEEE Energy Conversion Congress and Exposition*, pp. 1693–1699, Sept 2009.

[10] W. Li, K. T. Chau, T. W. Ching, Y. Wang, and M. Chen, "Design of a high-speed superconducting bearingless machine for flywheel energy storage systems," *IEEE Transactions on Applied Superconductivity*, vol. 25, pp. 1–4, June 2015.

[11] A. Chiba, T. Fukao, O. Ichikawa, M. Oshima, M. Takemoto, and D. G. Dorrell, *Magnetic bearings and bearingless drives*. Elsevier, 2005.

[12] B. Liu, "Survey of bearingless motor technologies and applications," in *2015 IEEE International Conference on Mechatronics and Automation (ICMA)*, pp. 1983–1988, Aug 2015.

[13] P. Hermann, "A radial active magnetic bearing," *London Patent*, no. 1, p. 478, 1973.

[14] A. Chiba, M. A. Rahman, and T. Fukao, "Radial force in a bearingless reluctance motor," *IEEE Transactions on Magnetics*, vol. 27, pp. 786–790, March 1991.

[15] J. Bichsel, "The bearingless electrical machine," 1992.

[16] A. O. Salazar and R. M. Stephan, "A bearingless method for induction machines," *IEEE Transactions on Magnetics*, vol. 29, pp. 2965–2967, Nov 1993.

[17] A. Chiba, T. Deido, T. Fukao, and M. A. Rahman, "An analysis of bearingless ac motors," *IEEE Transactions on Energy Conversion*, vol. 9, pp. 61–68, Mar 1994.

[18] M. Ooshima and C. Takeuchi, "Magnetic suspension performance of a bearingless brushless dc motor for small liquid pumps," *IEEE Transactions on Industry Applications*, vol. 47, pp. 72–78, Jan 2011.

[19] X. Cao, H. Yang, L. Zhang, and Z. Deng, "Compensation strategy of levitation forces for single-winding bearingless switched reluctance motor with one winding total short circuited," *IEEE Transactions on Industrial Electronics*, vol. 63, pp. 5534–5546, Sept 2016.

[20] T. Sekine, K. Hijikata, and Y. Tanaka, "Investigation of torque and suspension force characteristic in a reluctance type bearingless vernier motor," in *2017 IEEE International Electric Machines and Drives Conference (IEMDC)*, pp. 1–6, May 2017.

[21] A. Sinervo and A. Arkkio, "Rotor radial position control and its effect on the total efficiency of a bearingless induction motor with a cage rotor," *IEEE Transactions on Magnetics*, vol. 50, pp. 1–9, April 2014.

[22] A. Chiba, K. Sotome, Y. Iiyama, and M. A. Rahman, "A novel middle-point-current-injection-type bearingless pm synchronous motor for vibration suppression," *IEEE Transactions on Industry Applications*, vol. 47, pp. 1700–1706, July 2011.

[23] G. Feng, C. Lai, and N. C. Kar, "An analytical solution to optimal stator current design for pmsm torque ripple minimization with minimal machine losses," *IEEE Transactions on Industrial Electronics*, vol. 64, pp. 7655–7665, Oct 2017.

[24] C. Lin, S. Wang, M. Moallem, B. Fahimi, and C. Tschida, "Analysis of vibration in permanent magnet synchronous machines due to variable speed drives," *IEEE Trans. on Energy Conv.*, vol. 32, pp. 582–590, June 2017.

[25] J. L. Besnerais, "Vibroacoustic analysis of radial and tangential air-gap magnetic forces in permanent magnet synchronous machines," *IEEE Transactions on Magnetics*, vol. 51, pp. 1–9, June 2015.

[26] M. Valavi, A. Nysveen, R. Nilssen, R. D. Lorenz, and T. Rlvg, "Influence of pole and slot combinations on magnetic forces and vibration in low-speed pm wind generators," *IEEE Transactions on Magnetics*, vol. 50, pp. 1–11, May 2014.

[27] M. D. Prieto, G. Cirrincione, A. G. Espinosa, J. A. Ortega, and H. Henao, "Bearing fault detection by a novel condition-monitoring scheme based on statistical-time features and neural networks," *IEEE Transactions on Industrial Electronics*, vol. 60, pp. 3398–3407, Aug 2013.

[28] H. T. Yau, S. Y. Wu, C. L. Chen, and Y. C. Li, "Fractional-order chaotic self-synchronization-based tracking faults diagnosis of ball bearing systems," *IEEE Transactions on Industrial Electronics*, vol. 63, pp. 3824–3833, June 2016.

[29] C. Ma, Q. Liu, D. Wang, Q. Li, and L. Wang, "A novel black and white box method for diagnosis and reduction of abnormal noise of hub permanent-magnet synchronous motors for electric vehicles," *IEEE Trans. on Ind. Electr.*, vol. 63, pp. 1153–1167, Feb 2016.

[30] N. Kurihara, J. Bayless, H. Sugimoto, and A. Chiba, "Noise reduction of switched reluctance motor with high number of poles by novel simplified current waveform at low speed and low torque region," *IEEE Transactions on Industry Applications*, vol. 52, pp. 3013–3021, July 2016.

[31] J. Y. Chai and C. M. Liaw, "Reduction of speed ripple and vibration for switched reluctance motor drive via intelligent current profiling," *IET Electric Power Applications*, vol. 4, pp. 380–396, May 2010.

[32] D. Torregrossa, D. Paire, F. Peyraut, B. Fahimi, and A. Miraoui, "Active mitigation of electromagnetic vibration radiated by pmsm in fractional-horsepower drives by optimal choice of the carrier frequency," *IEEE Transactions on Industrial Electronics*, vol. 59, pp. 1346–1354, March 2012.

[33] X. Chen, J. Wang, and V. I. Patel, "A generic approach to reduction of magnetomotive force harmonics in permanent-magnet machines with concentrated multiple three-phase windings," *IEEE Transactions on Magnetics*, vol. 50, pp. 1–4, Nov 2014.

[34] Z. Q. Zhu, M. L. M. Jamil, and L. J. Wu, "Influence of slot and pole number combinations on unbalanced magnetic force in pm machines with diametrically asymmetric windings," *IEEE Transactions on Industry Applications*, vol. 49, pp. 19–30, Jan 2013.

[35] R. E. Cunningham, "Steady-state unbalance response of a three-disk flexible rotor on flexible, damped supports," *Journal of Mechanical Design*, vol. 100, no. 3, pp. 563–573, 1978.

[36] C. Hansen, S. Snyder, X. Qiu, L. Brooks, and D. Moreau, *Active control of noise and vibration*. CRC press, 2012.

[37] S. W. Dyer, J. Kerlin, and B. K. Hackett, "Eletromagnetically actuated rotating machine unbalance compensator," May 26 1998. US Patent 5,757,662.

[38] M. Neff, N. Barletta, and R. Schob, "Bearingless centrifugal pump for highly pure chemicals," in *Proc. 8th ISMB*, pp. 283–287, 2002.

[39] K. Raggl, B. Warberger, T. Nussbaumer, S. Burger, and J. W. Kolar, "Robust angle-sensorless control of a pmsm bearingless pump," *IEEE Transactions on Industrial Electronics*, vol. 56, pp. 2076–2085, June 2009.

[40] Y. Okada, N. Yamashiro, K. Ohmori, T. Masuzawa, T. Yamane, Y. Konishi, and S. Ueno, "Mixed flow artificial heart pump with axial self-bearing motor," *IEEE/ASME Transactions on Mechatronics*, vol. 10, pp. 658–665, Dec 2005.

[41] T. Reichert, T. Nussbaumer, and J. W. Kolar, "Bearingless 300-w pmsm for bioreactor mixing," *IEEE Transactions on Industrial Electronics*, vol. 59, pp. 1376–1388, March 2012.

[42] B. Warberger, R. Kaelin, T. Nussbaumer, and J. W. Kolar, "50-nm/2500-w bearingless motor for high-purity pharmaceutical mixing," *IEEE Transactions on Industrial Electronics*, vol. 59, pp. 2236–2247, May 2012.

[43] T. Reichert, T. Nussbaumer, and J. W. Kolar, "Investigation of exterior rotor bearingless motor topologies for high-quality mixing applications," *IEEE Transactions on Industry Applications*, vol. 48, pp. 2206–2216, Nov 2012.

[44] W. Bauer and W. Amrhein, "Electrical design considerations for a bearingless axial-force/torque motor," *IEEE Transactions on Industry Applications*, vol. 50, pp. 2512–2522, July 2014.

[45] J. Asama, D. Watanabe, T. Oiwa, and A. Chiba, "Development of a one-axis actively regulated bearingless motor with a repulsive type passive magnetic bearing," in *2014 International Power Electronics Conference (IPEC-Hiroshima 2014 - ECCE ASIA)*, pp. 988–993, May 2014.

[46] G. Munteanu, A. Binder, T. Schneider, and B. Funieru, "No-load tests of a 40 kw high-speed bearingless permanent magnet synchronous motor," in *SPEEDAM 2010*, pp. 1460–1465, June 2010.

[47] R. P. Jastrzebski, P. Jaatinen, O. Pyrhnen, and A. Chiba, "Design of 6-slot inset pm bearingless motor for high-speed and higher than 100kw applications," in *2017 IEEE International Electric Machines and Drives Conference (IEMDC)*, pp. 1–6, May 2017.

[48] S. Yuxin, L. Xianxing, W. Weiran, and X. Peifeng, "Design and finite element analysis of high speed motorized spindle system based on bearingless induction motor," in *2010 International Conference on Mechanic Automation and Control Engineering*, pp. 5483–5486, June 2010.

[49] M. Ooshima, S. Kobayashi, and H. Tanaka, "Magnetic suspension performance of a bearingless motor/generator for flywheel energy storage systems," in *IEEE PES General Meeting*, pp. 1–4, July 2010.

[50] Y. Yuan, Y. Sun, and Y. Huang, "Accurate mathematical model of bearingless flywheel motor based on maxwell tensor method," *Electronics Letters*, vol. 52, no. 11, pp. 950–952, 2016.

[51] Y. Okada, K. Dejima, and T. Ohishi, "Analysis and comparison of pm synchronous motor and induction motor type magnetic bearings," *IEEE Transactions on Industry Applications*, vol. 31, pp. 1047–1053, Sep 1995.

[52] M. Oshima, S. Miyazawa, T. Deido, A. Chiba, F. Nakamura, and T. Fukao, "Characteristics of a permanent magnet type bearingless motor," *IEEE Transactions on Industry Applications*, vol. 32, pp. 363–370, Mar 1996.

[53] A. Chiba, T. Fukao, and M. A. Rahman, "Performance characteristics and parameter identification for inset type permanent magnet bearingless motor drive," in *IEEE Power Engineering Society General Meeting, 2004.*, pp. 1268–1271 Vol.2, June 2004.

[54] X. Sun, Z. Xue, J. Zhu, Y. Guo, Z. Yang, L. Chen, and J. Chen, "Suspension force modeling for a bearingless permanent magnet synchronous motor using maxwell stress tensor method," *IEEE Transactions on Applied Superconductivity*, vol. 26, pp. 1–5, Oct 2016.

[55] W. Amrhein, S. Silber, and K. Nenninger, "Levitation forces in bearingless permanent magnet motors," *IEEE Transactions on Magnetics*, vol. 35, pp. 4052–4054, Sep 1999.

[56] H. I. Lee, S. y. Yoo, and M. D. Noh, "Toroidally-wound self-bearing bldc motor with lorentz force," *IEEE Transactions on Magnetics*, vol. 46, pp. 2148–2151, June 2010.

[57] D. Steinert, T. Nussbaumer, and J. W. Kolar, "Evaluation of one- and two-pole-pair slotless bearingless motors with toroidal windings," *IEEE Transactions on Industry Applications*, vol. 52, pp. 172–180, Jan 2016.

[58] L. Chen and W. Hofmann, "Analysis of radial forces based on rotor eccentricity of bearingless switched reluctance motors," in *The XIX International Conference on Electrical Machines - ICEM 2010*, pp. 1–6, Sept 2010.

[59] Z. Yuan, H. Yikang, and N. Heng, "The integrated mathematic model of a permanent magnet type bearingless motor," in *2005 International Conference on Electrical Machines and Systems*, vol. 2, pp. 898–902 Vol. 2, Sept 2005.

[60] J. Asama, Y. Hamasaki, T. Oiwa, and A. Chiba, "Proposal and analysis of a novel single-drive bearingless motor," *IEEE Transactions on Industrial Electronics*, vol. 60, pp. 129–138, Jan 2013.

[61] R. Schoeb and N. Barletta, "Principle and application of a bearingless slice motor," *JSME International Journal Series C Mechanical Systems, Machine Elements and Manufacturing*, vol. 40, no. 4, pp. 593–598, 1997.

[62] S. Silber, W. Amrhein, P. Bosch, R. Schob, and N. Barletta, "Design aspects of bearingless slice motors," *IEEE/ASME Transactions on Mechatronics*, vol. 10, pp. 611–617, Dec 2005.

[63] T. Nussbaumer, P. Karutz, F. Zurcher, and J. W. Kolar, "Magnetically levitated slice motors - an overview," *IEEE Transactions on Industry Applications*, vol. 47, pp. 754–766, March 2011.

[64] Z. Xie, H. Zhu, and Y. Sun, "Structure and control of ac-dc three-degree-of-freedom hybrid magnetic bearing," in *2005 International Conference on Electrical Machines and Systems*, vol. 3, pp. 1801–1806 Vol. 3, Sept 2005.

[65] W. Zhang and H. Zhu, "Improved model and experiment for ac-dc three-degree-of-freedom hybrid magnetic bearing," *IEEE Transactions on Magnetics*, vol. 49, pp. 5554–5565, Nov 2013.

[66] S. Yajima, M. Takemoto, Y. Tanaka, A. Chiba, and T. Fukao, "Total efficiency of a deeply buried permanent magnet type bearingless motor equipped with 2-pole motor windings and 4-pole suspension windings," in *Power Engineering Society General Meeting, 2007. IEEE*, pp. 1–7, IEEE, 2007.

[67] H. Wang, J. Bao, B. Xue, and J. Liu, "Control of suspending force in novel permanent-magnet-biased bearingless switched reluctance motor," *IEEE Transactions on Industrial Electronics*, vol. 62, pp. 4298–4306, July 2015.

[68] X. Sun, H. Zhu, and T. Zhang, "Nonlinear decoupling control for 5 degrees-of-freedom bearingless permanent magnet synchronous motor," in *Power Electronics and Motion Control Conference, 2009. IPEMC'09. IEEE 6th International*, pp. 1842–1847, IEEE, 2009.

[69] H. Grabner, W. Amrhein, S. Silber, and W. Gruber, "Nonlinear feedback control of a bearingless brushless dc motor," *IEEE/ASME Transactions on Mechatronics*, vol. 15, pp. 40–47, Feb 2010.

[70] H. I. Lee, S. y. Yoo, and M. D. Noh, "Toroidally-wound self-bearing bldc motor with lorentz force," *IEEE Transactions on Magnetics*, vol. 46, pp. 2148–2151, June 2010.

[71] H. i. Lee, H. Lee, and M. D. Noh, "System-level optimization of magnetically-levitated micro flywheel energy storage device," in *2009 IEEE/ASME International Conference on Advanced Intelligent Mechatronics*, pp. 1631–1636, July 2009.

[72] W. Gruber, M. Rothbck, and R. T. Schb, "Design of a novel homopolar bearingless slice motor with reluctance rotor," *IEEE Transactions on Industry Applications*, vol. 51, pp. 1456–1464, March 2015.

[73] L. Chen and W. Hofmann, "Speed regulation technique of one bearingless 8/6 switched reluctance motor with simpler single winding structure," *IEEE Transactions on Industrial Electronics*, vol. 59, pp. 2592–2600, June 2012.

[74] H. Wang, J. Liu, J. Bao, and B. Xue, "A novel bearingless switched reluctance motor with a biased permanent magnet," *IEEE Transactions on Industrial Electronics*, vol. 61, pp. 6947–6955, Dec 2014.

[75] Y. Okada, S. Miyamoto, and T. Ohishi, "Levitation and torque control of internal permanent magnet type bearingless motor," *IEEE Transactions on Control Systems Technology*, vol. 4, pp. 565–571, Sep 1996.

[76] M. Ooshima, S. Miyazawa, A. Chiba, F. Nakamura, and T. Fukao, "A rotor design of a permanent magnet-type bearingless motor considering demagnetization," in *Power Conversion Conference - Nagaoka 1997., Proceedings of the*, vol. 2, pp. 655–660 vol.2, Aug 1997.

[77] A. Chiba, R. Furuichi, Y. Aikawa, K. Shimada, Y. Takamoto, and T. Fukao, "Stable operation of induction-type bearingless motors under loaded conditions," *IEEE Transactions on Industry Applications*, vol. 33, pp. 919–924, Jul 1997.

[78] A. Chiba and J. Asama, "Influence of rotor skew in induction type bearingless motor," *IEEE Transactions on Magnetics*, vol. 48, pp. 4646–4649, Nov 2012.

[79] K. Radman, "Loss analysis of a bearingless flux-switching slice motor," in *14th Int. Symp. on Magnetic Bearings (ISMB), 2014*, 2014.

[80] E. L. Severson, R. Nilssen, T. Undeland, and N. Mohan, "Design of dual purpose no-voltage combined windings for bearingless motors," *IEEE Transactions on Industry Applications*, vol. 53, pp. 4368–4379, Sept 2017.

[81] W. K. S. Khoo, K. Kalita, and S. D. Garvey, "Practical implementation of the bridge configured winding for producing controllable transverse forces in electrical machines," *IEEE Transactions on Magnetics*, vol. 47, pp. 1712–1718, June 2011.

[82] W. K. S. Khoo, "Bridge configured winding for polyphase self-bearing machines," *IEEE Transactions on Magnetics*, vol. 41, pp. 1289–1295, April 2005.

[83] F. Ahmed, M. D. Choudhury, G. Kumar, and K. Kalita, "Modeling and analysis of bearingless switched reluctance motor equipped with specialized stator winding," in *2016 IEEE International Conference on Power Electronics, Drives and Energy Systems (PEDES)*, pp. 1–6, Dec 2016.

[84] J. Huang, B. Li, H. Jiang, and M. Kang, "Analysis and control of multiphase permanent-magnet bearingless motor with a single set of half-coiled winding," *IEEE Transactions on Industrial Electronics*, vol. 61, pp. 3137–3145, July 2014.

[85] M. Kang, J. Huang, J. q. Yang, and H. b. Jiang, "Analysis and experiment of a 6-phase bearingless induction motor," in *2008 International Conference on Electrical Machines and Systems*, pp. 990–994, Oct 2008.

[86] B. Li, J. Huang, H. Liu, and Z. Hou, "Analysis and control of seven-phase permanent-magnet bearingless motor with single set of half-coiled winding," in *2014 IEEE 23rd International Symposium on Industrial Electronics (ISIE)*, pp. 2080–2086, June 2014.

[87] M. Ooshima, T. Karasawa, and M. N. Uddin, "Stabilized control strategy under loaded conditions in a bearingless motor based on d-q axis current control," in *2013 IEEE Industry Applications Society Annual Meeting*, pp. 1–7, Oct 2013.

[88] G. Sala, D. Gerada, C. Gerada, and A. Tani, "Radial force control for triple three-phase sectored spm machines. part i: Machine model," in *2017 IEEE Workshop on Electrical Machines Design, Control and Diagnosis (WEMDCD)*, pp. 193–198, April 2017.

[89] G. Sala, D. Gerada, C. Gerada, and A. Tani, "Radial force control for triple three-phase sectored spm machines. part ii: Open winding fault tolerant control," in *2017 IEEE Workshop on Electrical Machines Design, Control and Diagnosis (WEMDCD)*, pp. 275–280, April 2017.

[90] E. E. Ward and H. Hrer, "Preliminary investigation of an invertor-fed 5-phase induction motor," *Electrical Engineers, Proceedings of the Institution of*, vol. 116, pp. 980–984, June 1969.

[91] E. Levi, R. Bojoi, F. Profumo, H. A. Toliyat, and S. Williamson, "Multiphase induction motor drives - a technology status review," *IET Electric Power Applications*, vol. 1, pp. 489–516, July 2007.

[92] M. Qiao, C. Jiang, Y. Zhu, and G. Li, "Research on design method and electromagnetic vibration of six-phase fractional-slot concentrated-winding pm motor suitable for ship propulsion," *IEEE Access*, vol. 4, pp. 8535–8543, 2016.

[93] E. Levi, "Multiphase electric machines for variable-speed applications," *IEEE Transactions on Industrial Electronics*, vol. 55, pp. 1893–1909, May 2008.

[94] F. Terrien, S. Siala, and P. Noy, "Multiphase induction motor sensorless control for electric ship propulsion," in *Second International Conference on Power Electronics, Machines and Drives (PEMD 2004).*, vol. 2, pp. 556–561 Vol.2, March 2004.

[95] M. Steiner, R. Deplazes, and H. Stemmler, "A new transformerless topology for ac-fed traction vehicles using multi-star induction motors," *EPE Journal*, vol. 10, no. 3-4, pp. 45–53, 2000.

[96] A. V. Brazhnikov, N. N. Dovzhenko, A. N. Minkin, O. V. Pomolotova, A. I. Litvinenko, and V. A. Shilova, "Multiphase hybrid traction drives for electrical vehicles," in *2014 International Symposium on Power Electronics, Electrical Drives, Automation and Motion*, pp. 583–588, June 2014.

[97] N. Schofield, X. Niu, and O. Beik, "Multiphase machines for electric vehicle traction," in *2014 IEEE Transportation Electrification Conference and Expo (ITEC)*, pp. 1–6, June 2014.

[98] A. Cavagnino, Z. Li, A. Tenconi, and S. Vaschetto, "Integrated generator for more electric engine: Design and testing of a scaled-size prototype," *IEEE Transactions on Industry Applications*, vol. 49, pp. 2034–2043, Sept 2013.

[99] W. Cao, B. C. Mecrow, G. J. Atkinson, J. W. Bennett, and D. J. Atkinson, "Overview of electric motor technologies used for more electric aircraft (mea)," *IEEE Transactions on Industrial Electronics*, vol. 59, pp. 3523–3531, Sept 2012.

[100] M. Villani, M. Tursini, G. Fabri, and L. Castellini, "High reliability permanent magnet brushless motor drive for aircraft application," *IEEE Transactions on Industrial Electronics*, vol. 59, pp. 2073–2081, May 2012.

[101] A. Tani, M. Mengoni, L. Zarri, G. Serra, and D. Casadei, "Control of multiphase induction motors with an odd number of phases under open-circuit phase faults," *IEEE Transactions on Power Electronics*, vol. 27, pp. 565–577, Feb 2012.

[102] E. Levi, M. Jones, S. N. Vukosavic, and H. A. Toliyat, "Operating principles of a novel multiphase multimotor vector-controlled drive," *IEEE Transactions on Energy Conversion*, vol. 19, pp. 508–517, Sept 2004.

[103] E. Levi, M. Jones, S. N. Vukosavic, and H. A. Toliyat, "A novel concept of a multiphase, multimotor vector controlled drive system supplied from a single voltage source inverter," *IEEE Transactions on Power Electronics*, vol. 19, pp. 320–335, March 2004.

[104] Y. Zhao and T. A. Lipo, "Space vector pwm control of dual three-phase induction machine using vector space decomposition," *IEEE Transactions on Industry Applications*, vol. 31, pp. 1100–1109, Sep 1995.

[105] L. D. Camillis, M. Matuonto, A. Monti, and A. Vignati, "Optimizing current control performance in double winding asynchronous motors in large power inverter drives," *IEEE Transactions on Power Electronics*, vol. 16, pp. 676–685, Sep 2001.

[106] A. Tessarolo, M. Bortolozzi, and A. Contin, "Modeling of split-phase machines in park's coordinates. part i: Theoretical foundations," in *Eurocon 2013*, pp. 1308–1313, July 2013.

[107] A. Tessarolo, M. Bortolozzi, and A. Contin, "Modeling of split-phase machines in park's coordinates. part ii: Equivalent circuit representation," in *Eurocon 2013*, pp. 1314–1319, July 2013.

[108] C. L. Fortescue, "Method of symmetrical co-ordinates applied to the solution of polyphase networks," *Transactions of the American Institute of Electrical Engineers*, vol. XXXVII, pp. 1027–1140, July 1918.

[109] A. Tessarolo, "On the modeling of poly-phase electric machines through vector-space decomposition: Theoretical considerations," in *2009 International Conference on Power Engineering, Energy and Electrical Drives*, pp. 519–523, March 2009.

[110] A. Tessarolo, "On the modeling of poly-phase electric machines through vector-space decomposition: Numeric application cases," in *2009 International Conference on Power Engineering, Energy and Electrical Drives*, pp. 524–528, March 2009.

[111] V. I. Patel, J. Wang, D. T. Nugraha, R. Vuleti, and J. Tousen, "Enhanced availability of drivetrain through novel multiphase permanent-magnet machine drive," *IEEE Transactions on Industrial Electronics*, vol. 63, pp. 469–480, Jan 2016.

[112] L. Parsa and H. A. Toliyat, "Five-phase permanent magnet motor drives for ship propulsion applications," in *IEEE Electric Ship Technologies Symposium, 2005.*, pp. 371–378, July 2005.

[113] M. Barcaro, N. Bianchi, and F. Magnussen, "Faulty operations of a pm fractional-slot machine with a dual three-phase winding," *IEEE Transactions on Industrial Electronics*, vol. 58, pp. 3825–3832, Sept 2011.

[114] M. Barcaro, N. Bianchi, and F. Magnussen, "Analysis and tests of a dual three-phase 12-slot 10-pole permanent-magnet motor," *IEEE Transactions on Industry Applications*, vol. 46, pp. 2355–2362, Nov 2010.

[115] M. Ooshima, A. Kobayashi, and T. Narita, "Stabilized suspension control strategy at failure of a motor section in a d-q axis current control bearingless motor," in *2015 IEEE Industry Applications Society Annual Meeting*, pp. 1–7, Oct 2015.

[116] X. Wang, X. Ren, and J. Y. Zhang, "Short-circuit fault-tolerant control of bearingless permanent magnet slice machine," in *2013 IEEE Energy Conversion Congress and Exposition*, pp. 1148–1153, Sept 2013.

[117] A. Laiho, A. Sinervo, J. Orivuori, K. Tammi, A. Arkkio, and K. Zenger, "Attenuation of harmonic rotor vibration in a cage rotor induction machine by a self-bearing force actuator," *IEEE Transactions on Magnetics*, vol. 45, pp. 5388–5398, Dec 2009.

[118] R. Herzog, P. Buhler, C. Gahler, and R. Larsonneur, "Unbalance compensation using generalized notch filters in the multivariable feedback of magnetic bearings," *IEEE Transactions on Control Systems Technology*, vol. 4, pp. 580–586, Sep 1996.

[119] C. Peng, J. Fang, and X. Xu, "Mismatched disturbance rejection control for voltage-controlled active magnetic bearing via state-space disturbance observer," *IEEE Transactions on Power Electronics*, vol. 30, pp. 2753–2762, May 2015.

[120] C. Peng, J. Sun, X. Song, and J. Fang, "Frequency-varying current harmonics for active magnetic bearing via multiple resonant controllers," *IEEE Transactions on Industrial Electronics*, vol. 64, pp. 517–526, Jan 2017.

[121] A. Noshadi, J. Shi, W. S. Lee, P. Shi, and A. Kalam, "System identification and robust control of multi-input multi-output active magnetic bearing systems," *IEEE Transactions on Control Systems Technology*, vol. 24, pp. 1227–1239, July 2016.

[122] A. Sinervo and A. Arkkio, "Rotor radial position control and its effect on the total efficiency of a bearingless induction motor with a cage rotor," *IEEE Transactions on Magnetics*, vol. 50, pp. 1–9, April 2014.

[123] A. Sinervo, A. Laiho, and A. Arkkio, "Low-frequency oscillation in rotor vibration of a two-pole induction machine with extra four-pole stator winding," *IEEE Transactions on Magnetics*, vol. 47, pp. 2292–2302, Sept 2011.

[124] A. Sinervo and A. Arkkio, "Eccentricity related forces in two-pole induction motor with four-pole stator damper winding analyzed using measured rotor orbits," *IEEE Transactions on Magnetics*, vol. 49, pp. 3029–3037, June 2013.

[125] K. P. Kovacs, "Two-pole induction-motor vibrations caused by homopolar alternating fluxes," *IEEE Transactions on Power Apparatus and Systems*, vol. 96, pp. 1105–1108, July 1977.

[126] A. Chiba, T. Fukao, and M. A. Rahman, "Vibration suppression of a flexible shaft with a simplified bearingless induction motor drive," *IEEE Transactions on Industry Applications*, vol. 44, pp. 745–752, May 2008.

[127] W. Zhu, S. Pekarek, B. Fahimi, and B. J. Deken, "Investigation of force generation in a permanent magnet synchronous machine," *IEEE Transactions on Energy Conversion*, vol. 22, pp. 557–565, Sept 2007.

[128] Z. Q. Zhu, M. L. M. Jamil, and L. J. Wu, "Influence of slot and pole number combinations on unbalanced magnetic force in pm machines with diametrically asymmetric windings," *IEEE Transactions on Industry Applications*, vol. 49, pp. 19–30, Jan 2013.

[129] P. Bolognesi, "A mid-complexity analysis of long-drum-type electric machines suitable for circuital modeling," in *2008 18th International Conference on Electrical Machines*, pp. 1–5, Sept 2008.

[130] L. Papini, T. Raminosoa, D. Gerada, and C. Gerada, "A high-speed permanent-magnet machine for fault-tolerant drivetrains," *IEEE Transactions on Industrial Electronics*, vol. 61, pp. 3071–3080, June 2014.

[131] P. Bolognesi, F. Papini, L. Papini, and O. Bruno, "Effects of saturation on eccentricity force in permanent magnet synchronous machines," in *SPEEDAM 2010*, pp. 324–330, June 2010.

[132] M. I. Friswell, *Dynamics of rotating machines*. Cambridge University Press, 2010.

[133] K. Ogata, *Modern Control Engineering*, vol. Fourth edition. Prentice Hall, 2002.

[134] G. F. Franklin, J. D. Powell, A. Emami-Naeini, and J. D. Powell, *Feedback control of dynamic systems*, vol. 3. Addison-Wesley Reading, MA, 1994.

[135] J. B. Burl, *Linear optimal control: H (2) and H (Infinity) methods*. Addison-Wesley Longman Publishing Co., Inc., 1998.

[136] B. D. Anderson and J. B. Moore, *Optimal control: linear quadratic methods*. Courier Corporation, 2007.

[137] S. Skogestad and I. Postlethwaite, *Multivariable feedback control: analysis and design*, vol. 2. Wiley New York, 2007.

[138] A. Galassini, G. L. Calzo, A. Formentini, C. Gerada, P. Zanchetta, and A. Costabeber, "ucube: Control platform for power electronics," in *2017 IEEE Workshop on Electrical Machines Design, Control and Diagnosis (WEMDCD)*, pp. 216–221, April 2017.

[139] Z. Q. Zhu, D. Howe, E. Bolte, and B. Ackermann, "Instantaneous magnetic field distribution in brushless permanent magnet dc motors. i. open-circuit field," *IEEE Transactions on Magnetics*, vol. 29, pp. 124–135, Jan 1993.

[140] Z. Q. Zhu and D. Howe, "Instantaneous magnetic field distribution in brushless permanent magnet dc motors. ii. armature-reaction field," *IEEE Transactions on Magnetics*, vol. 29, pp. 136–142, Jan 1993.

[141] Z. Q. Zhu and D. Howe, "Instantaneous magnetic field distribution in brushless permanent magnet dc motors. iii. effect of stator slotting," *IEEE Transactions on Magnetics*, vol. 29, pp. 143–151, Jan 1993.

[142] Z. Q. Zhu and D. Howe, "Instantaneous magnetic field distribution in permanent magnet brushless dc motors. iv. magnetic field on load," *IEEE Transactions on Magnetics*, vol. 29, pp. 152–158, Jan 1993.

[143] Z. Q. Zhu, Z. P. Xia, L. J. Wu, and G. W. Jewell, "Analytical modeling and finite-element computation of radial vibration force in fractional-slot permanent-magnet brushless machines," *IEEE Transactions on Industry Applications*, vol. 46, pp. 1908–1918, Sept 2010.

[144] M. Michon, R. C. Holehouse, K. Atallah, and J. Wang, "Unbalanced magnetic pull in permanent magnet machines," in *7th IET International Conference on Power Electronics, Machines and Drives (PEMD 2014)*, pp. 1–6, April 2014.

[145] H. Mahmoud and N. Bianchi, "Analytical comparison of synchronous reluctance and surface permanent magnet machines with rotor eccentricity," in *2015 IEEE Energy Conversion Congress and Exposition (ECCE)*, pp. 1765–1772, Sept 2015.